DEVELOPMENT OF ALGORITHMS FOR ASPHALT PAVEMENT COMPACTION MONITORING UTILIZING GROUND PENETRATING RADAR

BY

PENGCHENG SHANGGUAN

DISSERTATION

Submitted in partial fulfillment of the requirements
for the degree of Doctor of Philosophy in Civil Engineering
in the Graduate College of the
University of Illinois at Urbana-Champaign, 2014

Urbana, Illinois

Doctoral Committee:
Professor Imad L. Al-Qadi, Chair
Professor Jianming Jin
Professor John T. Harvey, University of California, Davis
Professor Erol Tutumluer
Professor Hasan Ozer

ABSTRACT

The density of asphalt mixture plays an important role in the performance of asphalt pavement. Compaction is critical for achieving the desired density during the construction of asphalt pavement. To ensure successful compaction, the density of asphalt pavement should be monitored in a timely manner, and the information should be fed back to the compactor operator to avoid under-compaction or over-compaction. This study proposes a technique based on ground penetrating radar (GPR) for monitoring the density of asphalt pavement during compaction continuously, non-destructively, and in real time.

The utmost challenge in developing this technique is to eliminate the effect of surface moisture, sprayed by the compactor during compaction, on GPR data. The increase of asphalt pavement density and surface moisture content can cause an increase in the amplitude of the reflection pulse in the GPR signals in time domain. To extract density information without the effect of surface moisture, numerical simulation, laboratory experiments, and field tests were conducted.

First, the difference between the effect of surface moisture variation and the effect of density variation on GPR signal was investigated. Numerical simulation was performed using the finite-difference time-domain (FDTD) method to study the propagation of GPR wave within pavement structure. Both simulation results and laboratory experimental results revealed the fundamental difference between the two effects: In frequency domain, the high frequency components of the GPR pulse is sensitive to density variation and variation of surface moisture content, and the low frequency components are only sensitive to the density variation. The difference

between the two effects is referred to as the “frequency-selective effect” in this dissertation.

Second, based on the findings of the “frequency-selective effect”, a “correction algorithm” was developed based on the “reference scan approach” to eliminate the effect of surface moisture and to extract density information. To develop and validate the algorithm, a full-scale test site was constructed with compaction pass number from 0 to 10, and a large amount of GPR data was collected from the pavement with different surface moisture contents. A total of 22 cores were taken for validation purposes. After applying the algorithm, it was found that the average density prediction error was reduced from 3.1% to 0.9%, thus indicating the effectiveness of the algorithm. The GPR system was tested in a field construction site. The system successfully monitored the density change after each roller pass during compaction. The density estimation results obtained from GPR after the final compaction had higher accuracy than the density results obtained from the nuclear density gauge.

ACKNOWLEDGMENT

I would like to express my heartfelt gratitude to Professor Imad Al-Qadi for giving me the opportunity to work on this interesting research and for guiding its successful completion with insightful suggestions along the way. His inspirational and supportive mentorship has greatly influenced my research and my life. I would also like to thank Professors Jianming Jin, John Harvey, Erol Tutumluer, and Hasan Ozer for serving on my doctoral committee and providing evaluations and suggestions for improvements.

Thanks are equally due to the research engineers at the Illinois Center for Transportation (ICT), Aaron Coenen, Jim Meister, Jeff Kern, and Greg Renshaw, who provided me with great help in laboratory experiments and field tests. My gratitude goes to ICT's staff and students for all the happy times we have spent together and for their help and support in different aspects of my research and my life.

During my Ph.D. studies, I took courses in the Department of Civil and Environmental Engineering (CEE), Department of Electrical and Computer Engineering (ECE), and Department of Computer Science (CS). I would like to thank the professors who instructed these courses. They are the world's top scholars in their respective fields and the experience of learning from them has shaped my skills, sparked my research ideas, and inspired me to be a creative researcher.

Last but not least, I especially thank my dear wife, Ronghua, who has always been with me, providing her love and support during this long process. Special thanks go to my beloved daughter, Emma, who came to my life and brought so much

happiness. My deepest gratitude goes to my parents, grandparents, uncles, aunties, and other family members for their unconditional love and encouragement.

Table of Contents

CHAPTER 1 INTRODUCTION

1.1 Background

Widely used in pavement construction, asphalt concrete (AC) provides smooth and quiet driving. While well-constructed asphalt pavement provides good service quality over its lifetime with minimum maintenance, poorly constructed asphalt pavement usually exhibits premature distresses, such as rutting, cracking, and deformation and requires costly repair and rehabilitation. Among the various factors that affect the performance of asphalt pavement, the density, or the air void content of the asphalt mixture, plays an important role. In pavement engineering, the terms asphalt mixture density and air void content can be used interchangeably; the relation between the two terms is described in Section 2.1. Density that is either too high or too low can lead to premature pavement failure.

During the construction of asphalt pavement, the asphalt mixture is laid on a bound or unbound base by the paver. The compactors then roll over the loose asphalt mat, expulsing the air voids from the asphalt mixture. The air-void content is reduced after each roller pass. Compaction is critical for achieving the desired density of asphalt pavement. The quality of newly constructed pavement depends largely on the quality of compaction during construction.

1.2 Problem Statement

To ensure successful compaction, it would be beneficial to develop a tool to monitor the change of asphalt pavement density after each roller pass. Because compaction is a continuous operation, the tool should be able to collect and interpret

data continuously, which means that the tool must not be in contact with the pavement. Assuming that such a tool exits, the operator of the compactor would be able to view the density formation in real time and adjust compaction parameters, such as vibration amplitude and frequency, rolling speed, number of rolling passes, sequence, and timing of the rolling passes.

None of the current techniques can perform the aforementioned functions. The laboratory measurement of cores and density gauges, including nuclear and non-nuclear density gauges, are considered two of the most commonly used methods for assessing the quality of compaction. However, both methods have limitations. Although the coring method provides accurate information about pavement density, it is destructive and only provides information at discrete locations. Furthermore, samples can be drilled only after compaction, which means that density information cannot be obtained during compaction. Nuclear or non-nuclear density gauges are non-destructive; however, the gauges must be in contact with the pavement surface, and data collection lasts several seconds to minutes. Similar to the coring method, density gauges provide information only at discrete locations and are incapable of providing real-time information. In addition, the nuclear density gauge uses radioactive material and thus requires special licensing to transport and operate, which entails increased operational costs.

The ground penetrating radar (GPR) is a non-destructive testing (NDT) tool that has been successfully applied to estimate pavement thickness *(1–9)*, locate anomalies beneath the pavement surface *(10, 11)*, and estimate asphalt pavement density *(12–14)* by sending and receiving electromagnetic (EM) waves. The principle of GPR is

introduced in Section 2.4. One of the advantages of using air-coupled GPR is the continuous collection of data at highway speed without destructing pavement or disturbing traffic flow *(3–6, 8, 12, 13)*.

Previous research has indicated that GPR is a promising technique for monitoring the status of compaction during the construction of asphalt pavement *(14, 15)*. However, while asphalt pavement density is measured using GPR, the technique is only applied after construction when the asphalt pavement is dry. Few researchers have used GPR to monitor the density of asphalt pavement during compaction because of the challenge of the unknown effect of surface moisture on GPR signals *(15)*. During compaction, the compactor sprays water on the drum to prevent the asphalt particles from sticking to the compactor's roller, as shown in Figure 1-1. The water remaining on the pavement surface influences the GPR signal and increases the amplitude of the reflection pulse at the pavement surface.

Figure 1-2 (a) depicts the procedure of density estimation using GPR data collected from dry pavement. The surface reflection amplitude is extracted from the GPR signal, and the dielectric constant value is obtained. The introduction of dielectric constant calculation is included in Section 2.4. By applying density model, the density of the pavement is then obtained. However, when surface moisture exists during compaction, the GPR data collected from wet pavement contains higher surface reflection amplitude, thus resulting in higher dielectric constant value, as shown in Figure 1-2 (b). By applying density model, the density of the AC is overestimated. Therefore, the effect of surface moisture on the GPR signal poses a significant challenge which prevents the direct application of density estimation model. This effect

has to be eliminated to allow for the accurate estimation of AC density using GPR during the construction of asphalt pavement.

Figure 1-1 Compactor sprays water on the roller during compaction.

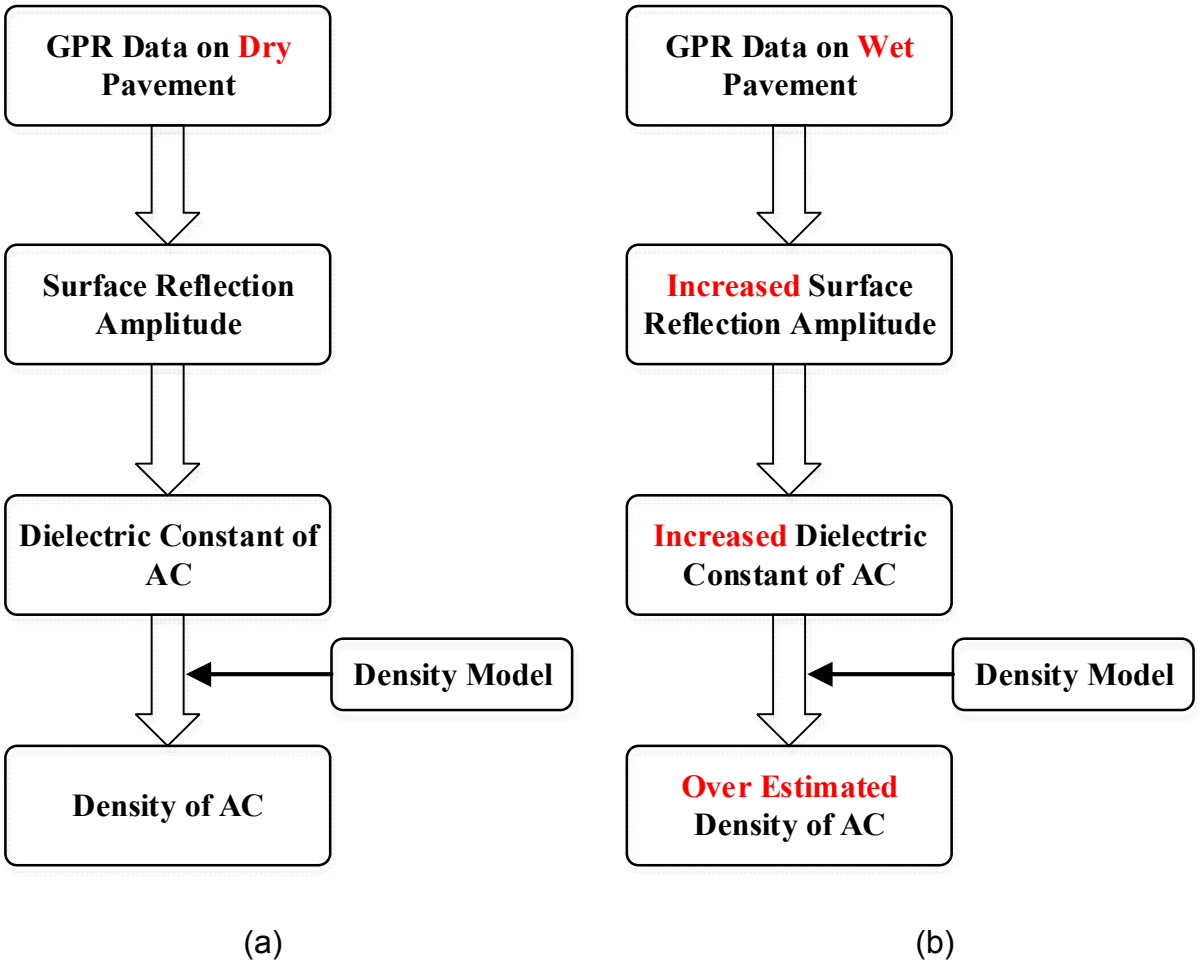

Figure 1-2 Effect of surface moisture on estimated density of asphalt pavement from GPR signal: (a) density estimation procedure on dry pavement; (b) density estimation procedure on wet pavement.

1.3 Research Objective and Approaches

The objective of this research is to develop algorithms to process and interpret the GPR data collected from asphalt pavement during compaction and to obtain density information after each roller pass. To achieve this objective, the research efforts focus on addressing the challenge of eliminating the effect of surface moisture on GPR signal

which has been investigated through different approaches, including numerical simulation and laboratory experiments. Signal processing techniques are used to eliminate the effect of surface moisture on GPR signal. The algorithms developed in this study aim to “correct” the GPR signal collected from the wet pavement surface in order to resemble the signal collected from dry pavement. The dielectric constant and the density of the asphalt mixture will then be obtained. GPR data are collected from both laboratory experiments and field construction sites to validate effectiveness of the algorithms.

The ultimate objective of this study is to integrate the GPR system with the compactor and other sensors, including global positioning system (GPS), accelerometer, and infrared sensor, to monitor the density change in real time during compaction. Further improvement can be made to achieve automatic adjustments of compaction parameters, such as vibration amplitude, frequency and rolling speed, to optimize the compaction efforts. This cannot be done without accurate measurement of density in real time. The research efforts presented in this dissertation is critical to achieve real “intelligent compaction”.

1.4 Organization of the Dissertation

This dissertation consists of five chapters. Chapter 1 presents the background of the research and an introduction of the research objectives and approaches. Chapter 2 presents the current state of knowledge on various techniques for compaction monitoring during the construction of AC; the principle of GPR technology and its application for estimating the density of AC are also introduced in this chapter. Chapter 3 describes the detailed research approaches, including numerical simulation,

laboratory experiments, and field tests. Chapter 4 details the data processing and interpretation of the GPR data generated from numerical simulation, laboratory experiments, and field tests; algorithms are developed in this chapter in order to achieve the research objectives defined in Chapter 1. Finally, Chapter 5 presents the findings, conclusions, and recommendations for further study.

1.5 Significance of the Research

Currently, most states in the U.S. are applying a “pay-for-performance/quality” mode for pavement construction. Contractors strive to achieve the required pavement layer density to avoid payment adjustments. An owner’s failure to achieve the required density may result in a reduction in the pavement service life. Developing a tool for monitoring the density of AC during compaction can effectively and efficiently help achieve the required pavement density, which is beneficial for both contractors and owners.

In a new application of GPR, the tool will be deployed to enhance the quality of compaction and ultimately improve the quality of newly constructed asphalt pavement. This dissertation addresses the utmost challenge of this application, which is the elimination of the effect of surface moisture on GPR signal during compaction. The algorithms developed in this dissertation will enable the pavement compactor operator to monitor the density change before and after each roller pass. With further development based on the outcome of this dissertation, the GPR system can be integrated with an intelligent compactor to monitor asphalt concrete density continuously, in real time, and without the effect of asphalt mat temperature. This will allow the

compactor operator to adjust compaction parameters, such as vibration amplitude and frequency, for optimizing layer compaction and achieving the desired density.

CHAPTER 2 RESEARCH BACKGROUND

2.1 Density of Asphalt Mixture

The density of the asphalt mixture is critical to the performance of flexible pavement. In pavement engineering, the terms asphalt mixture density and air void content are used interchangeably. They are related by the following equation *(16)*:

$$V_a = 100\left(\frac{G_{mm} - G_{mb}}{G_{mm}}\right) \quad (2\text{-}1)$$

where V_a is the air void content in percentage (%), G_{mm} is the theoretical maximum specific gravity of asphalt mixture, and G_{mb} is the lab-measured specific gravity of the asphalt mixture. The specific gravity is equal to the density of the asphalt mixture divided by the density of water at 4°C (39.2°F) and has a known value of 1g/cm^3 (62.4 lb/ft^3). Thus, G_{mm} and G_{mb} are dimensionless quantities that are numerically equal to the maximum density and bulk density of the asphalt mixture, respectively.

Various research studies have been conducted to study the effect of air void content on the performance of asphalt pavement *(17–19)*. It is generally concluded that the in-place air void content should remain within an acceptable range. High air void content leads to moisture damage, binder oxidation, and pavement raveling and cracking *(17)*. In dense-graded mixtures with air void content exceeding seven percent, a one-percent increase in the air void content could reduce pavement service life by ten percent *(18)*. On the other hand, low air void content generally leads to higher mixture stiffness and lower rutting potential *(17)*. However, if the air void content in a dense-

graded asphalt mixture drops below three percent, significant permanent deformation and shoving may occur *(17, 19)*.

The in-place density of new asphalt pavement depends primarily on two factors: mixture design and compaction. Asphalt mixture design comprises the selection of aggregate, binder, and the optimum combination of the two components. The density may be affected by several factors, including the gradation, shape, and fractured faces of aggregate as well as the chemical and physical properties and the amount of asphalt binder. Compaction is another important factor for achieving the desired asphalt pavement density. The impact of compaction on the density of asphalt pavement is discussed in Section 2.2.

2.2 Compaction of Asphalt Pavement

During construction, the densification of asphalt pavement is achieved by compaction after the asphalt mixture mat is placed. During compaction, the volume of the air void is reduced and the unit weight of the mixture is increased *(19)*.

Asphalt mixtures consist of asphalt binder, aggregate, and air void. During compaction, the air is expulsed by an external force that enables the mixture to occupy a smaller space *(19)*. The aggregate particles, which are coated by asphalt binder, are reoriented as the binder flows under the external compaction forces. The aggregate particles rotate and slide, and the shearing of binder occurs at the binder-aggregate interfaces, until both internal and external forces reach an equilibrium within the mixture *(20)*.

The factors affecting compaction include the thickness of asphalt mixture layer, properties of the underlying material, vibration magnitude and frequency of the vibratory

compactor, pattern of the compaction, and environmental conditions, such as temperature, at the time of construction *(19, 21)*.

Brown et al. *(22)* found that the density of the asphalt mixture obtained through compaction is related to the ratio of lift thickness, *t*, and the nominal maximum aggregate size (NMAS). To increase compatibility, Brown et al. recommended that the t/NMAS ratio be at least three for fine-graded mixes and four for coarse-graded mixes. In addition, they found that the faster the cooling of thin lift mixes, the lower the density results.

With regard to the mechanism of asphalt compaction, Masad et al. *(23)* proposed an automated image analysis procedure for analyzing the internal structure after laboratory compaction. The procedure resulted in revealing the aggregate orientation, aggregate contacts, and air void distribution. The study compared the internal structure of asphalt mixture specimens compacted by the Superpave gyratory compactor (SGC) with the structure of the specimens compacted by the linear kneading compactor (LKC). It was found that the aggregate of specimens compacted with SGC had preferable orientation and fewer contacts compared with the LKC specimens. Furthermore, the distribution of the air void also differed in both compaction methods.

Finite element models have been developed to study the compaction of asphalt pavement. Xia and Pan (2011) developed a three-dimensional finite element model to simulate vibratory compaction, thus showing that the greatest densification took place during the 1st roller pass while the subsequent roller passes provided diminishing gains in density. The authors also found that the vibratory compactor resulted in better compaction compared with the non-vibratory compactor.

2.3 Current and Emerging Techniques for Pavement Compaction Monitoring

During asphalt pavement construction, pavement density tests should be conducted to ensure that the prescribed level of density is achieved. Current test methods include the laboratory measurement of cores drilled from pavement, which is a destructive testing approach, and the in-place density measurement using a nuclear density gauge or non-nuclear density gauge. In addition, the intelligent compaction technique has recently gained attention. The infrared thermography technique has also been used in the asphalt paving process. Each of these techniques is briefly introduced hereafter.

2.3.1 Coring

The traditional method used for obtaining density information of asphalt pavement is the laboratory measurement of cores. This requires the extraction of cores from the pavement, as shown in Figure 2-1. The diameter of the core ranges between 4 in and 6 in (100 mm and 150 mm).

Figure 2-1 Core extraction from asphalt pavement.

After extraction, the cores are measured in the laboratory. Several methods are used to determine the density of field cores in the laboratory. The saturated surface dry (SSD) method is commonly used to obtain the G_{mb} value *(24, 25)*. Other methods include the Corelok *(26)* and the paraffin and parafilm methods *(27, 28)*. The SSD method is considered more accurate for cores with low air void content and less accurate for cores with high air void content, such as the cores with air void content exceeding 8 to 10 percent. For cores with high air void content, the Corelok method is used to obtain more accurate results.

Although the laboratory measurement of extracted cores is the most accurate method for obtaining density information of asphalt mixtures, this method has its own disadvantages; it is destructive, time consuming, and costly.

2.3.2 Nuclear Density Gauges

The nuclear density gauge is a NDT method widely used for the in-place measurement of asphalt pavement density. Figure 2-2 depicts the use of nuclear density gauges for checking the density of asphalt pavement. The principle of the nuclear density gauge is based on the interaction of gamma radiation with matter. Gamma rays, which are emitted from a gamma source such as Cesium-137 at the end of a retractable rod, interact with the electrons in the pavement. A detector counts the number of received gamma rays and translate it to the pavement density *(29)*.

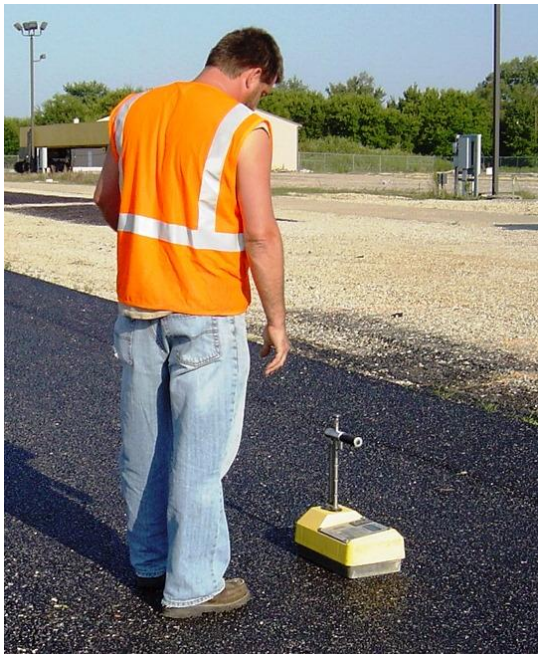

Figure 2-2 Use of nuclear density gauge on measuring asphalt pavement density.

Compared with the coring method, the nuclear density gauge saves time and effort. However, the gauges involve a variety of challenges, including the use of radioactive materials, which present potential health risks to operators and the public, and require licensing, certification, and special handling during operation and storage, which renders this method a costly choice. In addition, the nuclear density gauge measures the density at discrete locations only and therefore it fails to comprehensively represent the density of the compacted asphalt mat.

2.3.3 Non-nuclear Density Gauges

The recently developed non-nuclear density gauge has the advantage of being free of radioactive materials. This method, therefore, does not require stringent training or licensing for the operation of the gauge. The non-nuclear density gauge uses EM

waves to measure the density of asphalt pavement. It measures the change in the EM field when an electrical current is transmitted through the asphalt pavement. The dielectric constant value is obtained based on the impedance of the asphalt material to the electric flow. The density of pavement is obtained from the dielectric constant value based on the relationship between the dielectric constant and the density of asphalt pavement.

There are mainly two types of non-nuclear density gauges: Pavement Quality Indicator™ (PQI ™), which was developed by TransTech, Inc. *(30)*, and PaveTracker™, which is currently marketed by Troxler Electronic Laboratories Inc *(31)*. Figure 2-3 (a) shows PQI model 301 non-nuclear density gauge, and Figure 2-3 (b) shows PaveTracker model 2701-B non-nuclear density gauge.

(a) (b)

Figure 2-3 Non-nuclear density gauge: (a) PQI model 301; (b) PaveTracker model 2701-B *(32)*.

Since the invention of non-nuclear density gauges, continuous improvements were made to eliminate measurement errors. The accuracy of non-nuclear density gauges measurement results, which are affected by a number of factors, is not as good as the results of the coring and nuclear density gauge methods *(32)*. For instance, the readings of non-nuclear density gauges are significantly affected by moisture. Sargand et al. *(33)* reported that gauge readings decreased appreciably with the increase in surface moisture and increased in presence of internal moisture. The accuracy of density measurement could drop significantly if it is used during the compaction process in presence of roller-sprayed water on the pavement surface. Although non-nuclear density gauges collect data within a few seconds, which is much faster than the nuclear density gauge, they are considered sport test methods and therefore require surface contact with the pavement. Thus, the gauges cannot provide continuous measurement with the moving compactor.

2.3.4 Intelligent Compaction Technology

An emerging technology, intelligent compaction (IC) refers to the compaction of road materials, such as soil, aggregate base, and asphalt pavement using an in-situ measurement system and feedback control *(34)*. IC techniques are based on the effect of the compacted pavement stiffness on the vibration of the roller *(35)*. IC rollers are usually equipped with various types of sensors for data collection. For example, a GPS is used to collect information about the roller's location. Compaction meters or accelerometers are mounted on the roller to measure the effort, frequency, and response of the compacted material. The integration of the measurements, documents, and control system allows real-time monitoring of the compaction process and

adjustment of the compaction operation. Figure 2-4 shows the status of compaction monitoring with the compaction information system installed on a Sakai asphalt IC roller.

Figure 2-4 Compaction information system on a Sakai asphalt IC roller *(36)*.

However, the IC technique has limitations. For instance, the correlation between the IC measurement and the asphalt pavement density is low *(34)* because the technique is based on measuring the stiffness of the pavement system, which is affected by various factors, including the pavement temperature, conditions of underlying layers, and amplitude and frequency of the roller vibration *(34)*. Consequently, the increase in stiffness might be the result of other factors, such as a reduction in temperature rather than an increase in density.

2.3.5 Infrared Thermography

Temperature is considered an important factor affecting the compaction of asphalt pavement. The viscosity of the asphalt binder increases when the temperature drops and the asphalt mixture becomes difficult to compact. Cooler areas, which are usually developed during transportation of the material from plant to the job site, may have inadequate compaction and, therefore, develop lower density. The isolated low-density areas are characterized with low strength, reduced fatigue life, and moisture damage *(37)*. Therefore, the temperature of the asphalt mat should be monitored during construction. Temperature differentials greater than 13.9°C (25°F) may cause compaction problems *(38)*. Thermal segregation should be detected during the paving process to allow proper modifications in a timely manner.

Infrared thermography is applied to detect temperature variations on the pavement surface when the asphalt mixture is laid down. Figure 2-5 shows the Pave-IR system manufactured by the MOBA Automation Corp. Figure 2-5 (a) shows the setup of a thermal sensor beam, where 12 thermal cameras are mounted on an aluminum support bar. The thermal sensor beam measures the temperature across the pavement behind the paver. Temperature readings, in addition to other parameters, such as speed of the paver and GPR coordinates, are displayed on a multi-color screen so the operator can visually monitor the temperature and observe temperature segregations. Figure 2-5 (b) shows the newly developed setup of an infrared thermal scanner mounted above the paver deck. The new system can also generate the temperature profile covering the width of the pavement.

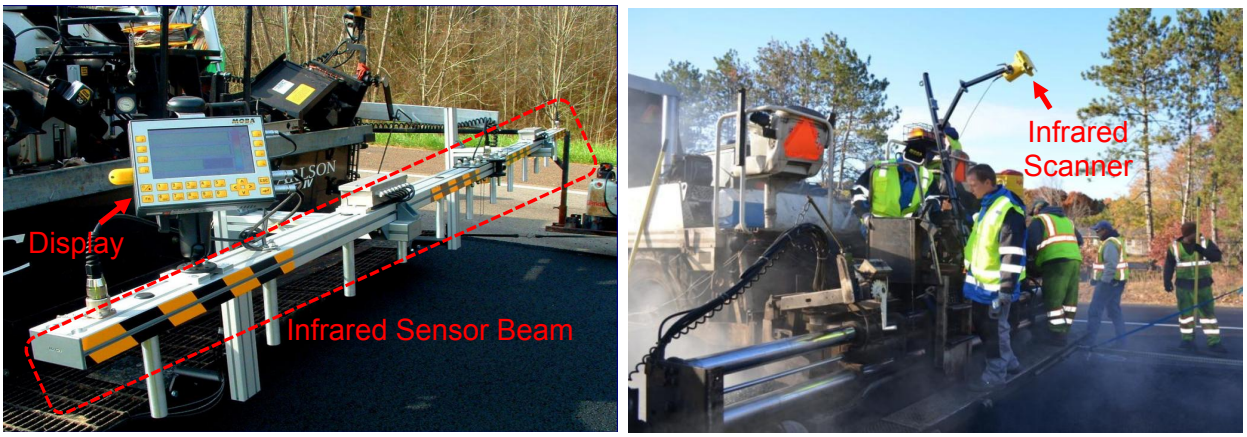

(a) (b)

Figure 2-5 Pave-IR system mounted on the paver: (a) Pave-IR system with temperature sensor beam; (b) new Pave-IR system with infrared scanner above paver deck *(39)*.

2.4 The Principle of Ground Penetrating Radar (GPR)

Ground penetrating radar is a NDT tool that has been successfully applied for decades for infrastructure assessment. The application of GPR in pavement engineering focuses on the measurement of thickness and the detection of anomalies beneath the surface. Recently, GPR has been applied for estimating asphalt pavement density *(12–14, 40)*. This chapter introduces the principle of GPR and presents a review of density estimation using GPR.

2.4.1 GPR Systems

The main components of a GPR system include: control unit, antennas, distance measuring instrument (DMI), and optional global navigation satellite system (GNSS). Figure 2-6 shows a GPR control unit, SIR-20 system, manufactured by Geophysical Survey Systems, Inc. (GSSI). Figure 2-7 shows the components of a vehicle-mounted

GPR system. Two antennas are mounted on the back of the vehicle. DMI is mounted on the back wheel. A GPS receiver is mounted on top of the vehicle.

During the GPR survey, the SIR-20 system sends the signal to the antennas. The transmitting antenna emits EM waves into the ground, and the receiving antenna collects the EM waves scattered back by the ground. The EM wave is translated to signals, and the signals are displayed on the SIR-20 system laptop screen, as shown in Figure 2-6. The signals are analyzed to obtain information about the structure and materials, such as layer thickness and subsurface defects. The DMI and GPS devices are connected to the SIR-20 system to control the emission of the EM wave; the devices incorporate distance and location information with the GPR data.

Figure 2-6 Control unit of a GPR system.

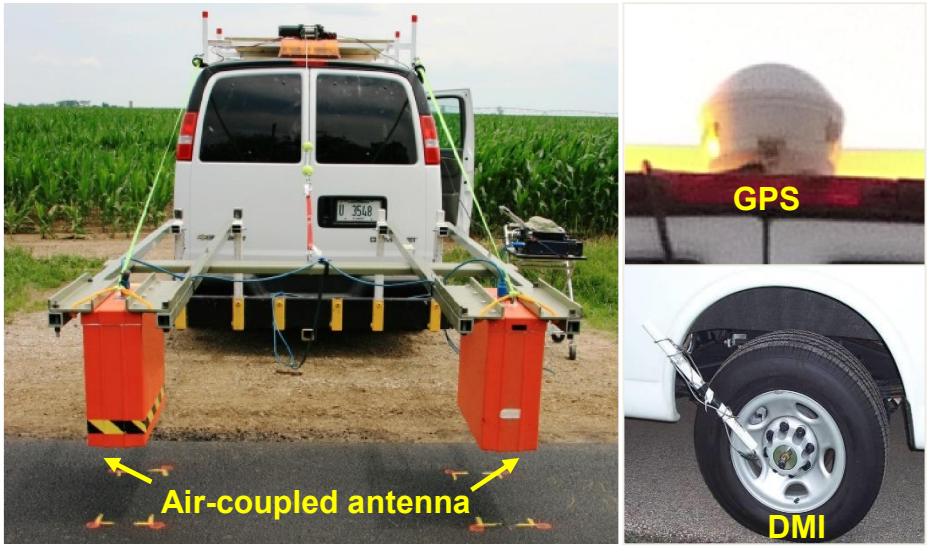

Figure 2-7 Components of a vehicle-mounted air-coupled GPR system.

Depending on the way the antennas are deployed, GPR antennas can be grouped into two categories: 1) air-coupled antennas; and 2) ground-coupled antennas. An air-coupled antenna is installed at a specific height, usually 6 in to 24 in (0.15 m to 0.50 m) above the ground surface, as shown in Figure 2-7. An air-coupled GPR system can collect GPR data at high speed without any contact with the ground. For pavement survey, the speed can be as high as highway speed (up to 96 km/h or 60 mph), and the survey can be done without interrupting traffic. Figure 2-8 depicts a ground-coupled GPR antenna on top of a concrete slab. The ground-coupled antenna system is in full contact with the surface of the surveyed objects. Thus, the speed of data collection in ground-coupled antennas is lower compared with the air-coupled antennas.

(a) (b)

Figure 2-8 Ground-coupled antenna: (a) top view; (b) side view.

Based on the number of antennas, GPR antennas can be grouped into monostatic (a single antenna is used as a transmitter and receiver), bistatic (one antenna is used as a transmitter and another as a receiver), or multistatic (a single or multiple antennas are used as transmitters and multiple antennas are used as receivers). The antennas shown in Figure 2-6 and Figure 2-7 are bistatic antennas.

Based on the signals emitted by the GPR system, there are mainly two types of signals used by commercial GPR systems: pulse (or impulse) signals and step-frequency signals. For civil engineering applications, range information such as pavement thickness and rebar depth is usually of interest. A signal with ultra-wide bandwidth (UWB) is preferred because, with its short duration in time domain, it is easier to set time markers representing the interfaces or inhomogeneities in the received signal. A broadband pulse is generated by two methods: the time domain impulse method and step-frequency method *(41)*.

The time domain impulse is the most commonly used method for generating UWB signal in GPR systems. A typical impulse signal is shown in Figure 2-9. The signal is collected using air-coupled antennas. The first pulse is the coupling pulse, which isthe EM wave travelling directly from the transmitter to the receiver. For air-coupled antennas, the coupling pulse does not contain information about the pavement and is, therefore, usually discarded. The second pulse, which is the largest pulse in the entire signal, is the pulse reflected at the pavement surface. The third pulse is at around 7.5 ns in the reflection pulse from another interface. These two pulses serve as time makers representing the interfaces for easy interpretation.

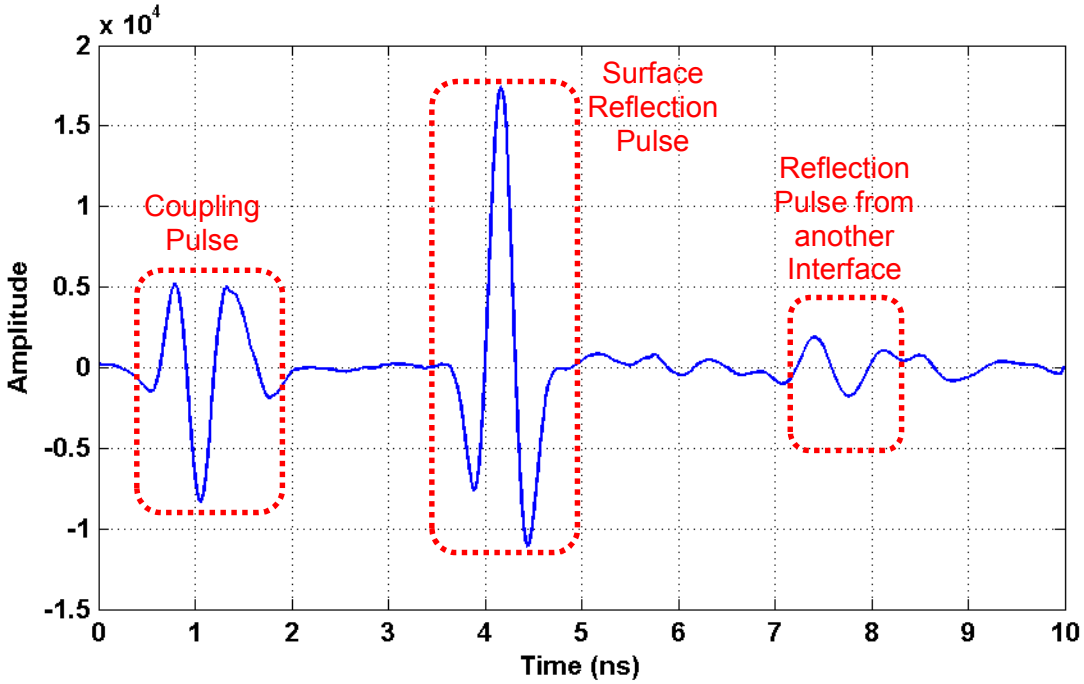

Figure 2-9 GPR signal collected from pavement using air-coupled antennas.

The recently developed 3D-Radar GPR system by 3D-Radar AS in Norway uses the step-frequency technique to generate broadband signals. Figure 2-10 depicts the

main components of the 3D-Radar system: antenna array, GeoScope radar unit (control unit), operator computer, survey wheel with DMI, and optional GPS. The components are similar to the GSSI radar. Instead of using single antenna unit, 3D-Radar GPR uses an antenna array. Figure 2-11 shows the alignment of antenna elements inside the antenna array. There are 11 transmitting elements (represented by “T”) and 11 receiving elements (represented by “R”). Each antenna element in the antenna array can transmit or receive EM waves. Altogether, the elements can generate 21 survey points.

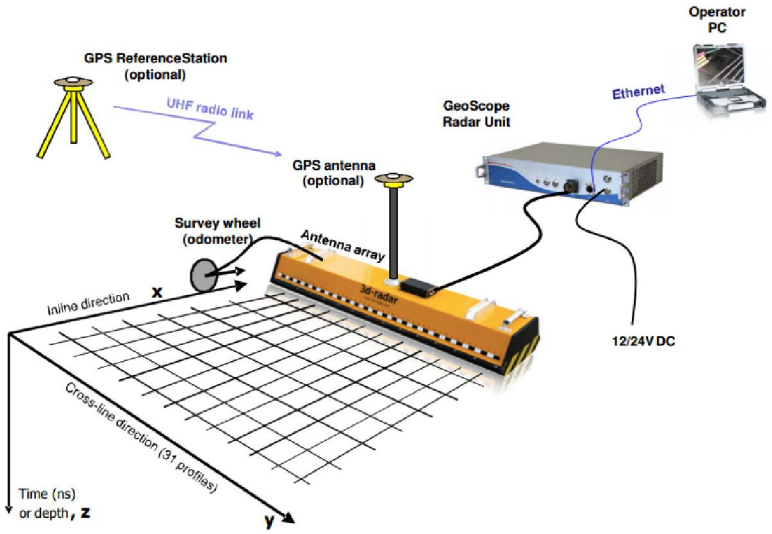

Figure 2-10 Operation principle of 3D-Radar GPR system *(42)*.

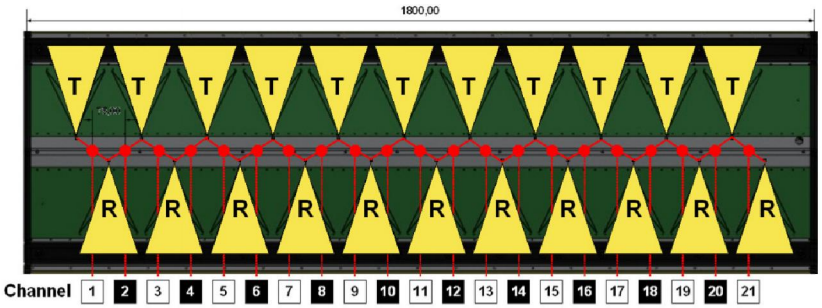

Figure 2-11 Antenna array with 21 channels*(43)*.

The concept of step frequency is shown in Figure 2-12. To generate a broadband signal, the system swipes the bandwidth with one frequency at each step. As shown in Figure 2-12 (a), dwell time is the time duration for one frequency. Frequency step is the size of the increase in frequency at each step. 3D-Radar generates waveforms from 100 MHz up to 3 GHz with as much as 1500 frequencies. The GPR system receives data in frequency domain by recording the amplitude and phase of each frequency. By applying inverse Fourier transform, data is transferred into time domain. An example of the time domain response is shown in Figure 2-12 (b). One of the advantages of using step-frequency technique is the ability to attain a higher signal-noise ratio because of the narrowband electronics. In addition, the step-frequency technique provides stable signal sources, thus resulting in increased measurement accuracy and stability *(41, 44)*. However, the disadvantage of using step frequency is that data collection time increases because of the addition of dwell time over the swiped frequencies. This could raise concerns when collecting data at high speed.

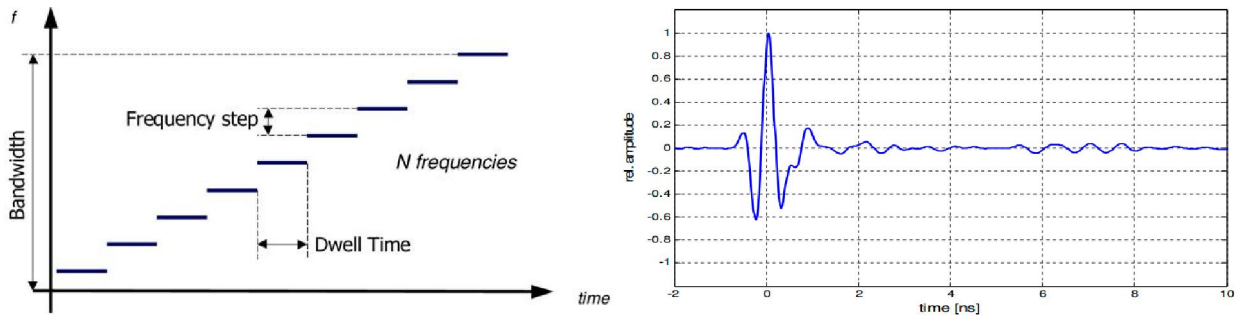

(a) (b)

Figure 2-12 Step-frequency signals: (a) step-frequency signal; (b) time domain response *(45)* .

For GPR systems, the selection of antenna frequency is of great importance. The frequency of the GPR wave affects the resolution and penetrating depth of the GPR system. A signal with a higher frequency has higher resolution and lower penetration depth. A signal with lower frequency provides greater penetration depth and lower resolution. For pavement applications, air-coupled antennas with 1 GHz and 2 GHz center frequencies have sufficient penetration depth (3 ft or 0.9 m for 1 GHz; 2.5 ft or 0.75 m for 2 GHz) and sufficient resolution (being able to distinguish interfaces of different layers). Furthermore, air-coupled antennas can collect data at high speed without contacting the pavement or disrupting the traffic and are therefore preferred for pavement survey.

2.4.2 Propagation of Electromagnetic Wave

The propagation of the EM wave within a medium is governed by Maxwell's equations and constitutive relations. Maxwell's equations relate the electric field and magnetic field to the sources, i.e., electric charges and currents. Maxwell's equations have different forms. In a continuous medium, Maxwell's equations can be expressed in differential form:

$$\nabla \times \mathbf{E} = -\frac{\partial \mathbf{B}}{\partial t} \text{ (Faraday's law)} \quad (2\text{-}2)$$

$$\nabla \times \mathbf{H} = \mathbf{J} + \frac{\partial \mathbf{D}}{\partial \boldsymbol{t}} \text{ (Maxwell-Ampère law)} \quad (2\text{-}3)$$

$$\nabla \cdot \mathbf{D} = \rho \text{ (Gauss' law)} \quad (2\text{-}4)$$

$$\nabla \cdot \mathbf{B} = 0 \text{ (Gauss' law-magnetic)} \quad (2\text{-}5)$$

where $\nabla \times$ is the curl operator, $\nabla \cdot$ is the divergence operator, $\mathbf{E}$ is the electric field intensity (volts/meter), $\mathbf{H}$ is the magnetic field intensity (amperes/meter), $\mathbf{D}$ is the electric flux density (coulombs/meter^2), $\mathbf{B}$ is the magnetic flux density (webers/meter^2), $\mathbf{J}$ is the electric current density (amperes/meter^2), and ρ is the electric charge density (coulombs/meter^3).

The constitutive relations define the effect of the medium on the EM fields, which are affected by the medium as a result of electric polarization, magnetic polarization, and electric conduction *(46)*. The constitutive relations can be described by the following equations:

$$\mathbf{D} = \varepsilon \mathbf{E} \quad (2\text{-}6)$$

$$\mathbf{B} = \mu \mathbf{H} \quad (2\text{-}7)$$

$$\mathbf{J} = \sigma \mathbf{E} \quad (2\text{-}8)$$

where ε is the permittivity of a medium (farads/meter), μ is the permeability of a medium (henries/meter), and σ is the conductivity of a medium (siemens/meter).

When applying GPR on asphalt pavement, the following assumptions are made regarding pavement mediums to simplify the analysis:

- Homogeneous: Asphalt mixtures consist of aggregate particles, asphalt binder, and air void. Aggregate particles are usually much smaller than the wavelength of the GPR wave. The internal scattering of EM waves is negligible. Therefore, it can be considered a homogeneous medium where $\nabla \varepsilon = \nabla \mu = \nabla \sigma$.
- Isotropic: The direction of $\mathbf{D}$ is parallel to that of $\mathbf{E}$, and the direction of $\mathbf{B}$ is parallel to that of $\mathbf{H}$.
- Non-dispersive: For a frequency range exceeding 0.5 GHz, which is the case for most GPR systems used in pavement surveys, the permittivity and permeability do not vary significantly. So, the values of ε and μ are considered independent from the frequency of the field.

The medium can be grouped into several categories based on conductivity. The medium is perfect dielectric or insulator when σ=0, perfect electric conductor (PEC) when σ→∞, and lossy medium when σ has a non-negligible finite value. In GPR surveys, a copper plate is used as a reflector to obtain the complete reflection signal. Copper plates are good conductors and are usually considered as PECs. Asphalt pavement has limited conductivity. In most GPR data analysis approaches, the material is considered as lossless. Lahouar *(47)* compared the thickness measurement results for lossy and lossless layers and noticed a similarity between both measurements. However, conduction represents one loss mechanism only. The other mechanism is polarization and magnetization when the medium is exposed to a time-varying EM field. This loss mechanism is characterized by the imaginary parts of permittivity and

permeability. But for asphalt pavement, polarization and magnetization losses are even smaller than conduction loss and are therefore neglected.

For a uniform plane wave, the phase velocity of the wave is given by the following:

$$v_p = \frac{\omega}{\beta} \tag{2-9}$$

where v_p is the phase velocity (meter/sec), ω is the angular frequency (rad/sec), and β is the phase constant (rad/meter).

For a lossless medium, $\beta = \omega\sqrt{\mu\varepsilon}$. The Equation (2-9) becomes Equation (2-10):

$$v_p = \frac{1}{\sqrt{\mu\varepsilon}} \tag{2-10}$$

The group velocity of the wave is given by Equatoin (2-11):

$$v_g = \frac{\Delta\omega}{\Delta\beta} \text{ for } \Delta\omega \to 0 \tag{2-11}$$

where Δ is vanishing small, and v_g is the group velocity.

For a lossless and non-dispersive medium, $\beta = \omega\sqrt{\mu\varepsilon}$ and μ and ε are independent of frequency. Equation (2-11) can be re-written as Equation (2-12):

$$\boldsymbol{v}_g = \frac{\Delta\omega}{\Delta\beta} = \left(\frac{\Delta\beta}{\Delta\omega}\right)^{-1} = \left(\frac{\boldsymbol{d}\beta}{\boldsymbol{d}\omega}\right)^{-1} = \frac{1}{\sqrt{\mu\varepsilon}} \tag{2-12}$$

In this case, the group velocity is equal to the phase velocity.

For vacuum, the permeability is $\mu = \mu_0 = 4\pi \times 10^{-7} = 1.256637061 \times 10^{-6}$ H/m, and the permittivity is $\varepsilon = \varepsilon_0 = 8.854187817 \times 10^{-12}$ F/m. Thus, the phase velocity and group velocity are the same as the speed of light:

$$\boldsymbol{v}_p = \boldsymbol{v}_g = \frac{1}{\sqrt{\mu_0\varepsilon_0}} = 2.997925 \times 10^8 \text{ m/s} \tag{2-13}$$

For lossless materials such as asphalt pavement material, permittivity and permeability can also be written as Equations (2-14) and (2-15):

$$\mu = \mu_0\mu_r \tag{2-14}$$

$$\varepsilon = \varepsilon_0\varepsilon_r \tag{2-15}$$

where μ_r is the relative permeability normalized with the permeability of vacuum, and ε_r is the relative permittivity normalized with the permittivity of vacuum.

For most of the material in reality, the value of μ_r is 1, where *c* represents the speed of light, and the group and phase velocity of the EM wave within the medium is:

$$\boldsymbol{v}_p = \boldsymbol{v}_g = \frac{1}{\sqrt{\mu\varepsilon}} = \frac{\boldsymbol{c}}{\sqrt{\varepsilon_r}} \tag{2-16}$$

In GPR applications, the pavement system is considered a flat-layered system. When the EM wave encounters interfaces of the layered system, part of the EM wave

energy is reflected back and part of the energy is transmitted through the interface into another medium. Portions of the reflected wave and transmitted wave are characterized by reflection coefficient and transmission coefficient.

For the planner-layered medium shown in Figure 2-13, the region is divided by the interface which coincides with the xy-plane. The medium in Region 1 in the half-space z<0 has permittivity ε_1 and permeability μ_1. The medium in Region 2 in the half-space z>0 has permittivity ε_2 and permeability μ_2. Figure 2-13 (a) depicts the reflection and transmission of transvers electric (TE) wave or perpendicular wave, and Figure 2-13(b) depicts the reflection and transmission of transvers magnetic (TM) wave or parallel wave.

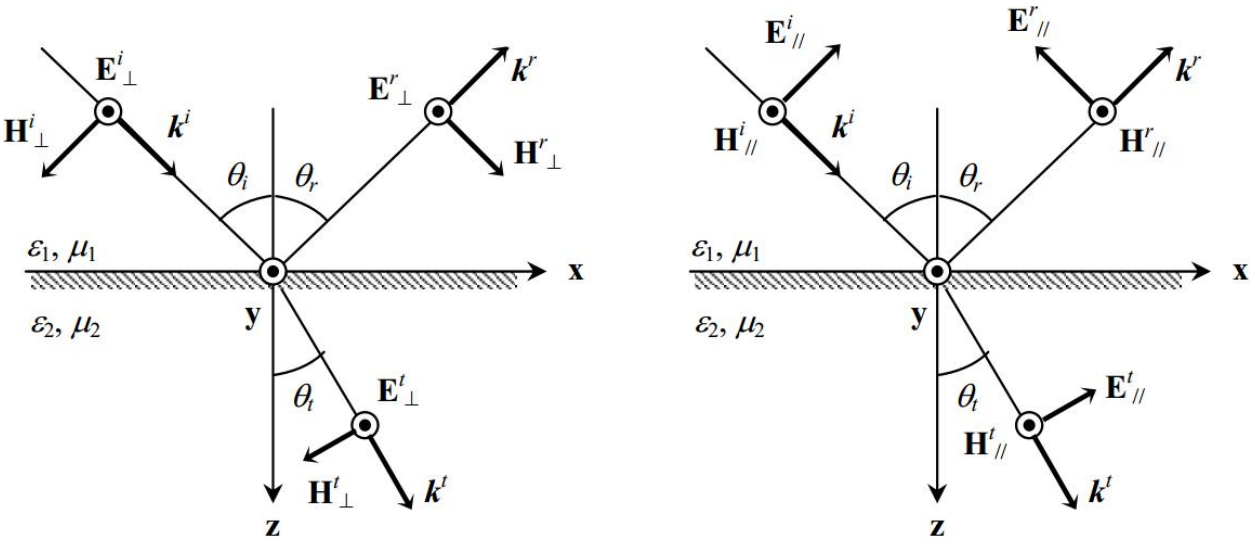

(a) (b)

Figure 2-13 Oblique reflection and transmission from a flat interface: (a) TE mode; (b) TM mode *(47)*.

The reflection and transmission coefficients for TE and TM mode waves are:

$$\boldsymbol{R}_{\perp} = \frac{\eta_2 \cos\theta_{\boldsymbol{i}} - \eta_1 \cos\theta_{\boldsymbol{t}}}{\eta_2 \cos\theta_{\boldsymbol{i}} + \eta_1 \cos\theta_{\boldsymbol{t}}} \tag{2-17}$$

$$\boldsymbol{T}_{\perp} = \frac{2\eta_2 \cos\theta_{\boldsymbol{i}}}{\eta_2 \cos\theta_{\boldsymbol{i}} + \eta_1 \cos\theta_{\boldsymbol{t}}} \tag{2-18}$$

$$\boldsymbol{R}_{\parallel} = \frac{\eta_2 \cos\theta_{\boldsymbol{t}} - \eta_1 \cos\theta_{\boldsymbol{i}}}{\eta_2 \cos\theta_{\boldsymbol{t}} + \eta_1 \cos\theta_{\boldsymbol{i}}} \tag{2-19}$$

$$\boldsymbol{T}_{\parallel} = \frac{2\eta_2 \cos\theta_{\boldsymbol{i}}}{\eta_2 \cos\theta_{\boldsymbol{t}} + \eta_1 \cos\theta_{\boldsymbol{i}}} \tag{2-20}$$

where $\boldsymbol{R}_{\perp}$ is the reflection coefficient for TE wave, $\boldsymbol{T}_{\perp}$ is the transmission coefficient for TE wave, $\boldsymbol{R}_{\parallel}$ is the reflection coefficient for TM wave, $\boldsymbol{T}_{\parallel}$ is the transmission coefficient for TM wave, θ_i is the angle of incident field, which is known, θ_t is the angle of the transmitted wave, and η_1 and η_2 are the impedance of Medium 1 and Medium 2, respectively, which are defined as follows:

$$\eta_1 = \sqrt{\frac{\mu_1}{\varepsilon_1}} \tag{2-21}$$

$$\eta_2 = \sqrt{\frac{\mu_2}{\varepsilon_2}} \tag{2-22}$$

The angles of incident wave θ_i, reflected wave θ_r, and transmitted wave θ_t satisfy the phase matching equations:

$$\beta_1 \sin\theta_i = \beta_1 \sin\theta_r = \beta_2 \sin\theta_t \tag{2-23}$$

Because $\beta_1 = \omega\sqrt{\mu_1\varepsilon_1}$ and $\beta_2 = \omega\sqrt{\mu_2\varepsilon_2}$, the following equations are obtained:

$$\theta_i = \theta_r \tag{2-24}$$

$$\frac{\sin\theta_t}{\sin\theta_i} = \sqrt{\frac{\mu_1\varepsilon_1}{\mu_2\varepsilon_2}} \tag{2-25}$$

Equations (2-24) and (2-25) are known as Snell's laws of reflection and refraction.

2.4.3 Calculation of Dielectric Constant

The most important material property in GPR applications is relative permittivity, or the dielectric constant. Figure 2-14 depicts a typical EM reflection from a layered pavement structure. The dielectric constant of the asphalt surface layer, ε_{AC}, is calculated using the amplitudes of the reflected pulses, as shown in Equation (2-26):

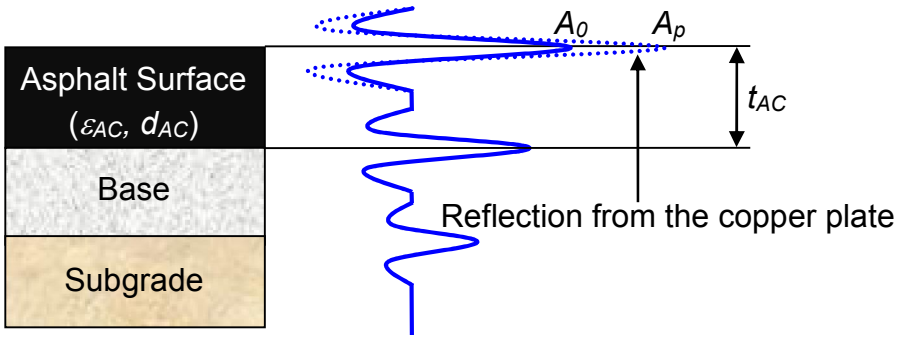

Figure 2-14 Typical GPR signal for a layered asphalt pavement.

$$\varepsilon_{AC} = \left(\frac{A_p + A_o}{A_p - A_o} \right)^2 \quad (2\text{-}26)$$

where ε_{AC} is the dielectric constant of the asphalt mixture in the surface layer, A_o is the amplitude of surface reflection, and A_p is the amplitude of the incident signal. A_p is measured by placing a copper plate under the antenna because copper reflects the GPR signal perfectly and will therefore reflect the GPR wave energy back to the receiving antenna.

It is extremely important to acquire the dielectric constant value of asphalt pavement layer for many GPR applications. To measure the thickness of asphalt pavement, for example, the dielectric constant value is needed for calculating the traveling speed of EM wave within the surface layer. To estimate the density of the AC layer, the dielectric constant value is used as an input of the density model for obtaining the density of the AC layer.

2.5 Applications of GPR on Asphalt Pavement Assessment

GPR has been applied on assessing asphalt pavement for different purposes. Two GPR applications are presented in this section, including thickness measurement and density estimation.

2.5.1 Thickness Measurements

The measurement of asphalt pavement layers thickness is the most common application of GPR in pavement engineering. Using the air-coupled GPR system, GPR survey can be conducted on pavement at high speed. The dielectric constant of the

asphalt surface layer can be calculated using Equation (2-26). The thickness of the surface layer can be calculated using:

$$d_{AC} = \frac{ct_{AC}}{2\sqrt{\varepsilon_{AC}}} \tag{2-27}$$

where d_{AC} is the thickness of the surface layer, and t_{AC} is the two way traveling time of EM wave between the pavement surface and the bottom of the surface layer, as shown in Figure 2-14.

The thickness of the base layer is also obtained by determining the dielectric constant of the base layer and the traveling time within the layer. The dielectric constant of the base layer is calculated as follows:

$$\varepsilon_{base} = \varepsilon_{AC}\left(\frac{F - R}{F + R}\right)^2 \tag{2-28}$$

where ε_{base} is the dielectric constant of the base layer, F is the factor defined as $F = \frac{4\sqrt{\varepsilon_{AC}}}{1 - \varepsilon_{AC}}$, and R is the ratio of the maximum reflected amplitude from the top of the base layer to the maximum amplitude from the top of the AC surface layer.

For newly constructed asphalt pavement, the error of the thickness measurement using GPR ranges from 2% to 5%, as reported in various studies *(4–6, 8, 48)*. The accuracy of thickness measurement for aged pavement is usually lower compared with that for new pavement because new pavement has relatively uniform material properties throughout the depth. The error of thickness measurement using GPR on aged pavement ranges from 3.8% to 12% *(7, 49)*. While the air-coupled GPR system is

successfully applied for measuring the thickness of asphalt pavement, the measurement of concrete pavement thickness using air-coupled GPR is unsuccessful. This failure is attributed to the high attenuation of the EM wave within concrete material and the low contrast of the dielectric constant values between concrete material and base material *(50, 51)*.

2.5.2 Asphalt Pavement Density Estimation Using GPR

The dielectric constant of the AC layer is related to the density of the asphalt mixture. Researchers have attempted to develop models for estimating the density based on the dielectric constant values obtained from GPR measurements. There are two types of density estimation models: The empirical model and the density estimation model.

The empirical model is based on a simple regression relationship between the asphalt mixture density or air void content and the dielectric constant. An example of the empirical model is the exponential relationship between the dielectric constant and air void content *(52–54)*:

$$V_a = a.e^{-b\cdot\varepsilon_{r,AC}} \tag{2-29}$$

where V_a is the air void content of the asphalt mixture in percentage (%), *a* and *b* are the parameters obtained through calibration, and $\varepsilon_{r,AC}$ is the dielectric constant of AC. This model is simple and easy to use; however, the relationship lacks physical meaning and theoretical support. Parameters *a* and *b* vary from one project to another depending on the extracted cores.

The density estimation model is based on EM mixing theories. Al-Qadi et al. *(12)* compared three EM mixing models, the complex refractive index (CRIM) model, the Rayleigh mixing model, and the Böttcher mixing model. The same authors developed the Al-Qadi Lahouar Leng (ALL) model to estimate the bulk specific gravity of the asphalt mixture from its dielectric constant *(13, 14, 40)*:

$$G_{mb} = \frac{\dfrac{\varepsilon_{AC} - \varepsilon_b}{3\varepsilon_{AC} - 2.3\varepsilon_b} - \dfrac{1 - \varepsilon_b}{1 - 2.3\varepsilon_b + 2\varepsilon_{AC}}}{\left(\dfrac{\varepsilon_s - \varepsilon_b}{\varepsilon_s - 2.3\varepsilon_b + 2\varepsilon_{AC}}\right)\left(\dfrac{1 - P_b}{G_{se}}\right) - \left(\dfrac{1 - \varepsilon_b}{1 - 2.3\varepsilon_b + 2\varepsilon_{AC}}\right)\left(\dfrac{1}{G_{mm}}\right)} \quad \text{(2-30)}$$

where G_{mb} and G_{mm} are the bulk and maximum specific gravities, respectively, of the asphalt mixture, G_{se} is the effective specific gravity of the aggregate, P_b is the binder content, ε_b, ε_s and ε_{AC} are the dielectric constant of the binder, the aggregate, and the asphalt mixture, respectively.

Compared with the exponential relationship, the ALL model has physical meaning, is theoretically supported, and describes the relationship of density and dielectric constant better than the exponential relationship. Although additional parameters are introduced in the ALL model, those parameters are obtained before construction of the asphalt pavement, except for the dielectric constant of aggregate ε_s which is obtained either from the back calculation of core data or from a database. Based on the ALL model, the density estimated using GPR is more accurate for asphalt pavement than the density estimated using the nuclear density gauge for asphalt pavement without slags *(14, 40)*.

2.6 Summary

Monitoring the compaction status during the construction of asphalt pavement can help achieve the desired density. Achieving the prescribed density is extremely important for the performance of the asphalt pavement. All the current techniques for density measurement and compaction monitoring have disadvantages. GPR is a promising technique which can potentially be applied on monitoring the density of asphalt pavement during compaction continuously, rapidly, non-destructively and in real time. The ALL density model can be used to convert GPR data into density values of dry asphalt pavement. In order to further apply GPR on compaction monitoring, the effect of surface moisture on GPR data should be investigated and eliminated before the application of ALL density model. This defines the main objective of this research study. The detailed research approaches and results are presented in the following chapters.

CHAPTER 3 RESEARCH APPROACHES

The objective of this research is to develop algorithms for generating density information through the interpretation of GPR data collected during the compaction of asphalt pavement. Surface moisture is the most critical factor affecting GPR measurements that needs to be investigated. The subgrade condition and pavement temperature affect the measurements of IC technology but do not have effect on GPR measurements. In a GPR signal collected from asphalt pavement, only the value of surface reflection amplitude, A_0, was used to calculate the dielectric constant and the density of asphalt mixture, as shown in Figure 2-14. The base and subgrade layers do not have any influence on the surface reflection amplitude and, thus, do not affect the results of density estimation. Furthermore, the temperature sensitivity of GPR signal was investigated by Leng et al. *(14)*.

Figure 3-1 depicts the surface reflection amplitude in GPR signal of an asphalt pavement at different temperatures. Except for some random fluctuations, the reflection amplitude remained constant when the temperature dropped from 88°C to 32°C (190°F to 90°F). The temperature effect on GPR signal was ignored when estimating the density of the asphalt mixture.

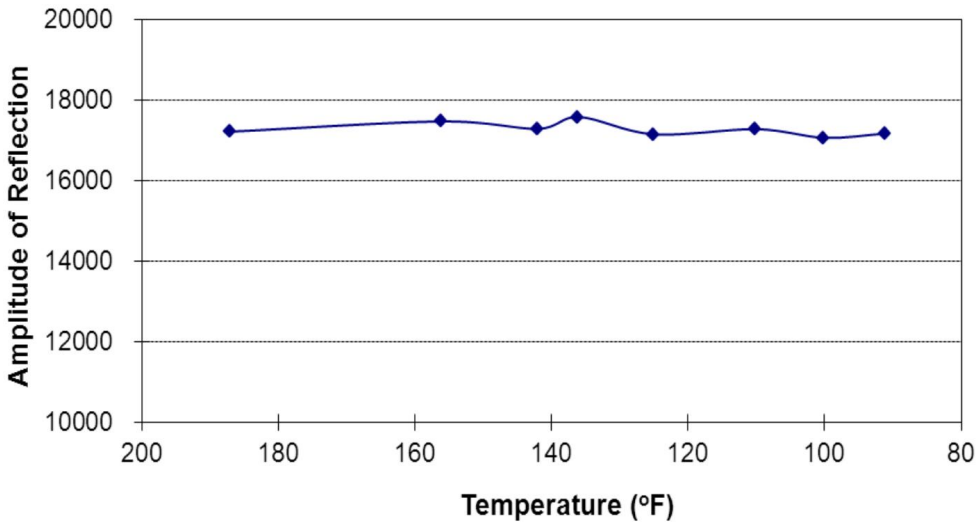

Figure 3-1 Relationship between the amplitude of GPR signal reflection and temperature *(14)*.

The effect of surface moisture on GPR signal during compaction was investigated for two reasons:

- The effect of roller-sprayed water remaining on asphalt pavement on GPR signal is not extensively researched in existing literature;
- Water has a dielectric constant of 81 which is significantly higher than the dielectric constant of asphalt mixture, which is usually smaller than 10. Thus, even a minimal amount of surface water might have a significant impact on the GPR signal.

To achieve the research objective, the following research tasks were conducted:

- Investigation of the effect of asphalt pavement density variation on GPR signals

- Investigation of the effect of surface moisture content variation on GPR signals
- Investigation of the difference between the two effects
- Development of algorithms for eliminating the effect of surface moisture variation while keeping the effect of density variation and for extracting the density information of asphalt pavement accurately.

The research tasks were accomplished through a comprehensive set of research approaches including numerical simulation, laboratory experiments, and field tests.

Numerical Modeling

Numerical modeling is a process that emulates a physical system or physical phenomena. In this research, numerical modeling of the propagation of GPR wave in pavement system was performed. Numerical modeling is preferable to physical experiments because it is considered an effective approach for solving inverse problems. GPR data interpretation is an inverse problem because the observed measurements are converted to information about a physical object. Understanding wave propagation within the medium is important for data interpretation. A forward process, simulation of GPR wave propagation could reveal the underlying properties of the physical phenomena and provide useful insights into the inverse problem. The model's variables are better controlled through numerical modeling. In real experiments, unwanted variables always create noises and mask the effects of the variables under study. In numerical modeling, the effects of unwanted variables can be diminished. In

addition, numerical modeling is less expensive in terms of time and budget, especially when large amount of data is needed.

Laboratory Experiments

Numerical modeling and numerical simulation could not replicate all aspects of a physical system. Simulation results should be calibrated and validated using real data. Thus, laboratory experiments were conducted and the collected data was compared with simulation results. The numerical model was calibrated based on real GPR data collected from the laboratory. Algorithms were developed to eliminate the effect of surface moisture on GPR signal on both simulation data and laboratory data.

Field Tests

To validate the effectiveness of the algorithms developed in the study, the algorithms were tested using the data collected from field construction sites. Compared with numerical simulation and laboratory experiments, field testing was the best approach for representing real construction conditions. But field tests included more variables which affected GPR measurements. By implementing GPR measurements at real construction sites during compaction, the performance of the hardware and software developed in this research were evaluated.

Details of the three approaches are described in Sections 3.1 - 3.3.

3.1 Numerical Modeling

The approach of numerical modeling of GPR responses was followed to study the mechanism of propagation and scattering of EM waves. In this section, the

formulation of numerical models is introduced. The numerical simulation of GPR wave propagation within pavement models is then presented.

3.1.1 Numerical Model Formulation

Computational electromagnetics (CEM) has been developed for solving a variety of EM problems. CEM methods are divided into two categories: time-domain methods and frequency-domain methods. An important time-domain method, the finite-difference time-domain (FDTD) method solves Maxwell's equations step by step in time. FDTD is ideally suitable for broadband problems or transient problems with only a few excitations *(46, 55)*. In this study, the GPR signal is an ultra-wideband signal with one excitation source, which is the transmitting antenna of the GPR system. Thus, the FDTD method was used in this study.

3-D FDTD models can provide comprehensive views of wave propagation in pavement structure. However, 3-D models require significant computational sources. Although 2-D models cannot provide complete views of the problem, the pavement geometry of the third dimension (transverse dimension in the direction of pavement width) is invariant in this study. Therefore, 2-D models can provide satisfactory results as long as the models are calibrated *(56)*. The 2-D FDTD models were thus used in this study for their fast computational capability.

The Yee scheme is widely accepted for modeling the FDTD problem *(46)*. Yee's scheme is used to transform the partial differential equations of a boundary-value problem into a set of discrete time and space marching field equations that can be used to compute an approximate solution.

In Yee's 2-D FDTD algorithm, the region of computation is assumed to be infinity in the z direction without any change in either shape or position in the transverse cross section. The source is also uniform along the z direction. All partial derivatives of the fields with respect to z must then be equal to zero. Maxwell equations for this problem are as follows *(46)*:

$$\frac{\partial E_z}{\partial y} = -\mu \frac{\partial H_x}{\partial t} \tag{3-1}$$

$$\frac{\partial E_z}{\partial x} = \mu \frac{\partial H_y}{\partial t} \tag{3-2}$$

$$\frac{\partial H_y}{\partial x} - \frac{\partial H_x}{\partial y} = \varepsilon \frac{\partial E_z}{\partial t} + \sigma E_z + J_z \tag{3-3}$$

where E_z is the magnitude of the electric field along the z direction; H_x and H_y are the magnitudes of the magnetic field along the *x* and *y* directions, respectively; μ, *ε,* and *σ* are the permeability, permittivity, and conductivity of the material, respectively; and J_z is the electric current of excitation source in the *z* direction.

To solve these equations numerically using Yee's algorithm, the computation domain was enclosed in a rectangular area and then divided into small rectangular cells. Figure 3-2 shows a rectangular cell with the assignments of the locations and directions of the electric fields and magnetic fields *(46, 57)*.

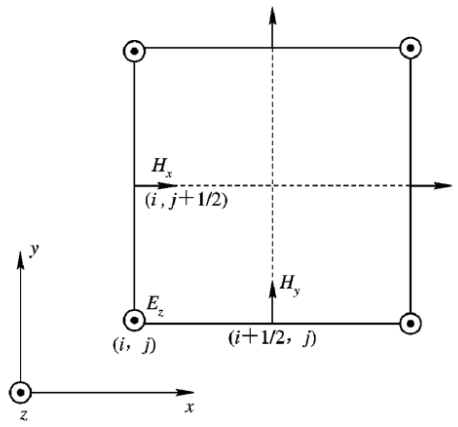

Figure 3-2 Assignment of field components on an FDTD cell *(46, 57)*.

By sampling the electric field at $t = n\Delta t$ and the magnetic field at $t = (n+1/2)\Delta t$ and by using central differencing, the equations were discretized as follows:

$$\frac{E_z^n(i,j+1) - E_z^n(i,j)}{\Delta y} = -\mu \frac{H_x^{n+1/2}(i,j+1/2) - H_x^{n-1/2}(i,j+1/2)}{\Delta t} \tag{3-4}$$

where *t* is the time discretized into a number of uniformly distributed instants represented by $t = n\Delta t$, where $n = 0, 1, 2, \ldots\ldots, N,$ and Δt denotes the time interval between two adjacent instants; Δy is the space interval in the y direction or the size of the cell in the *y* direction, as shown in Figure 3-2; $E_z^n(i,j)$ is the electric field along the *z* direction at time step $t = n\Delta t$ and at location (i, j) , as illustrated in Figure 3-2; $H_x^{n+1/2}(i,j+1/2)$ is the magnetic field along the *x* direction at time step $t = (n+1/2)\Delta t$ at location $(i, j+1/2)$; similarly, $E_z^n(i,j+1)$ and $H_x^{n-1/2}(i,j+1/2)$ are the electric field along the *z* direction at time step $t = n\Delta t$ at location $(i, j+1)$ and the magnetic field along the *x* direction at time step $t = (n-1/2)\Delta t$ at location $(i, j+1/2)$.

A time-stepping formula was obtained from Equation (3-4):

$$H_x^{n+1/2}(i,j+1/2) = H_x^{n-1/2}(i,j+1/2) - \frac{\Delta t}{\mu \Delta y}[E_z^n(i,j+1) - E_z^n(i,j)] \tag{3-5}$$

Similarly, the other two time-stepping formulas were obtained from Equations (3-1) to (3-3):

$$H_y^{n+1/2}(i+1/2,j) = H_y^{n-1/2}(i+1/2,j) + \frac{\Delta t}{\mu \Delta x}[E_z^n(i+1,j) - E_z^n(i,j)] \tag{3-6}$$

$$\begin{aligned} E_z^{n+1}(i,j) = \frac{1}{\beta(i,j)}\Bigg\{ & \alpha(i,j)E_z^n(i,j) + \frac{1}{\Delta x}[H_y^{n+1/2}(i+1/2,j) - H_y^{n+1/2}(i-1/2,j)] \\ & - \frac{1}{\Delta y}[H_x^{n+1/2}(i,j+1/2) - H_x^{n+1/2}(i,j-1/2)] - J_z^{n+1/2}(i,j)\Bigg\} \end{aligned} \tag{3-7}$$

where:

$$\alpha = \frac{\varepsilon}{\Delta t} - \frac{\sigma}{2} \tag{3-8}$$

$$\beta = \frac{\varepsilon}{\Delta t} + \frac{\sigma}{2} \tag{3-9}$$

Based on Equations (3-5) to (3-9), given the initial values of E_z, H_x, H_y at a time step, all fields were obtained at later time steps. This time-marching process is called leapfrog scheme *(58)*.

Discretization of space and time was performed using the FDTD time-stepping equations. In 2-D problems, Δx and Δy must be small enough to resolve the spatial

variation of the field, and Δt must be small enough to resolve the temporal variation of the field. The stability condition, shown in Equation (3-10), must be satisfied *(46)*.

$$\Delta t \le \frac{1}{\frac{1}{\sqrt{\varepsilon\mu}}\sqrt{\frac{1}{(\Delta x)^2}+\frac{1}{(\Delta y)^2}}} \tag{3-10}$$

The absorbing boundary condition (ABC) was used in FDTD computation to truncate the infinite space into a finite computational domain in order to solve the problem of unbounded EM in the region under study. The perfect matched layer (PML) is a region of artificial material that is theoretically designed to create no reflections regardless of frequency, polarization, and angle of incidence of a plane wave incident upon its interface. This feature enables the capability of broadband EM wave simulation in time-domain. To apply the PML technique, the time-stepping formulas were modified and the PML region was discretized into multiple layers where each layer attenuated the EM wave. Attenuation coefficients varied smoothly as an m_{th} -order polynomial:

$$\sigma_{x,y,z} = \sigma_{\max}\left(\frac{l}{L}\right)^m \tag{3-11}$$

where l denotes the distance from the PML surface, L is the thickness of the PML region, and $\sigma_{\max}$ is the maximum conductivity inside the PML region. For the desired reflection coefficient $R(0)$, the value of $\sigma_{\max}$ was determined by:

$$\sigma_{\max} = \frac{m+1}{2\eta L}\ln\left|R(0)\right| \tag{3-12}$$

where m is the order of the polynomial, and η is the impedance of the material.

3.1.2 Numerical Simulation of GPR Wave Propagation

FDTD simulation is performed using a free software program, GprMax, which has been successfully applied to simulate GPR wave propagation *(59, 60)*. GprMax is a set of MATLAB® codes which contain the FDTD formulas described in Section 3.1.1. The advantage of this tool is that it efficiently modifies the parameters in FDTD simulation. Using GprMax, the geometries of pavement structures, material properties of pavement layers, and excitation sources could be easily modified.

A typical model of dry pavement is shown in Figure 3-3 (a) which illustrates FDTD simulation. The pavement structure consists of two layers: an AC surface layer and a base layer. The pavement structure in the model was simple because only the EM wave reflection at the surface of the pavement was investigated. Reflections from the interfaces of underlying layers are not of interest. The width of the pavement model was 2.30 ft (0.70 m). The thicknesses of the AC layer and the base layer were 3.9 in (0.10 m) and 7.9 in (0.20 m), respectively. The dielectric constant values were 5.0 and 7.0 for the AC layer and the base layer, respectively. The dielectric constant value of the AC layer is shown in this example for illustration purposes only. In the numerical simulation, this value was changed to simulate the variation of the AC layer density. The entire computation region was discretized; the grid size was 0.098 in (0.0025 m) in both *x* and *y* directions, respectively.

The transmitting antenna and receiving antenna were placed 0.098 in (0.0025 m) apart at 1.31 ft (0.50 m) above the pavement surface. The transmitting antenna and receiving antenna were close to each other so that the incident wave onto the pavement could be considered normal incidence. The computation region was surrounded by PML

so that the artificial EM wave reflections could be minimized. The distance between the antennas and the upper side of the PML was 1.97 in (0.05 m), which was much smaller than the distance between the antennas and the pavement surface to isolate reflections from the upper region. The PML had 20 layers, which was sufficient to eliminate reflections. The material properties of the PML were defined based on Equations (3-11) and (3-12). The value of time step Δt was obtained using Equation (3-10). An excitation source was placed at the location of the transmitting antenna to excite the propagation of EM waves. The excitation source was a point source in the 2-D model, the equivalent to a line source with infinite length in the z direction in the 3-D model.

The pavement surface was smooth because the effect of pavement surface roughness on the GPR signal was negligible. Based on Rayleigh's criterion for a plane wave, a surface is considered smooth if the following equation is satisfied *(61)*:

$$\sigma < \frac{\lambda}{8\cos\theta_i} \tag{3-13}$$

where σ is the standard deviation of the ground irregularity, λ is the wavelength of the incident signal, and θ_i is the angle of the incident signal.

The irregularity of newly built asphalt pavement is mainly attributed to the texture of the pavement surface. For a normal incidence signal with a wavelength of 23.6 in (0.6 m) to 3.4 in (0.086 m), which corresponds to the frequency ranging from 0.5 GHz to 3.5 GHz, the value of $\lambda/(8 \cos \theta_i)$ ranged from 3.0 in (75 mm) to 0.4 in (10.75 mm). The values were much larger than the typical value of σ, which was approximately 0.04 in (1 mm) for a new built asphalt pavement. Therefore, Rayleigh's criterion was satisfied and the pavement surface was considered smooth at the frequencies under study.

The material property inputs for the pavement model in GprMax included the relative permittivity or the dielectric constant ε_r, the relative magnetic permeability μ_r, and the electrical conductivity σ. The magnetic permeability of the pavement material was almost the same as the magnetic permeability of free space, so the value of μ_r was set to be 1. The values of dielectric constant ε_r and electrical conductivity σ for the asphalt mixture depended on the material properties and volumetric properties of each component of the mixture.

To model surface moisture on asphalt pavement, two candidate approaches were considered. The first approach was based on the placement of a thin layer of water with a dielectric constant value of 81 on top of the pavement surface. However, an extremely thin water layer, less than 1 mm in thickness *(62)*, is difficult to handle in FDTD simulation *(46)* because the thickness is smaller than the grid size. The second approach was based on the placement of a wet AC layer, a mixture of asphalt material and water, on top of dry pavement. Compared with the layer of pure water, the wet AC layer had a larger thickness but a smaller dielectric constant value which was easier to handle in the FDTD simulation. Therefore, the second approach was adopted in this study.

As shown in Figure 3-3 (b), a wet AC layer was placed on the surface of the pavement structure. The thickness of the layer was 0.098 in (0.0025 m), which was equal to the size of the grid. The material properties of the wet AC layer were characterized by the dielectric constant and conductivity. Because water was one of the mixture components in this layer, which had higher dielectric constant and conductivity values, the effective dielectric constant and conductivity of the mixture were also higher

than the dry AC layer. The values of the dielectric constant and conductivity of wet AC layer will be discussed in CHAPTER 5.

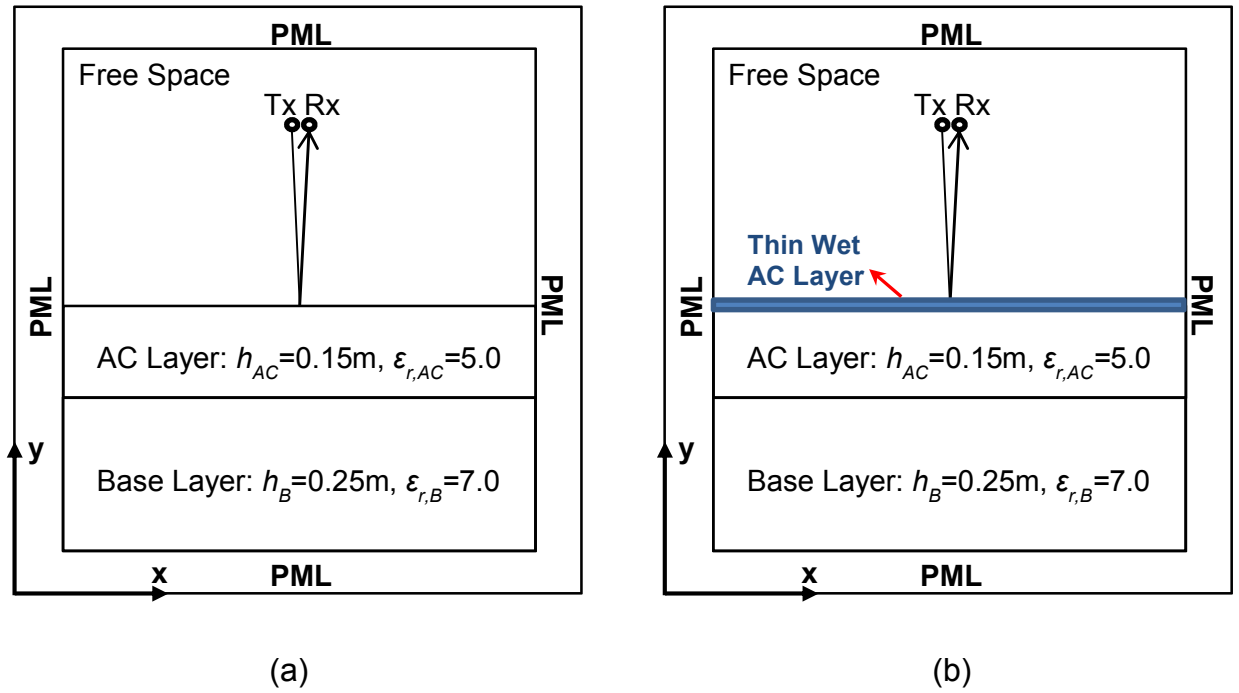

Figure 3-3 Numerical models for FDTD simulation: (a) dry pavement; (b) pavement with wet surface.

3.2 Laboratory Experiments

GPR data was collected from an existing test site built in 2009 and on a new test site built in 2013. Both test sites are located at the Advanced Transportation and Research Engineering Laboratory (ATREL) of the Illinois Center for Transportation (ICT). Information about the two test sites and details about the laboratory experiments are presented in this section.

3.2.1 The Existing Test Site

An existing test site constructed in 2009 at a large parking lot at ATREL was used for GPR data collection. It is referred to as test site A in this dissertation. As shown in Figure 3-4, test site A consists of six lanes which were constructed using five different types of asphalt mixtures as described in Table 3-1. Lane I(A) and lane I(B), shown in Figure 3-4, were constructed with the same asphalt mixture. The different segments of Lane I(A) had various thicknesses while lane I(B) had uniform thickness. The other four lanes were constructed using the asphalt materials described in Table 3-1.

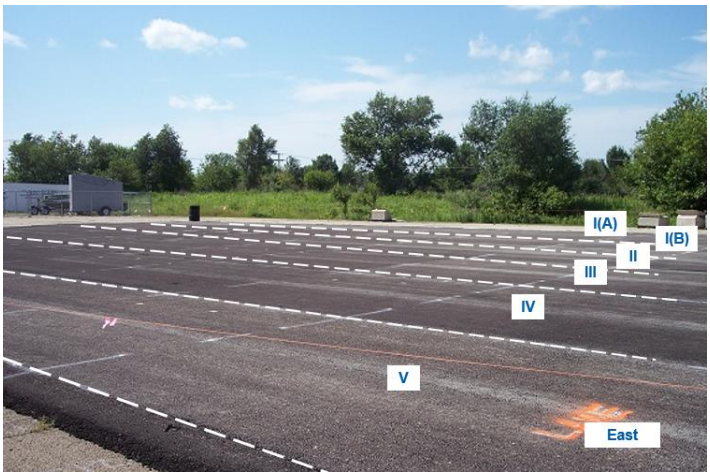

Figure 3-4 Existing test site (test site A) *(40)*.

Table 3-1 Mixture Information for Test Site A *(40)*

Mix No.	Mix Type	Nominal Max. Aggregate Size (mm)	Asphalt Type	Asphalt Content
Mix I	Limestone Surface Mix	9.5	PG64-22	Optimum
Mix II	Granite Surface Mix	9.5	PG70-22	Optimum
Mix III	Granite Surface Mix	9.5	PG64-22	Optimum
Mix IV	Granite Surface Mix	9.5	PG64-22	Optimum+1%
Mix V	Limestone Binder Mix	19.0	PG64-22	Optimum

3.2.2 The New Test Site

A new asphalt pavement test site was specially designed and constructed for the purpose of conducting the laboratory experiments in this study. This test site is referred to as test site B which is single-lane asphalt overlay on top of an existing asphalt pavement. Figure 3-5 depicts the existing pavement before the construction of test site B.

Figure 3-5 Existing pavement before construction of test site B.

The mixture information of test site B, as provided by the asphalt plant, is shown in Table 3-2. The test site was designed to simulate the scenario of density monitoring using GPR during compaction. Different number of roller passes was applied at different lane segments. GPR data was collected on top of different lane segments which were subjected to different number of roller passes. As shown in Figure 3-6 (a), there were 11 segments with each segment having a length of 15 ft (4.6 m) and a width of 4 ft (1.22 m).

The transition segment in the middle was for the compactor to turn off the lane and was not used for GPR testing. The number shown on each segment in Figure 3-6 (a) is the number of roller passes. For example, 0 means that the segment consists of loose mix without any roller pass, and 10 means that the segment was compacted with 10 roller passes. The compactor followed the compaction pattern shown in Figure 3-6 (b). The dash lines with arrows show the path and direction of the compactor for each pass during the construction.

Table 3-2 Mixture Information for Test Site B

Nominal Maximum Aggregate Size	Asphalt Binder Type	Asphalt Binder Content	G_{mm}	G_{sb}
3/8 in (9.5mm)	PG 64-22	5.7%	2.468	2.612

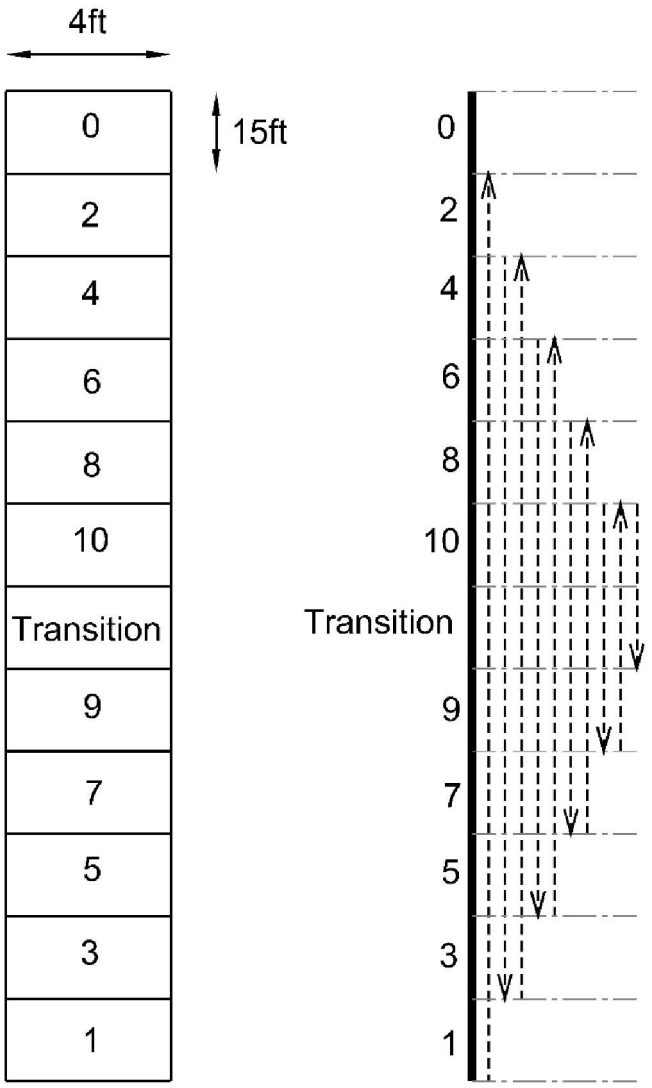

Figure 3-6 Test site B: (a) plan view with different pass number; (b) compaction pattern to achieve different roller pass for each segment.

(The numbers shown in the figure reflect the number of roller passes)

Figure 3-7 depicts the construction of test site B. As shown in Figure 3-7 (a), asphalt material was placed on the existing pavement by a paver. The width of the

asphalt mat was 9 ft (2.74 m). The mat was compacted by a vibratory compactor. The compactor used in the construction was CATERPILLAR CB224E asphalt compactor with a 4 ft (1.22 m) roller width. The compaction followed a straight line without any wandering as shown in the pattern depicted in Figure 3-6 (b) to ensure that the compaction effort of each roller pass was exerted on the same strip of the lane. Figure 3-8 depicts the test site after construction. Some asphalt mixture samples were collected to obtain the value of theoretical maximum specific gravity of asphalt mixture G_{mm}.

(a) (b)

Figure 3-7 Construction of test site B: (a) asphalt mixture is laid down on the existing pavement by a paver; (b) mixture is compacted by a vibrating roller.

Figure 3-8 Test site B after construction.

3.2.3 Test Site Preparation and GPR Hardware Modification

At each GPR test location on test site B, GPR data was collected from the same spot after spraying different amounts of water on the surface for the purpose of capturing the change in GPR signal when only the surface moisture content changed (the density of the asphalt mixture did not change because the data was collected from the same location). Because it took the pavement at least one day to dry after spraying water and different amounts of water were needed to be sprayed on the same spot of pavement, it was important to return the GPR antenna to the same location on different days. Thus a grid system for location reference was created on the pavement, and laser

pointers were installed on the GPR antenna to help align the antenna during data collection.

As shown in Figure 3-9, for each segment of test site B, a grid system was marked on the pavement surface. The size of each grid was determined based on the size of the GPR antenna (the air-coupled antenna manufactured by GSSI): the length of the grid was 10.625 in (270 mm) which was half the length of the antenna, 21.25 in (540 mm), and the width of the grid was 7.75 in (200 mm) which was equal to the width of the antenna. The area of the bottom of antenna projection was equal to the area of two grids. The shaded area in Figure 3-9 is the projected area of the GPR antenna when the antenna was placed on top of the grid 4-C. Figure 3-10 depicts the actual pavement with the grid system. The location of the GPR antenna is described using the section number and grid number. For example, section 6 grid 4-C means that the GPR antenna was above the shaded area, as shown in Figure 3-9, of section 6, which means that the roller pass number was 6.

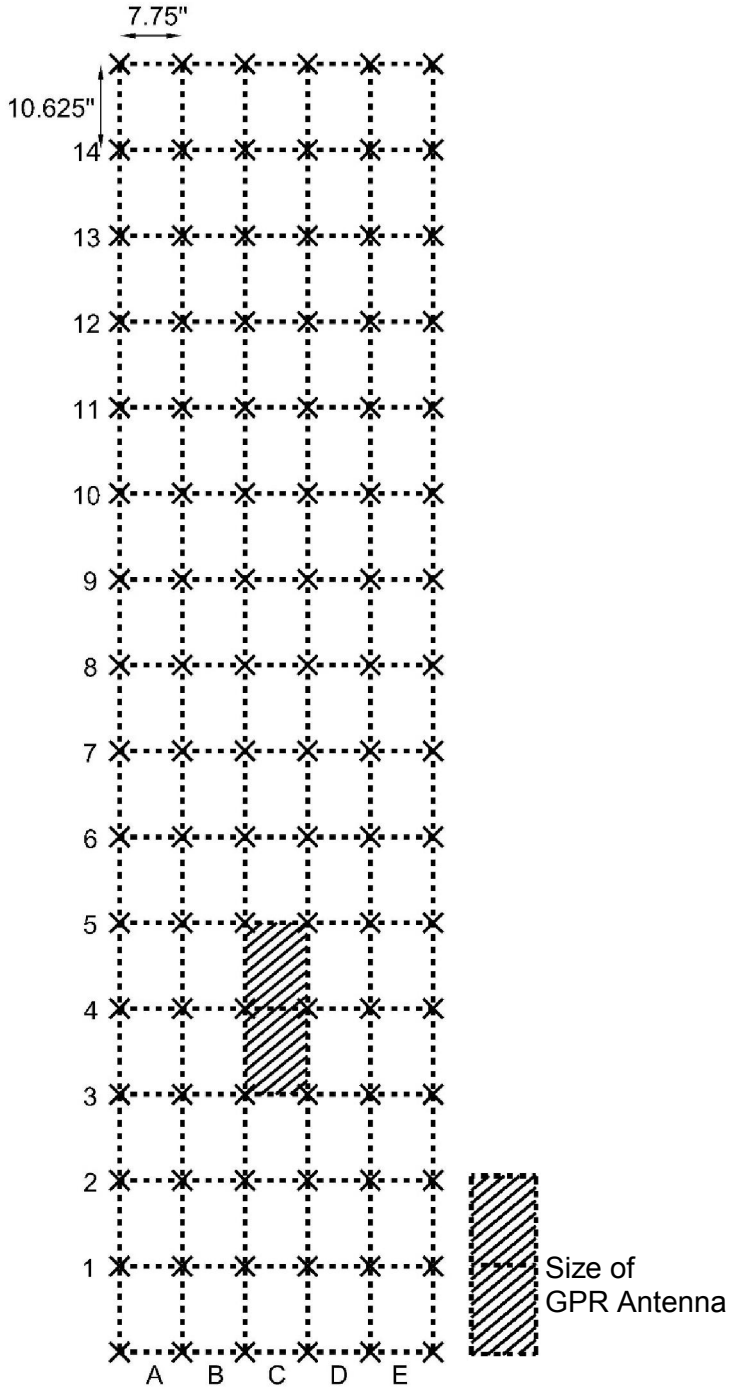

Figure 3-9 Grid system on each segment of test site B.

Figure 3-10 Grid system for location referencing on test site B.

On the GPR antenna, four laser pointers were installed at the four edges. Laser pointers acted like plumb lines so that the projection of the GPR antenna on the pavement could be clearly seen. Figure 3-11 (a) shows a laser pointer on the edge of the antenna. Figure 3-11 (b) shows the calibration of the laser pointer to ensure that the laser points on the ground overlap the projection points of the edge of the antenna.

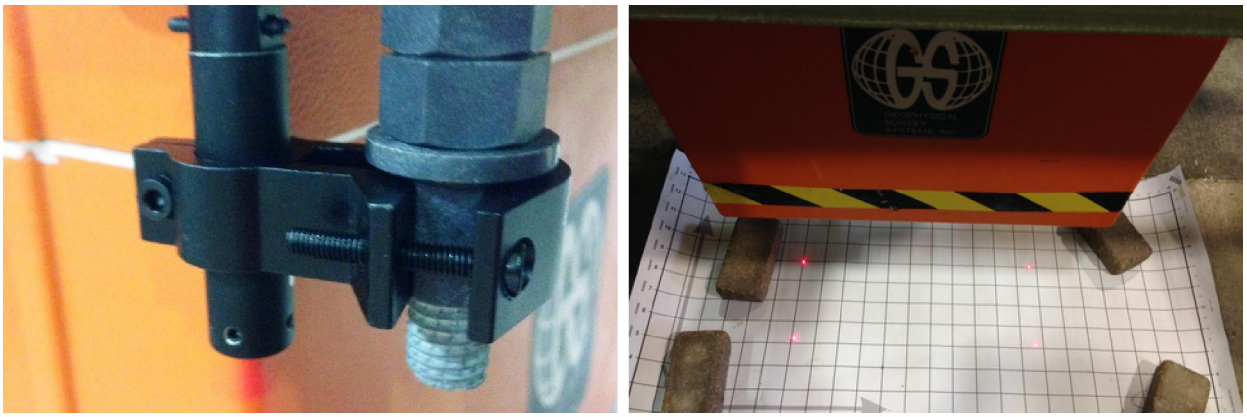

Figure 3-11 Laser pointers installed on the GPR antenna: (a) laser pointer; (b) calibration of the direction of laser pointer.

Figure 3-12 shows the setup of GPR antenna during data collection on test site B. For pavement GPR survey, the antenna is usually mounted on a vehicle so that the data can be collected at high speed. But for laboratory testing on test site B where some segments were not well compacted, GPR vehicle could possibly damage the pavement. The setup shown in Figure 3-12, where saw horses were used to support the antenna, was much lighter than a vehicle and was therefore used to avoid pavement damage. In addition, the antenna could be easily moved and aligned using this setup. As shown in Figure 3-13, with the grid system and laser pointers, the GPR antenna could be aligned to any specific grid by overlapping the laser points with pavement markings.

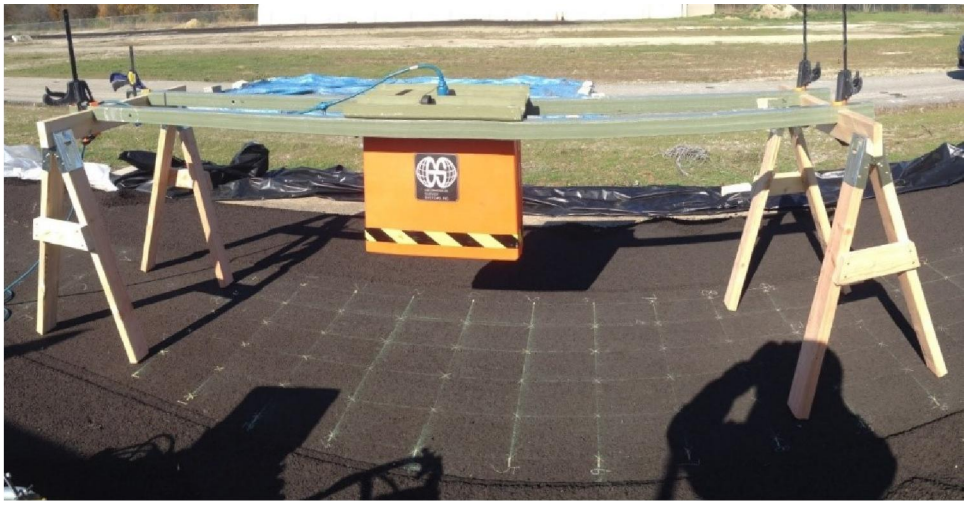

Figure 3-12 Setup of GPR antenna during data collection on test site B.

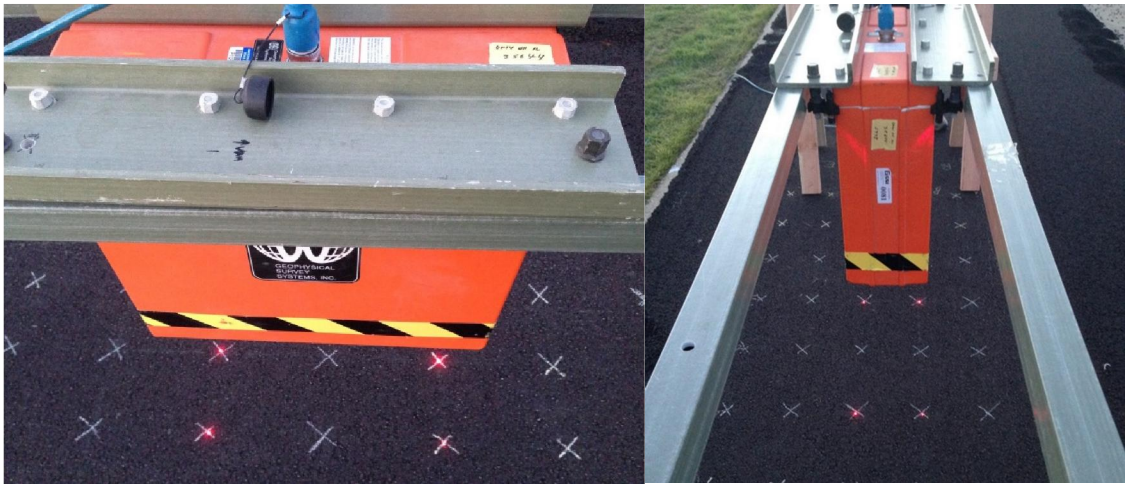

(a) (b)

Figure 3-13 Antenna aligned to specific grid using laser pointers: (a) side view 1; (b) side view 2.

3.2.4 Laboratory Testing Description

In this study, different laboratory tests were conducted for several purposes. First, the effect of density change on GPR signal was studied; GPR data was taken from pavement locations with different densities. Second, the effect of moisture content variation on GPR signal was investigated; GPR data was collected from asphalt pavement with surface moisture. The surface moisture was created by spraying water evenly on a pavement area which was large enough to cover the footprint of GPR wave. The water was sprayed by using sprayers powered by compressed air. Laboratory testing procedures, purposes of the tests, and data analysis of tests results are described in details in CHAPTER 6.

3.3 Field Tests

Field tests serve two purposes in this study. First, preliminary field data was collected to determine the amount of surface moisture added to the pavement during numerical simulation and laboratory experiments. Second, field testing results were used to validate the effectiveness of the algorithms developed in this study.

This research utilizes the existing GPR van, as shown in Figure 2-7, to collect data during field construction. The long-term objective is to install the GPR system on a compactor to monitor the density during compaction in real time. This section presents the effort of modifying the hardware to conduct field tests efficiently and introduces the field testing procedure.

3.3.1 Hardware Modification for Field Tests

To avoid interruption of the compaction process during GPR data collection, hardware modification was made on the GPR vehicle. As can be seen in Figure 3-14 (a)

and (b), GPR antennas were laid down in horizontal position. In this position, GPR antennas could be placed above the asphalt pavement to collect data. As shown in Figure 3-14 (c) and (d), the antennas were pulled up to a vertical position. Blocking the way of the compactor was therefore avoided. The two positions of the antennas could be switched by controlling an electric powered winch installed on top of the van, as shown in Figure 3-14 (e).

(a) (b)

Figure 3-14 Modification of the hardware for field tests: (a) antennas laid down - side view; (b) antennas laid down - back view; (c) antennas pulled up - side view; (d) antennas pulled up - back view; (e) electric power winch.

(c)

(d)

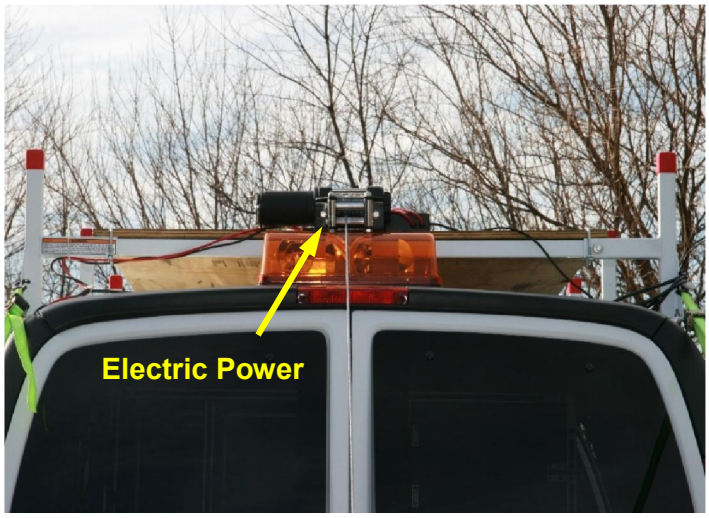

(e)

Figure 3-14 (cont.)

3.3.2 Field Testing Description

The GPR equipment after hardware modification was used in field testing. As shown in Figure 3-15 (a), the antennas were lifted to a vertical position (standby position) to avoid disturbance of the compactor before compaction. After the compactor passed by, the antennas were lowered to a horizontal position (data collection position) to collect the GPR data, as shown in Figure 3-15 (b). Right after data collection was finished, the antennas were lifted up again to standby position. The whole process, including lowering down the antennas to data collection position, collecting about 1000 GPR scans, and lifting up the antennas to standby position, took about 30 sec.

(a) (b)

Figure 3-15 GPR setup for compaction monitoring: (a) standby position; (b) data collection position.

3.4 Summary

This chapter presented the three approaches that this study followed: numerical simulation, laboratory experiments and field tests. Each approach has its own advantages and disadvantages, which were described in this chapter. The procedure and research tasks for each approach were also described. The results of the research tasks will be presented in CHAPTER 5, CHAPTER 6 and CHAPTER 7.

CHAPTER 4 PROCEDURE OF THE APPLICATION

This chapter presents the overall procedure of the application of GPR on compaction monitoring and a feasibility analysis.

4.1 Framework of the Methodology

The application follows the procedure outlined in Figure 4-1. First, GPR data was collected from wet asphalt pavement during compaction. As discussed in 0, the water spayed by the compactor remained on the asphalt pavement surface, yielding an increased amplitude of surface reflection in GPR data. Based on Equations (2-26) and (2-30), the direct use of surface reflection amplitude in the equations resulted in overestimations of the dielectric constant value of asphalt mixture, ε_{AC}, and the bulk specific gravity of asphalt mixture, G_{mb}. Thus, it was important to apply a correction algorithm to correct the signal collected from wet pavement to resemble the signal collected from dry pavement. The density model could then applied to obtain the pavement density.

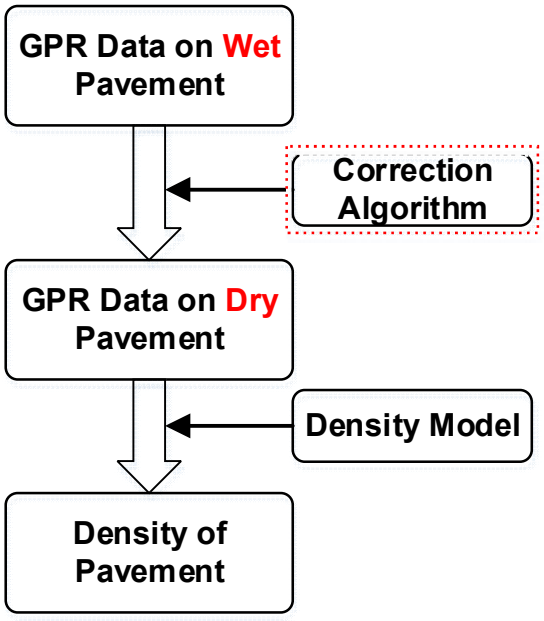

Figure 4-1 Outline of the application of asphalt pavement compaction monitoring using GPR.

The research tasks shown in Figure 4-2 were then conducted to develop the correction algorithm shown in Figure 4-1. Figure 4-2 depicts the four main research tasks. First, a calibration of the numerical model was conducted. Second, the GPR data obtained from numerical simulation and laboratory experiments were used to investigate and understand the effect of surface moisture on GPR signals. Third, based on the findings, algorithms were developed to eliminate the effect of surface moisture in step two. Finally, the developed algorithms were validated using the field test results.

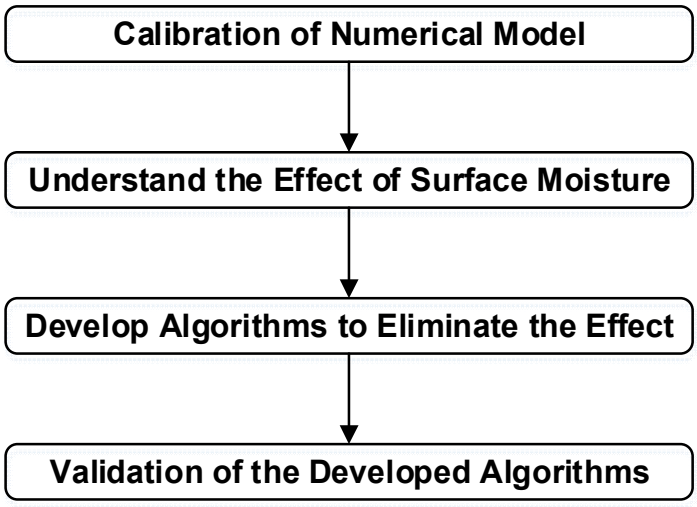

Figure 4-2 Research tasks.

4.2 Feasibility Analysis

A feasibility analysis was performed to ensure that the monitoring of asphalt pavement compaction using GPR was feasible. The feasibility analysis was performed for the following purposes:

- Ensure that the effect of surface moisture did not completely mask the effect of density increase on GPR signal
- Obtain the typical values of the percentage of GPR amplitude increase caused by surface moisture during compaction

Using the test setup shown in Figure 3-14, GPR data was collected on asphalt pavement during compaction in several field construction sites. Figure 4-3 depicts the surface reflection amplitudes at different number of roller passes. GPR data collected from two field construction sites are shown in Figure 4-3. Site 1 is a construction site of a county highway in Melvin, Illinois and Site 2 is a construction site located in a parking

lot in Urbana, Illinois. As can be seen from the figure, the surface reflection amplitude increased with the roller passes. The variation of the amplitude is attributed to two factors: The change of asphalt mixture density and the variation of surface moisture content during compaction. The trend of the increasing amplitude indicates that the effect of surface moisture variation did not completely mask the effect of density variation. Therefore, using GPR for monitoring density changes during compaction was feasible.

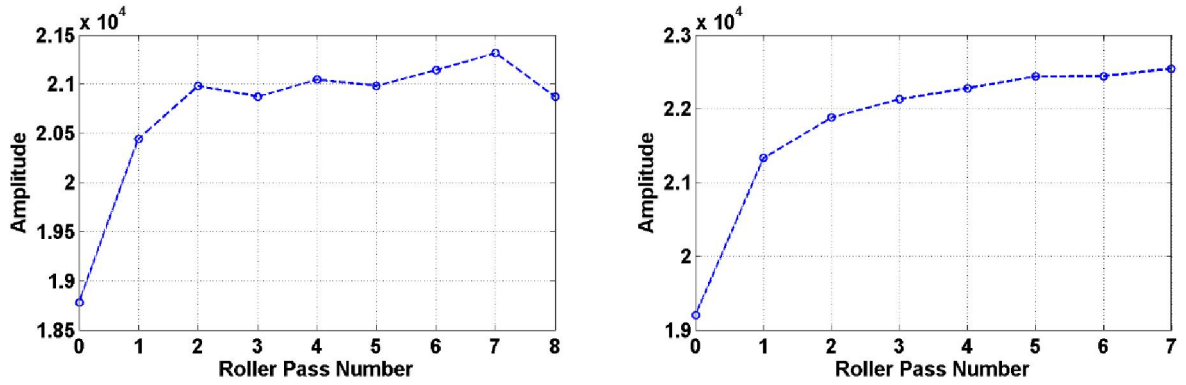

(a) (b)

Figure 4-3 Compaction curves: (a) field construction site 1; (b) field construction site 2.

The feasibility study was also conducted for the purpose of obtaining typical values of the percentage of amplitude increase caused by surface moisture. These values could be used to guide the laboratory experiments for determining the amount of water to be sprayed on the pavement. The percentage of the resulting increase in surface reflection amplitude should be comparable to the percentage of the increase in the field due to the introduction of surface moisture.

Figure 4-4 shows an example of GPR signal collected from a construction site in Champaign County, Illinois. The GPR data was collected from the asphalt pavement after the final roller pass when there was noticeable surface moisture remaining on the pavement after the finishing roller. The “wet” signal is shown as the red curve in Figure 4-4 (a) and (b). Another GPR data file was collected after 30 min on the same location when the pavement surface appeared dry. The “dry” signal is plotted as the blue curve in Figure 4-4 (a) and (b). The maximum amplitude was 1.9584×10^4 for wet data and 1.8846×10^4 for dry data in this measurement. The amplitude of wet data was 3.9% higher than the amplitude of dry data.

Similar tests were conducted at different pavement locations in different construction sites. The increase in surface reflection amplitude as a result of surface moisture randomly ranged from 1% to 6%. In the laboratory tests, the amount of water sprayed on the pavement should be determined so that the increase in the surface reflection amplitudes could cover this range.

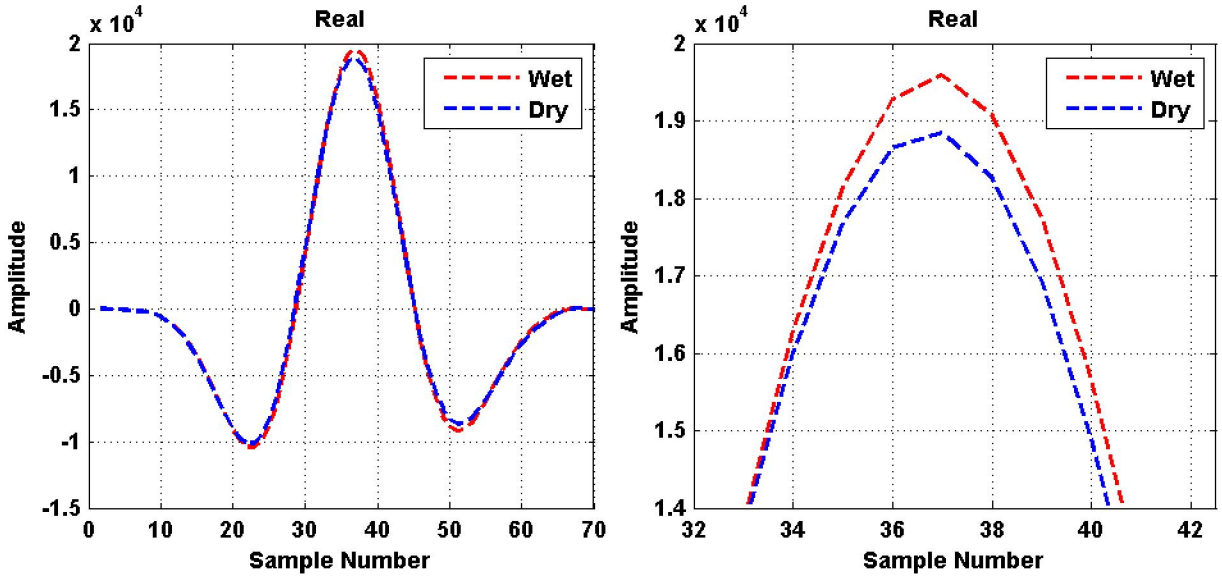

(a) (b)

Figure 4-4 Surface reflection of GPR signal on asphalt pavement in a field construction site: (a) wet and dry data; (b) magnified wet and dry data.

CHAPTER 5 NUMERICAL SIMULATION

5.1 Calibration of Numerical Modeling

Numerical modeling was conducted to investigate the fundamental difference between the effect of surface moisture variation and density variation on GPR signal. A calibration was performed before the modeling process.

Calibration is important to numerical modeling. A well calibrated numerical model can produce accurate results and help gain insights of the modeled physical phenomena. In this study, the waveforms of reflections from copper plate in numerical simulation and in laboratory experiment were compared. The waveforms of reflections from asphalt pavement surface in numerical simulation and in laboratory experiment were also compared. A calibration was conducted to ensure an exact match between simulated GPR signal and real GPR signal. It was important to perform this step before further applications of the numerical simulation because only the results generated from a calibrated model were meaningful.

5.1.1 Existing Excitation Sources

The excitation source at the transmitting antenna determines the waveform in time domain and the frequency spectrum of the received GPR signal. Gaussian derivatives are the most common excitation sources for simulation of impulse GPR signals. Researchers have used 0 order Gaussian function *(63–65)*, 1st order Gaussian derivative function *(66–68)*, and 2nd order Gaussian derivative function, which is also named Ricker function *(69, 70)*, as the excitation sources. The three excitation functions are shown in Figure 5-1. The excitation functions were plugged into the GprMax

software using the pavement model shown in Figure 3-3 (a) with a PEC layer placed on the AC layer.

The pulse reflected by the copper is referred to as “copper reflection” data. Figure 5-2 shows the copper reflection generated by Gaussian function. Figure 5-3 shows the copper reflection generated by 1st order Gaussian derivative function. Figure 5-4 shows the copper reflection generated by 2nd order Gaussian derivative function (Ricker function). Comparing these simulated copper reflections with the real copper reflection shown in Figure 5-5, it was observed that the most similar simulated copper reflection was generated using 1st order Gaussian derivative function.

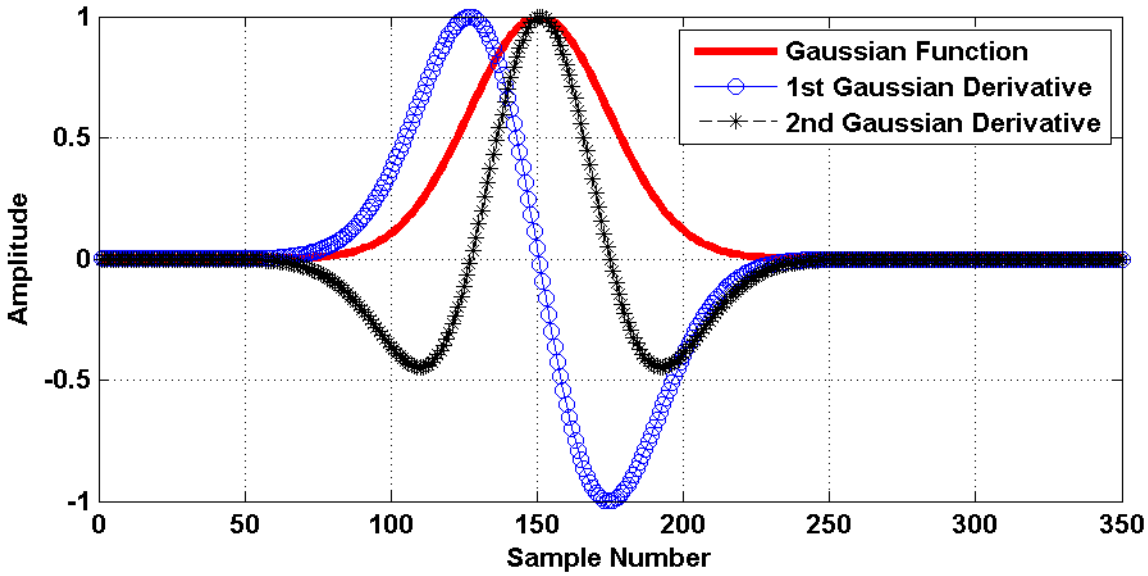

Figure 5-1 Different Gaussian derivative functions.

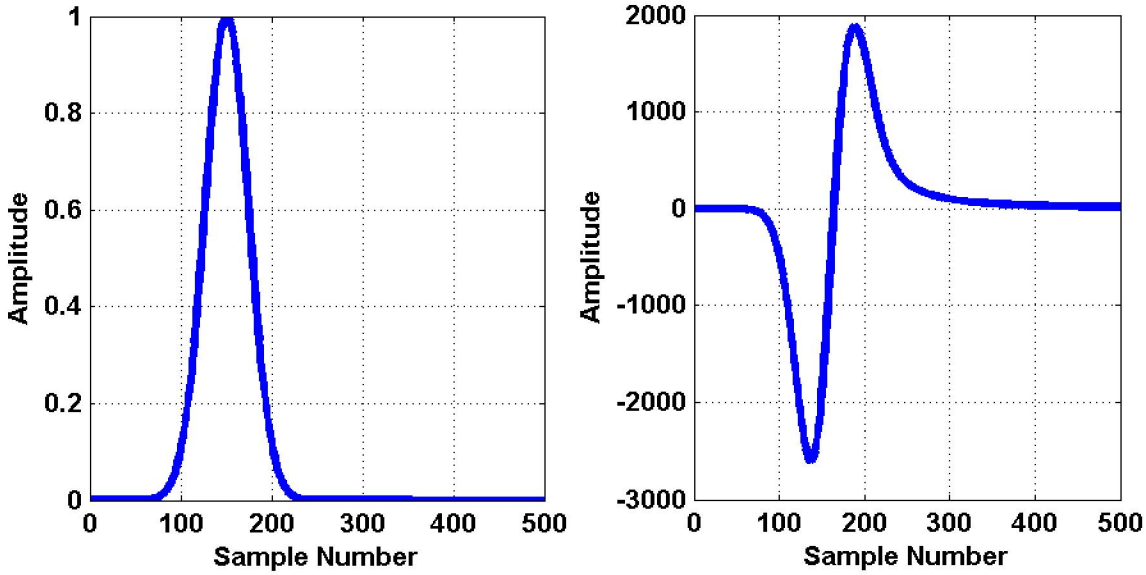

(a) (b)

Figure 5-2 Simulated GPR signal generated by Gaussian function: (a) Gaussian function; (b) copper reflection in FDTD simulation.

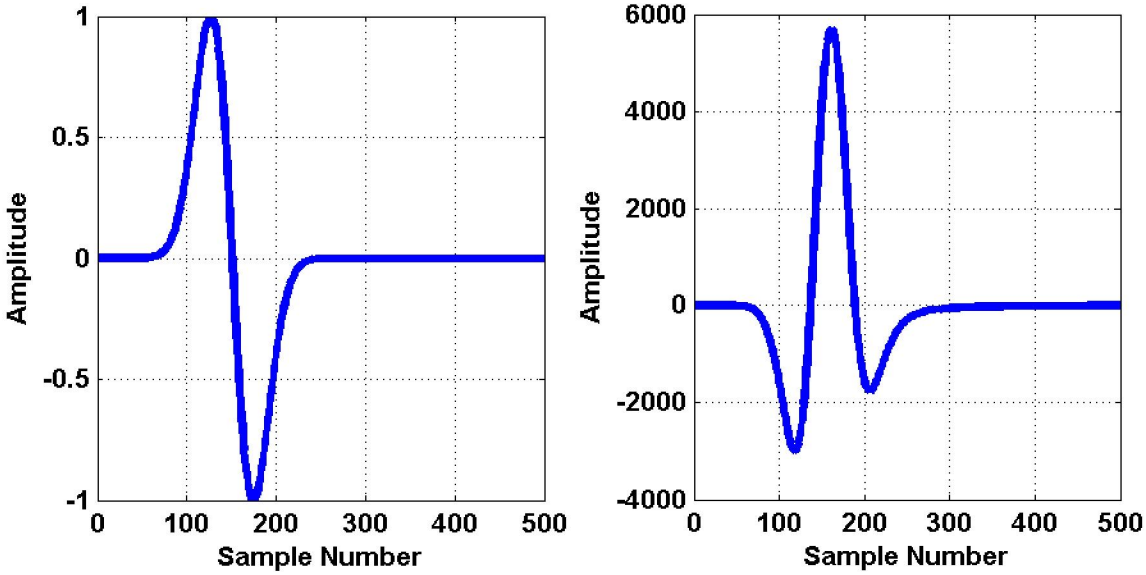

(a) (b)

Figure 5-3 Simulated GPR signal generated by 1st order Gaussian derivative function: (a) 1st Gaussian derivative function; (b) copper reflection in FDTD simulation.

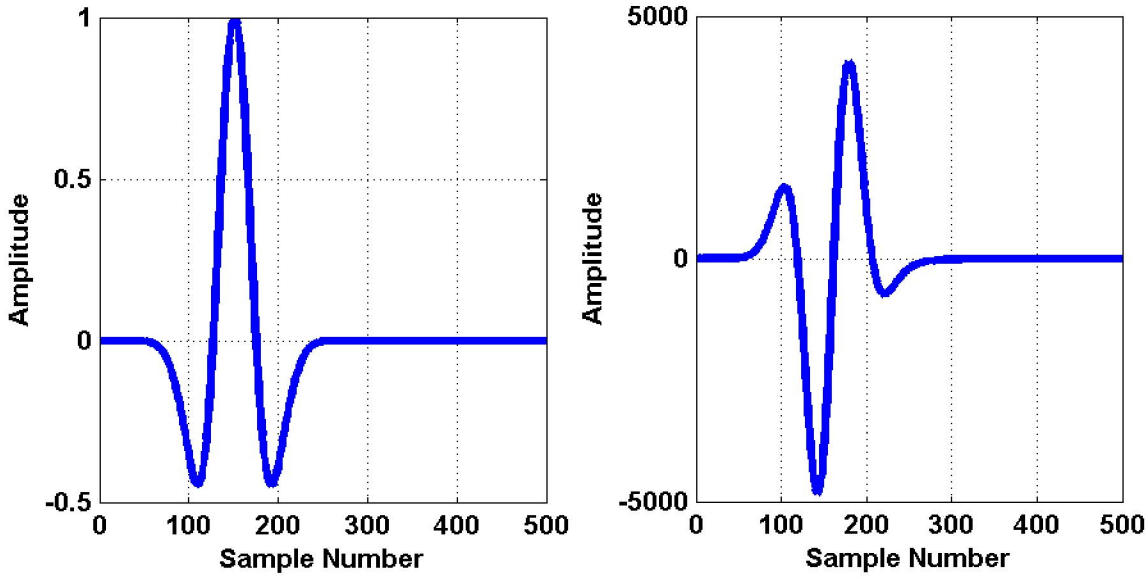

(a) (b)

Figure 5-4 Simulated GPR signal generated by 2nd order Gaussian derivative function: (a) 2nd Gaussian derivative function; (b) copper reflection in FDTD simulation.

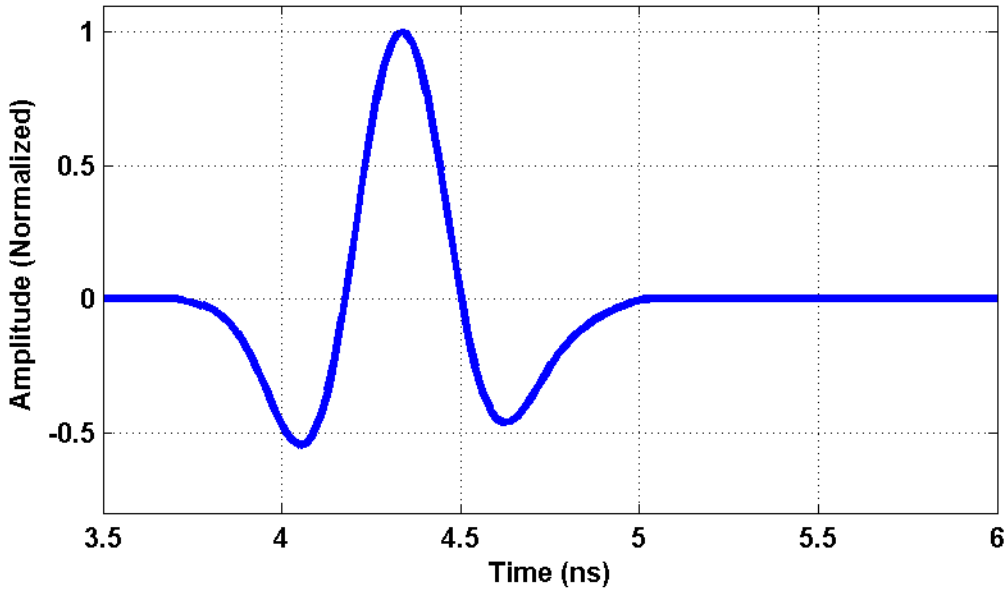

Figure 5-5 Real copper reflection.

A detailed comparison of simulated GPR signal (generated by 1st order Gaussian function) and real GPR signal was conducted in both time and frequency domain. The 1st order Gaussian derivative function was plugged into the FDTD simulation and the time range for data collection was 12 ns, as shown in Figure 5-6 (a). Other than collecting the copper reflection data, the pulse reflected at the surface of AC layer, referred to as “surface reflection” data, was also collected. Real GPR data was collected to be compared with the simulation data. The test was conducted at test site A as described in Section 3.2. A 2.0-GHz air-coupled antenna (with 2 GHz central frequency) and SIR20 GPR data collection system manufactured by GSSI were used. A comparison between simulated and real results is shown in Figure 5-6. The amplitude was normalized with copper reflection amplitude in time domain, as shown in Figure 5-6 (b) and (d). The amplitude in frequency domain was normalized with the amplitude of center frequency, as shown in Figure 5-6 (c) and (e).

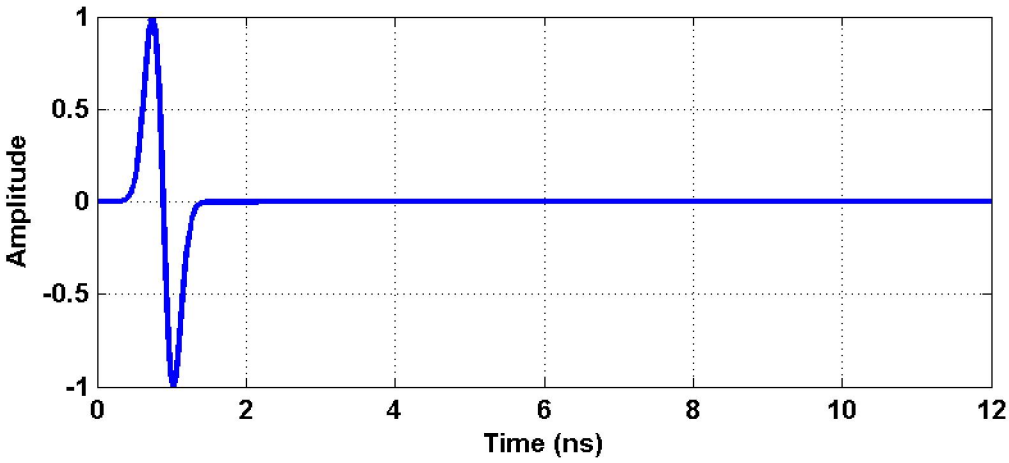

(a)

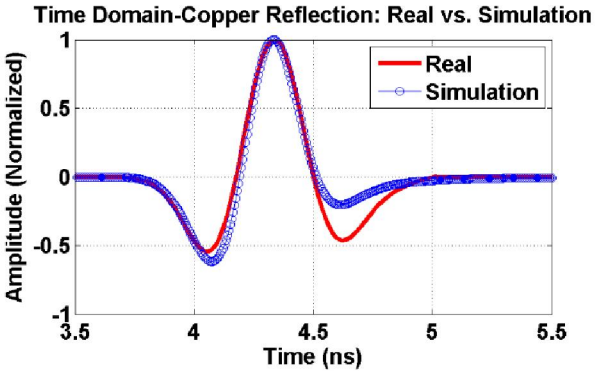

(b)

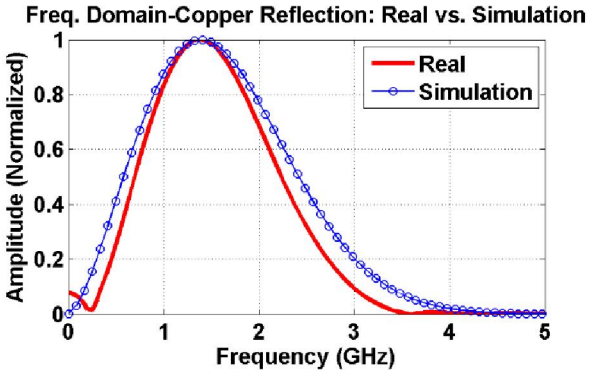

(c)

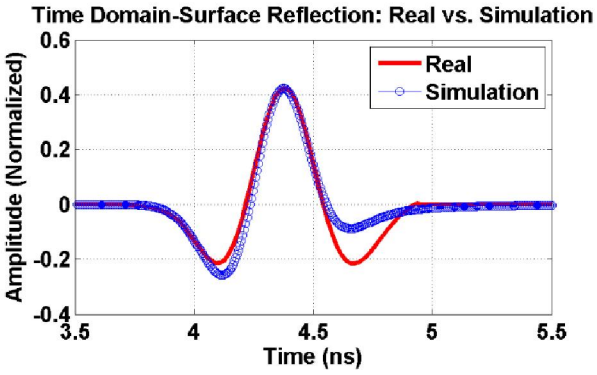

(d)

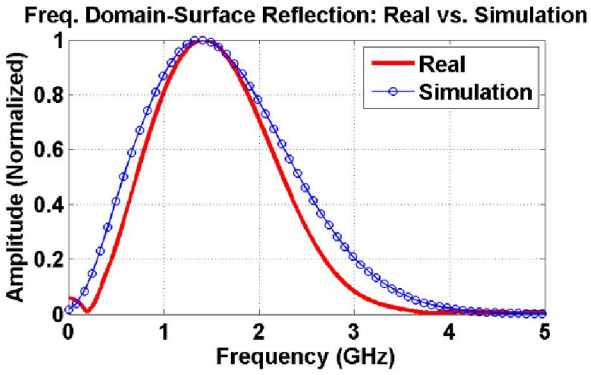

(e)

Figure 5-6 Comparison of simulated GPR signal using 1st order Gaussian derivative to real GPR data: (a) 1st order Gaussian derivative function; (b) comparison of real and

(Figure 5-6 cont.) simulation copper reflection in time domain; (c) comparison of real and simulation copper reflection in frequency domain; (d) comparison of real and simulation surface reflection in time domain; (e) comparison of real and simulation surface reflection in frequency domain.

As shown in Figure 5-6, the real signal and simulated signal are different in the time domain; the frequency spectrums do not match either. Therefore, although the 1st order Gaussian derivative function could generate the most similar reflection data among the three excitation functions, it could not model the GPR signal accurately. This would be less problematic if the FDTD simulation were used for qualitative studies, such as the detection of the rebar within the pavement and some quantitative studies, such as thickness measurement where the frequency spectrum is not the feature of interest. However, for the application of compaction monitoring, quantitative frequency analysis and filtering are expected to be performed. Providing an accurate match between the simulation signal and the real GPR signal in both the time domain and frequency domain is considered essential; otherwise, the simulation results would be meaningless. Thus, it was important to find an excitation source that could generate the same waveform as the real signal.

5.1.2 Calculation of Equivalent Excitation Source

It should be noted that the real excitation function of the GPR system is often unknown or proprietary. Even if the real excitation function is known, the generated GPR signal will not be the same as the real signal if 2D FDTD simulation is performed

because the real antenna structure of a GPR system is much more complex than the point source used in 2-D FDTD simulation, and the 3-D pavement model is different from the 2-D pavement model in this study. However, by modifying the excitation function at the point source, the same waveform as the real GPR signal could be generated in the 2-D FDTD simulation. This excitation function is called “the equivalent excitation source”. The efforts of finding equivalent excitation source are shown in literatures *(56, 71)*. A different calibration was conducted for the specific GPR system used in this study. In this section, a back-calculation procedure of finding the equivalent excitation source is described.

The FDTD simulation model is considered a linear system. The 1st order Gaussian derivative excitation function, *r(t)*, is the input of the system, and the received GPR signal, $y_{sim}(t)$, is the output of the system. The system function, or transfer function, of the system is *h(t)*. The system input-output relation can be written in a convolution form, as shown in Equation (5-1).

$$r(t) * h(t) = y_{sim}(t) \tag{5-1}$$

where *r(t)* is the 1st order Gaussian derivative function; *h(t)* is the system function of FDTD simulation; and $y_{sim}(t)$ is the received GPR signal in time domain.

Assuming that the desired equivalent excitation source is *x(t)*, the output of the system, which is the GPR signal generated by FDTD simulation, should match the real GPR signal, $y_{real}(t)$, as shown in the following:

$$x(t) * h(t) = y_{real}(t) \tag{5-2}$$

where *x(t)* is the desired equivalent excitation source, and $y_{real}(t)$ is the real GPR signal in time domain.

Transforming Equations (5-1) and (5-2) into frequency domain will convert the convolution operation to a multiplication operation, as shown in Equations (5-3) and (5-4):

$$R(f)H(f) = Y_{sim}(f) \tag{5-3}$$

$$X(f)H(f) = Y_{real}(f) \tag{5-4}$$

where *R(f)* is the Ricker function in frequency domain; *H(f)* is the system function in frequency domain; $Y_{sim}(f)$ is the simulation GPR signal in frequency domain using 1st order Gaussian derivative function as the excitation source; *X(f)* is the desired excitation function in frequency domain; and $Y_{real}(f)$ is the real GPR signal in frequency domain.

The desired excitation function *X(f)* can be obtained from Equations (5-3) and (5-4), and the time domain function, *x(t),* can be obtained from *X(f)* through inverse Fourier transform*,* as shown in the following:

$$X(f) = \frac{Y_{real}(f)}{Y_{sim}(f)} R(f) \tag{5-5}$$

$$x(t) = F^{-1}(X(f)) \tag{5-6}$$

A back calculation of the equivalent excitation source was conducted by using copper reflection data from simulation and reality, as shown in Figure 5-6 (c). Figure 5-7

shows a comparison of the calculated equivalent source and the 1st order Gaussian derivative function.

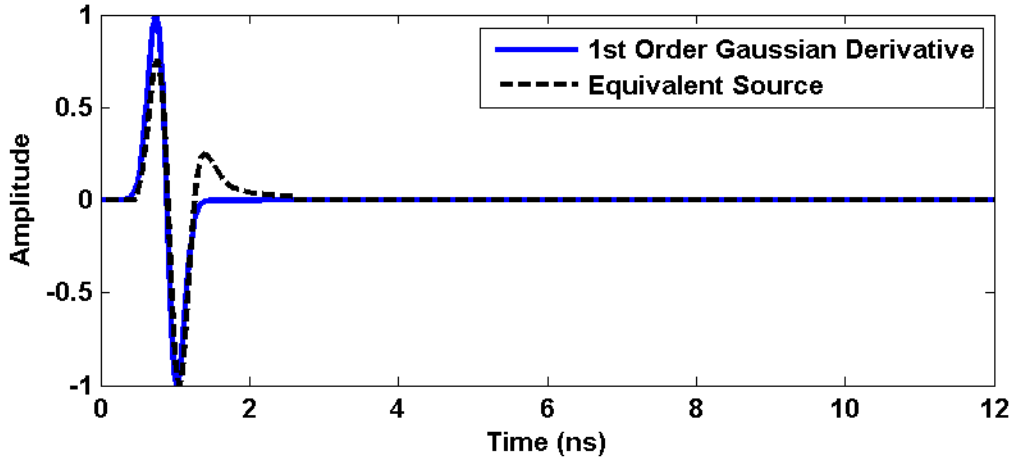

Figure 5-7 Comparison of the equivalent excitation source and the 1st order Gaussian Derivative Function.

5.1.3 De-Noising of Signals Using Wavelet Transform

The equivalent excitation source was plugged into the FDTD model to generate GPR signals. The received signal contained noise because the real GPR data, which was used for back calculation of the equivalent source, contained noise. Thus, the noise in the real GPR data was transferred to the equivalent source and then to the simulated GPR signal. Therefore, a de-noising process was needed to eliminate the noise in the signal. Discrete wavelet transform (DWT) was applied to de-noise the signal.

In signal processing, Fourier transform is usually used to obtain the frequency spectrum of the signal. While the signal is transformed from time domain to frequency domain, the time information is lost. Short-time Fourier transform (STFT) can keep the

information of the signal in both time and frequency domain *(72–75)*. The disadvantage of STFT is that it uses a window function with a preset window length. Once this window function is chosen, the resolutions are fixed at all frequencies and times. Wavelet transform is a multi-resolution signal processing technique with adjustable window length. The wavelet technique has been successfully applied in many areas such as signal de-noising, data compression, and image processing *(76–79)*.

Continuous wavelet transform (CWT) decomposes a signal into a family of functions which offers good time and frequency localization. A wavelet function (also called mother wavelet) $\psi(t)$ is used to carry out the wavelet decomposition. Typical mother wavelets can be found in the literature *(76, 80)*. The wavelet function is defined in the following equations *(81, 82)*:

$$\psi_{a,\tau}(t) = \frac{1}{\sqrt{a}}\psi\left(\frac{t-\tau}{a}\right), a \in R^{*} \ \tau \in R \tag{5-7}$$

$$C_f(a,\tau) = \int_R f(t)\psi^{*}_{a,\tau}(t)dt \tag{5-8}$$

where $\psi_{a,\tau}(t)$ is constructed by dilation and translation of mother wavelet $\psi(t)$; a is the parameter of dilation (or scaling); τ is the parameter of translation (or shifting); $C_f(a,\tau)$ is the CWT of the function *f(t);* and the superscript "*" means the complex conjugation.

Since CWT uses the continuous scaling factor a and shifting factor τ, respectively, which produce infinite number of wavelet coefficients, it is not computationally efficient. DWT uses discrete values of scaling and shifting factors,

which saves computation time. It is achieved by assigning scaling and shifting factors a and τ, respectively, with the power of two values *(83)*:

$$a = 2^j \tag{5-9}$$

$$\tau = k \cdot a = k \cdot 2^j \tag{5-10}$$

where *j* is the level at which the discrete wavelet analysis is performed and *k* is an integer parameter in DWT. By applying DWT on signal *f(k)*, two parts of coefficients can be obtained: approximation coefficients and detail coefficients. Approximation coefficients are the low frequency components and detail coefficients are the high frequency components of signal *f(k)*. The two coefficients are expressed as follows:

$$A_j = \sum_{n=0}^{\infty} f(n)\phi_{j,k}(n) = \sum_{n=0}^{\infty} f(n)\frac{1}{\sqrt{2^j}}\phi\left(\frac{n-k2^j}{2^j}\right) \tag{5-11}$$

$$D_j = \sum_{n=0}^{\infty} f(n)\frac{1}{\sqrt{2^j}}\psi\left(\frac{n-k2^j}{2^j}\right) \tag{5-12}$$

where A_j and D_j are approximation coefficient and detail coefficient, respectively, at level *j*. $\phi_{j,k}(n)$ is the scaling function associated with the wavelet function $\psi_{j,k}(n)$. As the decomposition level *j* increases, a hierarchical set of approximations and details can be obtained. This procedure is called multi-resolution analysis *(78, 84)*.

Figure 5-8 shows the procedure of signal decomposition using DWT. The original signal, denoted by *s*, is decomposed into level 1 approximation a_1 and detail d_1, where a_1 and d_1 can be obtained by Equations (5-11) and (5-12). Similarly, the level 1 approximation a_1 can be further decomposed into level 2 approximation a_2 and detail d_2.

After three levels of decomposition, the original signal is decomposed into 5 details and 1 approximation. The original signal can also be reconstructed by the details and approximation. By implementing the scheme shown in Figure 5-8, the noise contained in the original signal could be filtered by suppressing specific levels of detail coefficients.

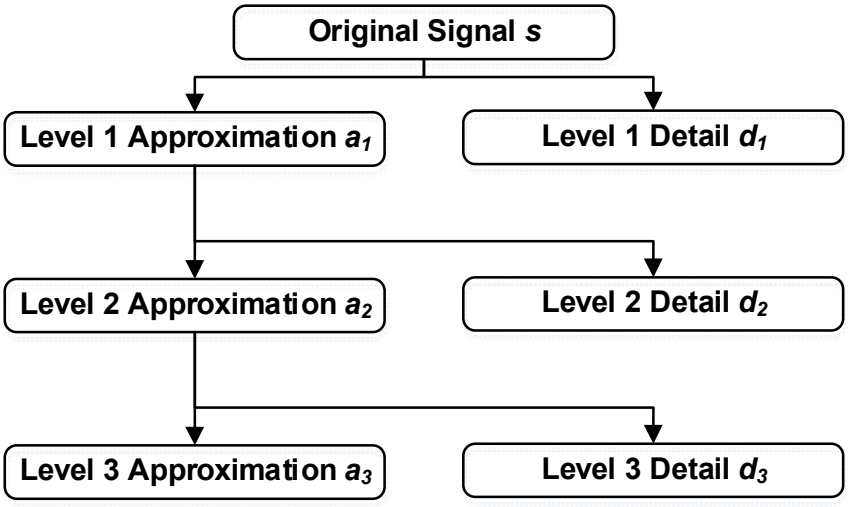

Figure 5-8 Three levels of discrete wavelet decomposition of signal *s*.

To perform wavelet decomposition, a proper wavelet function should be used. The wavelet coefficients describe how well the scaled and shifted wavelet function matches the original signal. Thus, it is better to choose a wavelet that is similar to the incident GPR signal *(84)*. Figure 5-9 shows four commonly used wavelet functions. It is obvious that the Haar wavelet and Morlet wavelet are not similar to the incident GPR signal. Sym5 and Daubechies 5 (db5) wavelets are similar to the incident signal. In this study, db5 wavelet was used as the wavelet function. Three-level wavelet decomposition was performed.

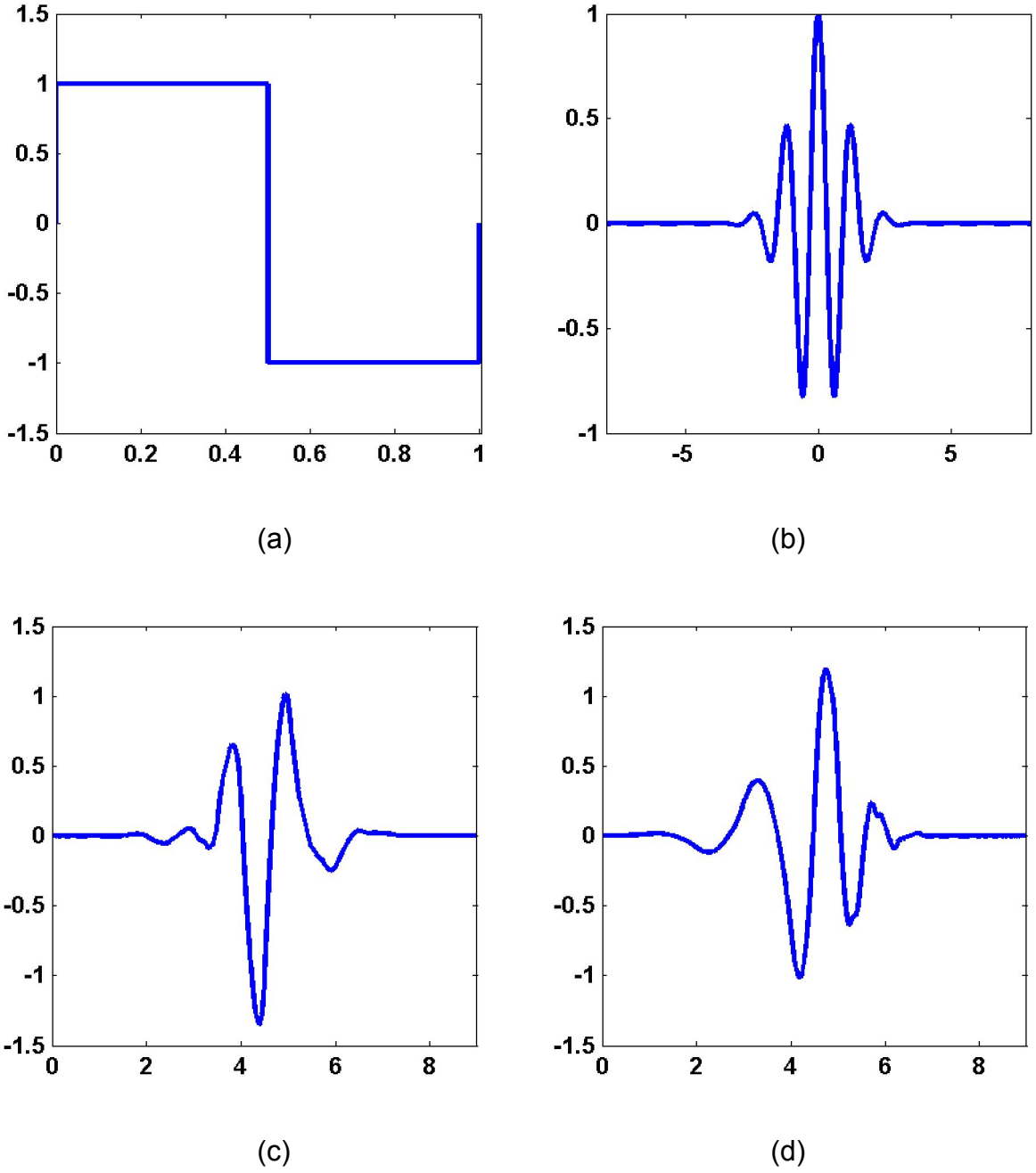

Figure 5-9 Different wavelet functions: (a) Haar; (b) Morlet; (c) Symlets 5; and (d) Daubechies 5.

As shown in Figure 5-10 (a), the original signal was noisy. The level 1 reconstructed approximation and detail are shown in Figure 5-10 (b) and (c). Level 1 detail consisted mostly of noise with amplitude ranging from -0.05 to 0.05. Level 1 approximation was further decomposed into level 2 approximation and detail, as shown in Figure 5-10 (d) and (e). Level 2 detail consisted of noise with amplitude ranging from -4×10^{-3} to 4×10^{-3}, and level 3 detail mainly consisted of noise, as shown in Figure 5-10(g). Reconstructed level 3 approximation represented the signal after de-noising, as shown in Figure 5-10 (f). The effect of DWT de-noising on copper reflection and surface reflection is shown in Figure 5-11. As can be seen, the noise was removed and the signals became smoother after de-noising in both cases.

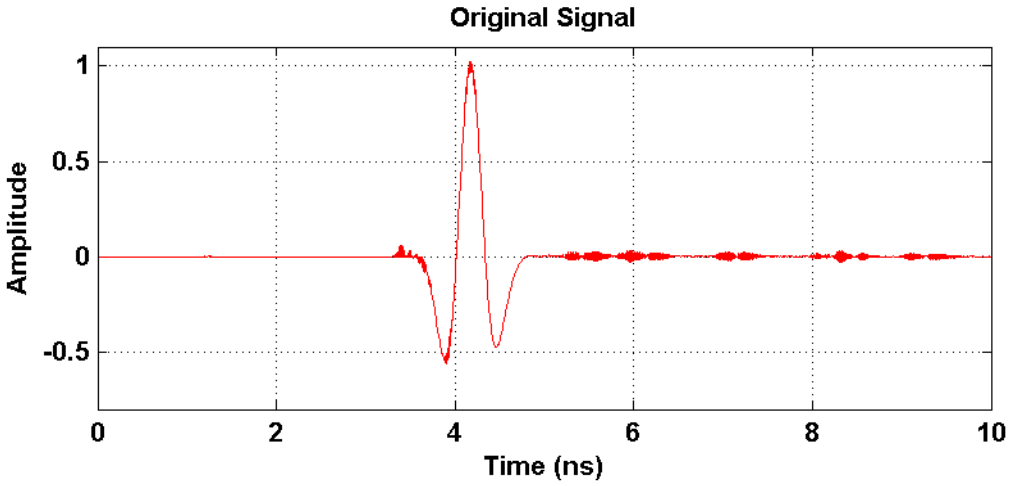

(a)

Figure 5-10 Three-level DWT decomposition using db5 wavelet and its de-noising effect: (a) original signal; (b) reconstructed level 1 approximation; (c) reconstructed level 1 detail; (d) reconstructed level 2 approximation; (e) reconstructed level 2 detail; (f) reconstructed level 3 approximation; (g) reconstructed level 3 detail.

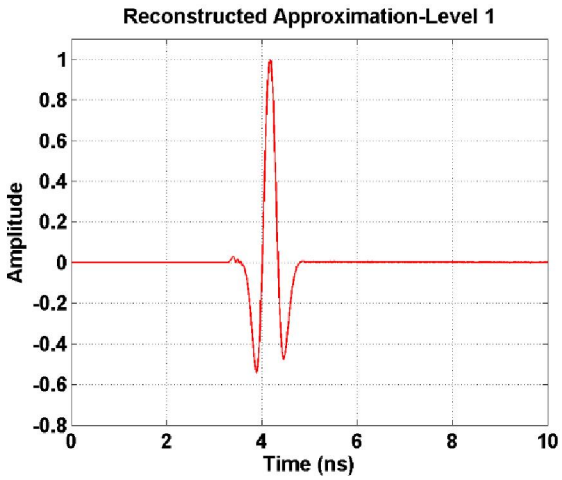

(b)

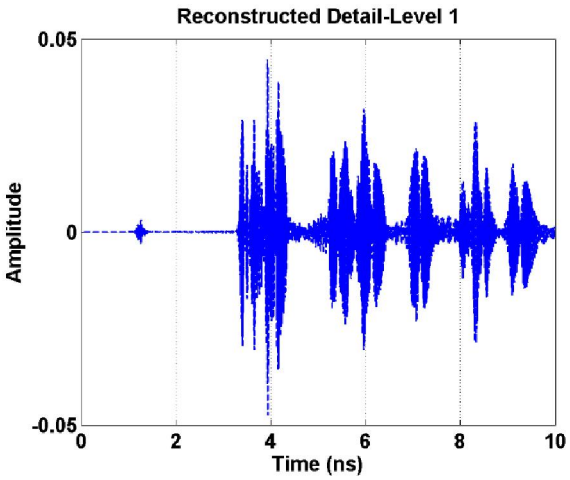

(c)

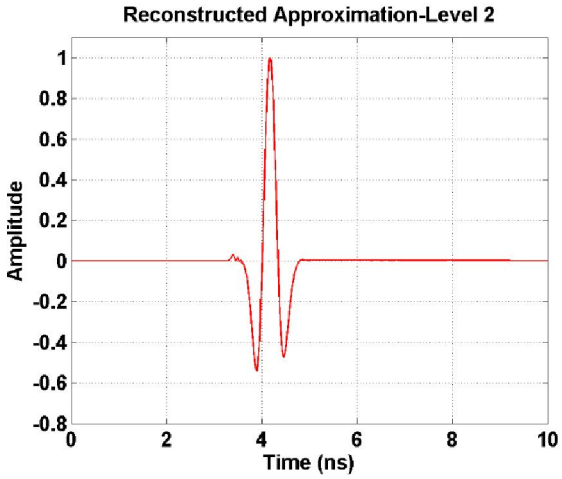

(d)

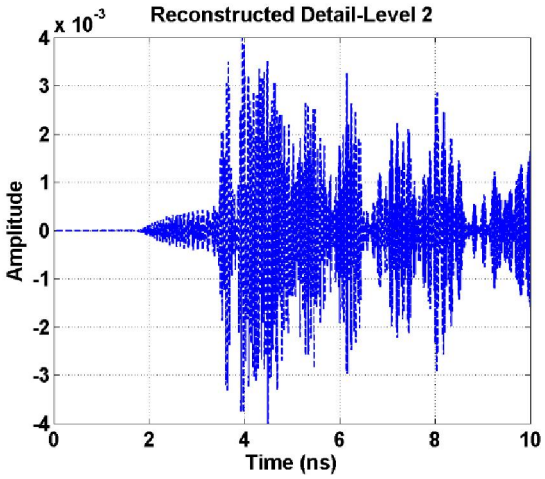

(e)

Figure 5-10 (cont.)

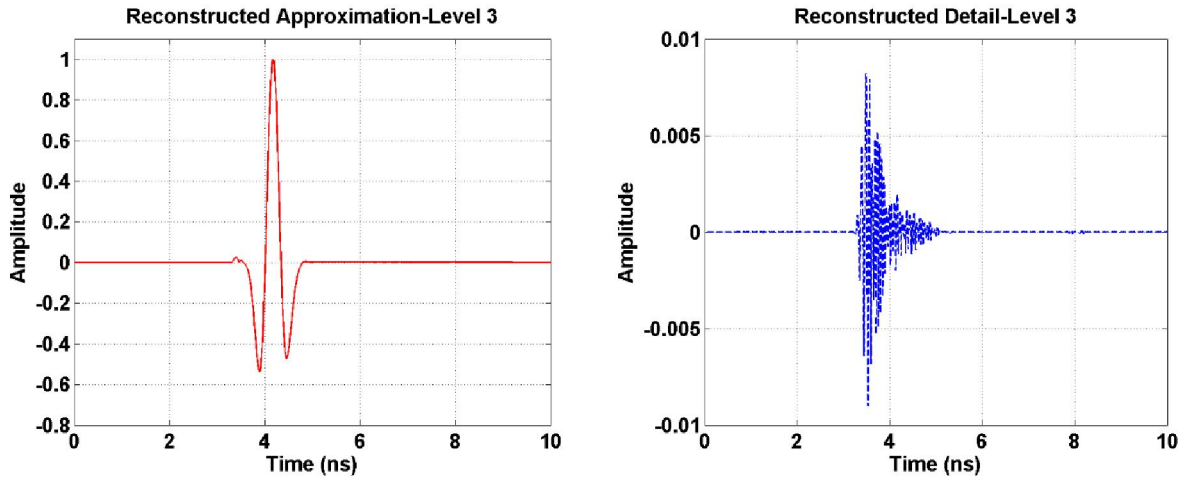

(f) (g)

Figure 5-10 (cont.)

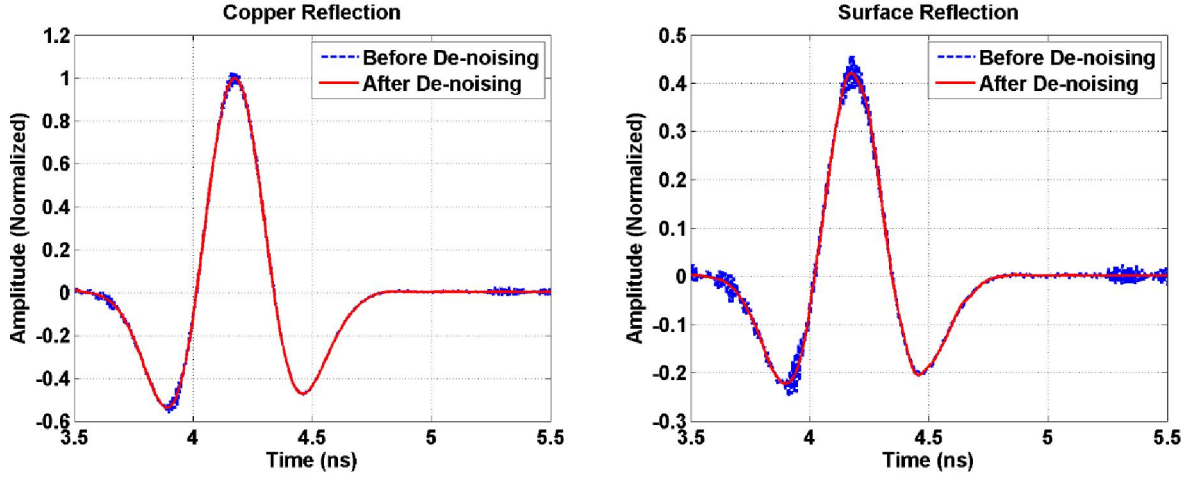

Figure 5-11 Effect of de-noising using DWT: (a) copper reflection; (b) surface reflection.

5.1.4 Calibration Results

By utilizing the equivalent excitation source and the DWT de-noising techniques described in previous sections, the FDTD simulation generated the same GPR signal. Figure 5-12 (a) and (b) shows a comparison of copper reflection between simulated

GPR signal and real GPR signal, in both time and frequency domains. The waveform and frequency components matched. Figure 5-12 (c) and (d) illustrates a good match of surface reflections from simulated GPR signal and real GPR signal. This means that the FDTD simulation was well calibrated to the real GPR data based on copper reflection and surface reflection.

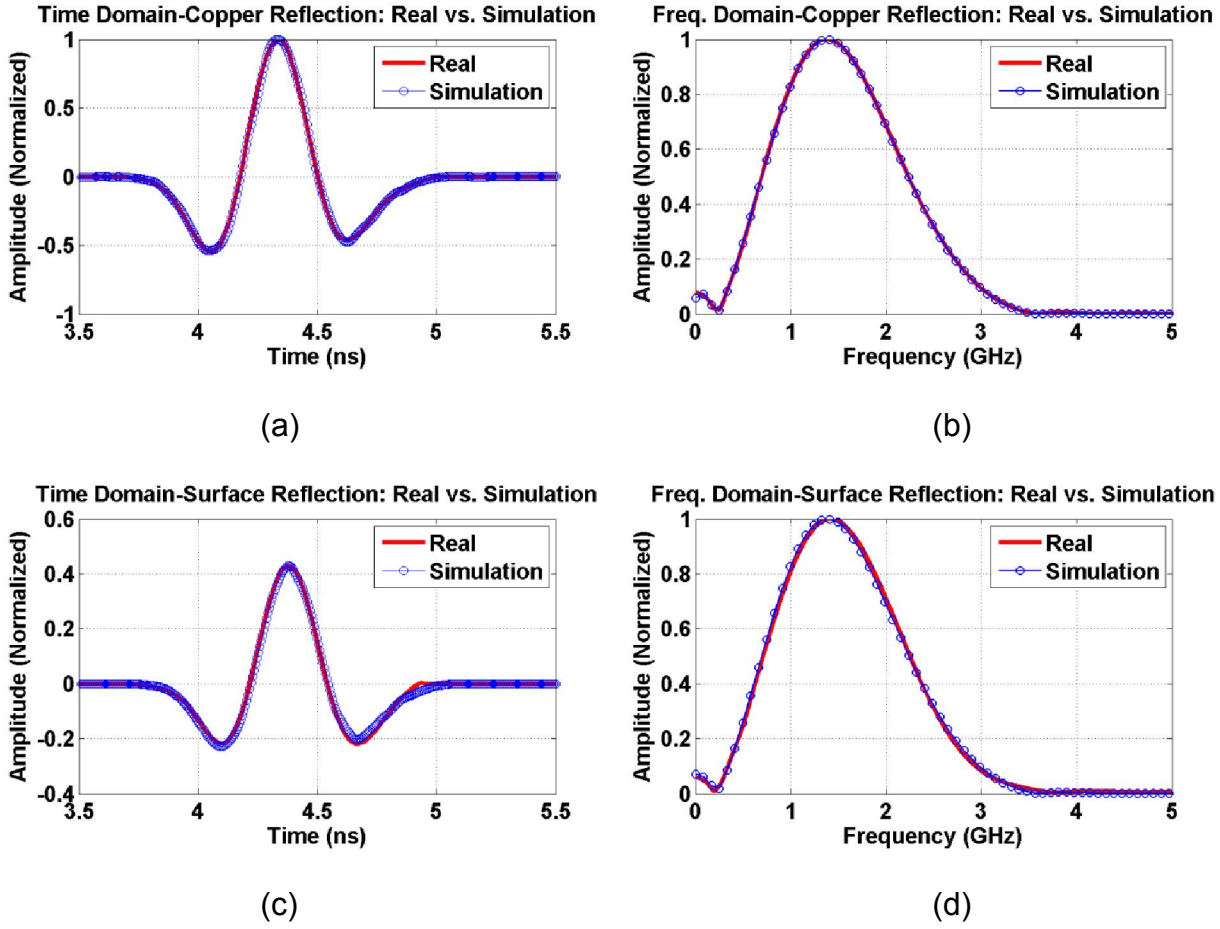

Figure 5-12 Comparison of simulation and real GPR signal using equivalent excitation source: (a) copper reflection in time domain; (b) copper reflection in frequency domain; (c) surface reflection in time domain; (d) surface reflection in frequency domain.

Even though the FDTD simulation was well calibrated, there were sources of errors within the simulation which could undermine the accuracy of the simulation results. For example, numerical discretization could cause numerical phase error and computational boundaries could produce reflections. Choosing proper discretization parameters and appropriate PML parameters controlled these errors. To evaluate how these errors affect the accuracy of the acquisition of pavement information using GPR data, a comparison of input dielectric constant values and dielectric constant values obtained from calculation using simulated GPR data were conducted.

Dielectric constant values obtained from 5 real test sections were used as the dielectric constant values of the AC layer in FDTD models. The received surface reflection of the GPR signals in FDTD is shown in Figure 5-13. The maximum amplitude of surface reflection increased with increasing value of the dielectric constant. The simulated GPR signals were used to back-calculate the dielectric constant of the AC layer using Equation (2-26). The results are shown in Table 5-1. The accuracy was high before the DWT de-noising (with 0.45% average error) and even higher after the DWT de-noising (with 0.07% average error). This indicates the selection of parameters in FDTD was reasonable.

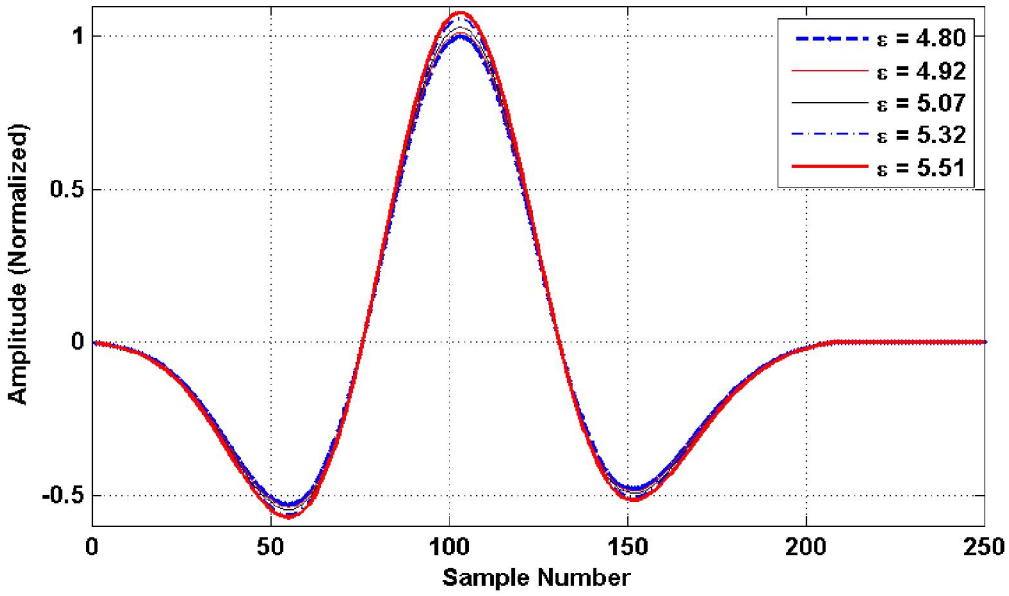

(a)

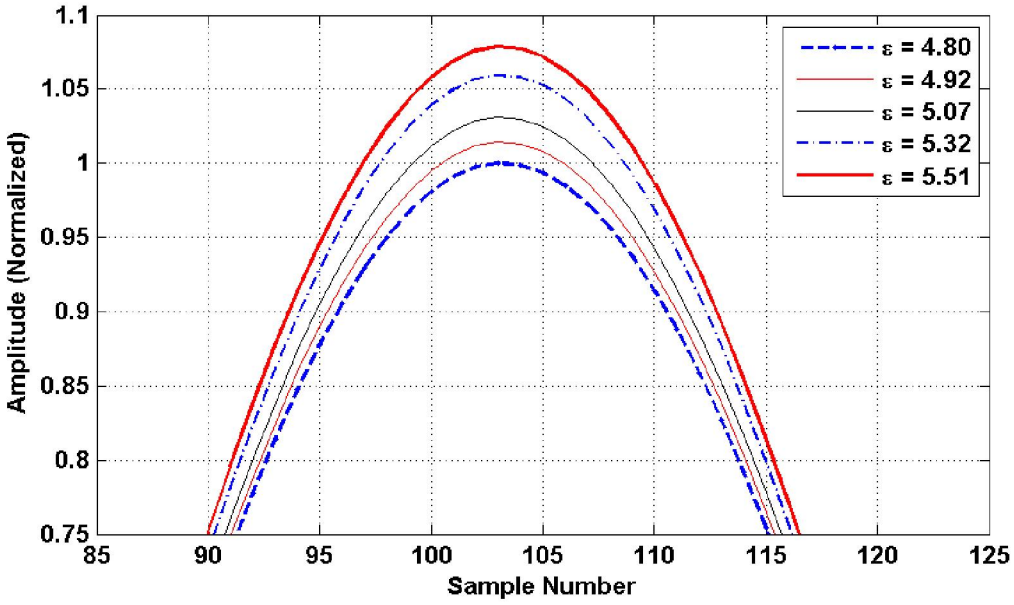

(b)

Figure 5-13 Surface reflection on dry pavement with different dielectric constant values in time domain: (a) surface reflection; (b) magnified partial of surface reflection.

Table 5-1 Accuracy of Back-calculated Dielectric Constant Results

Location	Actual ε_{AC}	ε_{AC} before De-noising	ε_{AC} after De-noising	Error before De-noising	Error after De-noising
1	4.801	4.822	4.797	0.43%	0.08%
2	4.922	4.943	4.918	0.44%	0.08%
3	5.070	5.092	5.066	0.44%	0.07%
4	5.325	5.348	5.322	0.44%	0.06%
5	5.509	5.535	5.506	0.49%	0.05%
			Mean Error	0.45%	0.07%

5.2 Frequency-Selective Effect

In this section, the difference of the effect of density variation and surface moisture variation on GPR signals is discussed.

5.2.1 Effect of Density Change on GPR Signal

As mentioned in Section 2.5.2, the dielectric constant and the density of asphalt mixture have a positive correlation. Higher density results in higher dielectric constant value. Thus, in FDTD simulation, the different dielectric constant values of asphalt mixture were used to reflect different densities. The dielectric constant values of asphalt pavement shown in Table 5-1 were used in the simulation. The electrical conductivity of the asphalt pavement is usually very small. In the FDTD simulation, the conductivity of asphalt pavement, σ, was set to be 1×10^{-4} S/m.

Figure 5-14 shows the propagation of EM wave within the compaction region of the dry pavement model. As can be seen, the PML boundaries absorbed the EM wave well. At the pavement surface (height = 0.3 m) and the interface of surface layer and base layer (height = 0.2 m), part of the EM wave energy was reflected back and part of the EM wave energy transmitted through the interfaces. The electric field E_z was recorded at the receiving antenna as the receiving signal. The pulse reflected from the pavement surface was extracted for further analysis.

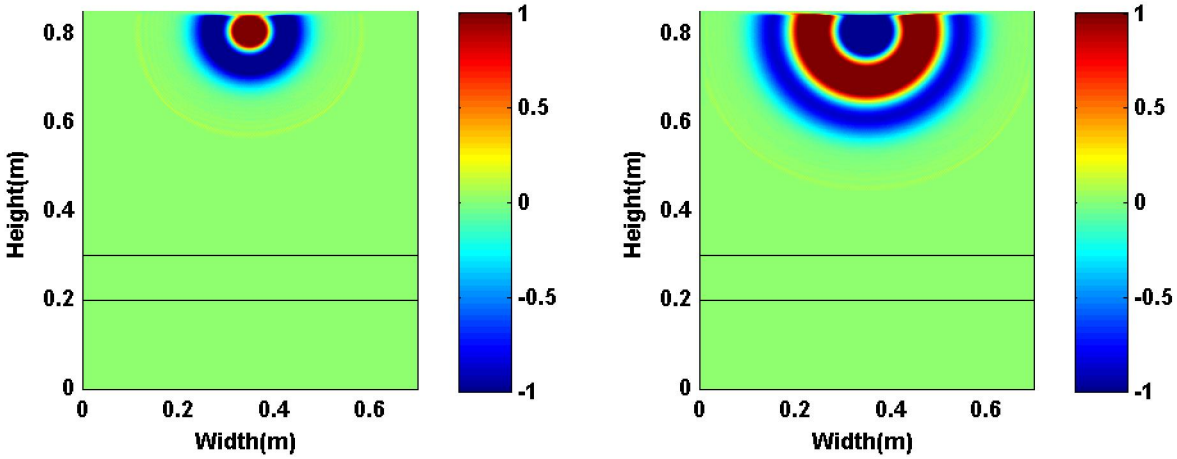

(a) (b)

Figure 5-14 Propagation of EM wave within the computation region of dry pavement model at: (a) 0.8 ns; (b)1.2 ns; (c) 1.8 ns; (d) 2.4 ns; (e) 2.6 ns; (f) 2.8 ns; (g) 3.0 ns; (h) 3.4 ns.

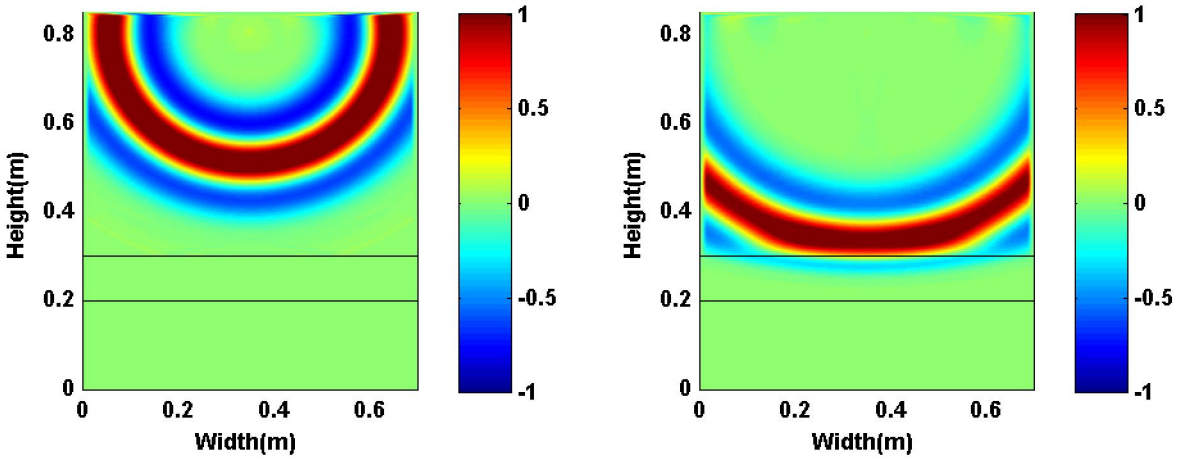

(c)

(d)

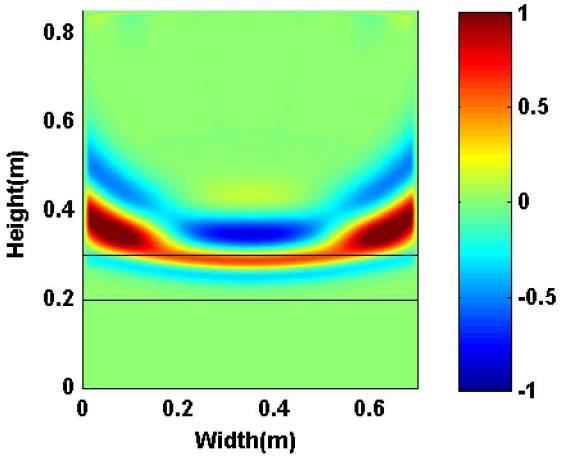

(e)

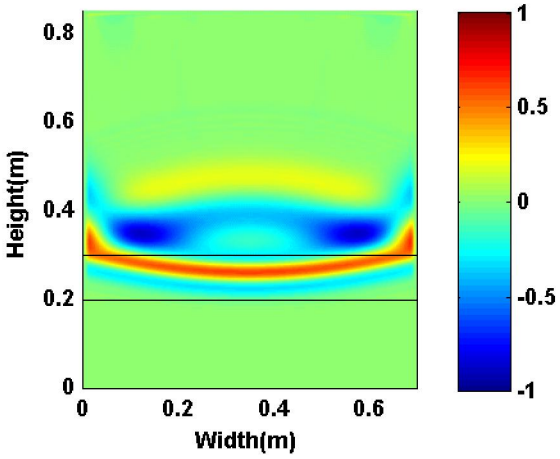

(f)

Figure 5-14 (cont.)

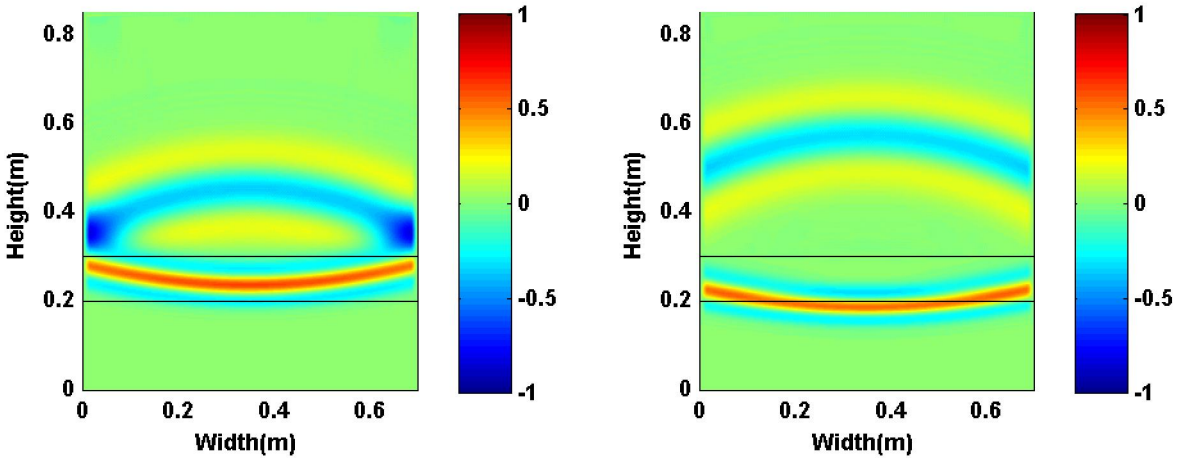

(g) (h)

Figure 5-14 (cont.)

The time domain surface reflections are shown in Figure 5-13. Figure 5-15 (a) shows the simulated GPR signals in frequency domain. Figure 5-15 (b) shows a magnified part of Figure 5-15 (a) for better visibility. When the dielectric constant value increased as a result of the increase in asphalt pavement density, the amplitude of GPR signal increased in frequency domain. It should be pointed out that the increase of amplitude in the frequency domain occurred over the entire frequency range, which means that the whole frequency components were sensitive to the increase of asphalt pavement density. This finding was verified by experimental results, as shown in Figure 5-15 (c) and (d).

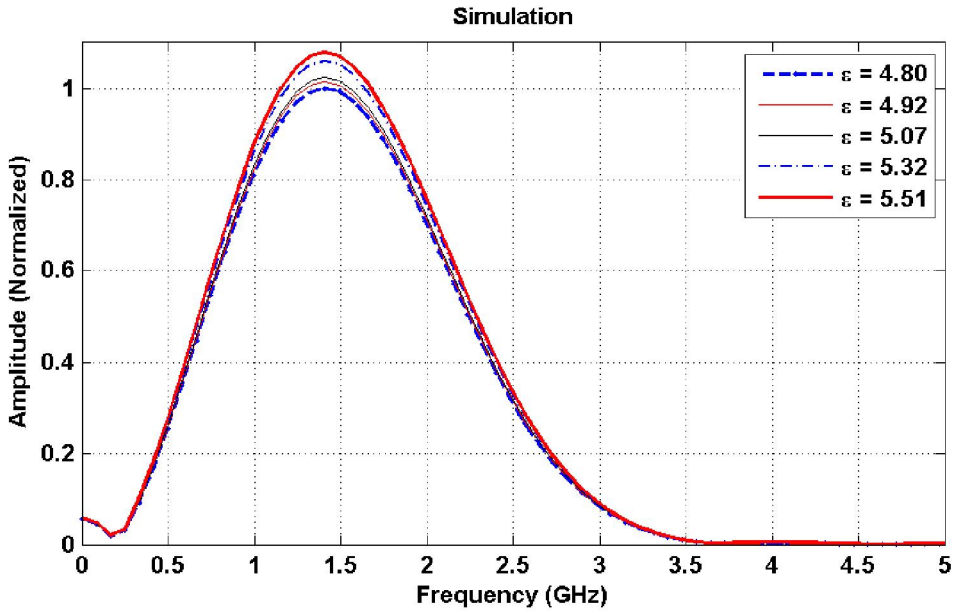

(a)

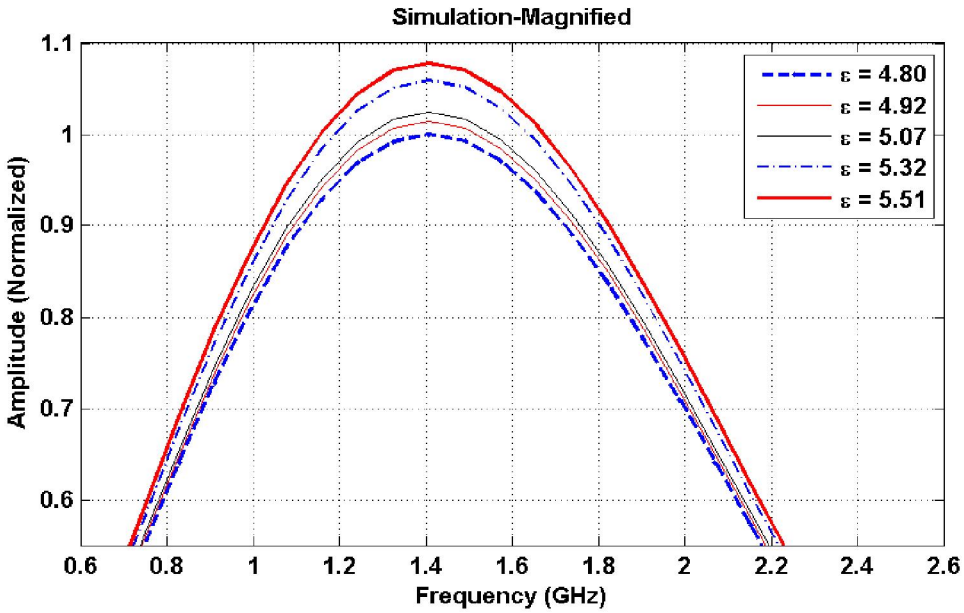

(b)

Figure 5-15 Frequency spectrum of surface reflection on pavement with five different dielectric constant values: (a) whole spectrum of simulation data; (b) magnified partial spectrum of simulation data; (c) whole spectrum of real data; (d) magnified partial spectrum of real data.

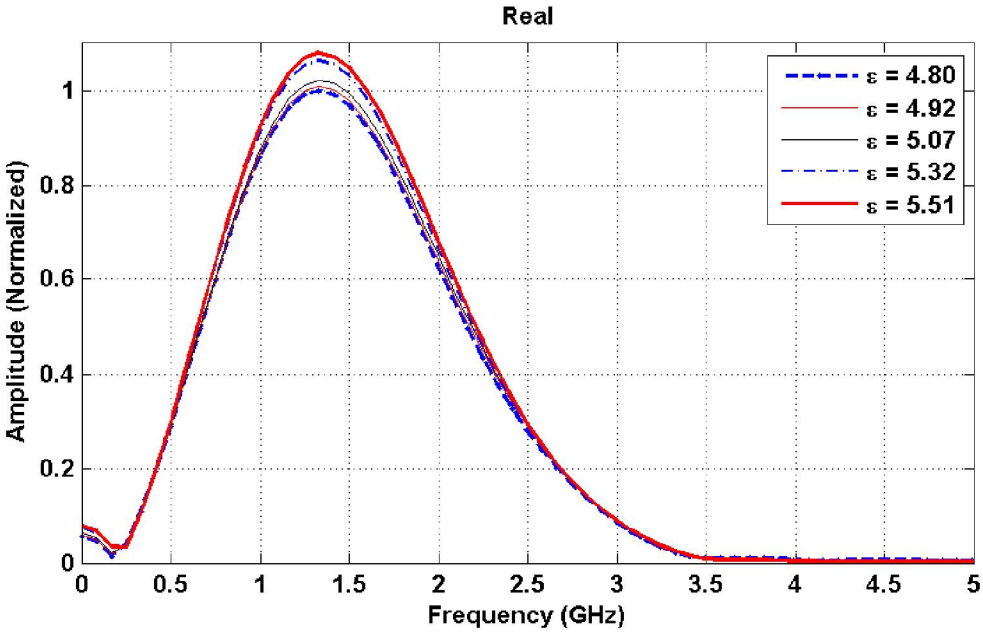

(c)

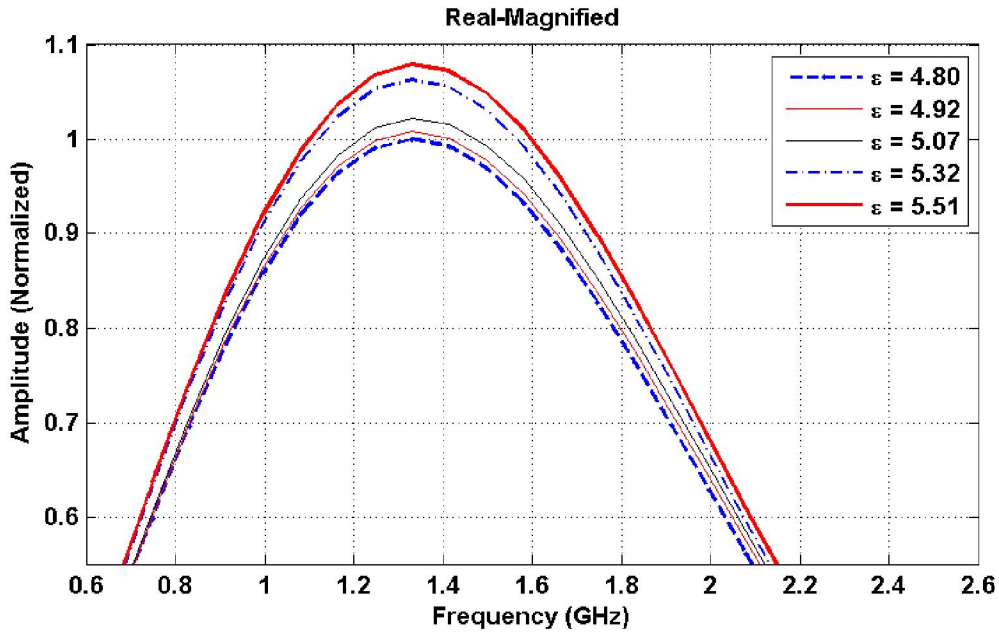

(d)

Figure 5-15 (cont.)

5.2.2 Effect of Surface Moisture Change on GPR Signal

Section 5.2.1 illustrates the effect of density change on GPR signals using simulated data and real data in time domain and frequency domain. In this section, the effect of surface moisture on GPR signal is discussed.

To generate the GPR signals corresponding to pavement with different surface moisture contents in FDTD simulation, the pavement model shown in Figure 3-3 (b) was used. Compared with the pavement model in Figure 3-3 (a), which was used to study the effect of density change, Figure 3-3 (b) has an additional wet AC layer placed on top of the dry AC layer. The variation of surface moisture contents was achieved by changing the material property of the wet AC layer. The dielectric constant and the conductivity of the wet AC layer changed to simulate the change of the surface moisture content. In this study, the dielectric constant value varied from 5.35 to 9 and the conductivity varied from 1×10^{-4} S/m to 200×10^{-4} S/m. The dielectric constant of 5.35 and conductivity of 1×10^{-4} S/m corresponded to the dry pavement without any moisture. The dielectric constant of 9.00 and conductivity of 200×10^{-4} S/m corresponded to the wet AC pavement with the highest moisture content in this study. The selection of these values was based on the data collected from various literatures *(85–87)*.

Figure 5-16 shows the EM wave propagation within the model of pavement with surface moisture. The thin wet AC layer is marked with the blue line in Figure 5-16 at the height of 0.3 m. The GPR wave reflected by the pavement structure was recorded by the receiving antenna as the received GPR signal.

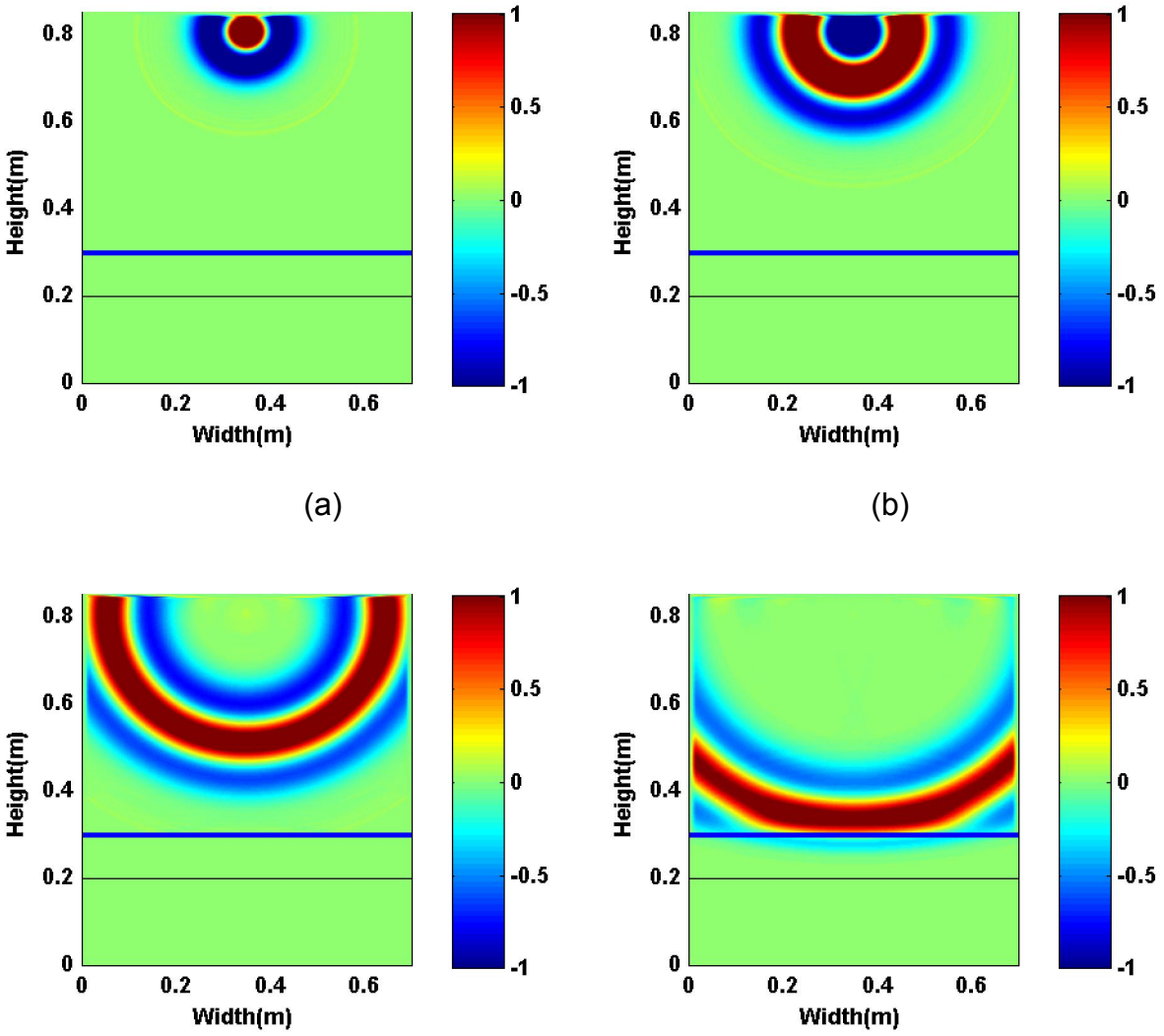

Figure 5-16 Propagation of EM wave within the computation region of wet pavement model at: (a) 0.8 ns; (b)1.2 ns; (c) 1.8 ns; (d) 2.4 ns; (e) 2.6 ns; (f) 2.8 ns; (g) 3.0 ns; (h) 3.4 ns.

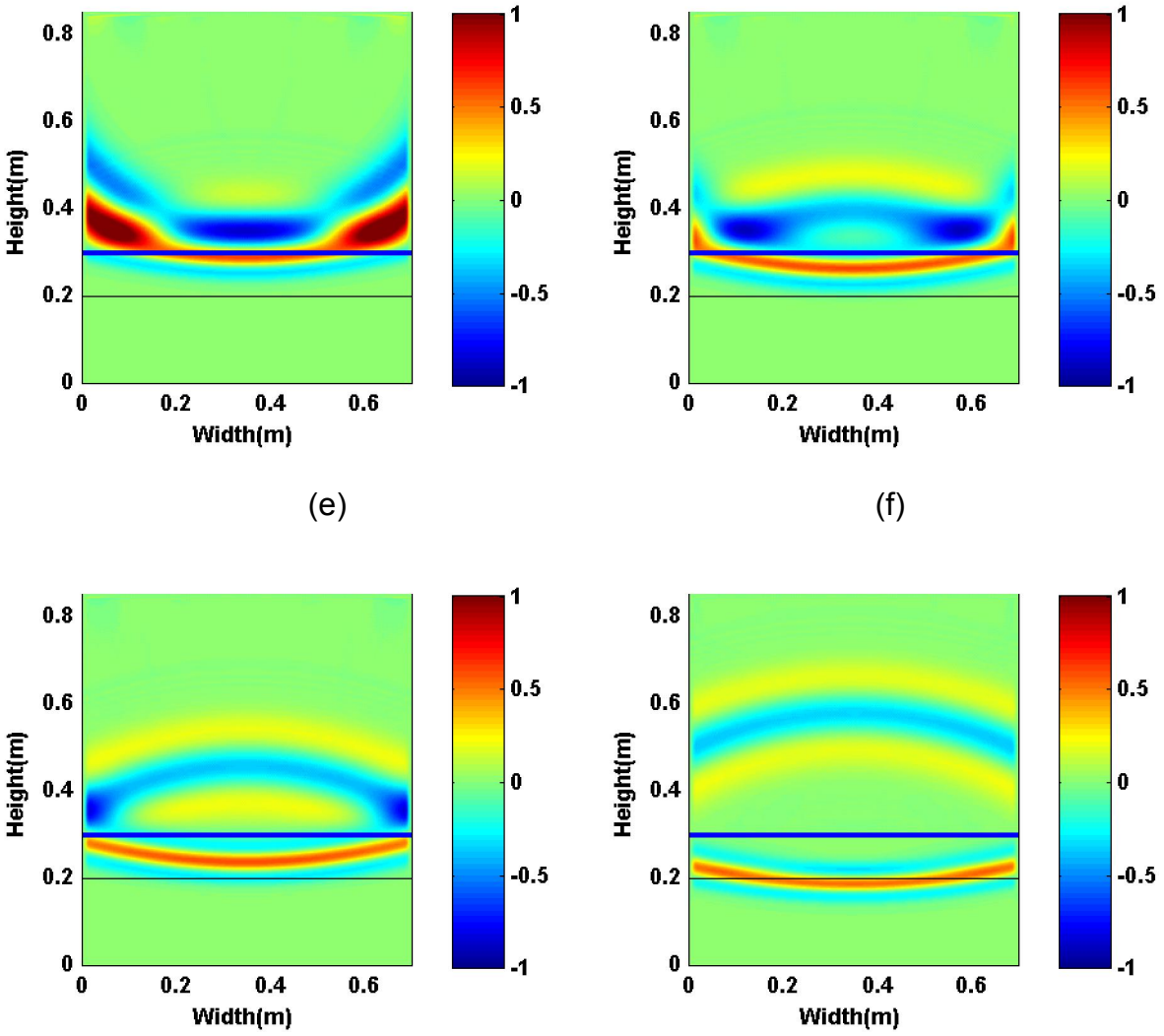

(e) (f)

(g) (h)

Figure 5-16 (cont.)

A parallel laboratory experiment was conducted on test site 1 to generate real GPR data which could be used to compare with the simulated GPR data. Figure 5-17 (a) shows the setup of the GPR antennas during the tests. Under each antenna, a 3 ft × 3 ft (0.91 m × 0.91 m) square area was sprayed with 8.5 oz. (250 mL) of water. A

compressed air sprayer, shown in Figure 5-17 (b), was used to spray a controlled amount of water evenly. The amount of water sprayed in the test was comparable to the amount sprayed by a compactor during compaction. The amount of water sprayed in the test was calculated by assuming a compactor with a 5.6 ft (1.7 m) wide drum spraying 198 gal. (750 L) water on 6,562 ft (2,000 m) of pavement *(62)*. The GPR data was collected after spraying the water at 1-min intervals until the pavement was dry. In this test, the change in the GPR signal with different amounts of remaining surface water was captured.

(a) (b)

Figure 5-17 Laboratory experiments to investigate the effect of surface moisture on GPR signal: (a) surface moisture areas under the antennas; (b) compressed air sprayer for even application of water.

In both FDTD simulation and laboratory experiments, the surface reflection of GPR signal increased with the increase of surface moisture content in time domain. The

surface reflection signals were then transferred to frequency domain using Fourier transform and the frequency spectrum shown in Figure 5-18.

The GPR data obtained from the FDTD simulation is shown in Figure 5-18 (a) and (b). Figure 5-18 (a) shows the entire frequency spectrum of the surface reflection in the simulated GPR signal. Part of Figure 5-18 (a) is magnified in Figure 5-18 (b) for better visibility. Higher frequency components increased more than lower frequency components as a result of the increase in surface moisture content. This was the major difference between the change of signal when moisture content varied and the change of signal when pavement density varied. And this “frequency-selective” effect shown in the simulation study was verified by experimental GPR data. Figure 5-18 (c) and (d) shows the GPR data obtained from the laboratory experiment. The red line in Figure 5-18 (c) and (d) shows that, right after water was sprayed on pavement, the amplitude increased to the highest level. The amplitude curve decreased with time because less and less water remained on the surface. After 35 min, the amplitude curve became very close to the amplitude curve of dry pavement, which indicates that the pavement was almost dry after 35 min of water evaporation. The registered variation was primarily attributed to higher frequency components (i.e. larger than 1 GHz) caused by the increase in moisture content. The lower frequency components (i.e. less than 1 GHz), on the other hand, almost kept the same amplitude.

In addition to the analysis of simulated GPR data and experimental GPR data, GPR data from real construction site were also investigated. Fourier transform was performed on the GPR data shown in Figure 4-4. The frequency spectrum is shown in Figure 5-19. As seen in Figure 5-19 (a) and (b), the increase of amplitude was mainly

attributed to the high frequency components and low frequency components almost kept the same amplitude. The field test results verify the findings in the simulation study and laboratory experimental study.

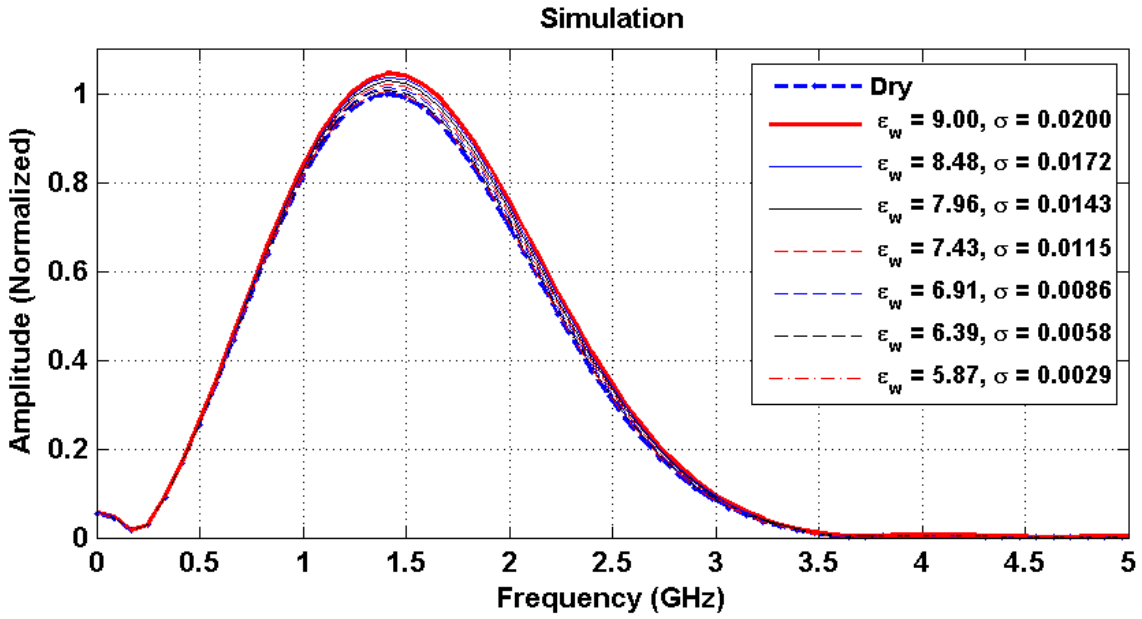

(a)

Figure 5-18 Frequency spectrum of surface reflection data on pavement with eight different surface moisture contents: (a) whole spectrum of simulation data; (b) magnified partial spectrum of simulation data; (c) whole spectrum of real data; (d) magnified partial spectrum of real data.

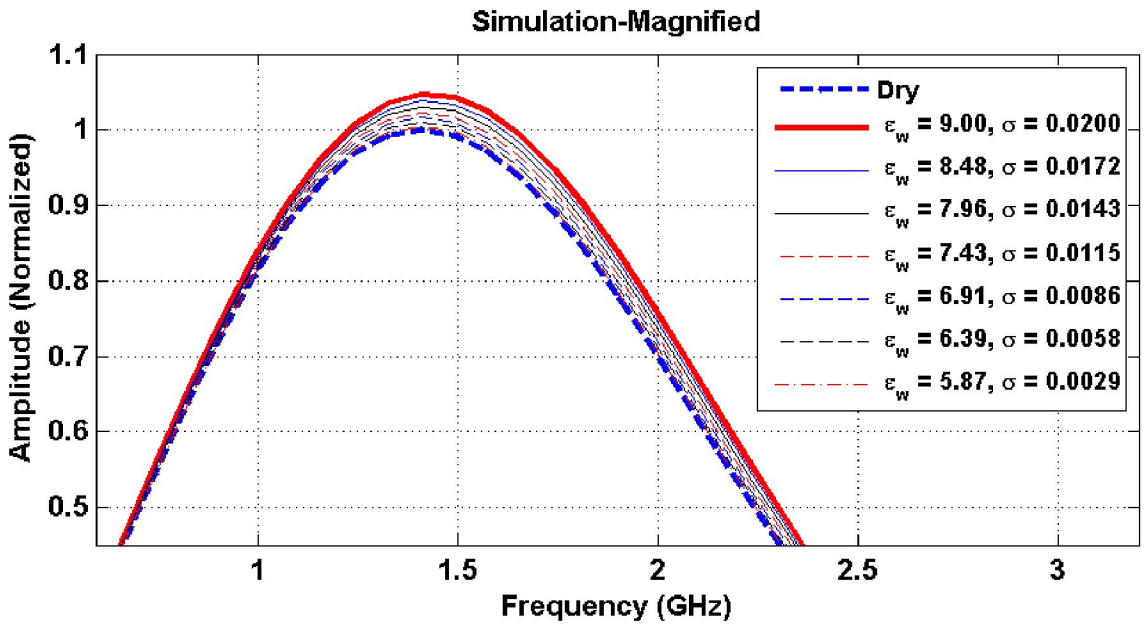

(b)

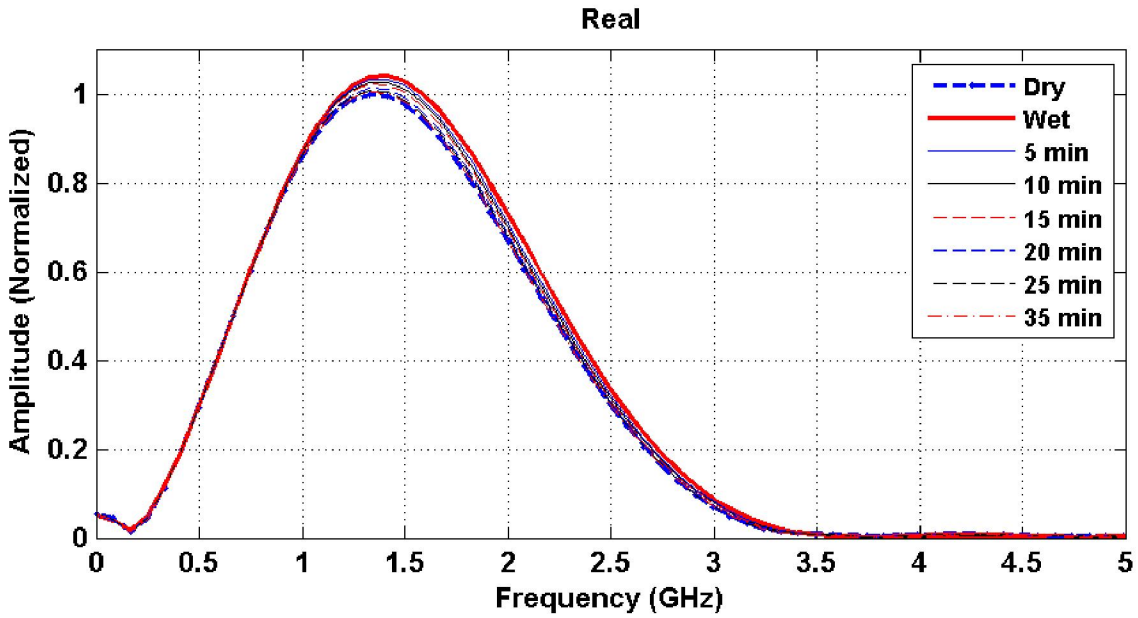

(c)

Figure 5-18 (cont.)

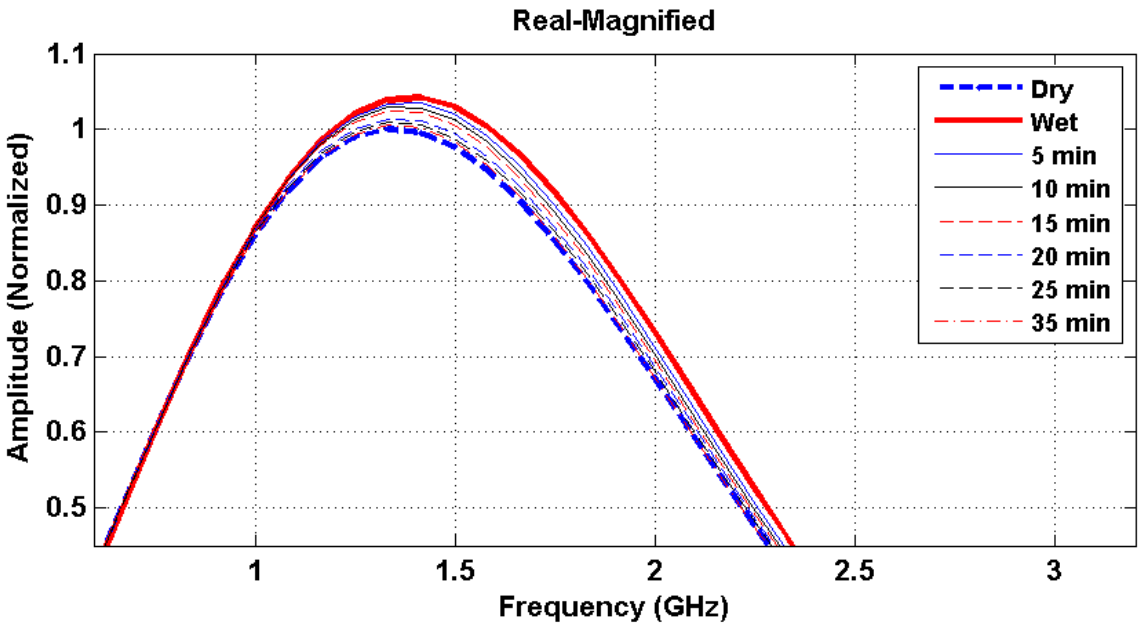

(d)

Figure 5-18 (cont.)

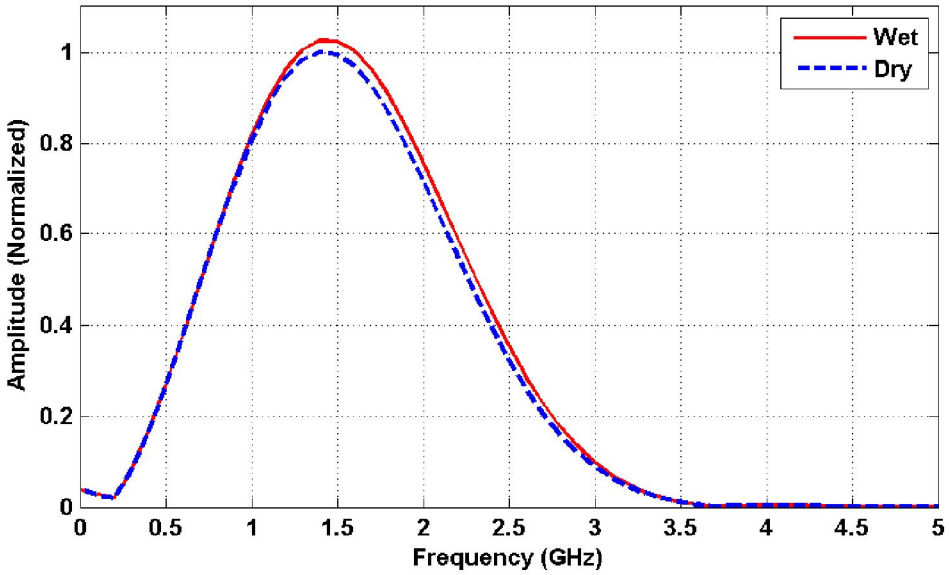

(a)

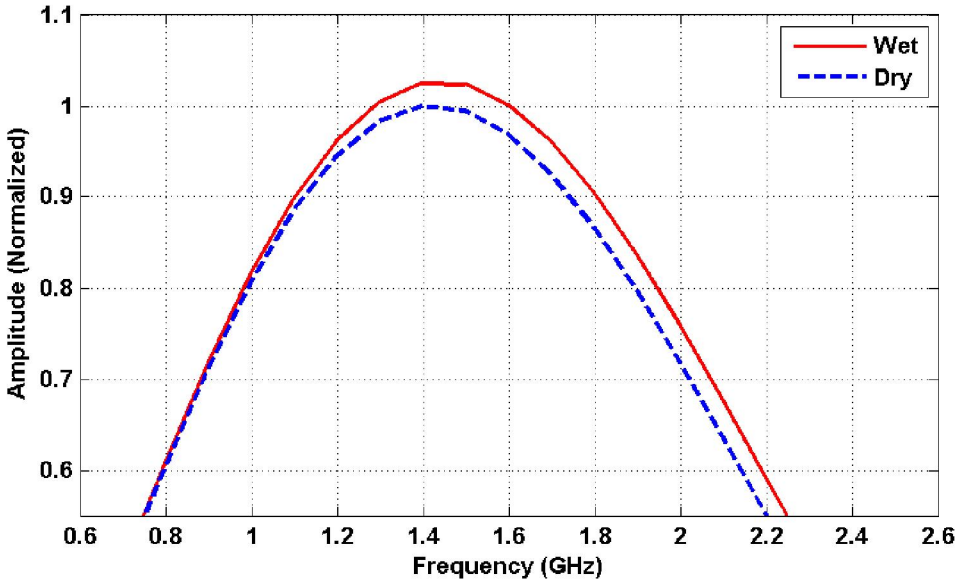

(b)

Figure 5-19 Frequency spectrum of surface reflection data on asphalt pavement in real construction site: (a) whole spectrum of GPR data collected from real construction site; (b) magnified partial spectrum of GPR data collected from real construction site.

In this section, the GPR data obtained from FDTD simulation, laboratory experiments, and real construction site was investigated. The data showed the frequency-selective effect when surface moisture content varied. Comparing Figure 5-15, Figure 5-18, and Figure 5-19, it is easy to distinguish the effect of density variation and the effect of surface moisture content variation on GPR signals. This indicates that lower frequency components, which are sensitive to density change but insensitive to moisture content variation, could be a good feature for monitoring density change during compaction with minimum influence from surface moisture variation.

CHAPTER 6 LABORATORY EXPERIMENTS AND ALGORITHM DEVELOPMENT

The difference between the effects of density variation and surface moisture variation on GPR signal was investigated and the frequency-selective effect was found. The next step was to develop algorithms to eliminate the effect of surface moisture while keeping the effect of density change. This section describes the research efforts made to develop this “correction algorithm”.

6.1 Stability Analysis of GPR Signal

Stability of the GPR data is of great importance to the accuracy of density measurements using GPR. In the application of compaction monitoring using GPR, the variation of surface reflection amplitude is mainly attributed to the change of density and variation of moisture content. However, even if neither density nor moisture content changes, and assuming there is no significant external noise, the surface reflection amplitude of the GPR signal could still fluctuate. This type of fluctuation is related to the hardware of the system, and it cannot be eliminated by the correction algorithm in this study. Therefore, it was critical to investigate the inherent stability of the GPR data to understand the limitation of the accuracy the correction algorithm could reach.

The instability of the GPR data could result from all components of the GPR equipment, including the transmitting and receiving antennas, power supply, analog-to-digital converter, timing system, and data acquisition control unit. Each of these components has particular characteristics and stability. When all components work together to generate GPR signals, fluctuation within the signals can be induced by factors such as temperature and humidity variation, internal electrical noises, and

feeding voltage fluctuation. To quantify the fluctuation caused by the hardware of GPR system, static GPR data collection (collecting data on one spot) is usually conducted and the variation of certain quantities from trace to trace is calculated.

The quantities of the stability test include the amplitude of the surface reflection or the time position of the surface reflection. Depending on the period of the evaluation, there are two types of stability tests: Short term and long term stability test *(88–90)*.

In this study, the amplitude stability was evaluated both in short term and long term. The amplitude stability is particularly important because the accuracy of density estimation depends on the accuracy of the calculation of dielectric constant, which is directly related to the accuracy of the amplitude of surface reflection.

Based on the criteria proposed by Texas Transportation Institute *(91)*, the short term amplitude stability is defined as the variation of the surface reflection amplitude from trace to trace in 100 GPR traces, which is shown in Equation (6-1):

$$J_{amp} = \frac{(A_{max} - A_{min})}{A_{ave}} \tag{6-1}$$

where J_{amp} represents the short term variation of the amplitude; A_{max} and A_{min} are the maximum and minimum values of the amplitude of the surface reflection for 100 traces, respectively; and A_{ave} is the average amplitude of the surface reflection of the 100 traces.

To obtain the long term amplitude variation (LAV), static GPR data was collected for 2 hours with the first 20 min as the warm-up period. LAV is defined by Equation (6-2):

$$LAV = \frac{(A_{max} - A_{min})}{A_{20}} \tag{6-2}$$

where *LAV* represents the long term variation of the amplitude; A_{max} and A_{min} are the maximum and minimum values of the amplitude of the surface reflection between 20 min and 120 min; and A_{20} is the amplitude of surface reflection of the signal collected at 20 min of warm up period.

The GSSI 2.0-GHz air-coupled antenna was placed on top of a copper plate and static GPR data was collected every minute for around 140 min. In each of the 140 data files, more than 600 GPR scans were collected. The scans from scan number 101 to scan number 600 were extracted and the average value of the reflection amplitude from copper for the 500 GPR scans was calculated. The value versus the time was plotted to evaluate the long term variation of the amplitude. As shown in Figure 6-1, the reflection amplitude decreased within the first 20 min and then became relatively stable. Figure 6-2 depicts the variation of reflection amplitude after 20 min. The variation was then plotted after 20 min in a histogram figure, as shown in Figure 6-3. After 20 min, the amplitude of the surface reflection varied within the range of ±0.8% of the mean value, except for one file. The value of LAV was 1.65%, which satisfies the requirement of being less than 3% *(91)*. The short term amplitude variation J_{amp} was calculated at every 10-minute interval. As shown in Figure 6-4, the value of J_{amp} did not drop after the warm-up period. Although warming up the GPR system did not lower down the J_{amp} values, all of the J_{amp} values were smaller than 1% with a mean value of 0.61%, which satisfies the requirement of being less than 1% *(91)*.

The long term stability value determines the upper limit of the accuracy of the correction algorithm. When two GPR data files were collected on the same pavement before and after spraying a certain amount of water, the difference of the surface amplitude was attributed to the surface moisture and the long term stability (density did not have effect because the two data files were collected from the same location). The correction algorithm could eliminate the effect of surface moisture, but the contribution of long term instability was not eliminated. Because the LAV was 1.65%, the hardware instability might cause ±0.825% of fluctuation in the signal.

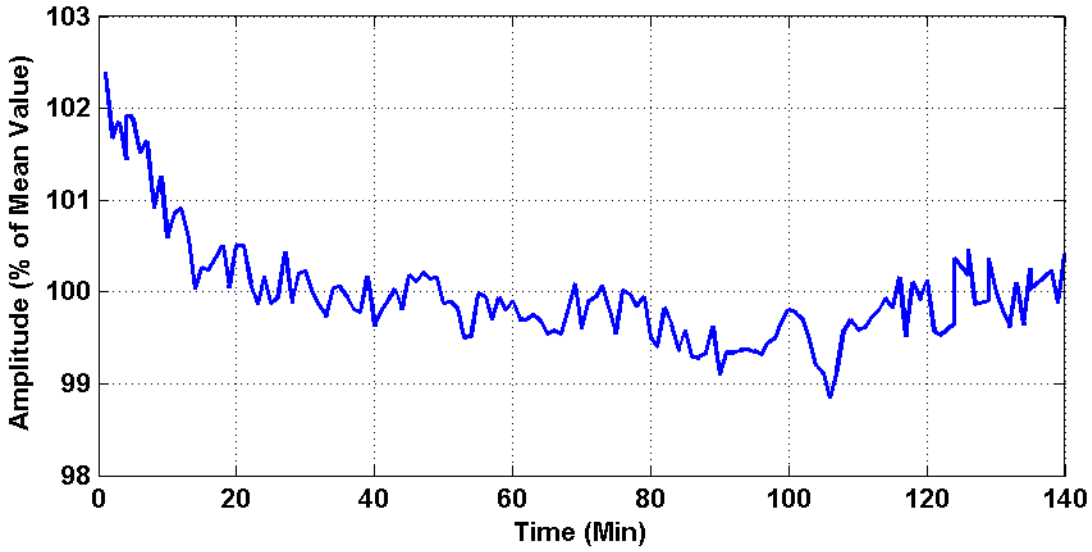

Figure 6-1 Long term variation of the reflection amplitude from copper.

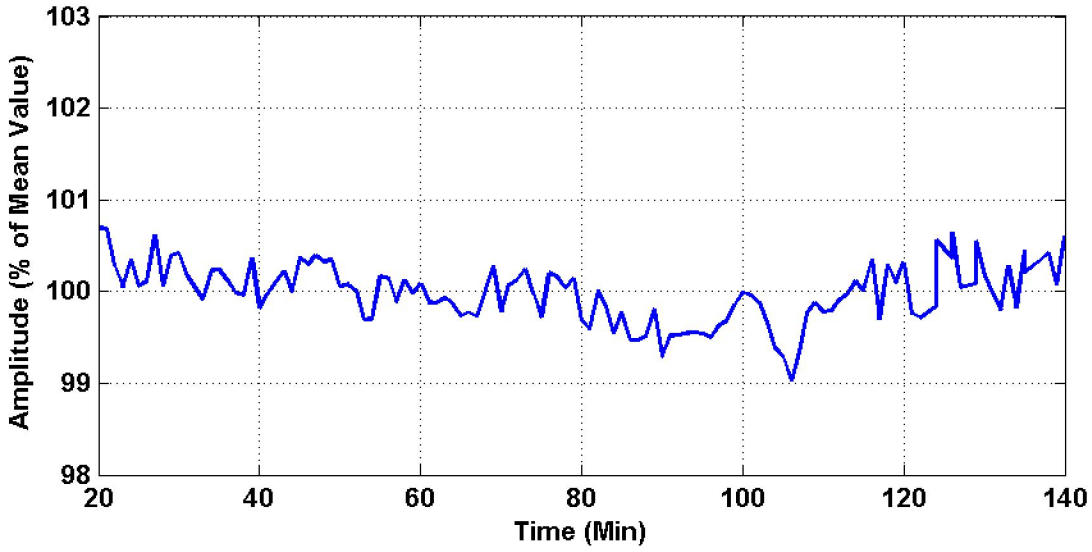

Figure 6-2 Long term variation of the reflection amplitude from copper after 20 min.

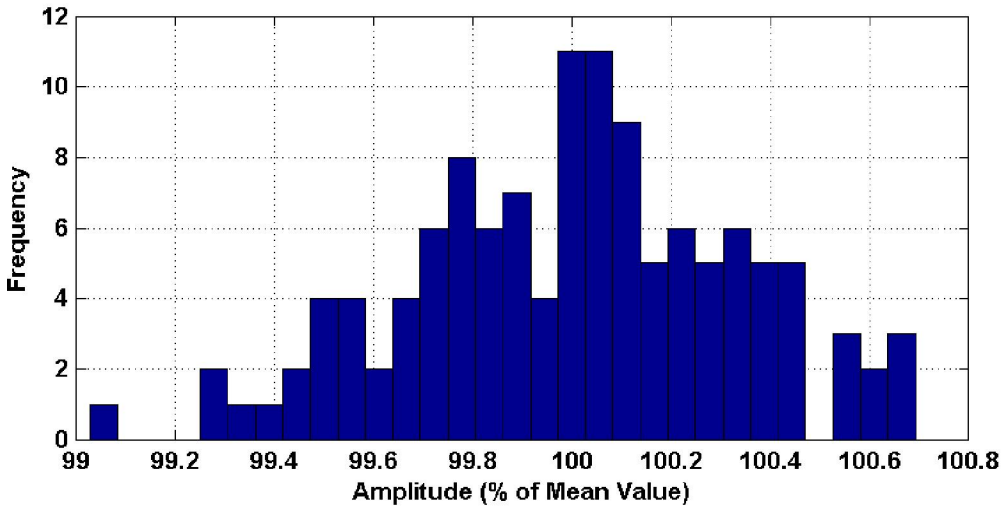

Figure 6-3 Histogram of reflection amplitude after 20 min using 30 bins.

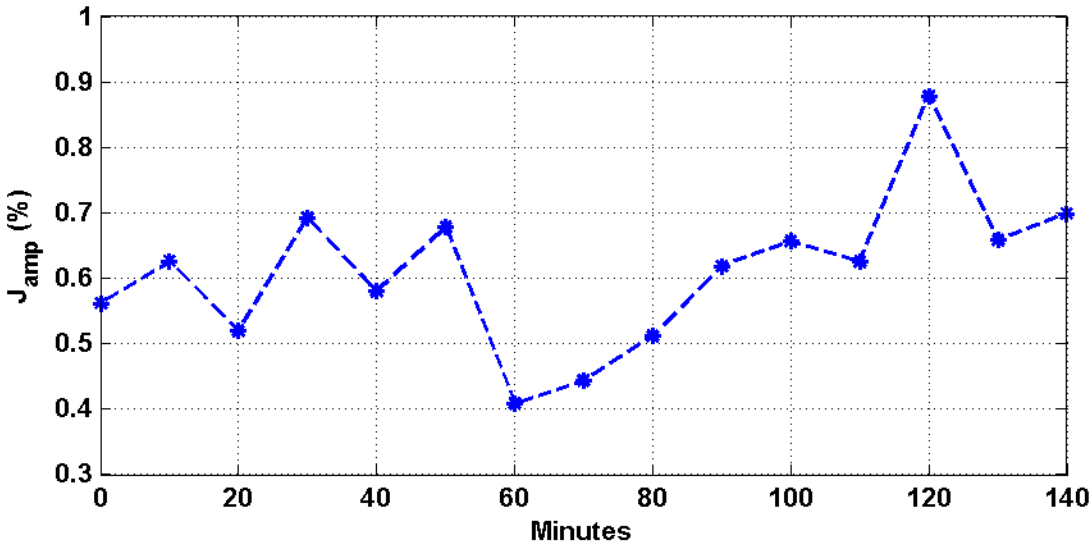

Figure 6-4 Short term stability J_{amp} at 10-min intervals.

6.2 Band-Pass Filtering Approach

As discussed in Section 5.2, the lower frequency components contain the density information, but are not affected by the variation of the surface moisture content. A band-pass filter could be applied to extract the low frequency components of the signal and turn it into a good feature indicating the density of the asphalt pavement.

Figure 6-5 (a) depicts an ideal band-pass filter. Only the frequency components between low-cutting frequency, f_l, and high-cutting frequency, f_h, are preserved *(92)*. The low frequency components of the signal could be preserved by using low frequency values as the cutting frequencies f_l and f_h. Figure 6-5 (b) shows an example of the signal after filtering. The surface reflection amplitude decreased from A_o to A_{fo} because the frequency components outside the passing band were discarded. By applying different

band-pass filters, it was possible to plot and compare the A_{fo} values at different times after the water was sprayed. The data processing procedure is summarized as follows:

- Extraction of the surface reflection from the original signal in the time domain
- Application of the band-pass filter (e.g., 200 MHz to 1.5 GHz) to each scan of the surface reflection
- Extraction of the amplitude of the surface reflection, A_{fo}, in the signal after filtering
- Obtaining the mean value in each GPR data file for all the selected scans
- Repetition of the above four steps for all other GPR data files and normalization of the mean values relative to the data of the dry pavement. The normalized value was considered the feature value corresponding to specific band-pass filtering
- Plotting the feature value versus the time after spraying water
- Adjustment of the cutting frequencies, f_l and f_h, and repetition of all the above steps

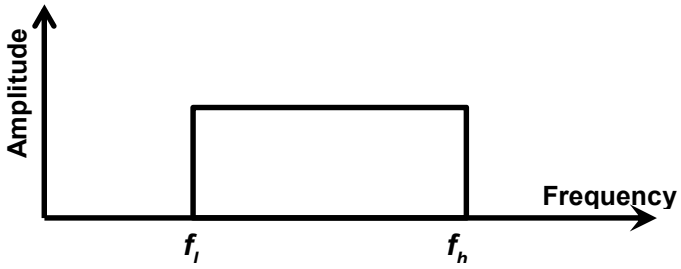

(a)

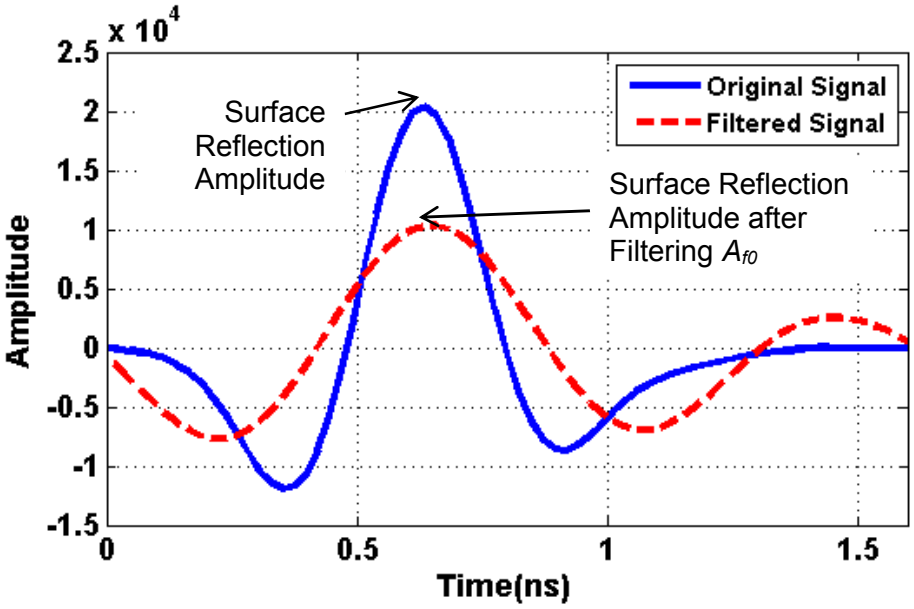

(b)

Figure 6-5 Filtering GPR surface reflection signal: (a) ideal band-pass filter; (b) original GPR surface reflection signal and post band-pass filtered signal.

Figure 6-6 shows several plots of feature values using different band-pass filters. When the water was sprayed on the pavement, the surface reflection amplitude of the original signal increased by 6.2%. When the water evaporated over time, the surface reflection amplitude became smaller and finally reached 100%, which indicated the

pavement was dry. If a band-pass filter with cutting frequencies of 0.2 GHz and 2 GHz was used, the increase in the reflection amplitude right after the water was sprayed was smaller compared with the original data without filtering. This feature indicated less sensitivity to surface moisture. When 0.2 to 0.8 GHz was used as cutting frequencies, the feature value remained around 100% (within 1% error) with different amounts of water, which meant it was insensitive to water.

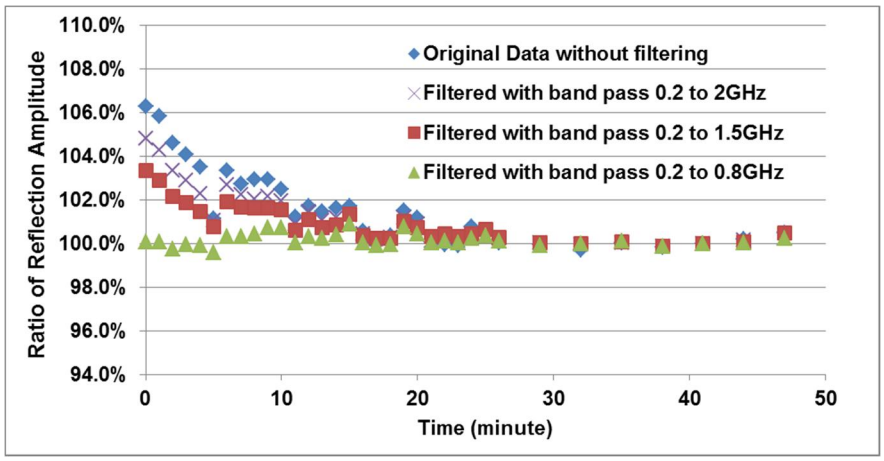

Figure 6-6 Comparison of feature value plots using different feature extraction approaches.

This approach can extract the feature which is insensitive to surface moisture. But the disadvantage of this approach is that it is difficult to obtain the real density values. The band-pass filtering keeps only part of the frequency components of the signal and the surface reflection amplitude is significantly smaller after the filtering. This prevents direct utilization of Equations (2-26) and (2-30) to obtain dielectric constant

and density values. Therefore, another approach was developed which will be described in Section 6.3.

6.3 Correction Algorithm Using Reference Scan Approach

The reference scan approach is based on the assumption that asphalt mixture is a homogeneous, frequency-independent, and lossless material for the GPR wave. When the density of the dry pavement increases, the amplitude of the surface reflection pulse also increases, but the shape of the surface pulse remains the same. The shape in time domain dominates the frequency spectrum in frequency domain. Therefore, in frequency domain, the amplitudes over the entire frequency range increase by the same percent and the distribution of the amplitude over the entire frequency range remains the same. This has been showed in Figure 5-15 as well as in Figure 6-7. As shown in Figure 6-7, the reflection coefficient remains the same over the frequency range from 0.2 to 3.5 GHz, which is the main frequency range of the GPR signal. The fluctuations close to 0 and 3.5 GHz might be caused by quantization error, when the amplitudes at these frequency range becomes very small.

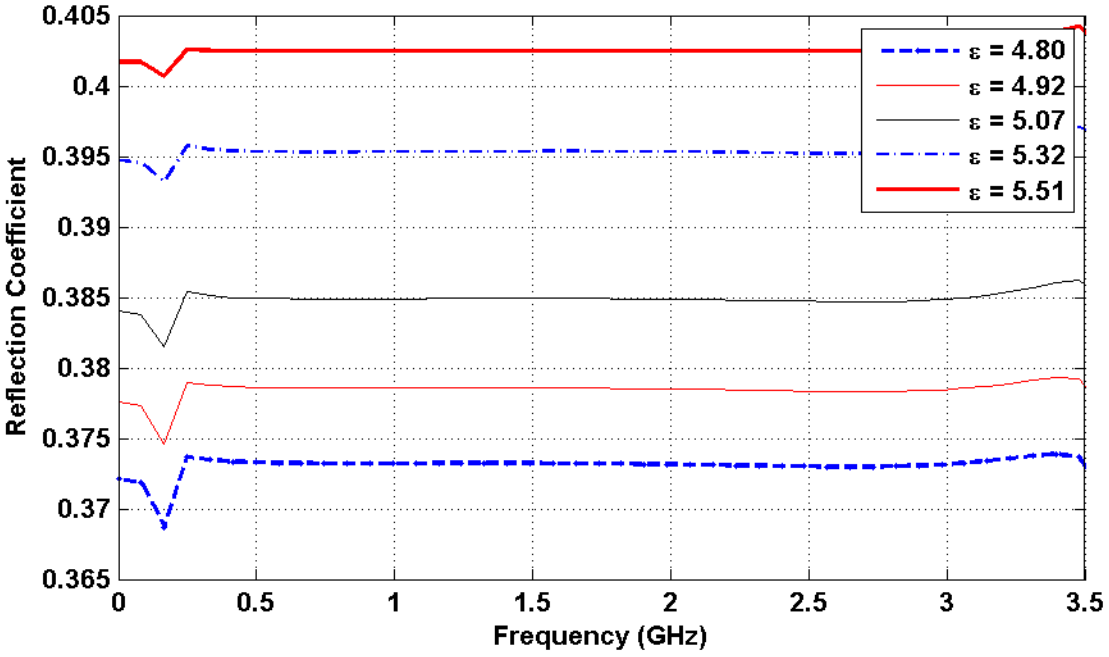

Figure 6-7 Change of reflection coefficients when density changes.

When water is sprayed on the pavement, the distribution of amplitude over frequency axis changes. Based on the frequency-selective effect, the change caused by surface moisture only occurs over the high frequency range. If a reference signal on dry pavement is known, which means the distribution of the amplitude over the entire frequency is known, the signal collected from the wet pavement can be recovered to the signal collected from the dry pavement by multiplying a correction factor to the amplitude of the reference signal over the whole the frequency. The correction factor is determined by comparing the amplitudes of the low frequency components of the reference signal and the amplitudes of the low frequency components of the signal collected from wet pavement. This approach is described in detail in the following procedure:

- A reference GPR scan is obtained for a specific asphalt mixture. The surface reflection pulse is extracted. The frequency spectrum of the surface reflection pulse is obtained using Fourier transform. It defines the distribution of the frequency spectrum of GPR surface pulses reflected by the dry asphalt pavement, which means that when the density changes, the amplitude changes but the distribution remains the same in frequency domain.
- The GPR surface reflection pulse collected from asphalt pavement with surface moisture is transformed into frequency domain using Fourier transform. By comparing the amplitude of its low frequency components with the amplitude of the low frequency components of the reference scan, a correction factor is obtained.
- By multiplying the correction factor with the reference scan in frequency domain, a new frequency spectrum is obtained. This spectrum has the same frequency distribution as the reference scan, with the only difference being the amplitude. This frequency spectrum is the “recovered” GPR signal. The amplitude of surface reflection in time domain can be obtained using inverse Fourier transform.

In real construction, the reference scan can be collected on a dry and well compacted test pad or a test strip. A test pad or test strip is usually constructed to determine the optimized number of roller passes before construction. In the laboratory experiments in this study, the reference scan was collected from section with maximum number of roller passes under dry condition.

To develop the reference scan approach, extensive GPR data collection was conducted on test site B. GPR data corresponding to different densities and different

moisture contents was collected. On each of the 11 sections, grid 4-C and grid 11-C were selected for GPR data collection. The section number means the number of roller passes (Figure 3-6). Grid 4-C and grid 11-C are two locations in the middle of the section (Figure 3-9). Because all GPR data were collected at grid C, the letter “C” is omitted hereafter. (e.g., section 10 grid 11-C is written as section 10 grid 11). A total of 22 locations were selected as GPR testing locations. The procedure of the test is described in the following:

- Alignment of GPR antenna to the test location
- Collection of GPR data on the dry asphalt pavement
- Spraying the prescribed amount of water on the pavement below the GPR antenna and collection of GPR data
- Repetition of the above procedure on different test locations of test site B
- After the pavement is completely dry (more than one day), repetition of the above procedure by spraying different amounts of water

Four different amounts of water were sprayed in this study, including 100 mL, 150 mL, 200 mL, and 300 mL to simulate different amounts of surface moisture on asphalt pavement during compaction. As discussed in Section 4.2, the amounts of sprayed water sprayed were determined based on the observations from field tests. The increase of the surface reflection amplitude of the GPR signals should cover the range of 1% to 6%. The true increase of the surface reflection amplitude after spraying the four amounts of water is shown in Figure 6-16 and will be discussed later.

As shown in Figure 6-8, water was sprayed using a sprayer powered by an air compressor. Water was sprayed evenly on a 1.94 ft × 3.54 ft (0.59 m × 1.08 m) area below GPR antenna which should be large enough to cover the footprint of the GPR wave. The area of surface moisture was equal to 12 pre-marked grids. Figure 6-9 depicts the moisturized area after spraying 150 mL water.

Figure 6-8 Spraying water on asphalt pavement using an air compressed sprayer.

Figure 6-9 Moisturized area under the GPR antenna after spraying 150 mL water.

An example is used to explain the reference scan approach. Figure 6-10 (a) depicts the GPR signal on section 6 grid 4 of the test site B. The blue curve is the GPR scan on dry pavement. The red curve is the GPR scan on wet pavement after spraying 150 ml water. Figure 6-10 (b) shows the surface reflection pulse. It can be seen clearly that the amplitude of the pulse increased after spraying the water. The maximum amplitude was 1.9653×10^4 for the GPR signal on dry pavement and 2.0138×10^4 for the signal on wet pavement. The increase of the amplitude as a result of the addition of surface moisture was 2.47%. The frequency spectrum of the surface reflection shown in Figure 6-10 (c) was obtained by applying Fourier transform on the time domain signal. In frequency domain, the frequency-selective effect was observed: the increase of amplitude occurred mainly over the high frequency range while the lower frequency components hardly changed.

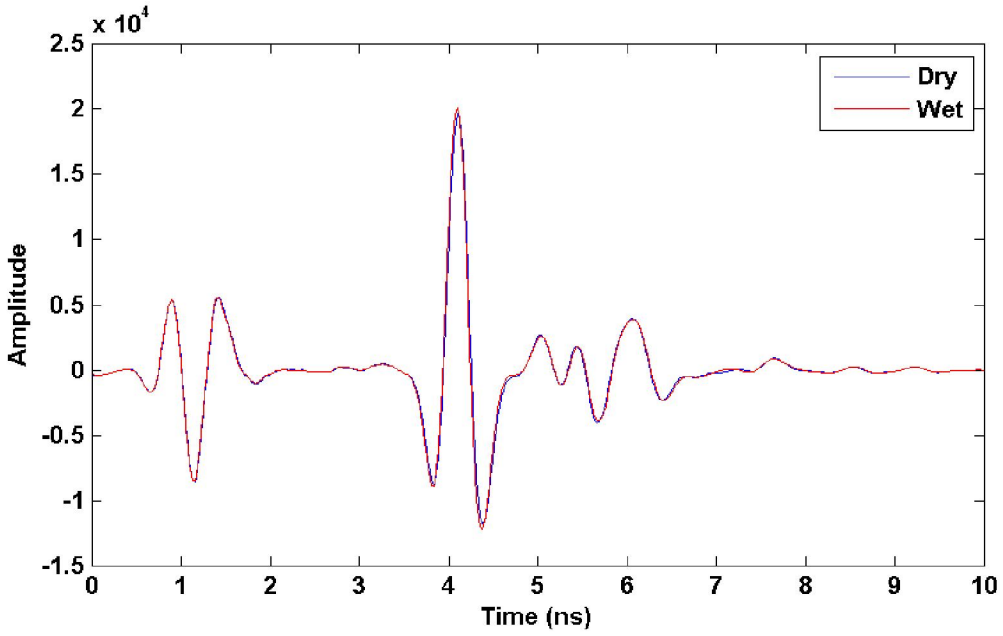

(a)

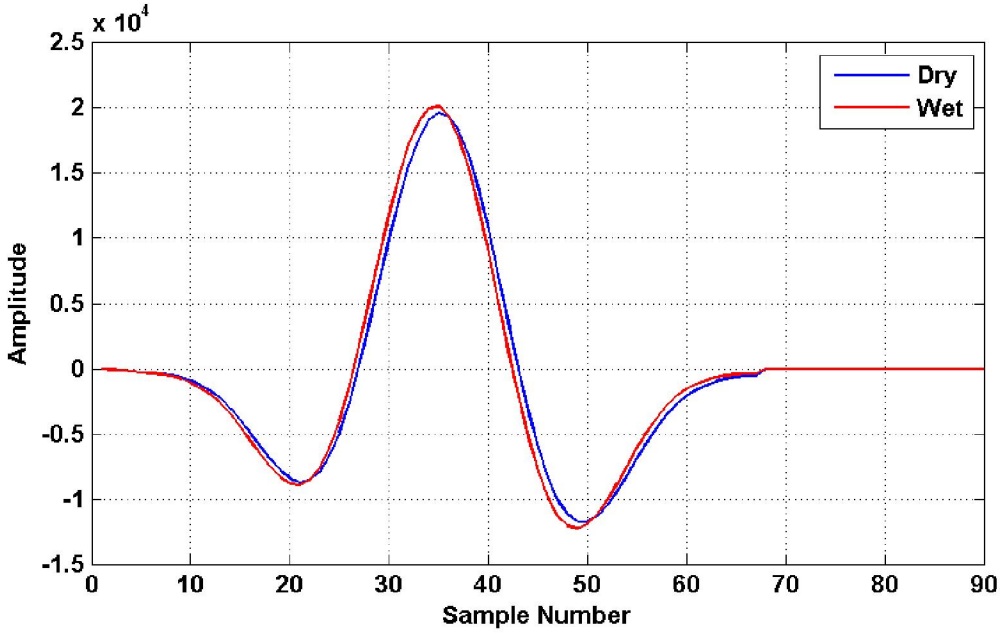

(b)

Figure 6-10 GPR signal on section 6 grid 4 – dry and wet condition: (a) original signal in time domain; (b) surface reflection pulse in time domain; (c) frequency spectrum of surface reflection pulse.

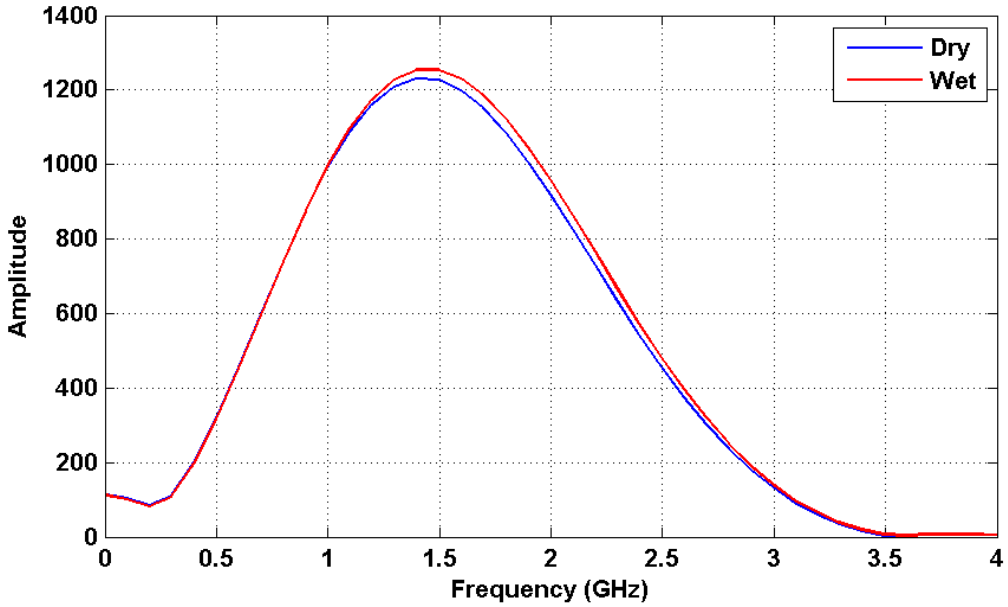

(c)

Figure 6-10 (cont.)

The next step was to choose a reference GPR scan. The GPR scan after the final compaction was used as the reference scan. Figure 6-11 (a) shows the reference scan collected from section 10 grid 4 which has 10 roller passes. Figure 6-11 (b) shows the surface reflection pulse of the reference scan. And Figure 6-11 (c) shows the frequency spectrum of the surface reflection pulse of the reference scan.

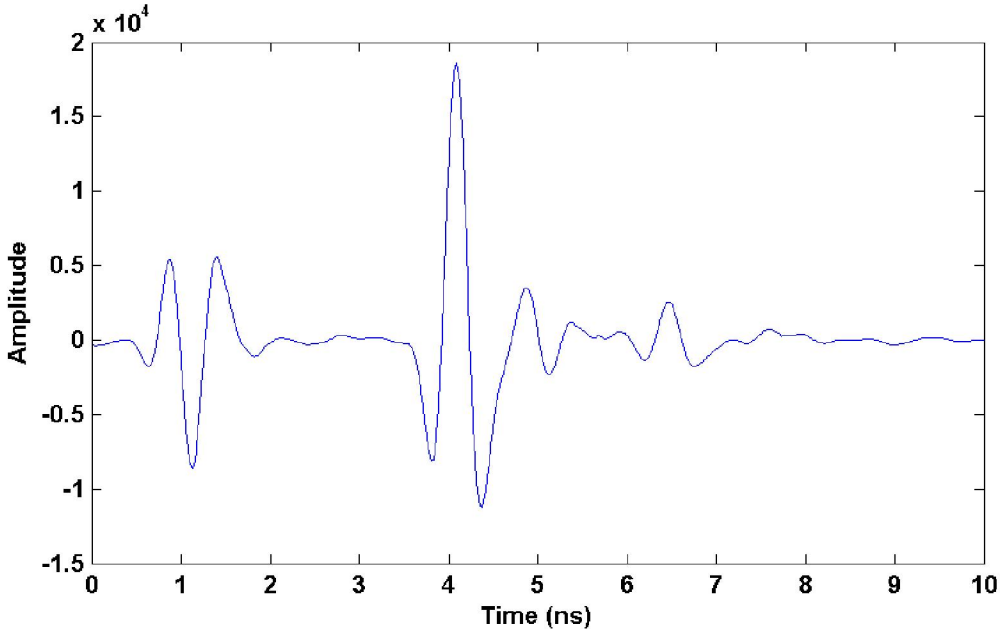

(a)

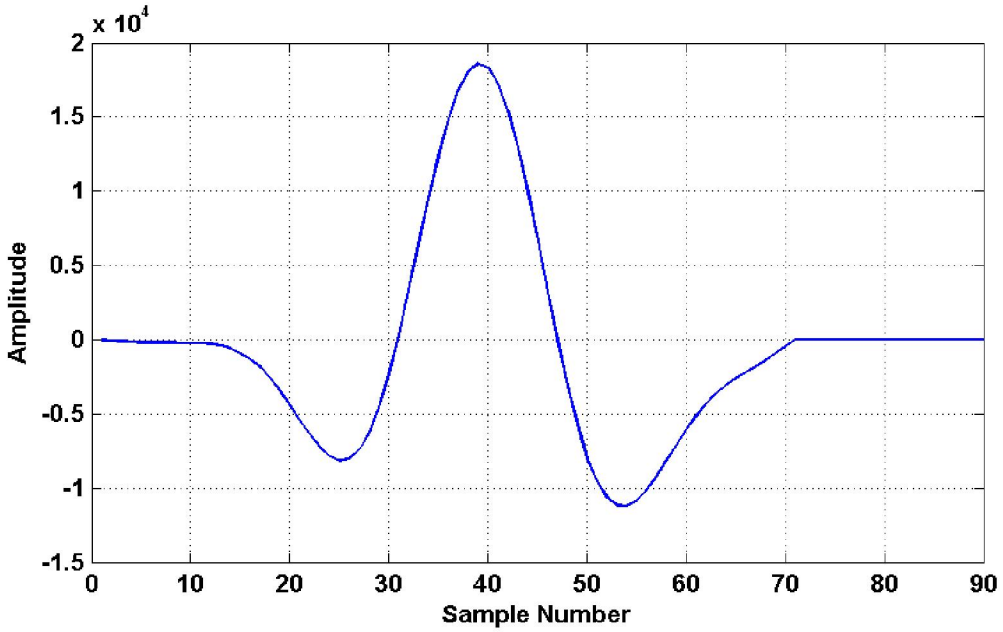

(b)

Figure 6-11 Reference GPR scan from section 10 grid under dry condition: (a) original signal in time domain; (b) surface reflection pulse in time domain; (c) frequency spectrum of surface reflection pulse.

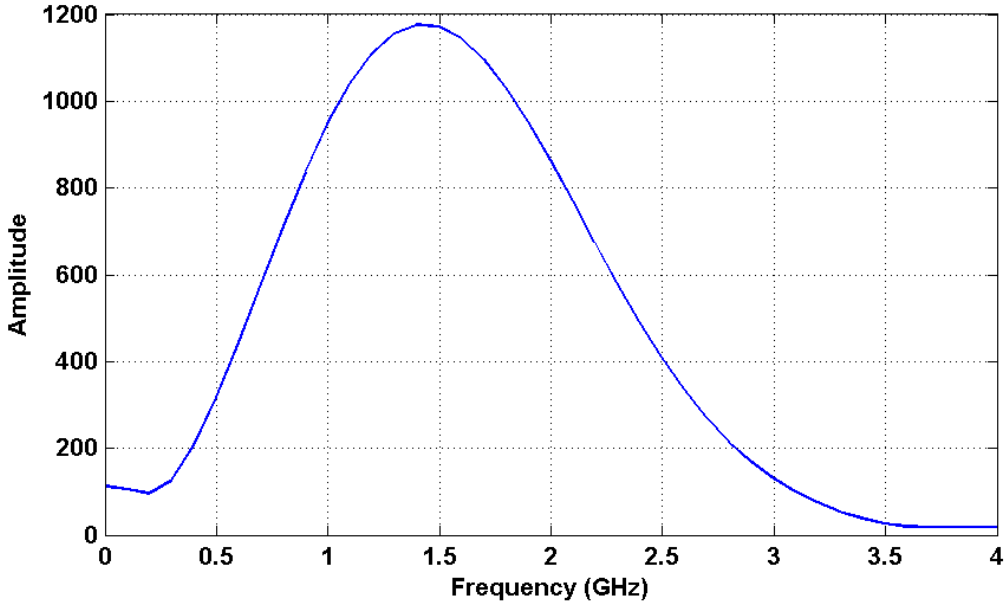

(c)

Figure 6-11 (cont.)

Figure 6-12 shows a comparison of frequency spectrums of GPR surface reflection pulses from dry pavement, wet pavement and reference scan. A correction factor was calculated by comparing the amplitudes of signal collected from wet pavement and the reference scan at low frequency.

In choosing the frequency point to obtain the correction factor, a trade-off should be considered. Theoretically, lower frequency is less affected by the surface moisture and should be used. However, in reality, if the amplitudes of the low frequency components are too small, larger relative error will be introduced into the calculation of the correction factor. In order to determine the optimum frequency point, a comparison of reflection coefficients obtained from theory, from simulation and from real measurement was made. Using Equation (A-7), the theoretical solution is plotted in

Figure 6-13 (a). When surface moisture was added in the simulation, the amplitude increases exponentially with frequency. The simulation results show the same trend, as shown in Figure 6-13 (b). The curves in Figure 6-13 (b) is slightly different from the theoretical solution in Figure 6-13 (a) because of quantization error and the error induced from discretization of the time and space. As shown in Figure 6-13 (c), in real cases, the amplitude also increases exponentially with frequency. The curves in the real cases display more fluctuations and the values at specific frequencies also differ from the theoretical solution and simulation cases. This is expected because of the increased complexity of the real condition as compared to the simulation condition. But generally the trend of the curves are the same both in the simulaiton cases and in the real cases.

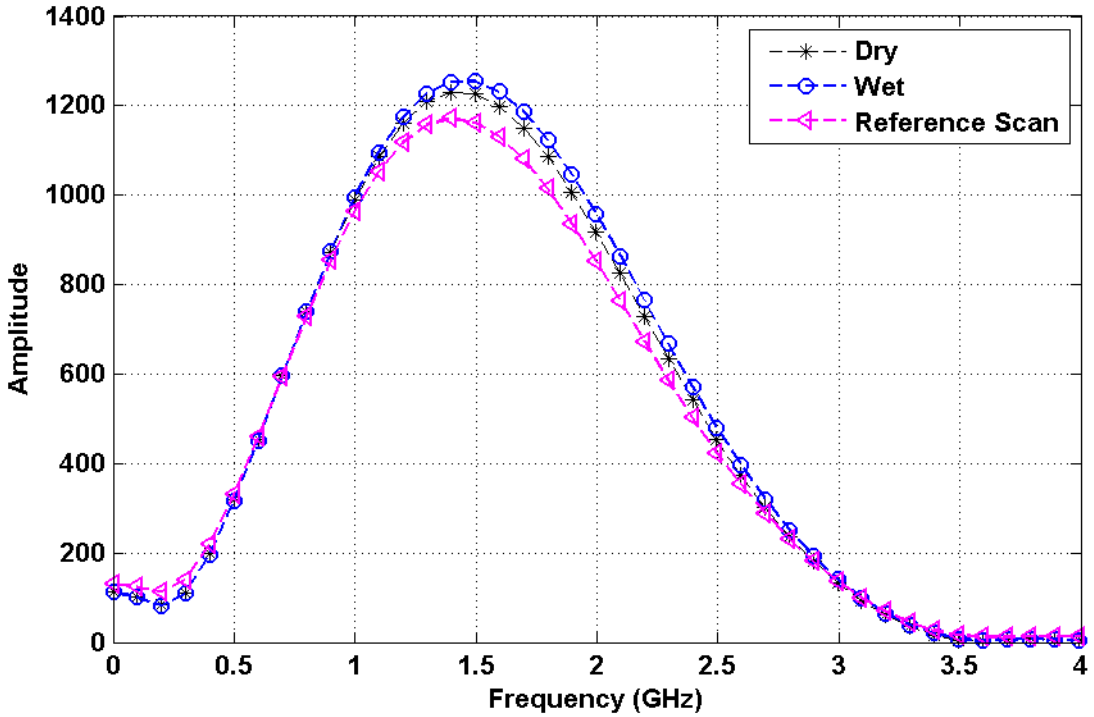

Figure 6-12 Frequency spectrums of GPR surface reflection of dry scan, wet scan and reference scan.

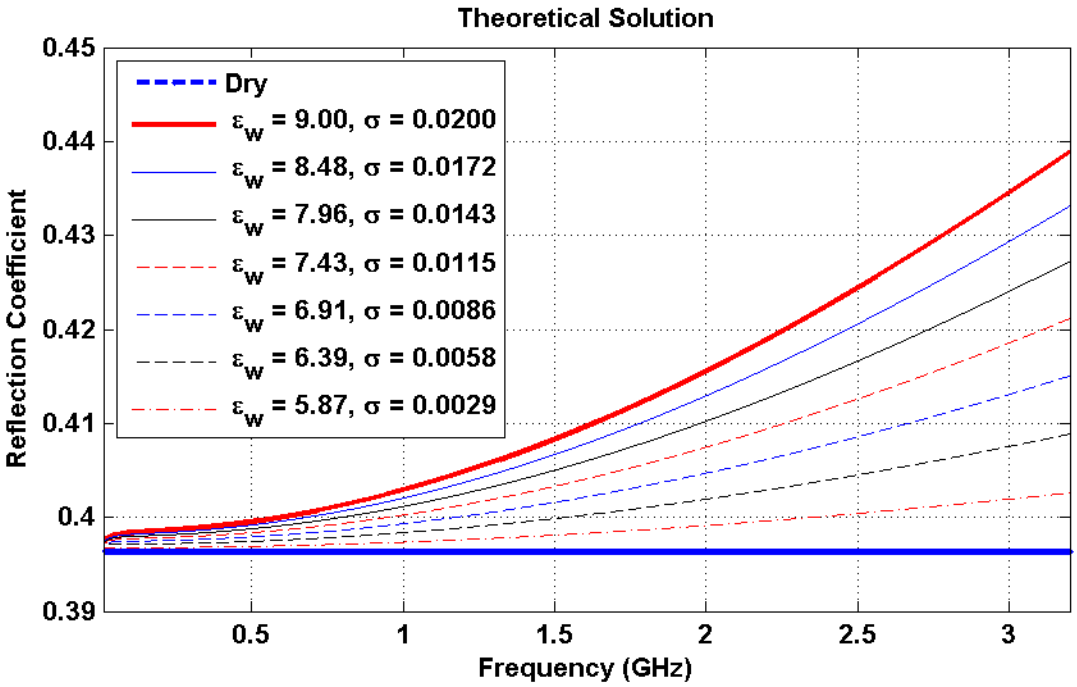

(a)

Figure 6-13 Reflection coefficient when different amount of surface moisture contents applied: (a) theoretical data; (b) simulation data; (c) real data.

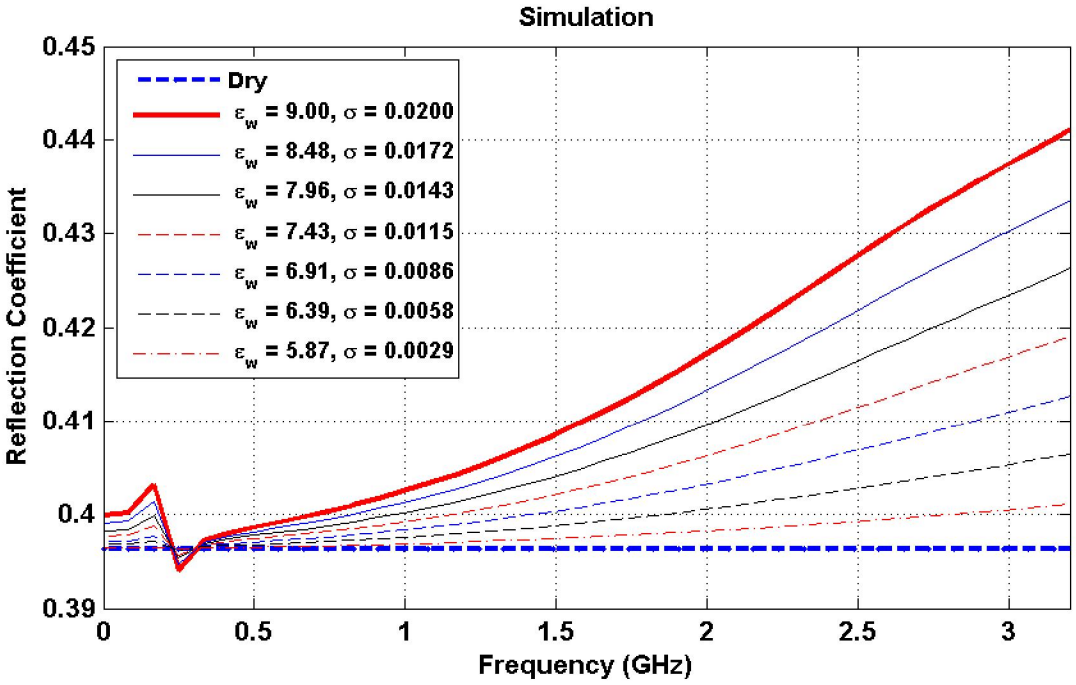

(b)

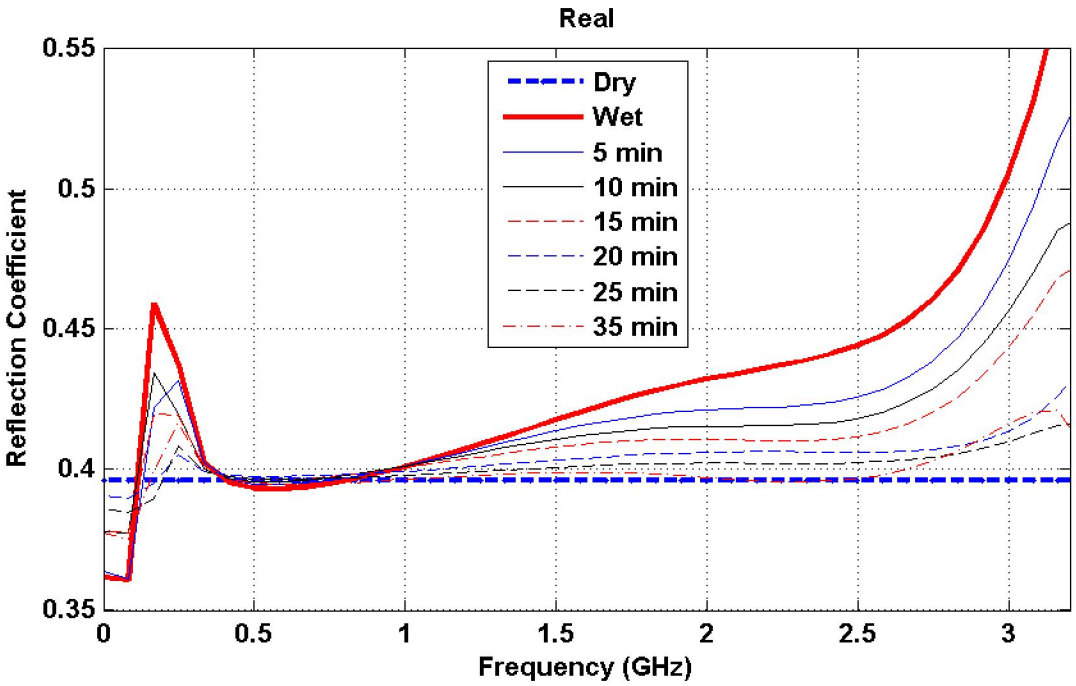

(c)

Figure 6-13 (cont.)

The curves in the real cases, Figure 6-13 (c), are used to determine the optimum frequency point. It is found that 1.1 GHz is a good frequency point for calculating the correction factor for two reasons: (1) 1.1 GHz is significantly lower than the central frequency so the amplitude at this frequency is close to 1, which is shown in Figure 6-13 (b); (2) 1.1 GHz is large enough (larger than frequency point such as 0.5 GHz) so it has relatively good stability. Therefore, it was selected in this study. The amplitude at 1.1 GHz is 1041.5 for reference scan and 1096.2 for the signal from wet pavement. So, the correction factor is 1096.2/1041.5 = 1.0525.

By multiplying the correction factor with the reference scan in frequency domain, the signal was obtained after correction in frequency domain, as shown Figure 6-14. The signal after correction did not perfectly match the signal collected from dry pavement, but both signals were very similar. The time domain signal obtained using inverse Fourier transform, as shown in Figure 6-15. Figure 6-15 (b) shows that the signal after correction was also very close to the signal collected from dry pavement.

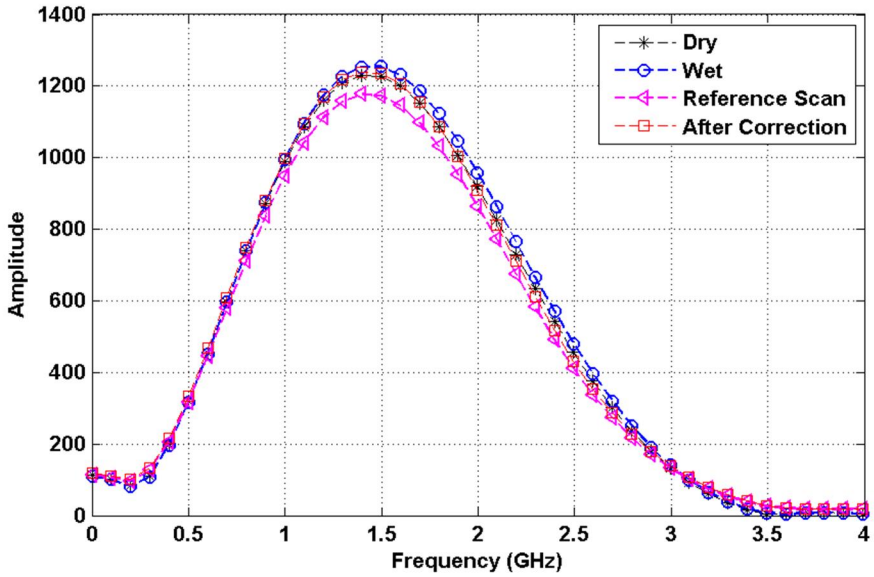

(a)

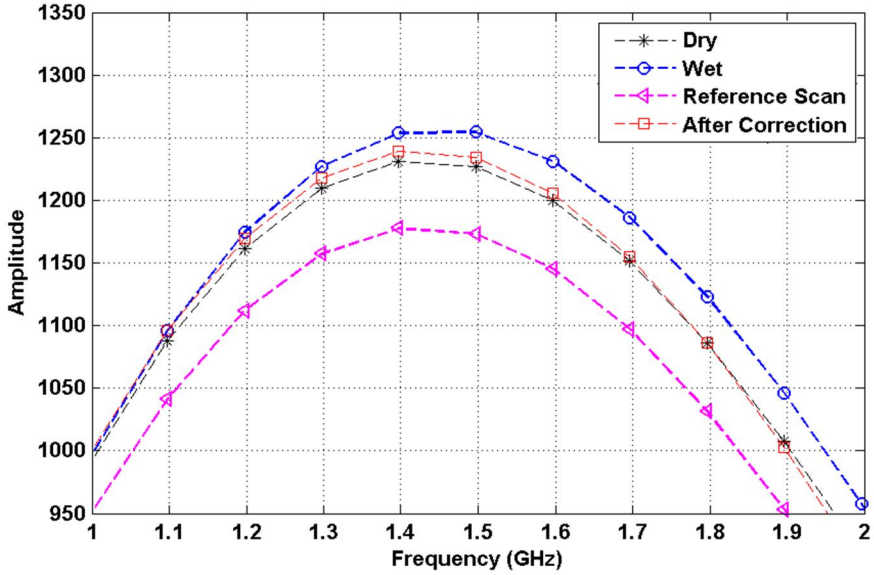

(b)

Figure 6-14 Frequency spectrums of GPR surface reflection of dry scan, wet scan, reference scan and the scan after correction: (a) whole spectrum; (b) magnified partial of the spectrum.

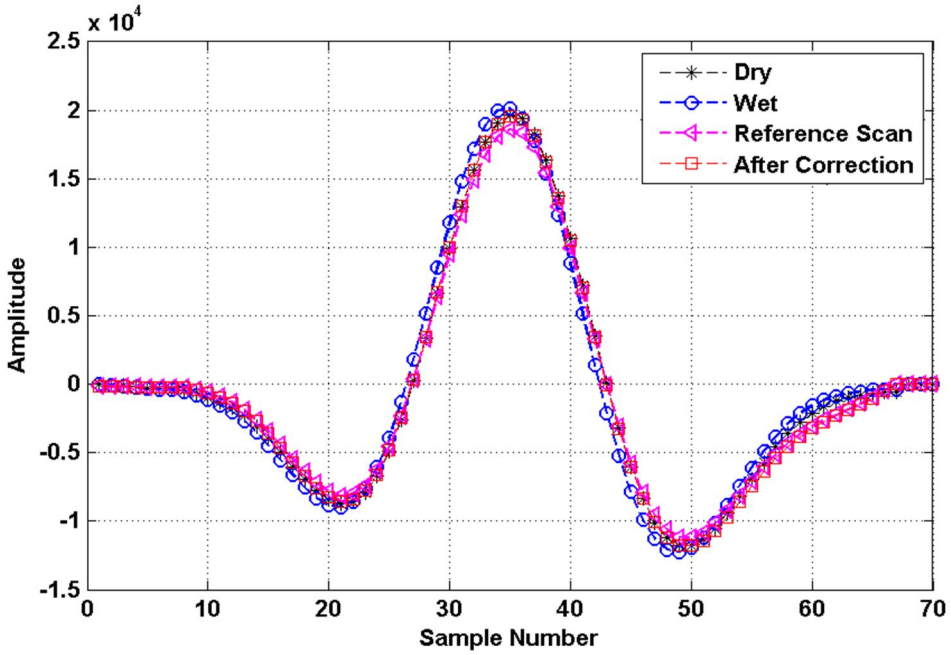

(a)

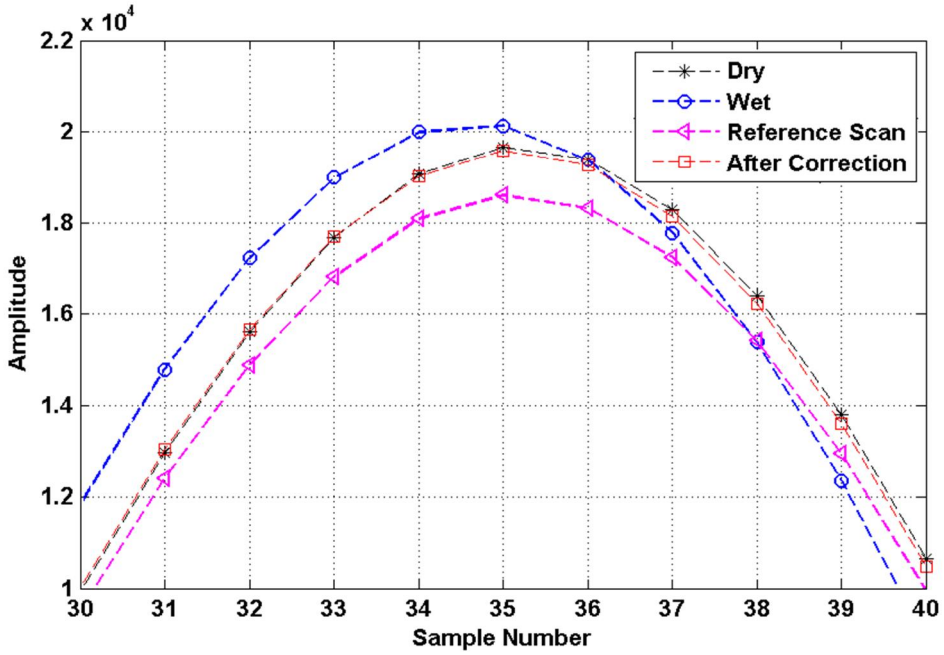

(b)

Figure 6-15 Time domain GPR surface reflection of dry scan, wet scan, reference scan and the scan after correction: (a) whole surface pulse; (b) magnified partial of the peak.

The effectiveness of the correction algorithm using reference scan approach is shown in Table 6-1. The error caused by surface moisture before the correction algorithm was 2.47%. After correction, the error was reduced to 0.3%, indicating the effectiveness of the correction algorithm.

Table 6-1 Effect of Correction Algorithm on GPR Signal Collected on Section 4 Grid 6

Type of Signal	Dry	Wet	After Correction
Surface Reflection Amplitude ($\times 10^4$)	1.9653	2.0138	1.9594
Error (%)	-	2.47	0.30

The above example showed the performance of the correction algorithm when 150 ml water was sprayed onto the pavement at section 6 grid 4. The GPR test matrix on test site B included data collection on 22 locations with 4 different amounts (100 mL, 150 mL, 200 mL and 300 mL) of water sprayed on the pavement. The same procedure was applied to correct each signal collected from wet pavement to resemble the signal collected from dry pavement. The performance of the algorithm on the 22 locations is discussed hereafter.

After spraying water, the surface reflection amplitude increased. The percentage of increase in surface reflection amplitude is shown in Figure 6-16. The x-axis is the location expressed by section number and grid number. For example, “S0G4” means section 0 grid 4, and “S0G11” means section 0 grid 11 (see Figure 3-6 and Figure 3-9). As expected, when more water was sprayed, the surface reflection amplitude increased.

There were two exceptions at locations S1G11 (section 1 grid 11) and S8G11 (section 8 grid 11) where the increase of amplitude was slightly higher when spraying 100 mL compared with the increase of amplitude when 150 mL of water was sprayed. This might be caused by the imperfect control of spraying water and the measurement error.

Figure 6-16 shows that when the same amount of water was sprayed on different locations, the increases of amplitude were different. Generally, the increase of amplitudes on less compacted sections (such as section 0 and section 1) was higher than the increase of amplitudes on well compacted sections (such as section 9 and section 10). This could be explained by the different distribution of water on pavement with different levels of compaction. This trend was more obvious when 100 mL, 150 mL and 200 mL water were sprayed. When 300 mL water was sprayed, the trend was less obvious. The percentage of the increase after spraying 300 mL water was extremely high (ranges from 10% to 20%), which is less likely to occur in the field. But this case is included in this study to cover a wider range.

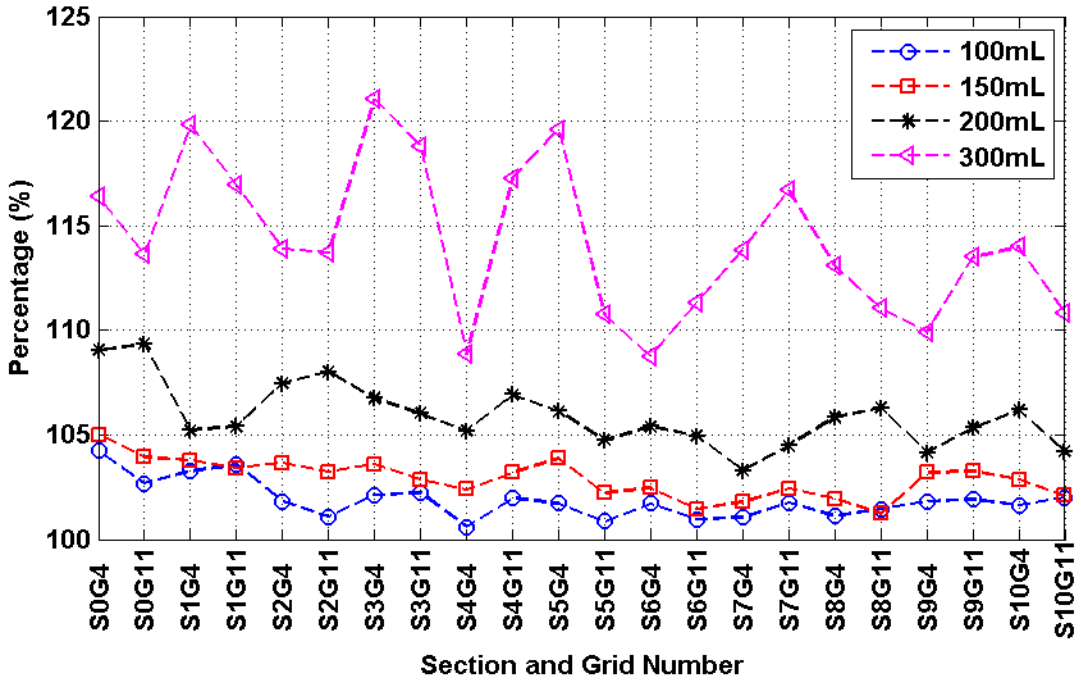

Figure 6-16 Percentage of the surface reflection amplitude after spraying water over the amplitude when pavement is dry.

An ideal correction algorithm should be able to transform the 88 values in Figure 6-16 into 100%. By using the reference scan approach as the correction algorithm, the percentage values were corrected towards 100%. The accuracy of the correction algorithm when different amounts of water were sprayed is presented hereafter.

Table 6-2 shows the change in reflection amplitude when 100 mL water was sprayed. The average increase of the amplitudes before the correction algorithm was 1.89%. After the application of the correction algorithm, the average percentage of the amplitudes on wet pavement over the amplitudes on dry pavement was 99.61% and the average error was 0.96%. The data in Table 6-2 are plotted in Figure 6-17 and Figure

6-18. As shown in Figure 6-17, the percentage values decreased after the application of correction algorithm. Some of the percentage values dropped below 100%. Similarly in Figure 6-18, most of the errors decreased but the error values at locations of S2G11, S3G4, S3G11 and S4G4 were higher than the original errors. This means that in these cases the correction algorithm “over-corrected” the signals. This type of errors could be caused by a few reasons such as the difference of frequency distributions of reference scan and the GPR signal collected from dry pavement, the noise from hardware and the environment noise. Overall, the correction algorithm resulted in a good performance as it successfully eliminated the effect of the surface moisture on most locations when 100 mL water was sprayed.

Table 6-2 Change of Reflection Amplitudes after Spraying 100 mL Water

Section No.	Grid No.	Ratio of Amplitude: Wet Over Dry (%)	Error (%)	Ratio of Amplitude after Correction (%)	Error (%)
0	4	104.23	4.23	100.01	0.01
0	11	102.67	2.67	100.78	0.78
1	4	103.27	3.27	100.54	0.54
1	11	103.58	3.58	100.35	0.35
2	4	101.83	1.83	99.15	0.85
2	11	101.08	1.08	97.42	2.58
3	4	102.14	2.14	97.21	2.79
3	11	102.22	2.22	97.70	2.30
4	4	100.59	0.59	98.03	1.97
4	11	101.97	1.97	99.79	0.21
5	4	101.73	1.73	99.84	0.16
5	11	100.86	0.86	99.54	0.46
6	4	101.72	1.72	99.62	0.38
6	11	100.98	0.98	99.01	0.99
7	4	101.07	1.07	100.10	0.10
7	11	101.77	1.77	100.93	0.93
8	4	101.12	1.12	100.50	0.50
8	11	101.44	1.44	98.75	1.25
9	4	101.81	1.81	99.54	0.46
9	11	101.90	1.90	101.64	1.64
10	4	101.63	1.63	101.47	1.47
10	11	102.02	2.02	99.54	0.46
Average		**101.89**	**1.89**	**99.61**	**0.96**

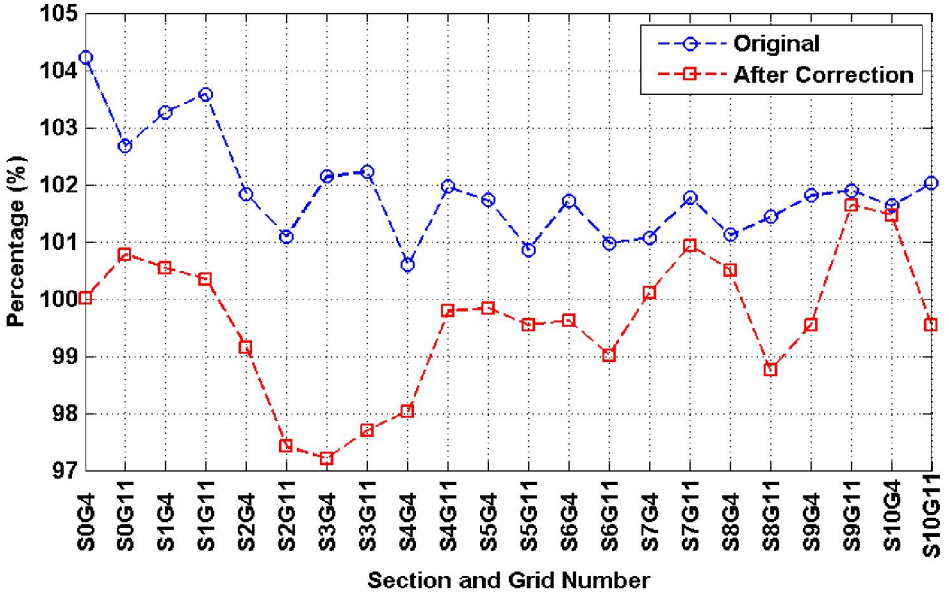

Figure 6-17 Percentage of the surface reflection amplitude after spraying 100 mL water over the amplitude when pavement is dry – before and after correction algorithm.

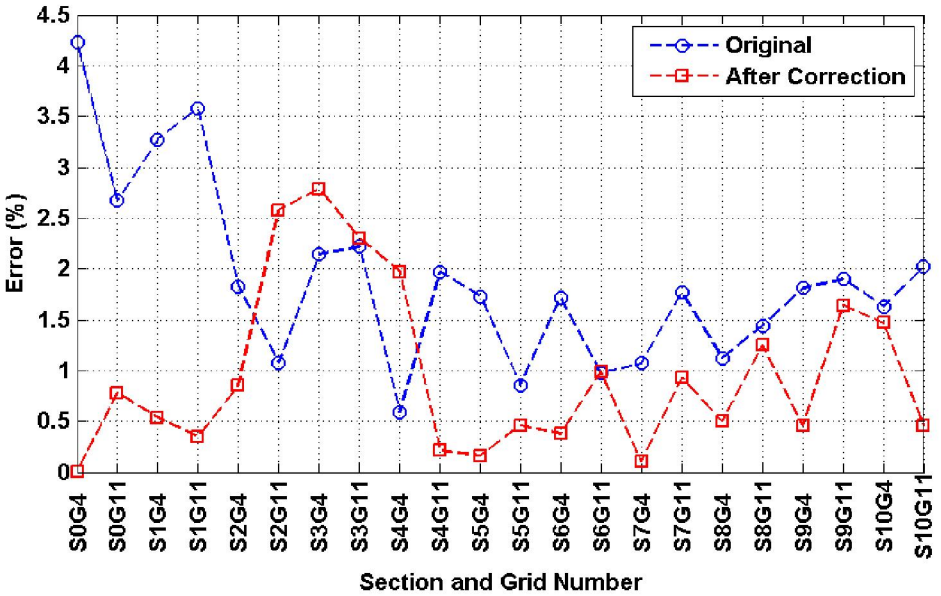

Figure 6-18 Error of the surface reflection amplitude after spraying 100 mL water – before and after correction algorithm.

The performance of the correction algorithm when 150 mL water was sprayed is shown in Table 6-3, Figure 6-19, and Figure 6-20. The average error of the surface reflection amplitude was 2.91% before the correction algorithm. After the application of correction algorithm, the error decreased to 1.27%. As shown in Figure 6-20, except for the errors at locations of S3G11 and S8G11, which slightly increased after applying the correction algorithm, most errors decreased.

Table 6-3 Change of Reflection Amplitudes after Spraying 150 mL Water

Section No.	Grid No.	Ratio of Amplitude: Wet Over Dry (%)	Error (%)	Ratio of Amplitude after Correction (%)	Error (%)
0	4	105.01	5.01	101.14	1.14
0	11	103.95	3.95	101.99	1.99
1	4	103.79	3.79	101.92	1.92
1	11	103.41	3.41	99.88	0.12
2	4	103.67	3.67	97.56	2.44
2	11	103.22	3.22	96.95	3.05
3	4	103.60	3.60	98.24	1.76
3	11	102.87	2.87	97.00	3.00
4	4	102.39	2.39	98.10	1.90
4	11	103.19	3.19	99.95	0.05
5	4	103.87	3.87	100.82	0.82
5	11	102.21	2.21	99.20	0.80
6	4	102.47	2.47	99.70	0.30
6	11	101.44	1.44	99.45	0.55
7	4	101.78	1.78	99.66	0.34
7	11	102.44	2.44	100.95	0.95
8	4	101.94	1.94	100.84	0.84
8	11	101.24	1.24	98.33	1.67
9	4	103.19	3.19	100.37	0.37
9	11	103.25	3.25	102.02	2.02
10	4	102.87	2.87	101.48	1.48
10	11	102.11	2.11	99.54	0.46
Average		**102.91**	**2.91**	**99.78**	**1.27**

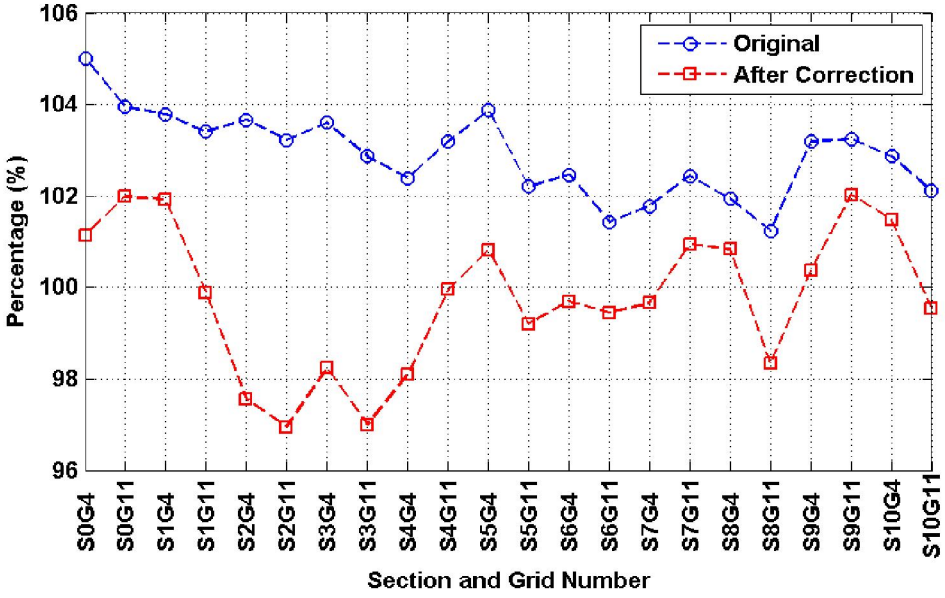

Figure 6-19 Percentage of the surface reflection amplitude after spraying 150 mL water over the amplitude when pavement is dry – before and after correction algorithm.

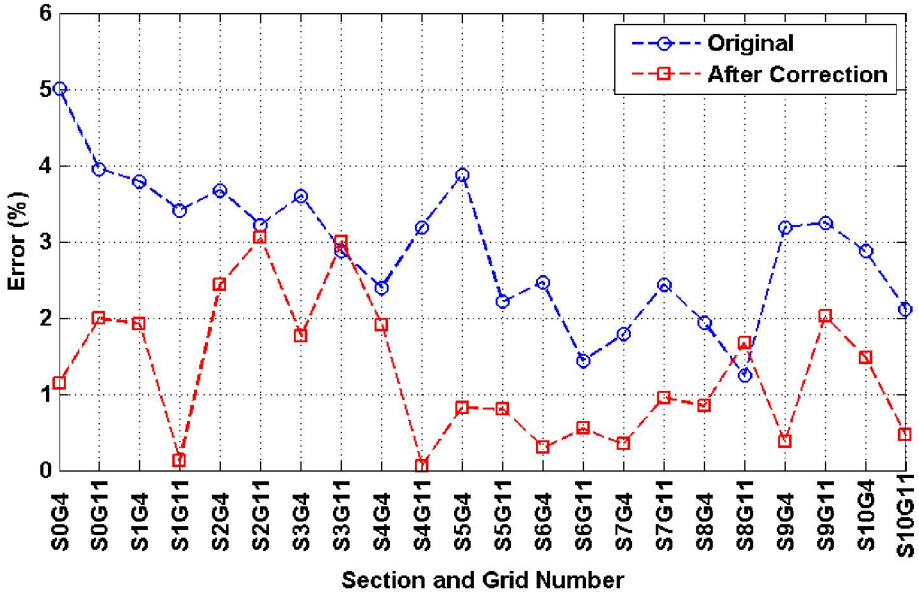

Figure 6-20 Error of the surface reflection amplitude after spraying 150 mL water – before and after correction algorithm.

The performance of the correction algorithm when 200 mL water was sprayed is shown in Table 6-4, Figure 6-21, and Figure 6-22. The average error decreased from 5.93% to 1.44%. As can be seen from Figure 6-22, all errors decreased after the correction algorithm was applied.

Table 6-4 Change of Reflection Amplitudes after Spraying 200 mL Water

Section No.	Grid No.	Ratio of Amplitude: Wet Over Dry (%)	Error (%)	Ratio of Amplitude after Correction (%)	Error (%)
0	4	109.06	9.06	102.60	2.60
0	11	109.34	9.34	104.18	4.18
1	4	105.21	5.21	101.13	1.13
1	11	105.41	5.41	100.42	0.42
2	4	107.45	7.45	97.71	2.29
2	11	108.02	8.02	95.20	4.80
3	4	106.76	6.76	98.73	1.27
3	11	106.03	6.03	97.53	2.47
4	4	105.18	5.18	97.54	2.46
4	11	106.93	6.93	100.26	0.26
5	4	106.14	6.14	100.20	0.20
5	11	104.74	4.74	99.92	0.08
6	4	105.41	5.41	99.81	0.19
6	11	104.95	4.95	99.32	0.68
7	4	103.28	3.28	99.47	0.53
7	11	104.49	4.49	101.00	1.00
8	4	105.84	5.84	101.52	1.52
8	11	106.30	6.30	100.09	0.09
9	4	104.14	4.14	99.40	0.60
9	11	105.35	5.35	101.43	1.43
10	4	106.20	6.20	102.55	2.55
10	11	104.20	4.20	99.06	0.94
Average		**105.93**	**5.93**	**99.96**	**1.44**

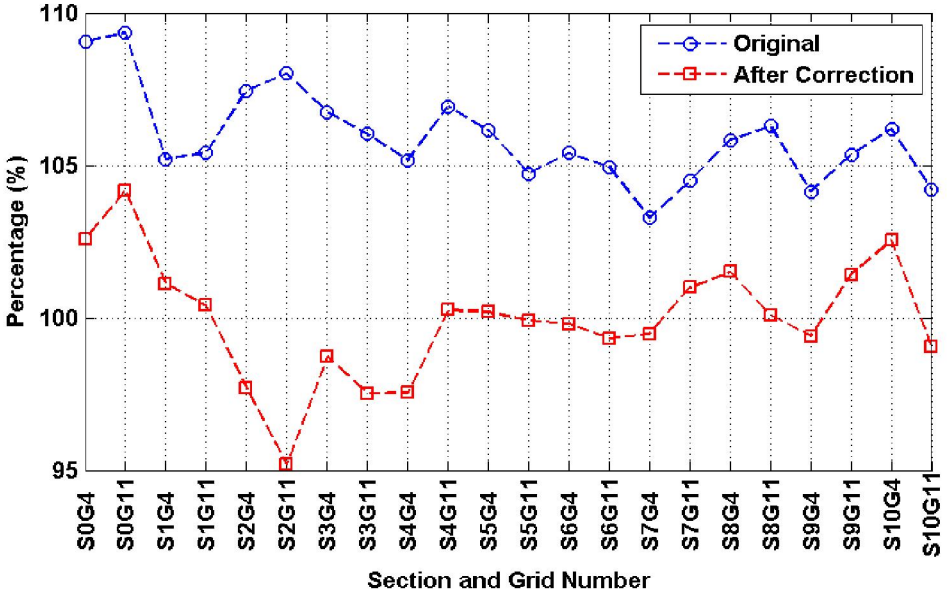

Figure 6-21 Percentage of the surface reflection amplitude after spraying 200 mL water over the amplitude when pavement is dry – before and after correction algorithm.

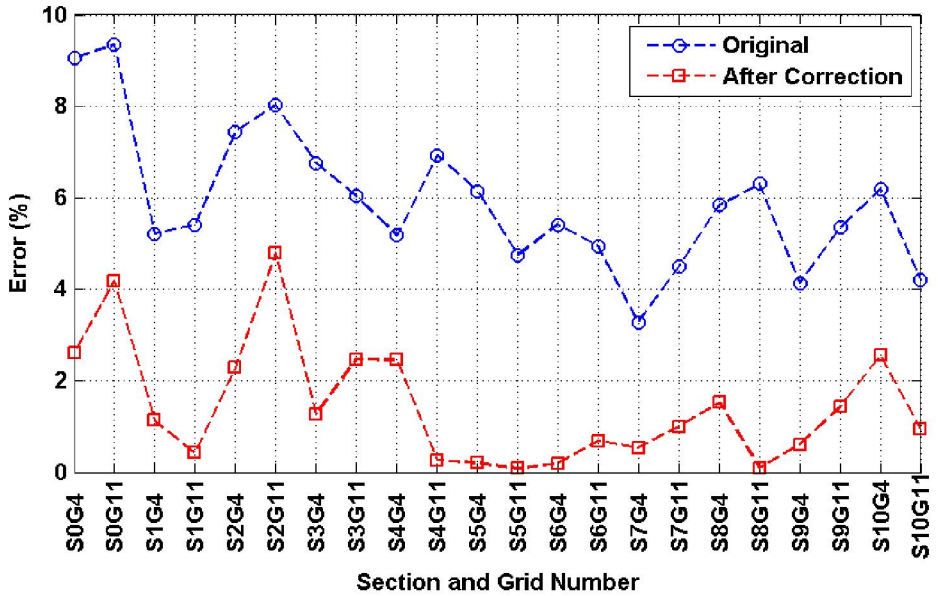

Figure 6-22 Error of the surface reflection amplitude after spraying 200 mL water – before and after correction algorithm.

The performance of the algorithm when 300 mL water was sprayed is shown in Table 6-5, Figure 6-23, and Figure 6-24. The average decreased from 14.25% to 2.3%. As shown in Figure 6-24, all errors for different locations decreased after the correction algorithm was applied.

Table 6-5 Change of Reflection Amplitudes after Spraying 300 mL Water

Section No.	Grid No.	Ratio of Amplitude: Wet Over Dry (%)	Error (%)	Ratio of Amplitude after Correction (%)	Error (%)
0	4	116.39	16.39	97.48	2.52
0	11	113.63	13.63	97.81	2.19
1	4	119.80	19.80	103.00	3.00
1	11	116.92	16.92	101.23	1.23
2	4	113.88	13.88	100.53	0.53
2	11	113.71	13.71	95.73	4.27
3	4	121.04	21.04	103.33	3.33
3	11	118.81	18.81	101.90	1.90
4	4	108.84	8.84	96.16	3.84
4	11	117.25	17.25	100.83	0.83
5	4	119.60	19.60	103.79	3.79
5	11	110.73	10.73	100.38	0.38
6	4	108.76	8.76	96.86	3.14
6	11	111.30	11.30	98.67	1.33
7	4	113.82	13.82	101.70	1.70
7	11	116.68	16.68	103.45	3.45
8	4	113.07	13.07	100.60	0.60
8	11	111.03	11.03	98.98	1.02
9	4	109.91	9.91	99.25	0.75
9	11	113.51	13.51	103.03	3.03
10	4	114.00	14.00	103.54	3.54
10	11	110.82	10.82	95.78	4.22
Average		**114.25**	**14.25**	**100.18**	**2.30**

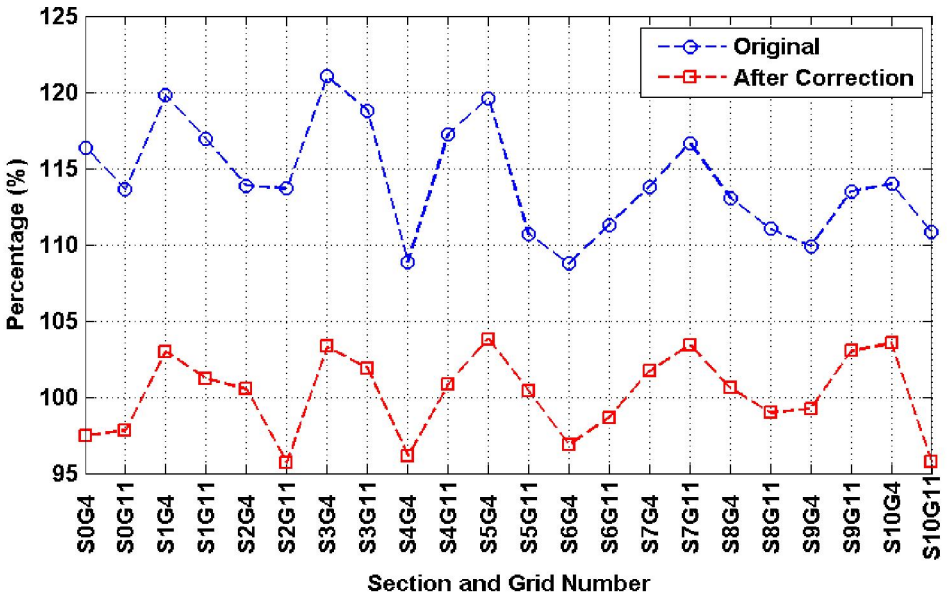

Figure 6-23 Percentage of the surface reflection amplitude after spraying 300 mL water over the amplitude when pavement is dry – before and after correction algorithm.

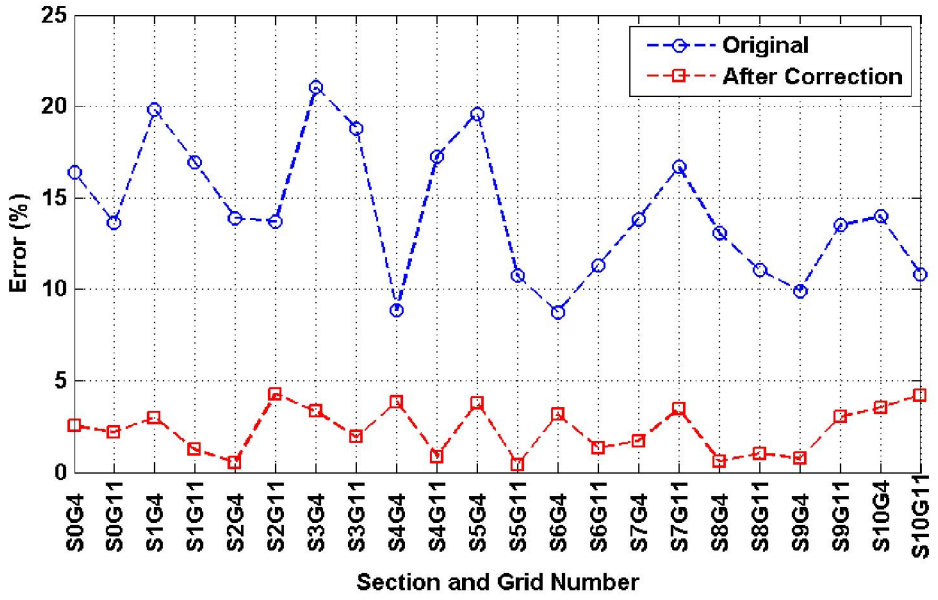

Figure 6-24 Error of the surface reflection amplitude after spraying 300 mL water – before and after correction algorithm.

Overall, the correction algorithm successfully reduced the errors of the reflection amplitudes caused by surface moisture. A reduced error in the reflection amplitude would result in a reduced error in estimation of the density of asphalt pavement. In the next section, the errors of the density estimation will be compared before and after the application of the correction algorithm.

6.4 Density Estimation Results

After the application of the correction algorithm on the GPR data collected from wet pavement, density estimation model could be applied to obtain the density of the asphalt mixture. In this study, the ALL model, shown in Equation (2-30), was used to obtain G_{mb} values from the dielectric constant values of the mixture.

On test site B, 22 cores were taken from the GPR data collection locations, as shown in Figure 6-25. As discussed in Section 2.3.1, the SSD method is not as accurate as the CoreLok method for measuring the densities of asphalt cores with high air void contents. The 22 cores included samples with high air void contents. Therefore, the SSD method was not suitable for the density measurement and, therefore, the CoreLok method was used in this study. In addition, although the maximum specific gravity G_{mm} was given by the asphalt plant before the construction of test site B, it was better to obtain the lab-measured G_{mm} using the sample taken form the test site. Therefore, G_{mm} measurement test was also conducted in the laboratory using the CoreLok machine. As shown in Table 3-2, the G_{mm} value from the asphalt plant was 2.468. The laboratory measured G_{mm} using the sample collected during the construction was 2.462. The difference between these two values was 0.2%. The value of 2.462 was used in this

study. During the measurement of the G_{mb}, it was critical to ensure the samples were completely dry. CoreDry machine, as shown in Figure 6-26, was used to dry all the cores. Figure 6-27 depicts the CoreLok machine which was used to obtain the G_{mb} value.

Figure 6-25 Cores taken from test site B.

Figure 6-26 CoreDry machine used to ensure the sample is dry.

Figure 6-27 CoreLok machine for G_{mb} tests.

The value of G_{se}, which is needed for applying ALL model, is sometimes not given by the asphalt plant. The G_{se} value could be easily calculated by using the Equation (6-3). For the material used on test site B, the G_{se} value was 2.694.

$$G_{se} = \frac{100 - P_b}{\frac{100}{G_{mm}} - \frac{P_b}{G_b}} \tag{6-3}$$

where G_b is the specific gravity of asphalt, which is usually a constant around 1.015.

To obtain the density of the asphalt pavement using GPR, the first step was to obtain the dielectric constant values. The dielectric constant of the dry pavement is shown in Figure 6-28. Despite some fluctuations, the trend of the dielectric constant value was clear: The dielectric constant value increased with more roller passes.

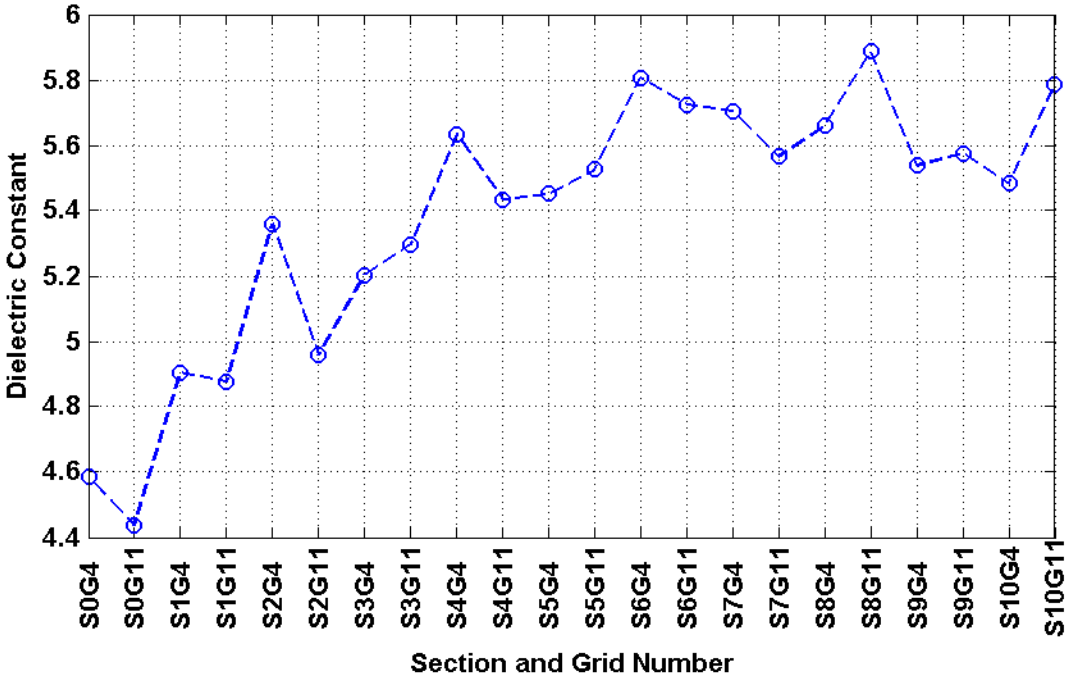

Figure 6-28 Dielectric constant values obtained using GPR data collected from dry pavement.

The second step was to apply the ALL model to obtain G_{mb} values. All the parameters in the ALL model, as shown in Equation (2-30), were known except for one unknown value, the dielectric constant of aggregate ε_s. The value of ε_s could be back-calculated using the G_{mb} value of one core. The location of S10G11 (section 10 grid 11) was selected as the core location for back-calculating ε_s. The G_{mb} value was 2.301 from

the core. The back-calculated dielectric constant value of aggregate ε_s was 7.305. The densities for all 22 locations could be obtained, as shown in Table 6-6. The values of G_{mb} and air void content from cores and from GPR are plotted in Figure 6-29 and Figure 6-30.

As seen in Table 6-6, the G_{mb} and air void content values obtained from GPR measurement on the less-compacted locations had higher errors compared with those on well-compacted locations. For example, on section 0 grid 4, the air void content V_a was 20.9% from the core. The V_a from the GPR measurement was 15.6% with a 5.3% difference. The G_{mb} estimation error from GPR was 6.7%. In contrast, on the location of section 9 grid 11, the error of G_{mb} estimation from GPR was 0.5% and the difference of V_a was 0.5%. The errors were much smaller than the errors on section 0 grid 4 because the ALL model is developed based on the data obtained from well-compacted asphalt mixture.

The performance of the model for the estimation of the density on less-compacted asphalt mixture (such as loose mix and mixture with only 1 or 2 roller passes) was not as good as its performance on well-compacted asphalt mixture. Luckily, the inaccuracies at roller passes of 0, 1 and 2 were not problematic because in most asphalt pavement constructions, the roller passes exceeded three and the initial densities of the asphalt mixture after the placement of paver were not of great interest as they could not affect the total number of roller passes.

As seen from Table 6-6, the average error of G_{mb} values of the 22 locations was 1.5%. If the data was considered after 2 passes only (sections 0, 1, and 2 were excluded), the average G_{mb} error would be 0.8%. If the data was considered after 3

passes only (sections 0, 1, 2, and 3 were excluded), the average G_{mb} error would be 0.7%. Similarly, the average difference of air void contents of all the 22 locations was 1.2%. The average difference dropped to 0.7% when the sections were considered after 2 roller passes. The value dropped to 0.6% when the sections were considered after 3 roller passes. Using GPR data and the ALL model, the density of the dry asphalt pavement could be obtained with reasonable accuracy.

Table 6-6 Comparison of Densities Obtained from Cores and from GPR Data Collected on Dry Pavement

Section No.	Grid No.	G_{mb} from Cores	G_{mb} from GPR	Error of G_{mb} (%)	V_a (%) from Cores	V_a (%) from GPR	Difference of V_a (%)
0	4	1.947	2.077	6.7	20.9	15.6	5.3
0	11	1.940	2.059	6.1	21.2	16.4	4.8
1	4	2.069	2.126	2.7	15.9	13.7	2.3
1	11	2.093	2.121	1.4	15.0	13.8	1.2
2	4	2.172	2.211	1.8	11.8	10.2	1.6
2	11	2.141	2.135	0.3	13.0	13.3	0.3
3	4	2.122	2.180	2.7	13.8	11.5	2.3
3	11	2.208	2.198	0.4	10.3	10.7	0.4
4	4	2.252	2.268	0.7	8.5	7.9	0.6
4	11	2.240	2.226	0.6	9.0	9.6	0.6
5	4	2.237	2.229	0.4	9.1	9.5	0.3
5	11	2.268	2.245	1.0	7.9	8.8	0.9
6	4	2.298	2.305	0.3	6.7	6.4	0.3
6	11	2.289	2.287	0.1	7.0	7.1	0.1
7	4	2.286	2.283	0.1	7.1	7.3	0.1
7	11	2.284	2.253	1.3	7.2	8.5	1.3
8	4	2.316	2.273	1.8	5.9	7.7	1.7
8	11	2.313	2.324	0.5	6.1	5.6	0.4
9	4	2.265	2.247	0.8	8.0	8.7	0.7
9	11	2.267	2.255	0.5	7.9	8.4	0.5
10	4	2.273	2.236	1.6	7.7	9.2	1.5
10	11	2.301	2.301	0.0	6.5	6.5	0.0
Average				**1.5**			**1.2**
Average (after 2 passes)				**0.8**			**0.7**
Average (after 3 passes)				**0.7**			**0.6**

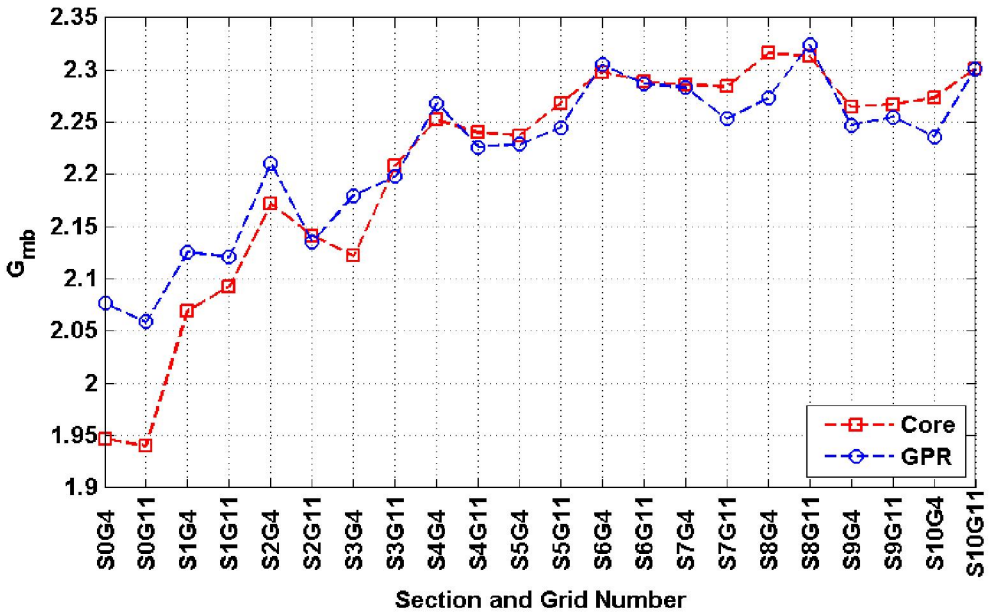

Figure 6-29 Comparison of G_{mb} values obtained from cores and from GPR data collected on dry pavement.

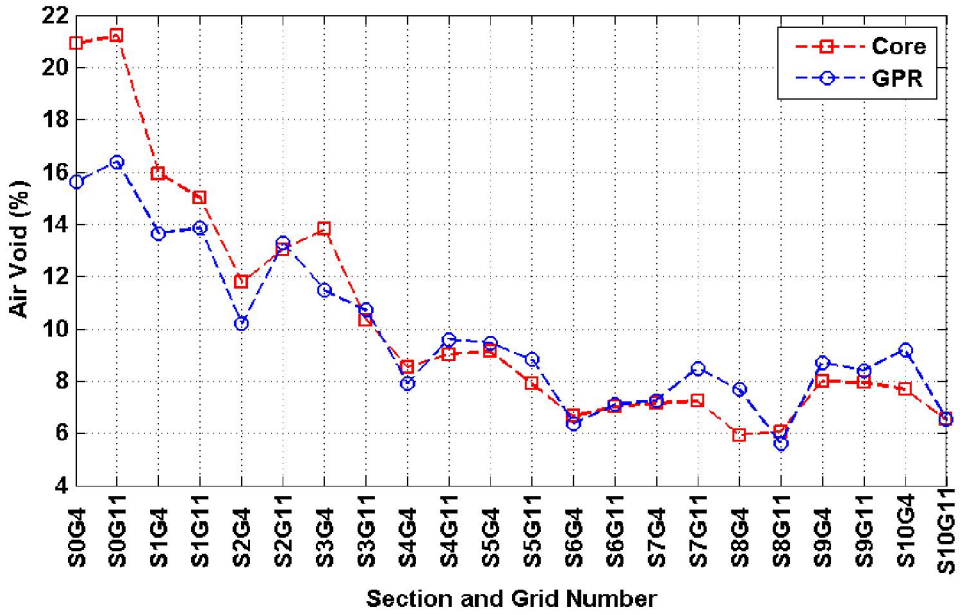

Figure 6-30 Comparison of air void contents obtained from cores and from GPR data collected on dry pavement.

Table 6-7, Figure 6-31, and Figure 6-32 show the density estimation results when 100 mL water was sprayed on the asphalt pavement. Before the application of correction algorithm, the average error of G_{mb} estimation for all the 22 locations was 2.4% which was higher than the average G_{mb} estimation error on dry pavement shown in Table 6-6. This was mainly caused by the additional source of error which was introduced by spraying the water. After the application of the correction algorithm, the average error dropped to 1.6%. The average error of G_{mb} estimation after 2 roller passes dropped from 1.4% to 0.9% after the algorithm (the difference of V_a dropped from 1.3% to 0.8%). The average error of G_{mb} estimation after 3 roller passes dropped from 1.2% to 0.8% after the algorithm (the difference of V_a dropped from 1.1% to 0.7%). As shown in Figure 6-31 and Figure 6-32, the difference between the red curve and black curve represents the error of density estimation before the correction algorithm. After the correction algorithm, the density estimation results are represented by the blue curve, which is closer to the red curve, indicating the reduction of errors.

Table 6-7 Densities Obtained from GPR Data after Spraying 100 mL Water

Section No.	Grid No.	G_{mb} before Correction	G_{mb} after Correction	G_{mb} Error before Correction (%)	G_{mb} Error after Correction (%)	V_a (%) before Correction	V_a (%) after Correction	Difference of V_a (%) before Correction	Difference of V_a (%) after Correction
0	4	2.129	2.077	9.3	6.7	13.5	15.6	7.4	5.3
0	11	2.084	2.065	7.4	6.5	15.4	16.1	5.9	5.1
1	4	2.179	2.134	5.3	3.1	11.5	13.3	4.4	2.6
1	11	2.178	2.126	4.1	1.6	11.5	13.6	3.5	1.4
2	4	2.250	2.194	3.6	1.0	8.6	10.9	3.2	0.9
2	11	2.152	2.099	0.5	2.0	12.6	14.7	0.4	1.7
3	4	2.221	2.132	4.7	0.5	9.8	13.4	4.0	0.4
3	11	2.244	2.156	1.7	2.3	8.8	12.4	1.5	2.1
4	4	2.282	2.223	1.3	1.3	7.3	9.7	1.2	1.2
4	11	2.270	2.222	1.3	0.8	7.8	9.8	1.2	0.8
5	4	2.268	2.226	1.4	0.5	7.9	9.6	1.2	0.5
5	11	2.265	2.235	0.1	1.4	8.0	9.2	0.1	1.3
6	4	2.351	2.296	2.3	0.1	4.5	6.8	2.1	0.1
6	11	2.312	2.263	1.0	1.1	6.1	8.1	0.9	1.1
7	4	2.310	2.286	1.0	0.0	6.2	7.2	1.0	0.0
7	11	2.295	2.275	0.5	0.4	6.8	7.6	0.5	0.4
8	4	2.301	2.285	0.7	1.3	6.6	7.2	0.6	1.2
8	11	2.363	2.291	2.2	0.9	4.0	6.9	2.0	0.9
9	4	2.290	2.237	1.1	1.2	7.0	9.1	1.0	1.1
9	11	2.301	2.294	1.5	1.2	6.6	6.8	1.4	1.1
10	4	2.273	2.269	0.0	0.2	7.7	7.8	0.0	0.2
10	11	2.355	2.290	2.3	0.5	4.3	7.0	2.2	0.5
Average				**2.4**	**1.6**			**2.1**	**1.4**
Average (after 2 passes)				**1.4**	**0.9**			**1.3**	**0.8**
Average (after 3 passes)				**1.2**	**0.8**			**1.1**	**0.7**

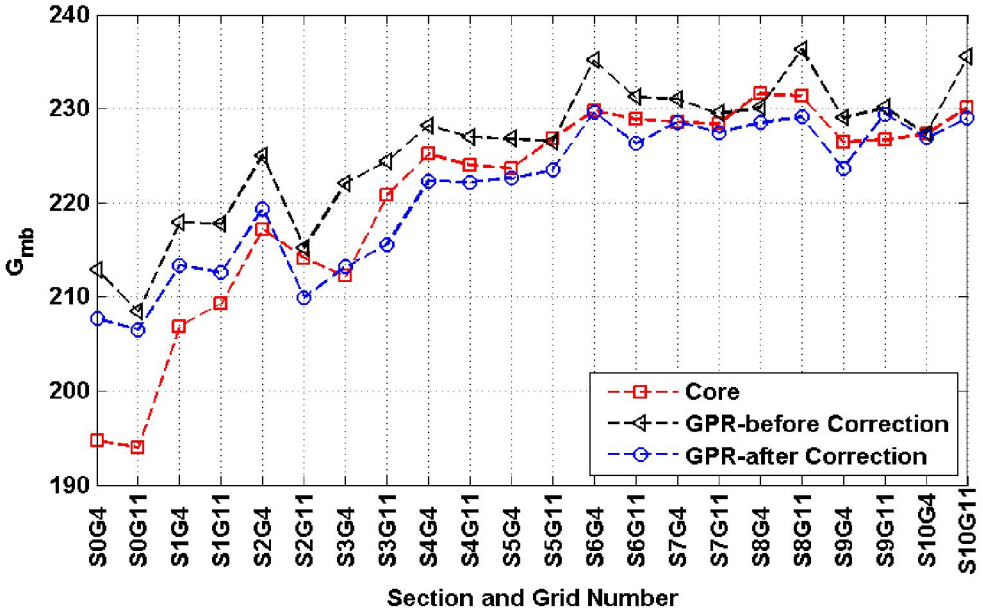

Figure 6-31 Densities (G_{mb}) obtained from cores and GPR data collected after spraying 100 mL water.

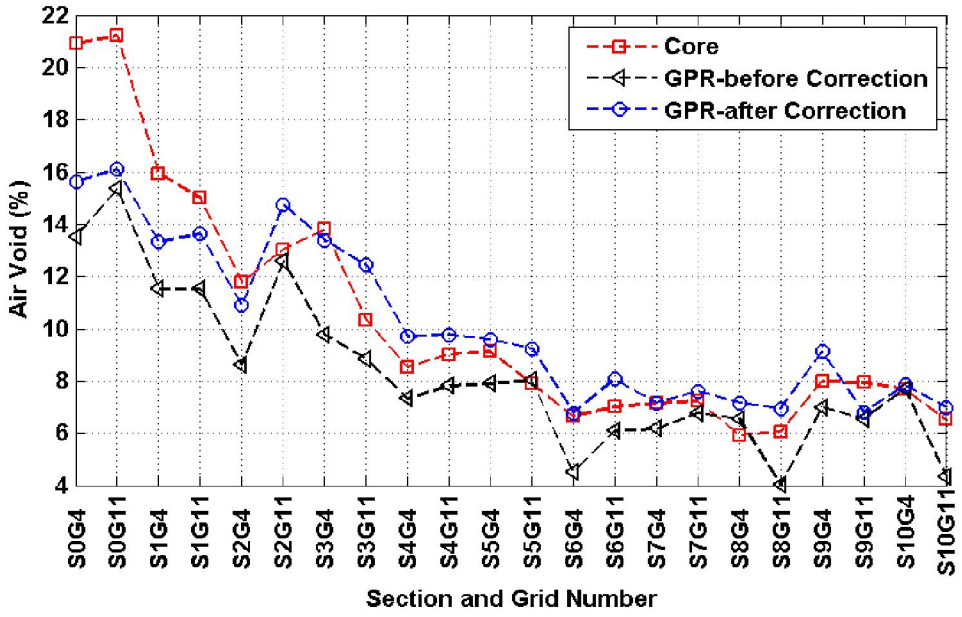

Figure 6-32 Densities (air void content) obtained from cores and GPR data collected after spraying 100 mL water.

Similarly, when 150 mL water was sprayed on the pavement, the density estimation results are shown in Table 6-8, Figure 6-33, and Figure 6-34. The application of the correction algorithm reduced the average G_{mb} estimation error after 2 roller passes from 2.4% to 0.9%. The algorithm reduced the average G_{mb} estimation error after 3 roller passes from 2.2% to 0.8%. The average difference of V_a estimation after 2 roller passes was reduced from 2.2% to 0.9%. The average difference of V_a estimation after 3 roller passes was reduced from 2.0% to 0.7%. As can be seen from Figure 6-33 and Figure 6-34, the blue curve, which represents the densities results (G_{mb} and V_a) from GPR after correction, is closer to the red curve, which represents the densities results (G_{mb} and V_a) from cores, than the black curve, which represents the density results (G_{mb} and V_a) from GPR before correction.

Table 6-8 Densities Obtained from GPR Data after Spraying 150 mL Water

Section No.	Grid No.	G_{mb} before Correction	G_{mb} after Correction	G_{mb} Error before Correction (%)	G_{mb} Error after Correction (%)	V_a (%) before Correction	V_a (%) after Correction	Difference of V_a (%) before Correction	Difference of V_a (%) after Correction
0	4	2.140	2.089	9.9	7.3	13.1	15.1	7.8	5.8
0	11	2.099	2.077	8.2	7.1	14.8	15.6	6.5	5.6
1	4	2.188	2.156	5.7	4.2	11.1	12.4	4.8	3.5
1	11	2.175	2.120	3.9	1.3	11.6	13.9	3.4	1.1
2	4	2.292	2.164	5.5	0.4	6.9	12.1	4.9	0.3
2	11	2.189	2.093	2.2	2.3	11.1	15.0	2.0	2.0
3	4	2.252	2.149	6.1	1.3	8.5	12.7	5.3	1.1
3	11	2.259	2.144	2.3	2.9	8.3	12.9	2.1	2.6
4	4	2.327	2.225	3.3	1.2	5.5	9.6	3.0	1.1
4	11	2.299	2.225	2.6	0.7	6.6	9.6	2.4	0.6
5	4	2.320	2.247	3.7	0.4	5.8	8.7	3.4	0.4
5	11	2.297	2.227	1.3	1.8	6.7	9.5	1.2	1.6
6	4	2.372	2.298	3.2	0.0	3.7	6.7	3.0	0.0
6	11	2.324	2.274	1.5	0.7	5.6	7.6	1.4	0.6
7	4	2.329	2.275	1.9	0.5	5.4	7.6	1.7	0.5
7	11	2.312	2.275	1.2	0.4	6.1	7.6	1.1	0.4
8	4	2.322	2.294	0.2	1.0	5.7	6.8	0.2	0.9
8	11	2.357	2.281	1.9	1.4	4.2	7.4	1.8	1.3
9	4	2.324	2.256	2.6	0.4	5.6	8.4	2.4	0.4
9	11	2.335	2.304	3.0	1.6	5.2	6.4	2.8	1.5
10	4	2.303	2.269	1.3	0.2	6.5	7.8	1.2	0.2
10	11	2.358	2.290	2.4	0.5	4.2	7.0	2.3	0.5
Average				**3.4**	**1.7**			**2.9**	**1.4**
Average (after 2 passes)				**2.4**	**0.9**			**2.2**	**0.9**
Average (after 3 passes)				**2.2**	**0.8**			**2.0**	**0.7**

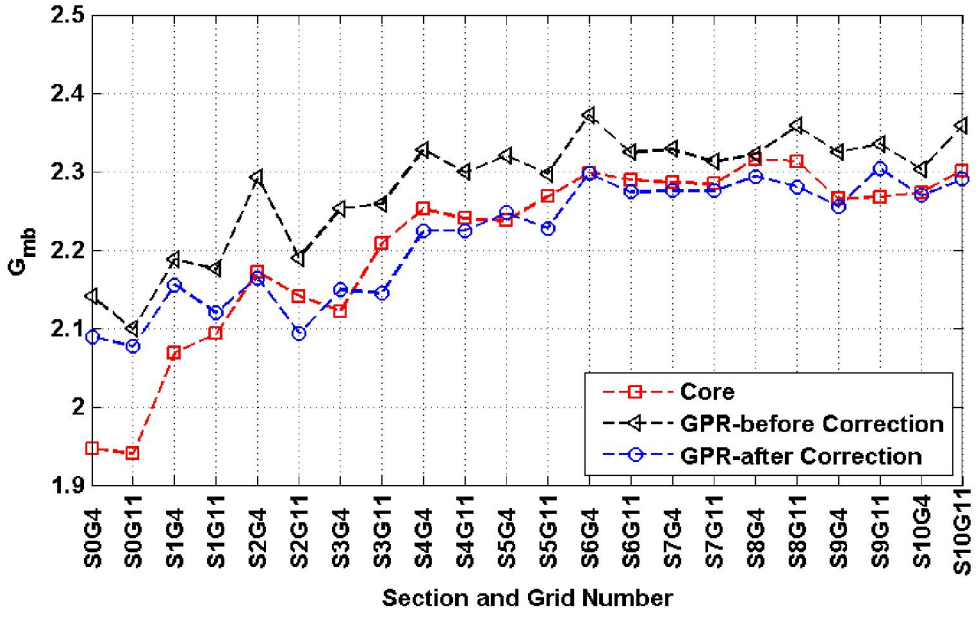

Figure 6-33 Densities (G_{mb}) obtained from cores and GPR data collected after spraying 150 mL water.

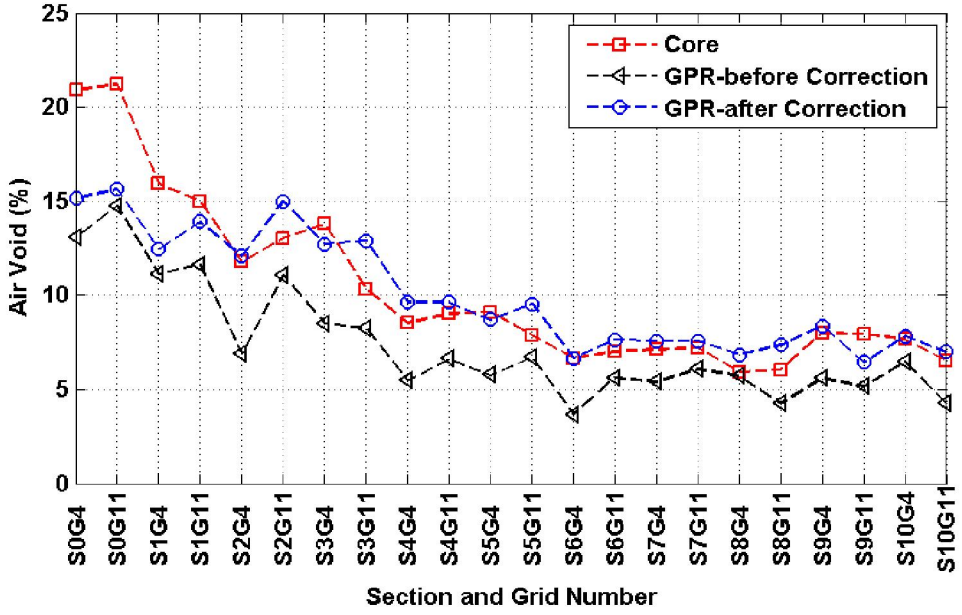

Figure 6-34 Densities (air void content) obtained from cores and GPR data collected after spraying 150 mL water.

The density estimation results when 200 mL water was sprayed are shown in Table 6-9, Figure 6-35, and Figure 6-36. At the location of section 8 grid 11, the air void content V_a before the correction algorithm was less than 0 because of the elevated G_{mb} value caused by the larger reflection amplitude. When plotting the air void content in Figure 6-36, the value of V_a at that location was plotted as 0, and when calculating the average errors shown in Table 6-9, the data of section 8 and grid 11 was excluded from the calculation.

Table 6-9 shows that the average G_{mb} estimation error dropped from 5.6% to 0.9% after 2 roller passes and from 4.9% to 0.7% after 3 roller passes after the application of the correction algorithm. The average difference of V_a estimation dropped from 5.2% to 0.9% after 2 roller passes and from 4.9% to 0.7% after 3 roller passes after the application of the correction algorithm. As can be seen from Figure 6-35 and Figure 6-36, the initial differences between the density results from GPR and the density results from cores were high (the black curve is far away from the red curve). After application of the correction algorithm, the errors reduced as the blue curve is closer to the red curve.

Table 6-9 Densities Obtained from GPR Data after Spraying 200 mL Water

Section No.	Grid No.	G_{mb} before Correction	G_{mb} after Correction	G_{mb} Error before Correction (%)	G_{mb} Error after Correction (%)	V_a (%) before Correction	V_a (%) after Correction	Difference of V_a (%) before Correction	Difference of V_a (%) after Correction
0	4	2.208	2.107	13.4	8.2	10.3	14.4	10.6	6.5
0	11	2.175	2.101	12.2	8.3	11.6	14.6	9.6	6.6
1	4	2.215	2.143	7.0	3.6	10.0	13.0	5.9	3.0
1	11	2.212	2.127	5.7	1.6	10.1	13.6	4.9	1.4
2	4	2.391	2.167	10.1	0.2	2.9	12.0	8.9	0.2
2	11	2.289	2.073	6.9	3.2	7.0	15.8	6.0	2.8
3	4	2.327	2.157	9.6	1.7	5.5	12.4	8.3	1.4
3	11	2.335	2.153	5.7	2.5	5.2	12.5	5.2	2.2
4	4	2.405	2.213	6.8	1.7	2.3	10.1	6.2	1.6
4	11	2.398	2.231	7.0	0.4	2.6	9.4	6.4	0.4
5	4	2.380	2.234	6.4	0.2	3.3	9.3	5.8	0.2
5	11	2.363	2.243	4.2	1.1	4.0	8.9	3.9	1.0
6	4	2.461	2.300	7.1	0.1	0.1	6.6	6.6	0.1
6	11	2.423	2.271	5.8	0.8	1.6	7.8	5.4	0.8
7	4	2.369	2.270	3.6	0.7	3.8	7.8	3.4	0.6
7	11	2.366	2.277	3.6	0.3	3.9	7.5	3.3	0.3
8	4	2.432	2.311	5.0	0.2	1.2	6.1	4.7	0.2
8	11	2.514	2.326	8.7	0.6	-2.1	5.5	8.2	0.5
9	4	2.349	2.234	3.7	1.4	4.6	9.3	3.4	1.3
9	11	2.393	2.289	5.6	1.0	2.8	7.0	5.1	0.9
10	4	2.391	2.295	5.2	0.9	2.9	6.8	4.8	0.9
10	11	2.418	2.277	5.1	1.1	1.8	7.5	4.7	1.0
Average				**6.7**	**1.8**			**5.9**	**1.6**
Average (after 2 passes)				**5.6**	**0.9**			**5.2**	**0.9**
Average (after 3 passes)				**5.3**	**0.8**			**4.9**	**0.7**

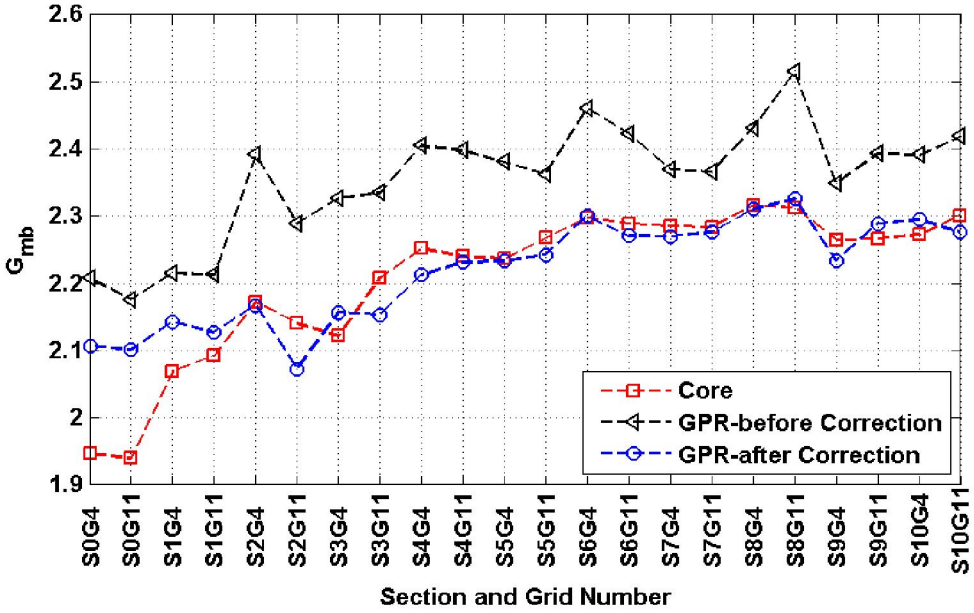

Figure 6-35 Densities (G_{mb}) obtained from cores and GPR data collected after spraying 200 mL water.

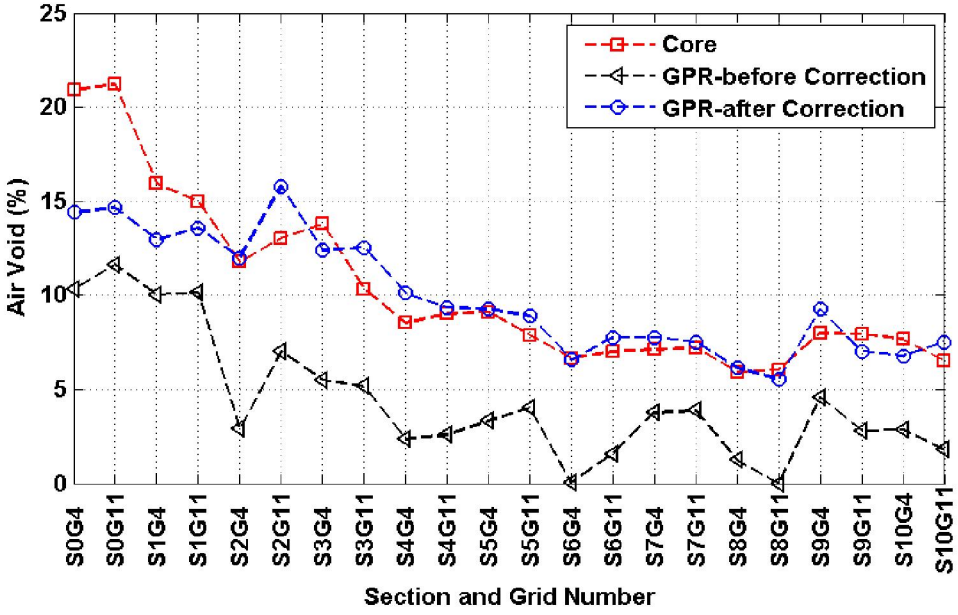

Figure 6-36 Densities (air void content) obtained from cores and GPR data collected after spraying 200 mL water.

The density estimation results when 300 mL water was sprayed are shown in Table 6-10, Figure 6-37, and Figure 6-38. The increase in G_{mb} values was extremely high. Before application of the correction algorithm, the G_{mb} values were even higher than the G_{mm} value. Thus, the air void content values V_a before the correction algorithm are not shown. As can be seen from Table 6-10, the average G_{mb} estimation error after the correction algorithm was 2.2% after 2 roller passes and 2.0% after 3 passes. The average difference of V_a estimation after the correction algorithm was 2.0% after 2 roller passes and 1.9% after 3 passes. This indicates the algorithm was also effective in the extreme case when large amount of surface moisture existed.

Table 6-10 Densities Obtained from GPR Data after Spraying 300 mL Water

Section No.	Grid No.	G_{mb} before Correction	G_{mb} after Correction	G_{mb} Error before Correction (%)	G_{mb} Error after Correction (%)	V_a (%) after Correction	Difference of V_a (%) after Correction
0	4	4.396	2.054	125.8	5.5	16.6	4.3
0	11	4.282	2.043	120.8	5.3	17.0	4.2
1	4	5.173	2.174	150.0	5.1	11.7	4.2
1	11	4.984	2.139	138.1	2.2	13.1	1.9
2	4	5.415	2.222	149.3	2.3	9.8	2.0
2	11	4.599	2.079	114.8	2.9	15.6	2.5
3	4	5.534	2.246	160.8	5.9	8.8	5.1
3	11	5.490	2.237	148.7	1.3	9.1	1.2
4	4	5.230	2.185	132.2	3.0	11.2	2.7
4	11	5.521	2.244	146.5	0.2	8.9	0.2
5	4	5.863	2.318	162.0	3.6	5.9	3.3
5	11	5.567	2.253	145.5	0.6	8.5	0.6
6	4	5.455	2.230	137.4	3.0	9.4	2.8
6	11	5.576	2.255	143.5	1.5	8.4	1.4
7	4	5.901	2.326	158.1	1.8	5.5	1.6
7	11	5.953	2.338	160.6	2.4	5.0	2.2
8	4	5.726	2.288	147.3	1.2	7.1	1.1
8	11	5.768	2.297	149.4	0.7	6.7	0.6
9	4	5.459	2.231	141.0	1.5	9.4	1.4
9	11	5.914	2.329	160.9	2.8	5.4	2.6
10	4	5.870	2.320	158.2	2.0	5.8	1.9
10	11	5.326	2.204	131.4	4.2	10.5	4.0
Average				**144.6**	**2.7**		**2.4**
Average (after 2 passes)				**149.0**	**2.2**		**2.0**
Average (after 3 passes)				**148.1**	**2.0**		**1.9**

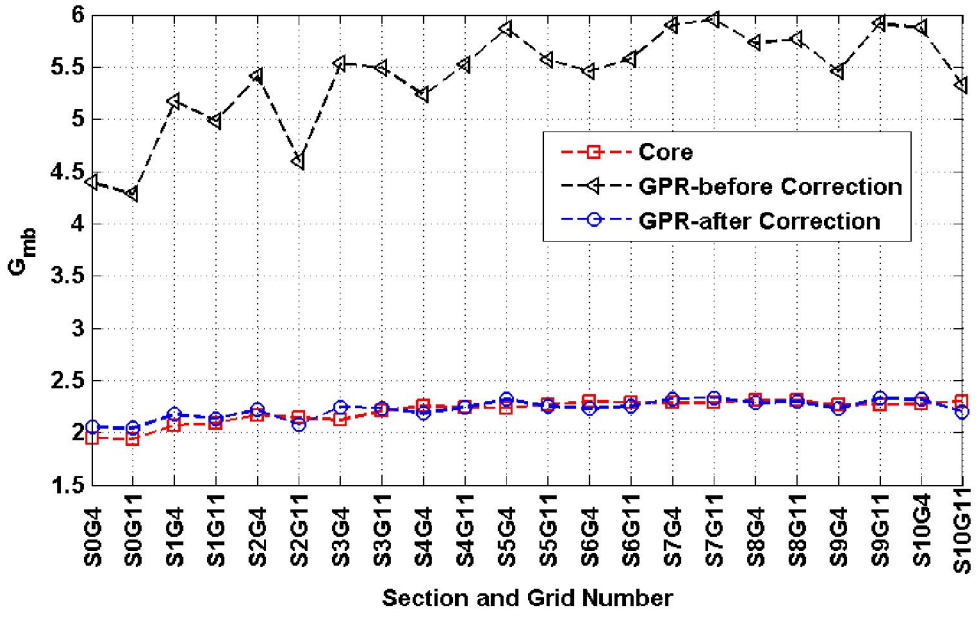

Figure 6-37 Densities (G_{mb}) obtained from cores and GPR data collected after spraying 300 mL water.

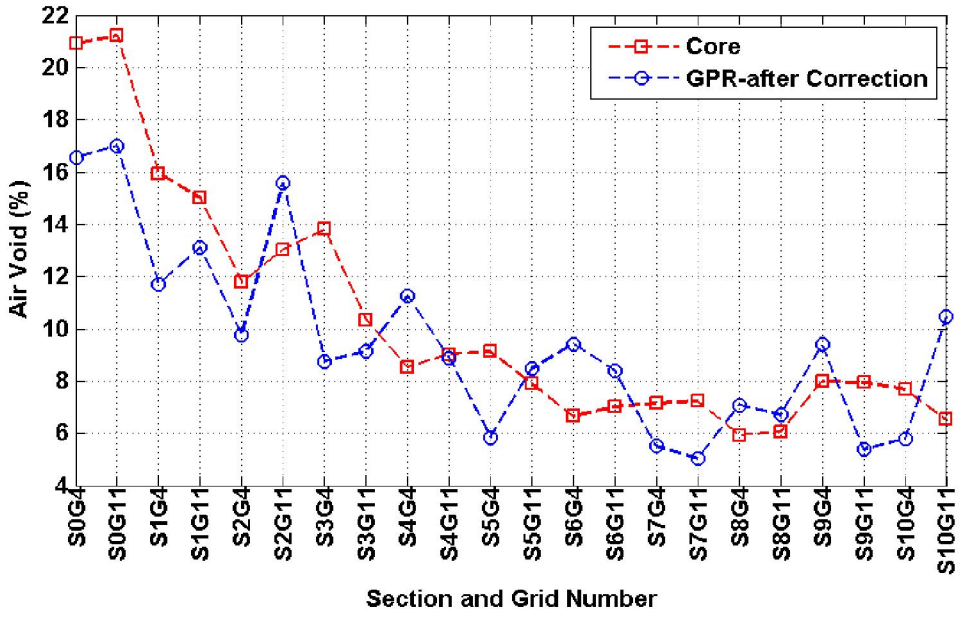

Figure 6-38 Densities (air void content) obtained from cores and GPR data collected after spraying 300 mL water.

Overall, the application of the correction algorithm successfully eliminated the effect of surface moisture and extracted the density information. The density values obtained from GPR data after applying the correction algorithm were reasonably accurate.

6.5 Statistical Analysis of the Experimental Results

A statistical analysis of errors of reflection amplitudes and of the G_{mb} values was conducted. The results were shown in Table 6-11. Figure 6-39 shows the boxplots of errors of reflection amplitudes before and after the correction algorithm when different amounts of water were sprayed. The upper bound of the box represents the 75% quantile value and the lower bound of the box represents the 25% quantile value. The red line in the box represents the median value, or 50% quantile value. The upper bar outside the box represents the maximum value and the lower bar outside the box represents the minimum value. The "+" sign in red color represents the outliers in the data set. As can be seen from the figure, in all the cases, the errors were reduced after applying the correction algorithm. The standard deviation values were also reduced. Similarly, the boxplots of G_{mb} errors before and after the correction algorithm when different amounts of water were sprayed were shown in Figure 6-40 and Figure 6-41. As can be seen from Figure 6-40, the outliers were mainly from the data at the first 2 passes. The errors were also reduced after applying the correction algorithm. The case when spraying 300 mL water was separately shown in Figure 6-41 because of the huge difference of the errors. Before applying the correction algorithm, the reflection amplitude increased dramatically because of the large amount of surface moisture so

the errors of the calculated G_{mb} values were unreasonably high. After the application of the correction algorithm, the errors were brought to reasonable values.

Table 6-11 Statistical Analysis of Errors of Reflection Amplitude and Errors of G_{mb}

Amount of Sprayed Water (mL)		100-before Corr.	100-after Corr.	150-before Corr.	150-after Corr.	200-before Corr.	200-after Corr.	300-before Corr.	300-after Corr.
Error of Amp. (%)	Average	1.9	1.0	2.9	1.3	5.9	1.4	14.3	2.3
	Median	1.8	0.7	3.0	1.0	5.6	1.1	13.8	2.4
	Standard Deviation	0.9	0.8	0.9	0.9	1.5	1.3	3.6	1.3
	t-Test (2-tail) Prob.	4.62E-03		8.51E-07		4.29E-14		7.82E-13	
Error of G_{mb} (%)	Average	2.4	1.6	3.4	1.7	6.7	1.8	144.7	2.7
	Median	1.5	1.2	2.6	1.1	6.1	1.1	146.9	2.4
	Standard Deviation	2.4	1.8	2.4	2.0	2.6	2.3	13.5	1.7
	t-Test (2-tail) Prob.	1.17E-02		7.00E-05		8.39E-11		6.51E-23	

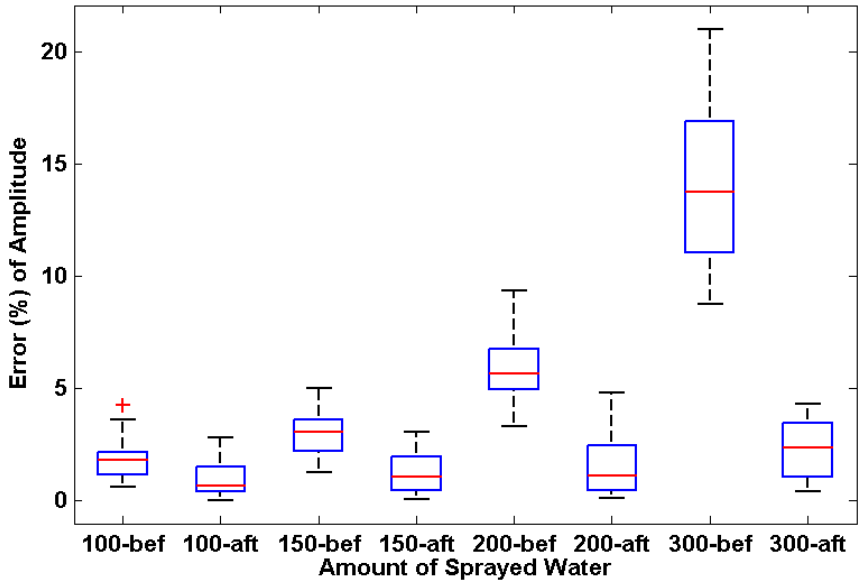

Figure 6-39 Boxplots of the errors of reflection amplitudes before and after the correction algorithm when different amounts of water were sprayed.

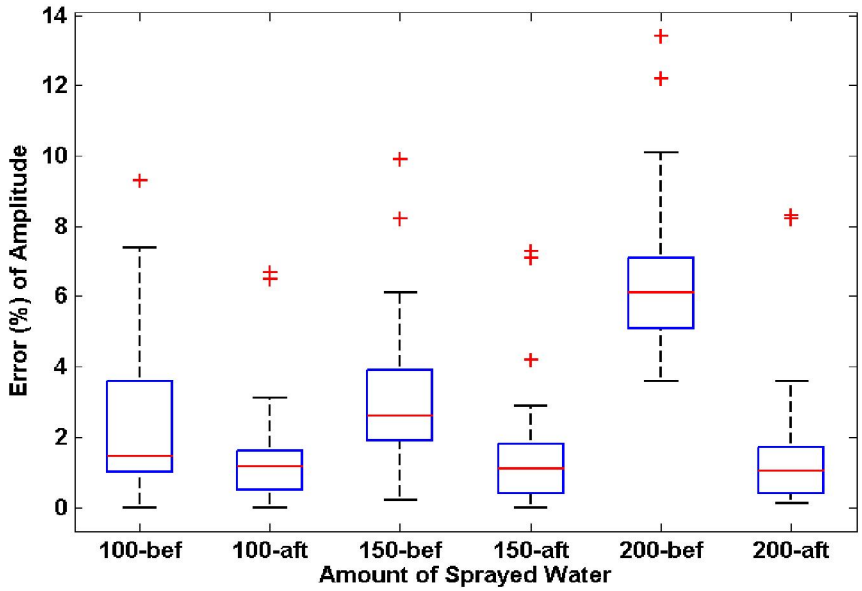

Figure 6-40 Boxplots of the G_{mb} errors before and after the correction algorithm when different amounts of water were sprayed (the cases of spraying 300mL excluded).

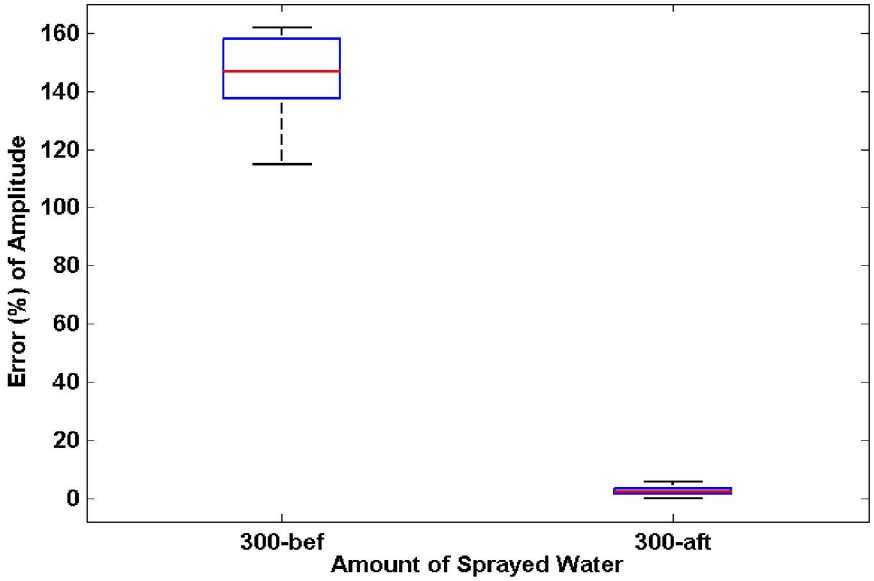

Figure 6-41 Boxplots of the G_{mb} errors before and after the correction algorithm when 300mL water was sprayed.

CHAPTER 7 FIELD TESTING

Using the GPR setup shown in Figure 3-14, GPR data was collected in a asphalt pavement construction site. The description of the test site, the data collection procedure, and the data analysis results are presented in this section.

7.1 Description of the Field Test Site

The construction site was located on East Main Street in Danville Illinois. Two layers of asphalt mixture were placed on top of an existing asphalt pavement. A leveling binder course was first placed on the existing asphalt pavement. Then, a surface course was placed over the leveling binder course. The mix design information of the two asphalt layers is shown in Table 7-1. The two mixtures were both fine graded. The leveling binder layer had a design thickness of 1.75 in (44.5 mm) and the surface layer had a design thickness of 1.5 in (38.1 mm). Before construction of the pavements, the construction company built a separate test pad for quality control purposes. The test pad was laid on an existing asphalt pavement parking lot in Urbana, Illinois. The leveling binder mix shown in Table 7-1 was used as the material of the test pad. GPR data was first collected from the test pad in Urbana and then from the construction site in Danville while the leveling binder layer was being constructed.

Table 7-1 Asphalt Mixture Design Information of the Field Test Site

Layer Type	Nominal Maximum Aggregate Size (mm)	Gradation	Binder Type	Binder Content (%)	G_{mm}
Leveling Binder Mix	9.5	Fine Graded	PG 70-22	6.6	2.482
Surface Mix	9.5	Fine Graded	PG 70-22	5.9	2.511

7.2 Data Collection on Test Pad

There are two purposes for GPR data collection on the test pad:

- To collect a reference scan which was needed when applying the reference scan approach
- To obtain the value of dielectric constant of the aggregate, ε_s, which was needed for the density estimation model

As shown in Figure 7-1, the asphalt mixture was laid down by a paver on the milled surface of the existing pavement. A compactor with vibratory steel wheels followed the paver to compact the asphalt mixture, as shown in Figure 7-2. GPR data was collected after the pavement was completely dry (approximately two hours after the final compaction). As shown in Figure 7-3, two channels of GPR data were collected using two 2.0-GHz GSSI air-coupled antennas. Two cores were taken at the locations where GPR data were collected, as shown in Figure 7-4.

Figure 7-1 Asphalt mixture laid down by a paver.

Figure 7-2 A vibratory steel roller on the asphalt pavement.

Figure 7-3 GPR data collection on dry pavement.

Figure 7-4 Core extraction at the location of GPR measurement.

Using Equation (6-3) and the information shown in Table 7-1, the effective specific gravity of aggregate G_{se} could be calculated. The value of G_{se} was 2.7643. The G_{mb} and air void content of the two cores were measured in the laboratory using CoreLok method. The dielectric constant of the aggregate could be back-calculated. The results are shown in Table 7-2. The average value of ε_s from the two cores, which was 7.680, was used as the dielectric constant of the aggregate.

Table 7-2 Volumetric and Dielectric Information from the Cores

Core No.	G_{mm}	G_{mb}	Air Void (%)	Dielectric Constant from GPR	Back-calculated ε_s
1	2.482	2.252	9.3	5.658	7.771
2	2.482	2.297	7.5	5.748	7.589

Figure 7-5 and Figure 7-6 depict the two reference scans for channel 1 and channel 2, which were collected from the test pad in time and frequency domains. Note that the amplitude of channel 2 data was higher than channel 1 data because of the difference in the antennas. The difference did not affect the data analysis because the higher reflection amplitude of the signal from pavement was offset by the higher reflection amplitude of the signal from copper plate, which resulted in similar dielectric constant values calculated by Equation (2-26). As shown in Table 7-2, the dielectric constant values of the two channels were similar.

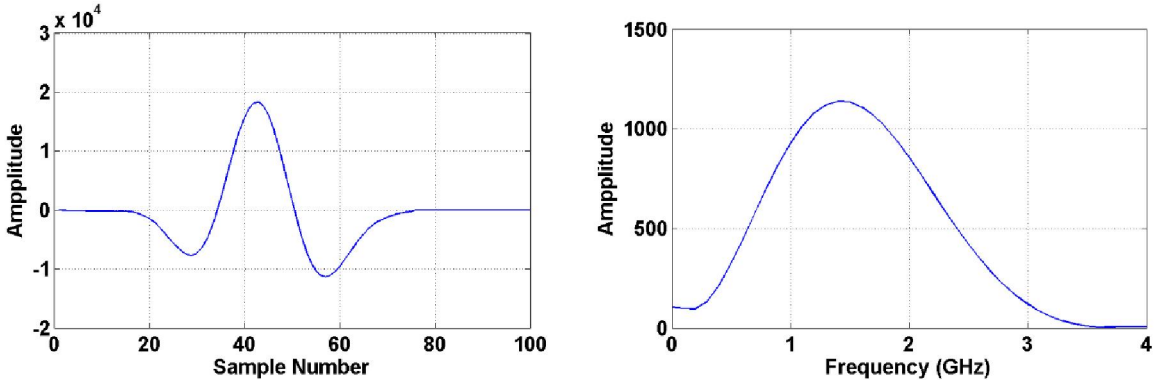

(a) (b)

Figure 7-5 Reference scan of channel 1: (a) time domain; (b) frequency domain.

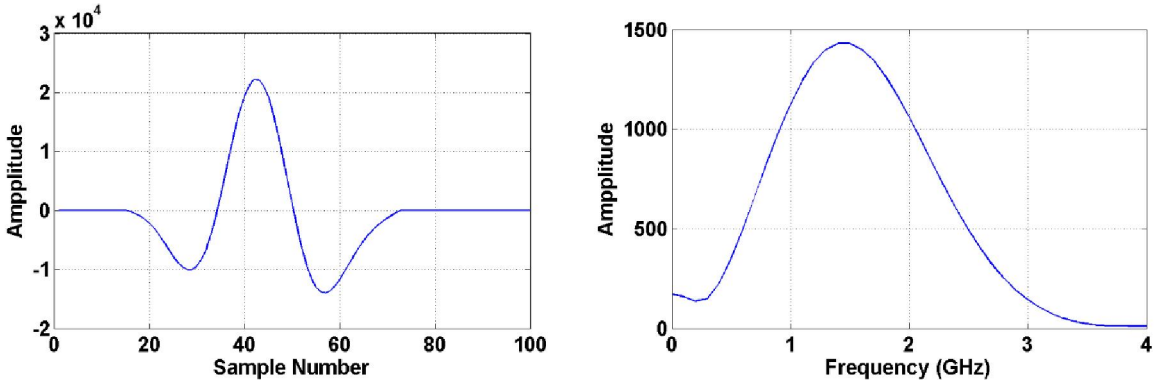

(a) (b)

Figure 7-6 Reference scan of channel 2: (a) time domain; (b) frequency domain.

After the data collection on test pad, the dielectric constant of aggregate and the reference scan were obtained and could be used in the field GPR tests to determine the densities of asphalt pavement after each roller passes.

7.3 Field Testing on Construction Site

After the asphalt mixture was laid down on the existing pavement by the paver, the asphalt mixture was compacted by a series of four rollers. As shown in Table 7-3, the first two rollers were vibratory steel rollers, the third roller was a pneumatic roller, and the fourth roller was a finishing roller with static steel drum. During construction, the GPR antennas were placed above the pavement to collect data right after the roller finished a pass, as shown in Figure 7-7. When data collection was finished, the antennas were lifted up to avoid disturbance to the operation of rollers. After final compaction, a nuclear density gauge was used to check the densities of the two locations for GPR data collection, as shown in Figure 7-9 (a). After that, the cores were extracted from the two locations, as shown in Figure 7-9 (b). The densities obtained from GPR, nuclear density gauge, and cores were compared for validation purposes.

Table 7-3 Descriptions of Compactors in the Field Construction

Compactor No.	Type	Model	Compaction Width
1	Vibratory steel roller	Ingersoll Rand DD-118HF	78.7 in (200 cm)
2	Vibratory steel roller	Ingersoll Rand DD-90HF	66 in (168 cm)
3	Pneumatic roller	Caterpillar PS150C	68 in (173 cm)
4	Static steel roller	NA	48 in (122 cm)

Figure 7-7 GPR data collection during compaction.

Figure 7-8 GPR antennas raised up to avoid disruption to roller.

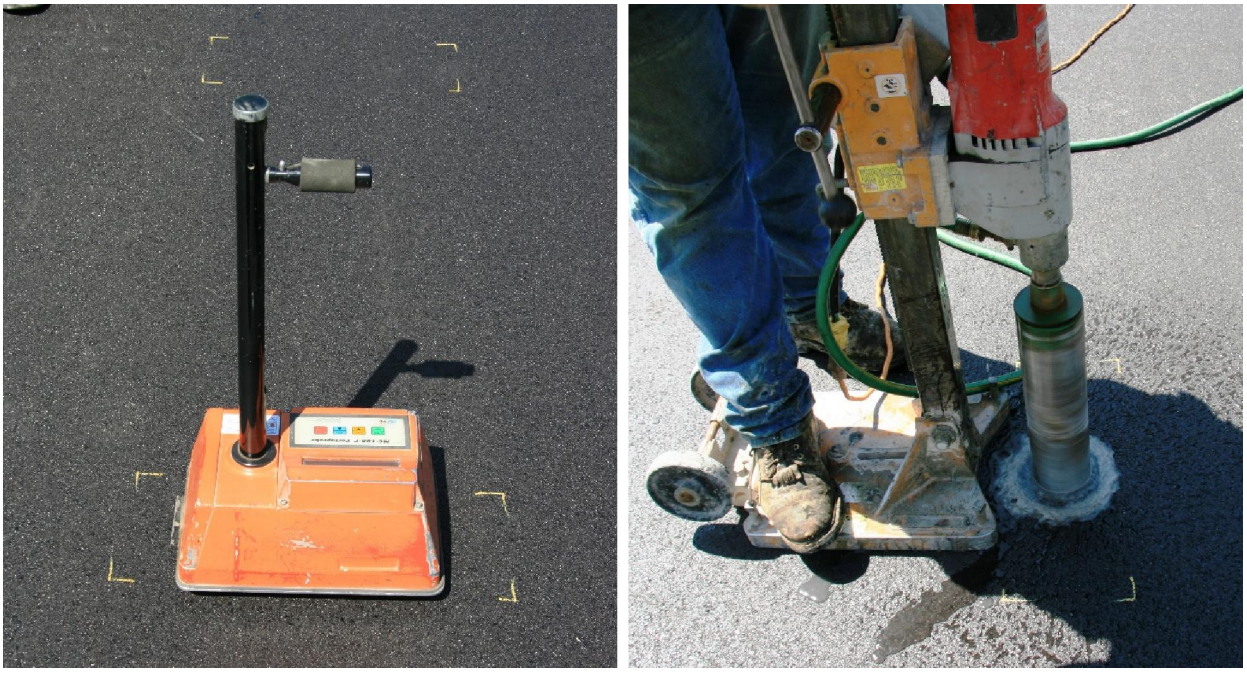

(a) (b)

Figure 7-9 Density check using: (a) nuclear density gauge; (b) cores.

The GPR data collected through channel 1 was first analyzed. The surface reflection amplitude was plotted after each roller in Figure 7-10. The four compactors had 18 roller passes on the GPR data collection locations. The 1st, 2nd, 3rd, and 4th compactor had 3, 8, 5, and 2 roller passes, respectively.

As shown in Figure 7-10, the reflection amplitude increased dramatically at the 1st roller pass. The increase of the reflection amplitude became gradual after the 1st roller pass. At 13th roller pass, a second dramatic increase was found and the amplitudes after 13th roller pass decreased. During the data collection, it was observed that the 3rd compactor sprayed a large amount of water on the roller and noticeable water remained on the pavement at 13th roller pass. Therefore, the dramatic increase at

13th roller pass was greatly attributed to the large amount of surface moisture on the pavement.

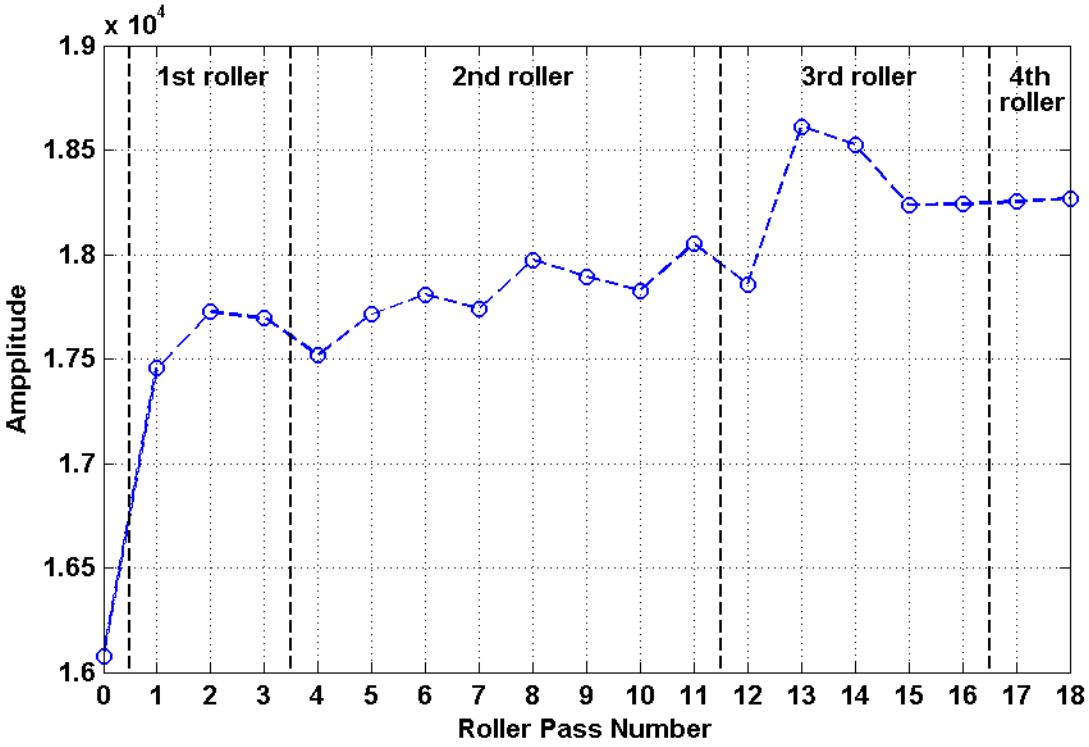

Figure 7-10 Amplitudes of pavement surface reflection after different number of roller passes from channel 1 GPR data.

The correction algorithm was applied on the GPR data to remove the effect of surface moisture. The reference scan approach was used following the procedure described in Section 6.3. The GPR signal shown in Figure 7-5 was used as the reference scan for channel 1. Figure 7-11 depicts the reflection amplitudes before and after the correction algorithm. It can be seen that all the reflection amplitudes decreased after the application of the correction algorithm, with one exception at 4th roller pass.

The small amount of increase of the reflection amplitude at 4th roller pass was possibly caused by the acceptable inaccuracy of the correction algorithm.

At the 13th and 14th roller passes, the reflection amplitudes decreased much more after the correction algorithm compared with the reflection amplitudes at other roller passes. The compactor sprayed much more water at the 13th and 14th roller passes which resulted in higher increase of the reflection amplitude and the correction algorithm removed a larger portion of the increase of amplitude caused by the surface moisture. Therefore the reduction of reflection amplitude was larger.

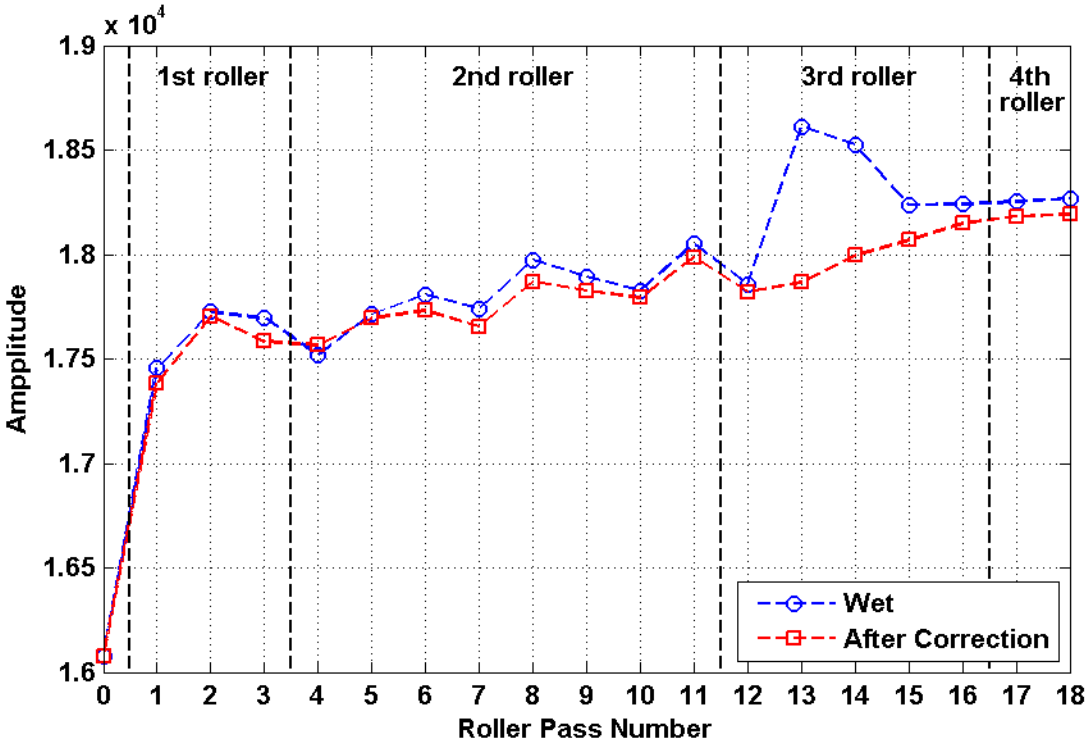

Figure 7-11 Amplitudes of pavement surface reflection after different number of roller passes from channel 1 GPR data: before and after correction algorithm.

Details of the correction process on GPR signals at 13th and 14th roller passes are illustrated in Figure 7-12 to Figure 7-15. As shown in Figure 7-12, the reference scan for channel 1 collected from the test pad, as shown in Figure 7-5 (b), was plotted with the surface reflection in the GPR signal collected from wet pavement in frequency domain. The correction factor was calculated at the frequency at 1.1 GHz. By multiplying the reference scan with the correction factor, a new signal was obtained, which was plotted as the red curve in Figure 7-12. The new signal was the signal after correction in which the effect of surface moisture was removed. The signal after correction should resemble the signal collected from the dry pavement. The frequency-selective effect is obvious in Figure 7-12. The time domain signals were obtained by applying inverse the Fourier transform, as shown in Figure 7-13. The reflection amplitude was reduced by 4% after the correction algorithm was applied. For the GPR data collected at 14th roller pass, the signal after correction in frequency domain is shown as the red curve in Figure 7-14. The signals before and after correction in time domain are shown in Figure 7-15. The reflection amplitude was reduced by 3% after the correction algorithm was applied.

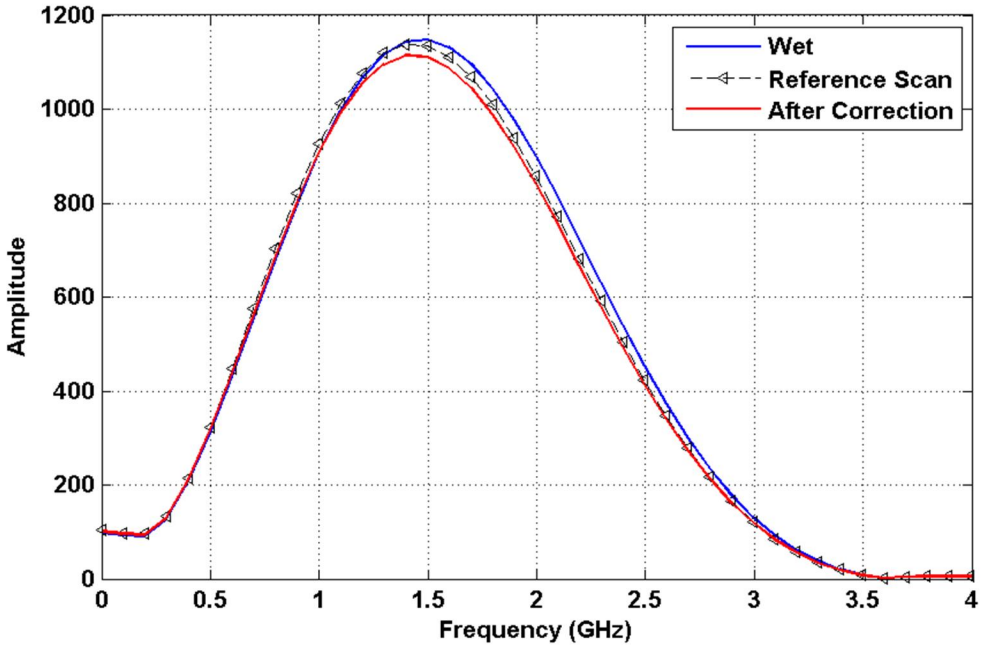

Figure 7-12 Correction algorithm applied on channel 1 GPR signal at 13th roller pass - frequency domain.

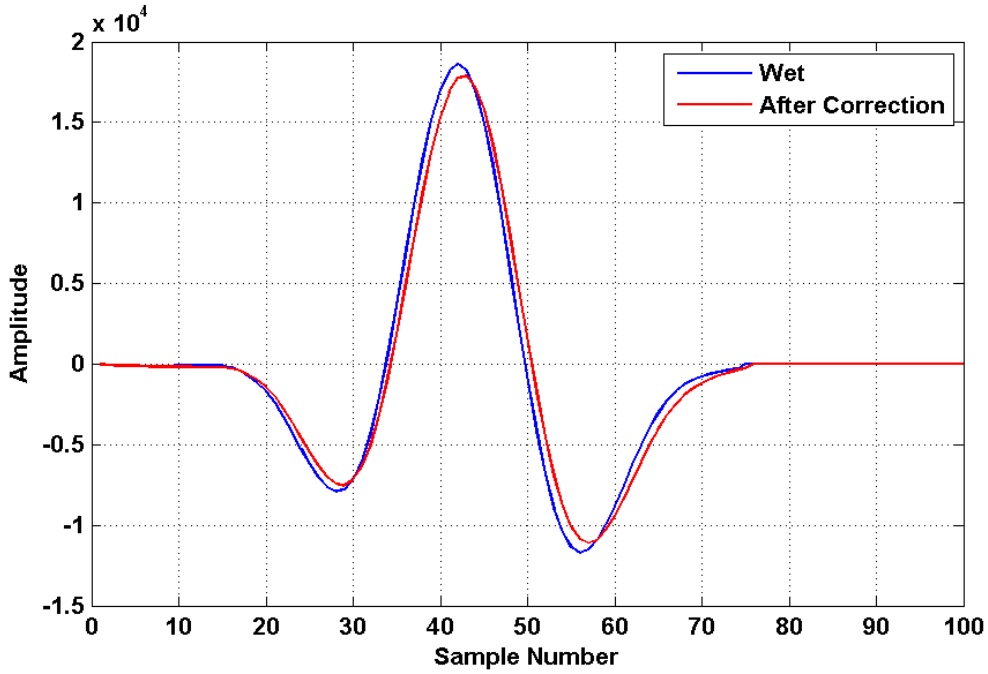

Figure 7-13 Correction algorithm applied on channel 1 GPR signal at 13th roller pass - time domain.

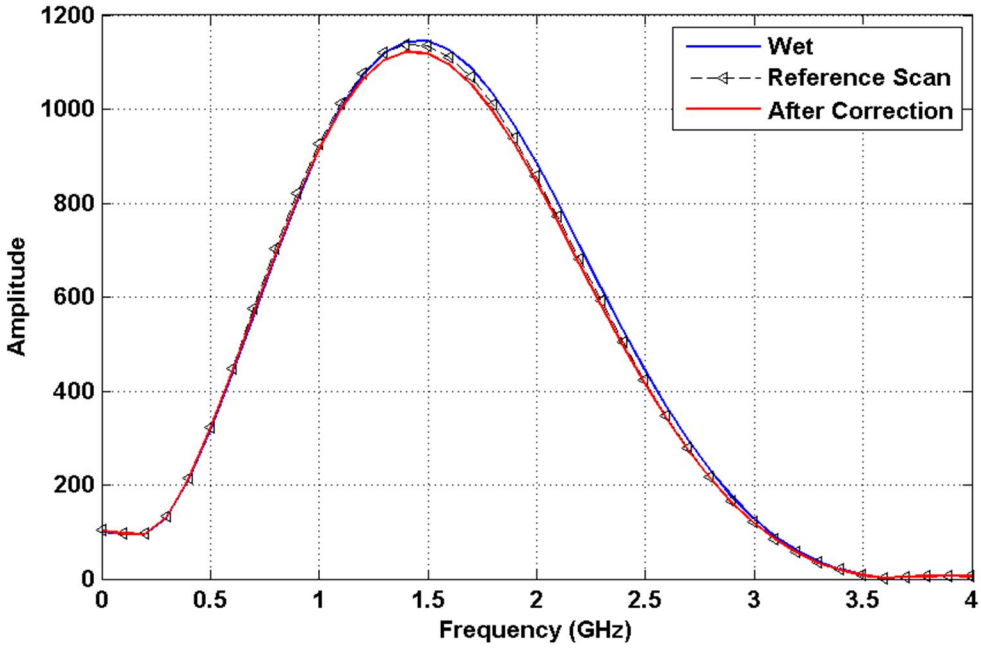

Figure 7-14 Correction algorithm applied on channel 1 GPR signal at 14th roller pass - frequency domain.

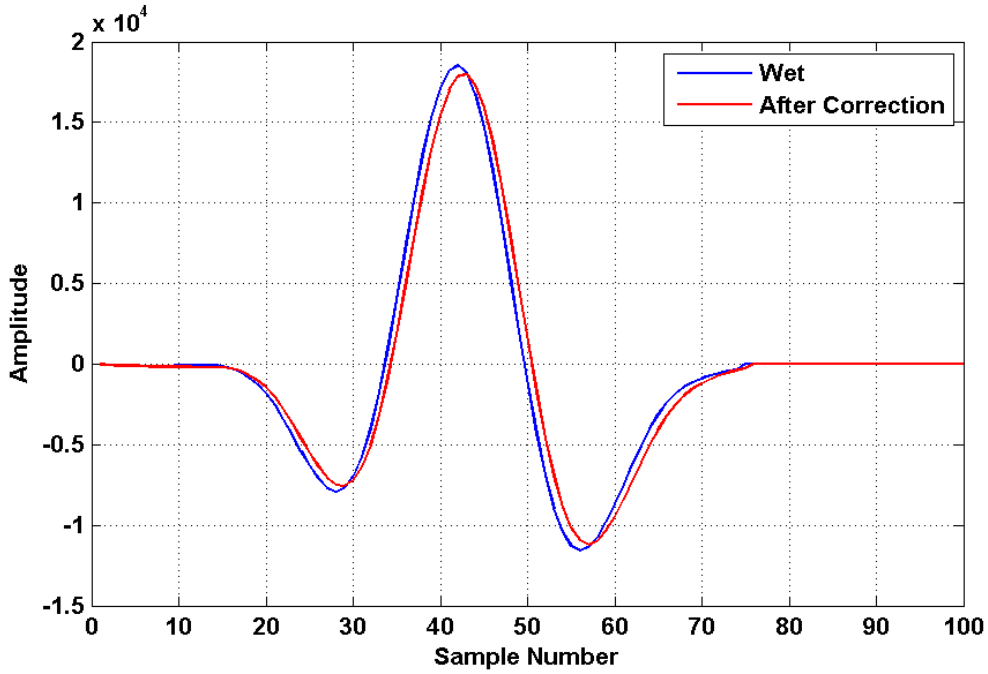

Figure 7-15 Correction algorithm applied on channel 1 GPR signal at 14th roller pass - time domain.

After applying the correction algorithm, the reflection amplitudes were corrected. The dielectric constant corresponding to each roller pass was then obtained. The density of asphalt mixture was obtained after each roller pass using the ALL model. Table 7-4 summarizes the results of density estimation. The initial air void content of loose mixture before compaction was 15.4%, the air void after final roller pass was 5.6% before the application of the correction algorithm, and 6.0% after the correction algorithm. The density estimation result at the final roller pass was compared with the results from cores and from the nuclear density gauge. As shown in Table 7-5, the G_{mb} value obtained from the core was 2.305. The G_{mb} value obtained from nuclear density gauge was 2.338 with an error of 1.4%. The G_{mb} value obtained from GPR signal without the correction algorithm was 2.344 with an error of 1.7%. The G_{mb} value obtained from GPR signal after the correction algorithm was 2.332 with an error of 1.2%. The air void content values obtained from different methods are shown in Table 7-6. The air void content obtained from the core was 7.1%. The air void content obtained from nuclear density gauge was 5.8% which was 1.3% lower than the value from the core. The air void content was 5.6% from the GPR signal without the correction algorithm, which was 1.5% lower that the value from the core and 6.0% from the GPR signal after the correction algorithm, which was 1.1% lower than the value from the core. Using the GPR and correction algorithm resulted in a more accurate estimation of the density of the asphalt mixture than using the nuclear density gauge.

Figure 7-16 shows the change of dielectric constant values with a different number of roller passes. Figure 7-17and Figure 7-18 show the G_{mb} and air void content

values obtained from GPR at different roller passes. The density information of the asphalt mixture after compaction obtained from the nuclear density gauge and the core is also shown in Figure 7-17 and Figure 7-18.

Table 7-4 Calculation of Densities of Asphalt Mixture after Different Number of Roller Passes Using GPR Data from Channel 1

Compactor No.	Roller Pass No.	Dielectric Constant before Correction Algorithm	Dielectric Constant after Correction Algorithm	G_{mb} before Correction Algorithm	G_{mb} after Correction Algorithm	Air Void (%) before Correction Algorithm	Air Void (%) after Correction Algorithm
NA	0	4.740	4.740	2.100	2.100	15.4	15.4
1	1	5.505	5.462	2.234	2.225	10.0	10.3
	2	5.671	5.659	2.268	2.265	8.6	8.7
	3	5.653	5.584	2.264	2.250	8.8	9.4
2	4	5.542	5.573	2.242	2.248	9.7	9.4
	5	5.664	5.651	2.266	2.264	8.7	8.8
	6	5.723	5.676	2.279	2.269	8.2	8.6
	7	5.680	5.627	2.270	2.259	8.6	9.0
	8	5.829	5.763	2.301	2.287	7.3	7.9
	9	5.778	5.736	2.290	2.281	7.7	8.1
	10	5.735	5.713	2.281	2.277	8.1	8.3
	11	5.880	5.838	2.312	2.303	6.8	7.2
3	12	5.753	5.732	2.285	2.280	7.9	8.1
	13	6.263	5.761	2.397	2.287	3.4	7.9
	14	6.202	5.843	2.383	2.304	4.0	7.2
	15	6.005	5.891	2.339	2.314	5.8	6.8
	16	6.005	5.944	2.339	2.326	5.8	6.3
4	17	6.014	5.968	2.341	2.331	5.7	6.1
	18	6.025	5.974	2.343	2.332	5.6	6.0

Table 7-5 Accuracy of the G_{mb} Measurement Using Channel 1 GPR Data and Nuclear Density Gauge

Core	Nuclear Density Gauge	Error (%)	GPR before Correction Algorithm	Error (%)	GPR after Correction Algorithm	Error (%)
2.305	2.338	1.4	2.344	1.7	2.332	1.2

Table 7-6 Accuracy of Air Void Content (%) Measurement Using Channel 1 GPR Data and Nuclear Density Gauge

Core	Nuclear Density Gauge	Difference	GPR before Correction Algorithm	Difference	GPR after Correction Algorithm	Difference
7.1	5.8	1.3	5.6	1.6	6.0	1.1

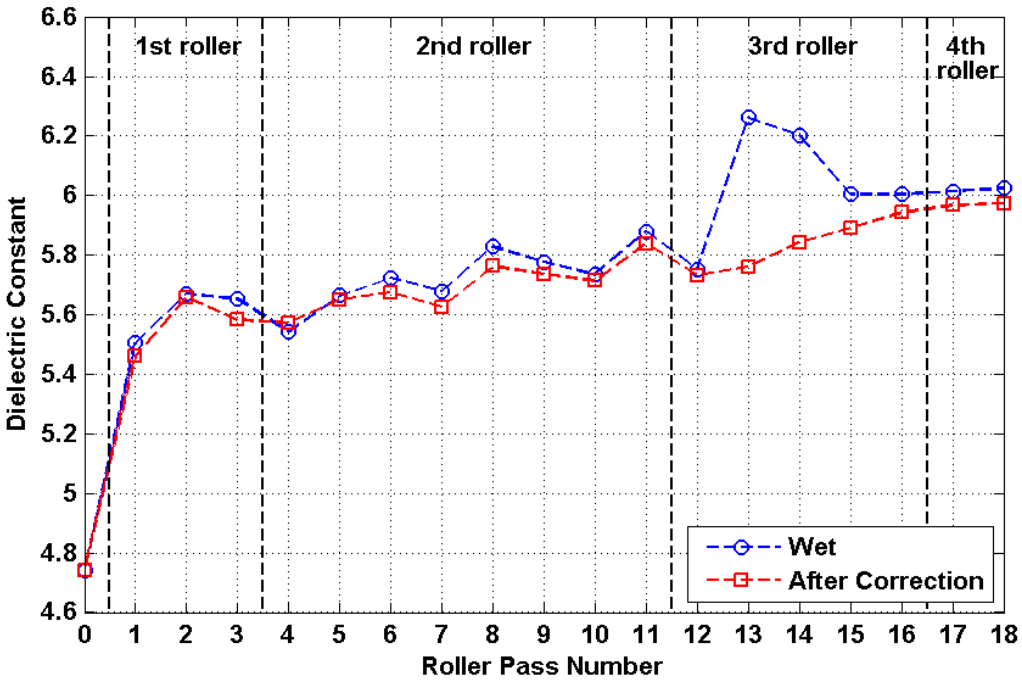

Figure 7-16 The dielectric constant values after different number of roller passes from channel 1 GPR data: before and after correction algorithm.

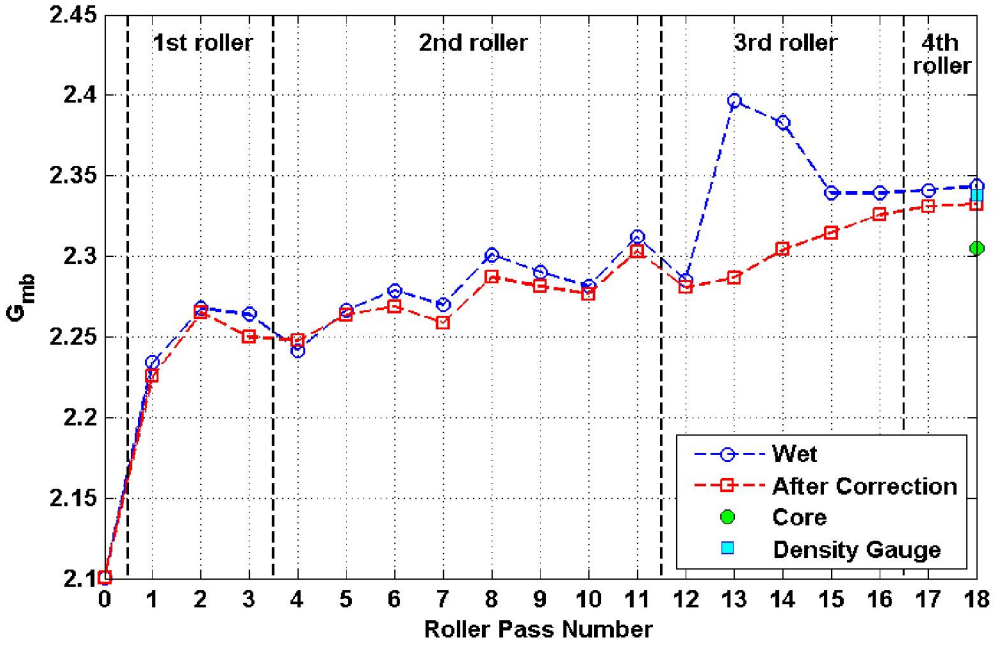

Figure 7-17 The G_{mb} values after different number of roller passes from channel 1 GPR data: before and after correction algorithm.

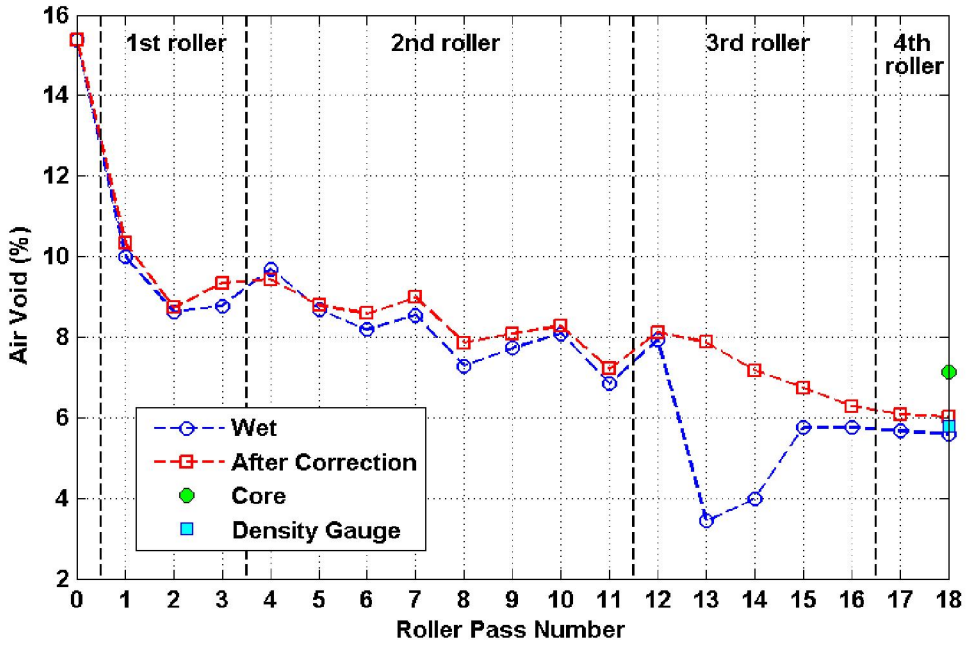

Figure 7-18 The air void contents after different number of roller passes from channel 1 GPR data: before and after correction algorithm.

For the GPR data collected through channel 2, the amplitudes of the raw GPR data are plotted in Figure 7-19. The amplitude increased dramatically at the 1st roller pass and the increase became gradual after the 1st roller pass. At 13th roller pass, the amplitude increased dramatically because of the large amount of sprayed water. The amplitude decreased after the 13th roller pass.

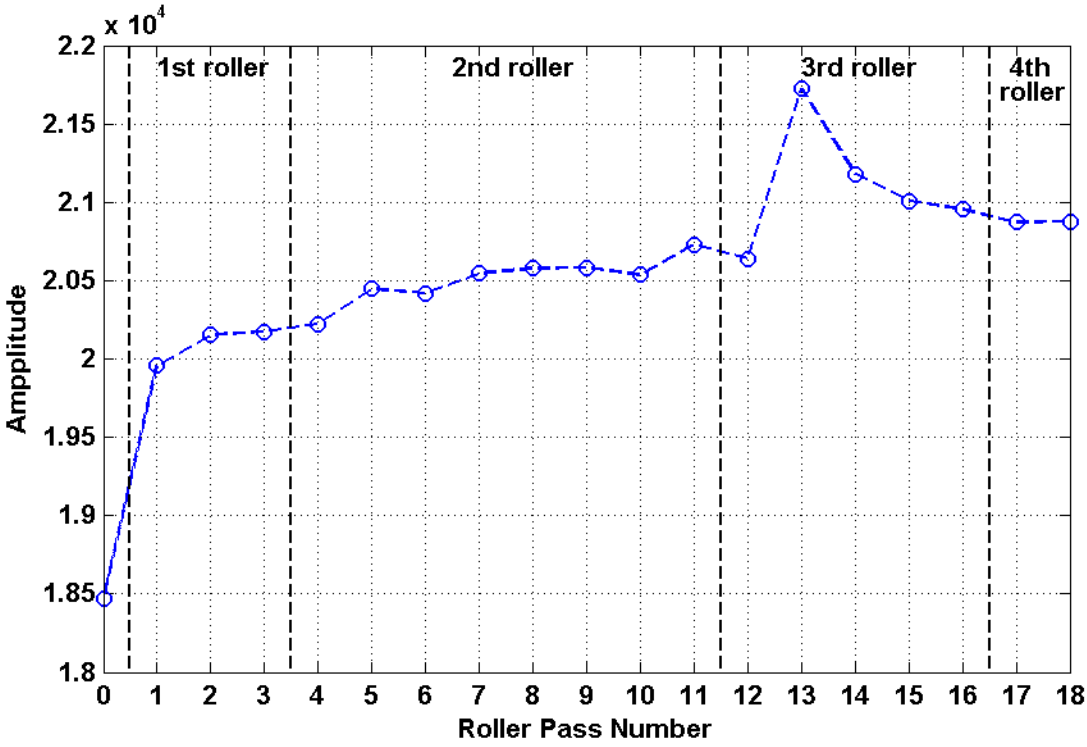

Figure 7-19 Amplitudes of pavement surface reflection after different number of roller passes from channel 2 GPR data.

After application of the correction algorithm using the reference scan approach with the reference scan shown in Figure 7-6, the reflection amplitudes decreased, as

shown in Figure 7-20. The only two exceptions were at the 3rd and 4th roller passes where the amplitudes slightly increased. The effect of the correction algorithm was most obvious at 13th and 14th roller passes where the largest amounts of surface moisture existed.

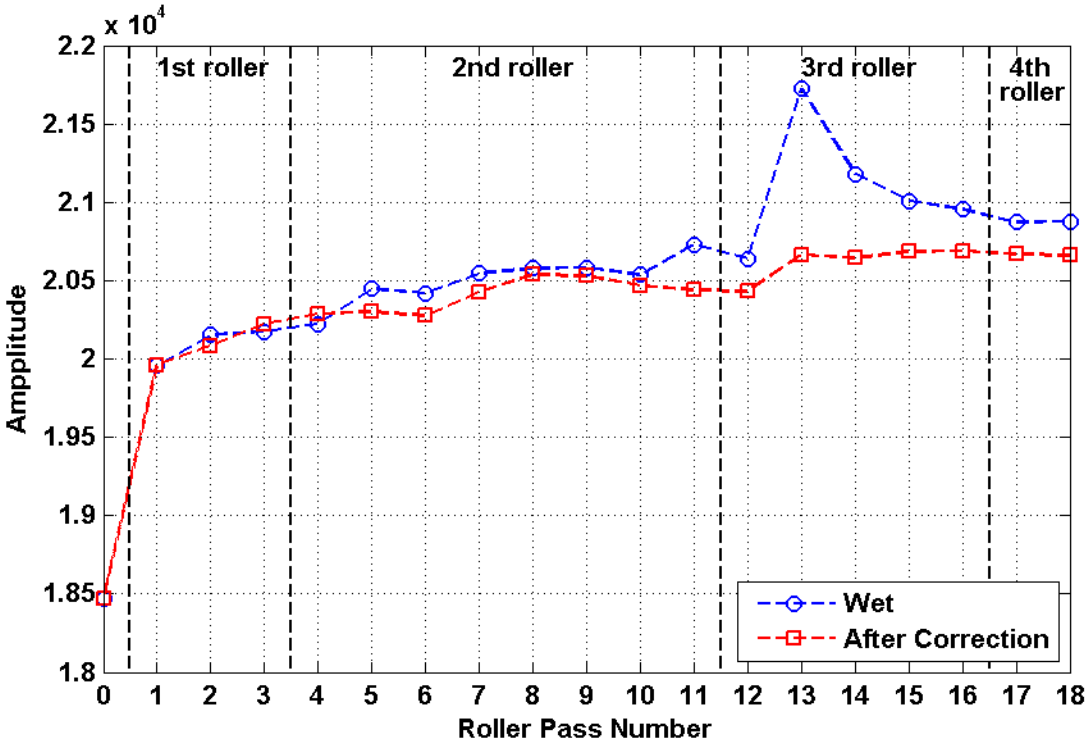

Figure 7-20 Amplitudes of pavement surface reflection after different number of roller passes from channel 2 GPR data: before and after correction algorithm.

Details of the correction process on GPR signals at 13th and 14th roller passes using reference scan approach are shown in Figure 7-21 to Figure 7-24. A correction factor was obtained by comparing the amplitudes of reference scan and wet scan at 1.1 GHz in frequency domain. The signal after correction was obtained by multiplying the

reference scan with the correction factor. As shown in Figure 7-21, the frequency-selective effect was observed: The lower frequency components of the wet signal and signal after correction were almost the same. The time domain signal was obtained using inverse Fourier transform. As shown in Figure 7-22, the reflection amplitude decreased by 5% after the correction algorithm. For the signal at the 14th roller pass, the frequency spectrum of the surface reflection pulse is plotted in Figure 7-23. The time domain signal is shown in Figure 7-24. The reduction of the amplitude after the correction algorithm was 3%.

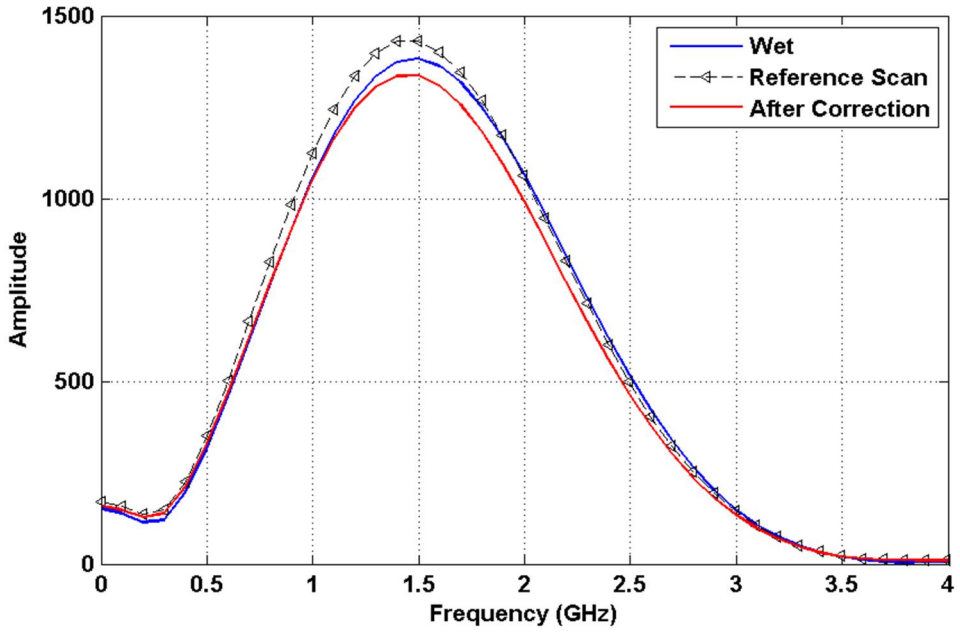

Figure 7-21 Correction algorithm applied on channel 2 GPR signal at 13th roller pass - frequency domain.

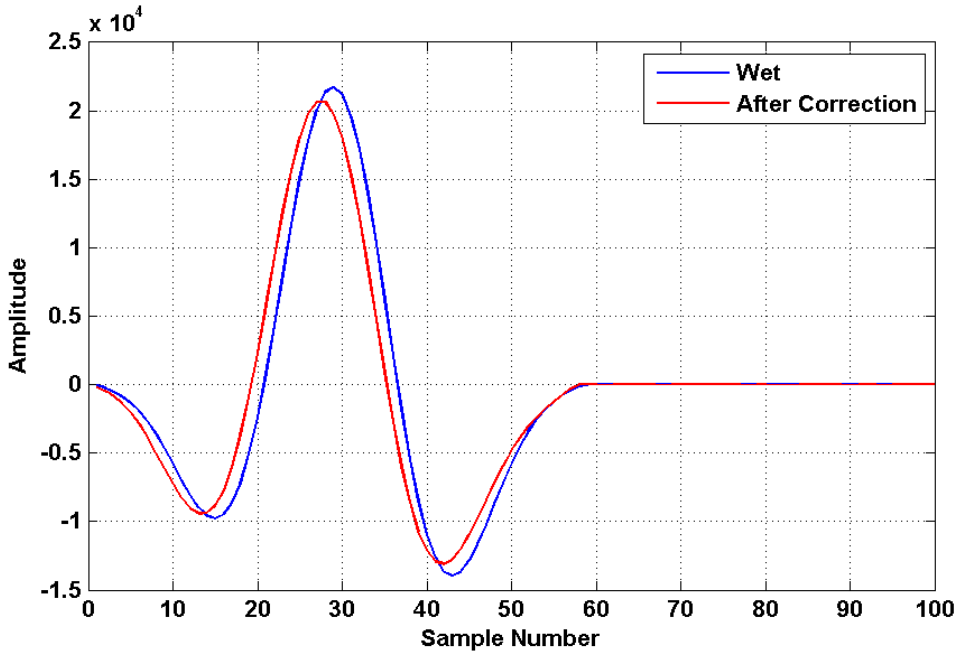

Figure 7-22 Correction algorithm applied on channel 2 GPR signal at 13th roller pass - time domain.

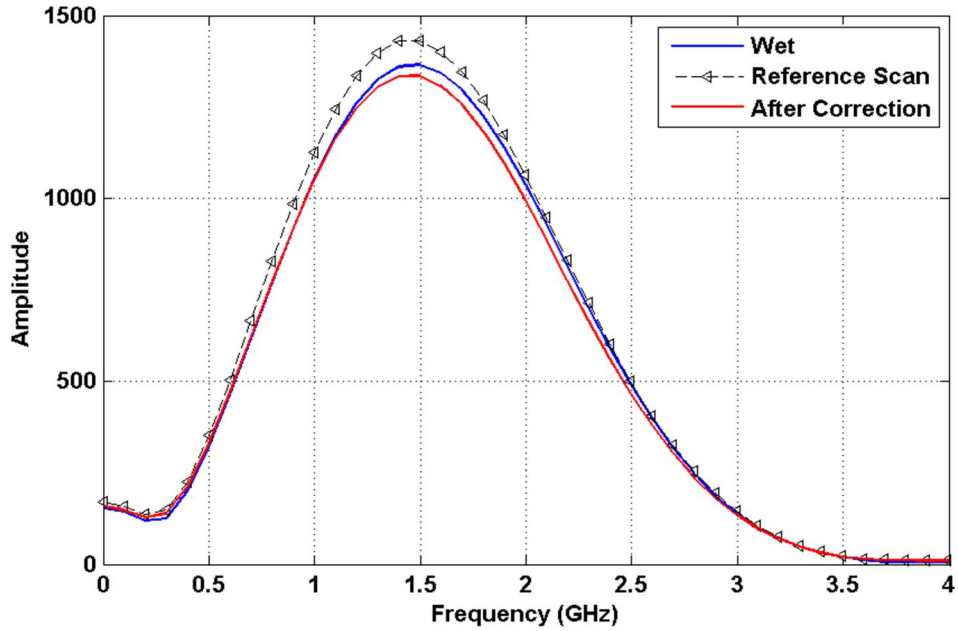

Figure 7-23 Correction algorithm applied on channel 2 GPR signal at 14th roller pass - frequency domain.

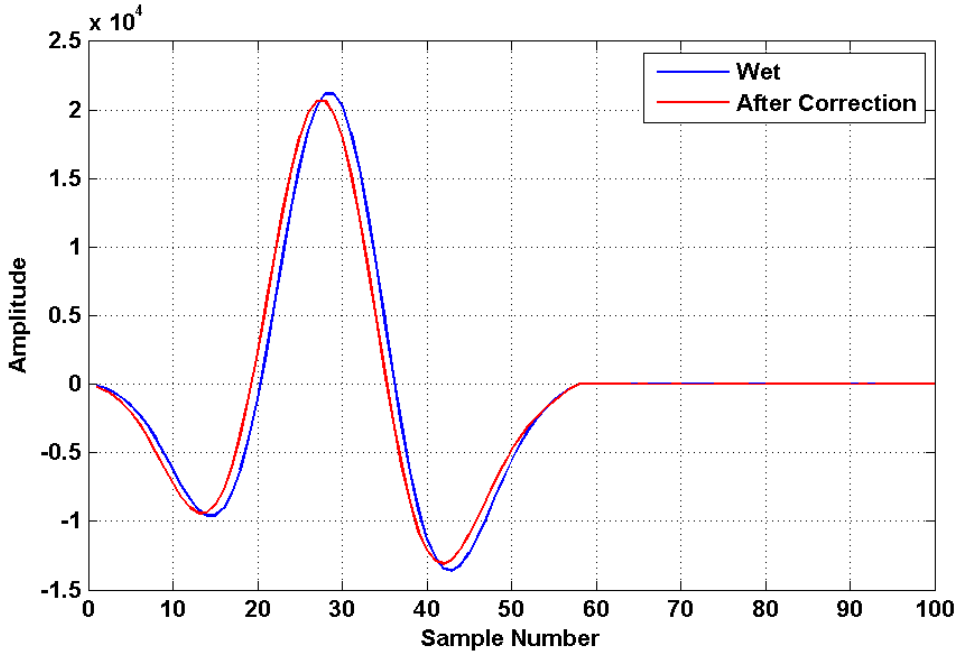

Figure 7-24 Correction algorithm applied on channel 2 GPR signal at 14th roller pass - time domain.

After correction of the reflection amplitude, the values of dielectric constant, G_{mb} and air void content V_a could be obtained. The results are shown in Table 7-7. The air void content decreased from 15.7% at 0th roller pass, when the asphalt pavement was loose mixture, to 7.9% at 18th pass, when the final compaction was completed, using GPR data after application of the correction algorithm. The density result at 18th pass from GPR was compared with the density results from nuclear density gauge and cores, as shown in Table 7-8 and Table 7-9, respectively. The G_{mb} value from nuclear density gauge had an error of 2.7%. The error of G_{mb} value from GPR data before correction algorithm was 0.8%. The error was reduced to 0.3% after the application of correction

algorithm. The difference of air void compared with the value from the core was 2.5%, 0.7% and 0.3% using nuclear density gauge, GPR signal before correction, and GPR signal after correction, respectively. Similar to channel 1 data, the density results from GPR after correction algorithm was more accurate than the results obtained from the nuclear density gauge. The dielectric constant values at different roller passes are shown in Figure 7-25. The G_{mb} and air void content V_a values are plotted in Figure 7-26 and Figure 7-27.

Table 7-7 Calculation of Densities of Asphalt Mixture after Different Number of Roller Passes Using GPR Data from Channel 2

Compactor No.	Roller Pass No.	Dielectric Constant before Correction Algorithm	Dielectric Constant after Correction Algorithm	G_{mb} before Correction Algorithm	G_{mb} after Correction Algorithm	Air Void (%) before Correction Algorithm	Air Void (%) after Correction Algorithm
NA	0	4.684	4.684	2.092	2.092	15.7	15.7
1	1	5.384	5.386	2.210	2.211	10.9	10.9
	2	5.485	5.449	2.230	2.223	10.2	10.4
	3	5.496	5.522	2.232	2.238	10.1	9.9
2	4	5.522	5.555	2.237	2.244	9.9	9.6
	5	5.640	5.562	2.261	2.246	8.9	9.5
	6	5.626	5.549	2.258	2.243	9.0	9.6
	7	5.693	5.631	2.272	2.260	8.4	9.0
	8	5.712	5.690	2.276	2.272	8.3	8.5
	9	5.714	5.686	2.277	2.271	8.3	8.5
	10	5.690	5.652	2.272	2.264	8.5	8.8
	11	5.795	5.638	2.294	2.261	7.6	8.9
3	12	5.747	5.633	2.284	2.260	8.0	8.9
	13	6.383	5.759	2.424	2.286	2.3	7.9
	14	6.054	5.748	2.350	2.284	5.3	8.0
	15	5.954	5.771	2.328	2.289	6.2	7.8
	16	5.923	5.773	2.321	2.289	6.5	7.8
4	17	5.875	5.761	2.311	2.287	6.9	7.9
	18	5.878	5.758	2.312	2.286	6.9	7.9

Table 7-8 Accuracy of the G_{mb} Measurement Using Channel 2 GPR and Nuclear Density Gauge

Core	Nuclear Density Gauge	Error (%)	GPR before Correction Algorithm	Error (%)	GPR after Correction Algorithm	Error (%)
2.294	2.356	2.7	2.312	0.8	2.286	0.3

Table 7-9 Accuracy of Air Void Content (%) Measurement Using Channel 2 GPR and Nuclear Density Gauge

Core	Nuclear Density Gauge	Difference	GPR before Correction Algorithm	Difference	GPR after Correction Algorithm	Difference
7.6	5.1	2.5	6.9	0.7	7.9	0.3

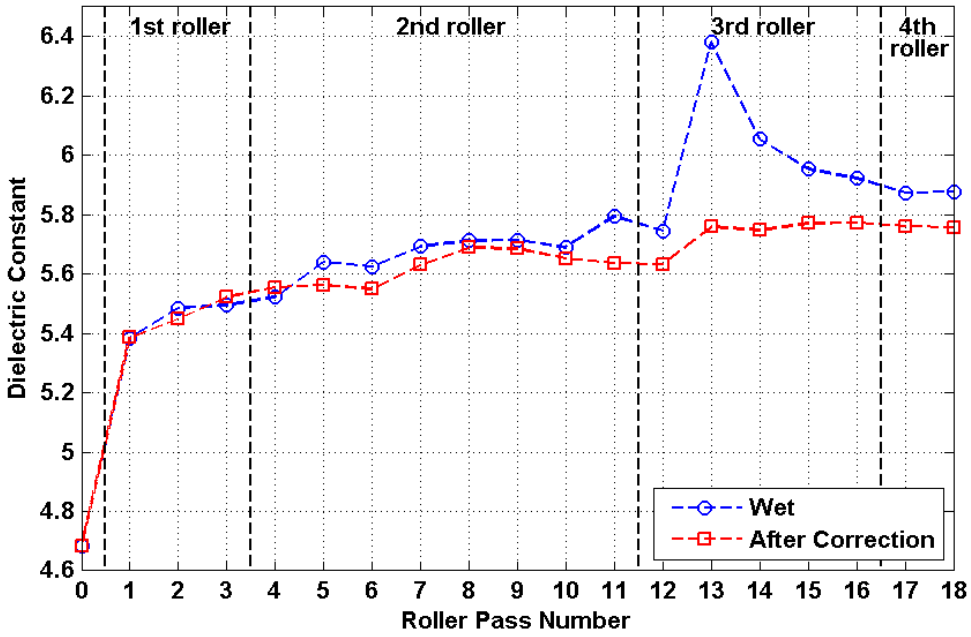

Figure 7-25 The dielectric constant values after different number of roller passes from channel 2 GPR data: before and after correction algorithm.

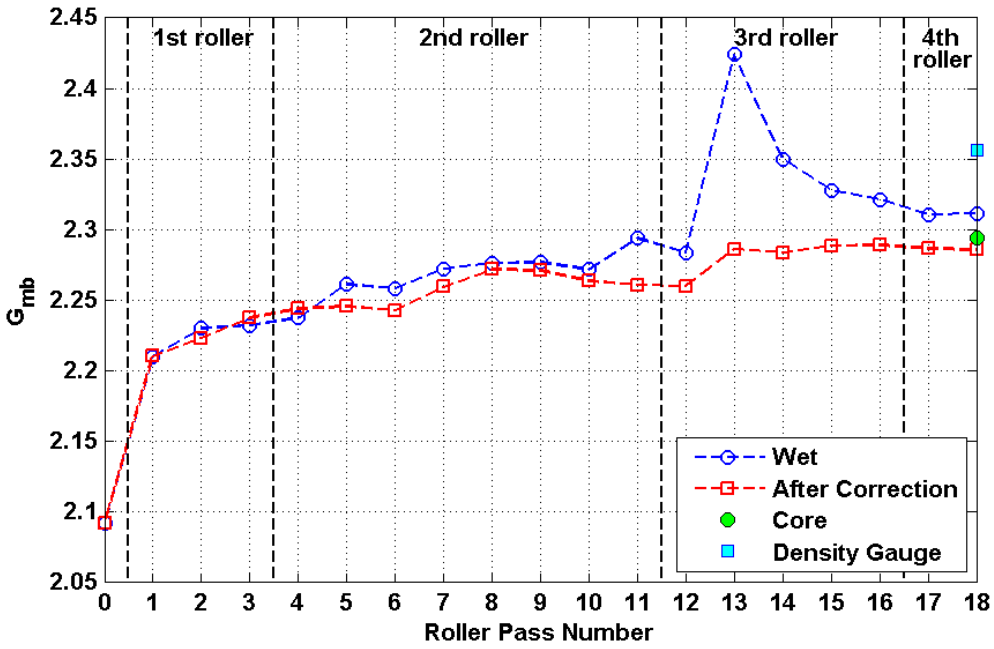

Figure 7-26 The G_{mb} values after different number of roller passes from channel 2 GPR data: before and after correction algorithm.

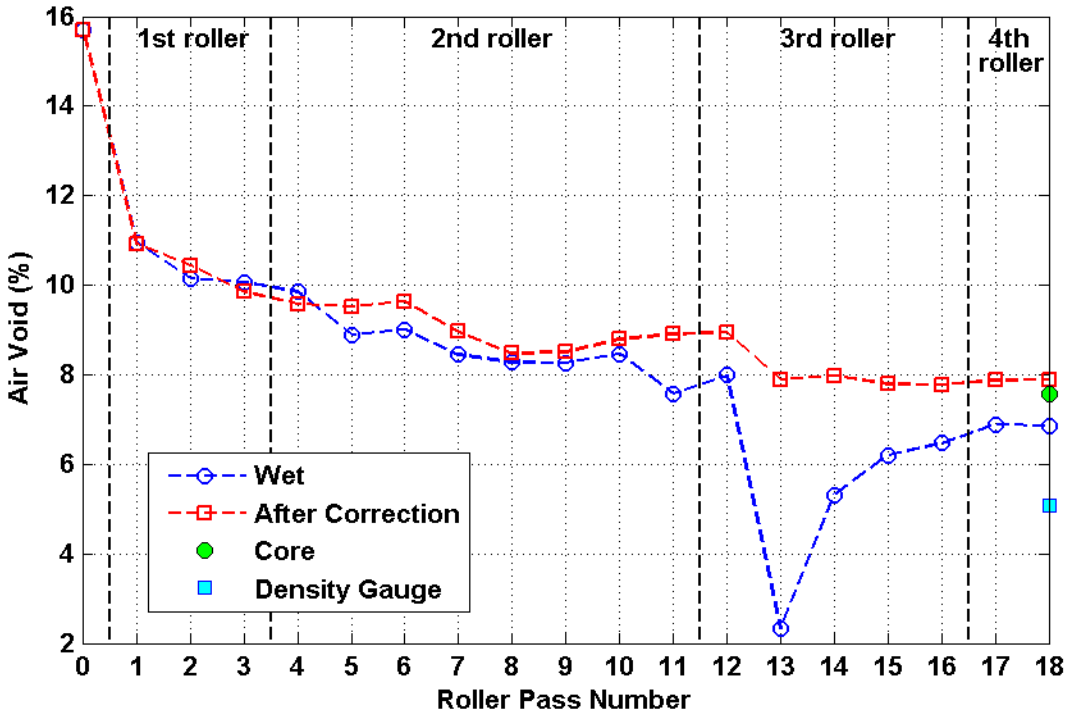

Figure 7-27 The air void contents after different number of roller passes from channel 2 GPR data: before and after correction algorithm.

CHAPTER 8 FINDINGS AND CONCLUSIONS

8.1 Summary

Compaction is a critical process for the construction of asphalt pavement. During compaction, the density of asphalt mixture increases to the prescribed density level. Over-compaction and under-compaction should be avoided because they both result in downgraded asphalt pavement. This study aims to develop a tool to monitor the density of asphalt pavement during compaction using GPR. GPR has many advantages over current techniques, such as coring and nuclear density gauge, and it has been successfully applied to estimate the density of asphalt pavement using the ALL density estimation model. However, the unknown effect of surface moisture on GPR data during compaction remains a significant challenge. This effect prevents the direct application of the ALL model, which is designed for use on dry asphalt mixtures. Therefore, this study focuses on the development of algorithms for processing and interpreting GPR data collected from asphalt pavement during compaction and obtaining density information after each roller pass. The algorithms should be able to eliminate the effect of surface moisture while keeping the density information.

A comprehensive literature review was conducted on asphalt pavement compaction, current and emerging techniques for pavement compaction monitoring, principles of GPR technology, and existing applications of GPR on asphalt pavement. To achieve the research objective, three research approaches were adopted, including numerical modeling, laboratory experiments, and field tests.

Numerical modeling was performed using the FDTD method. A calibration process was conducted and an equivalent excitation source was developed to ensure

an accurate match between the simulated GPR signal and the real GPR signal. The calibrated FDTD model simulated the propagation of GPR waves within the asphalt pavement when the densities of asphalt pavement and surface moisture contents varied. The difference between the effect of density variation and effect of surface moisture variation on GPR signal was found in frequency domain, which was referred to as “frequency-selective effect”. This effect was verified by the realistic GPR data from laboratory experiments.

Based on the difference between the density effect and surface moisture effect on GPR signal, a correction algorithm was developed using a “reference scan approach” to “correct” the GPR signal collected from “wet” asphalt pavement to “resemble” a GPR signal collected from “dry” asphalt pavement. The correction algorithm was applied on the GPR data collected from asphalt pavement with different densities and different surface moisture contents. It was found that the algorithm successfully eliminated the effect of surface moisture on the surface reflection amplitude in GPR data with high accuracy. A total of 22 cores were taken from the laboratory test site and their densities were measured in the laboratory. The density results collected from the GPR data were compared with the density results from the cores. It was found that the density estimation had improved accuracy after the application of the correction algorithm, indicating the effectiveness of the correction algorithm.

Field tests were conducted during the construction of asphalt pavement to validate the algorithms developed in this study. A separate test pad was built prior to actual construction. GPR data was collected from the test pad to obtain the reference scan which was needed for the correction algorithm and the back-calculated dielectric

constant value of aggregate which was needed for the ALL density model. During the actual construction of the asphalt pavement, GPR data was collected after each roller pass. The compaction curve was obtained, and the correction algorithm successfully eliminated the effect of surface moisture during compaction. The density results obtained after the final compaction from GPR, nuclear density gauge, and cores were compared. Density results from GPR were found to have higher accuracy than the results from nuclear density gauge after applying the algorithms developed in this study.

8.2 Findings

The main findings of this study are summarized in the following:

- Calibration is necessary for FDTD simulation of GPR wave propagation. The commonly used Gaussian function and Gaussian derivative functions cannot generate the GPR signal that exactly simulates the real GPR signal. In this study, by using the equivalent excitation function and the DWT de-noising technique, the simulated GPR signal matched the real GPR signal accurately. It should be noted that this excitation function is only valid for the GPR system used in this study. But the procedure of finding an equivalent excitation source could be applied to any other GPR systems.
- The difference between the effect of density variation and the effect of surface moisture content variation on GPR signals was found. Although it was difficult to distinguish one effect from the other in time domain, the difference between the two effects was obvious in frequency domain. In the frequency spectrums of the surface reflection pulses, the “frequency-

selective effect" was found. The increase of the amplitude as a result of the increase of pavement density occurred over the entire frequency range, while the increase of the amplitude as a result of the increase of surface moisture content occurred mainly at high frequency range. The low frequency components were sensitive to density change but insensitive to the change in surface moisture.

- Based on the frequency-selective effect, the approach of using the band-pass filtering technique was attempted in this study. Based on the band-pass filtering technique, a feature representing the amplitude of low frequency components of the surface reflection pulse was obtained. This feature was insensitive to the variation of the surface moisture content. However, it was difficult to obtain the dielectric constant and density values based on this feature. Therefore, this approach was not adopted in this study.
- The reference scan approach was used as the correction algorithm to eliminate the effect of water. Based on the laboratory experimental data, the errors of the reflection amplitude in GPR data as a result of surface moisture were reduced after the application of the correction algorithm. The average error for the 22 locations on test site B was reduced from 1.89% to 0.96% in the case of spraying 100 mL water, from 2.91% to 1.27% in the case of spraying 150 mL water, from 5.93% to 1.44% in the case of spraying 200 mL water, and from 14.25% to 2.3% in the case of spraying 300 mL water. The average error for all the cases excluding the case

when 300 mL water was sprayed was 3.68% before the correction algorithm and 1.22% after the correction algorithm.

- The correction algorithm using reference scan approach increased the accuracy of estimating the densities of asphalt mixture using the GPR data collected from pavement with surface moisture. After applying the correction algorithm, the average error in estimating G_{mb} value using the GPR data from locations after 2 roller passes was reduced from 1.4% to 0.9% in the case of spraying 100 mL water, from 2.4% to 0.9% in the case of spraying 150 mL water, from 5.6% to 0.9% in the case of spraying 200 mL water, and from 149.0% to 2.2% in the case of spraying 300 mL water. The average error for all the cases excluding the case of spraying 300 mL water was reduced from 3.1% to 0.9%.
- Field test data validated the effectiveness of the algorithm. The compaction curve lowered down after the correction algorithm because the algorithm removed the effect of surface moisture. When the compactor sprayed a large amount of water, the surface reflection amplitude in the raw data increased dramatically. After the application of the correction algorithm, the portion of the increase in amplitude as a result of surface moisture was removed. The density estimation results obtained from GPR after the final compaction had higher accuracy than the density results obtained from the nuclear density gauge.

8.3 Conclusions

In this study, the research objective is achieved through a comprehensive set of research approaches. The following conclusions are drawn:

- The challenge caused by the unknown effect of surface moisture on GPR data when applying GPR on compaction monitoring was solved.
- The frequency-selective effect was the main difference between the effect of density variation and effect of surface moisture on GPR signals. Based on the frequency-selective effect, a correction algorithm was developed using the reference scan approach. The correction algorithm was successful in eliminating the effect of surface moisture.
- Along with the algorithm, the ALL model could accurately estimate the asphalt pavement density even with the existence of surface moisture, which enabled the GPR to monitor the density during compaction of the asphalt pavement.

8.4 Recommendations for Further Study

The ultimate goal of this study is to integrate the GPR system with the compactor so that the compactor operator can monitor the density of asphalt pavement continuously in real time. This study addresses the utmost challenge, which is to eliminate the effect of surface moisture on GPR data. To achieve the ultimate goal, further study is needed. The recommendations for future study are proposed below.

- A mounting system should be developed to mount the GPR system on the compactor. The way to mount the antennas should be optimized to satisfy both the requirement of compaction operation (GPR system should not interrupt compaction operation) and the GPR data collection (compactor operation should not affect GPR data). Research efforts should focus on optimizing the following variables: Locations of the antennas to be mounted, the height of the antennas, and the distance of the antennas to the compactor. A mounting system should be developed to ensure that the GPR system is mounted securely on the compactor.
- The algorithms developed in this study should be further investigated using GPR systems with other central frequencies. The results and findings in this study are obtained using the GSSI 2.0-GHz antennas and GSSI SIR-20 data collection system. If GPR systems with other central frequencies are used, the optimal parameters in the algorithms may be different. Furthermore, the error of the density measurement is partially attributed to the instability of the signal and other system errors. Different GPR systems might have different number of samples per scan, different signal to noise ratio, and different signal stability. The accuracy of the density measurement may also be different.
- It is recommended to incorporate the GPR data with the data from other sensors used in compaction monitoring such as GPS, accelerometer, and infrared sensor. Successful data fusion can bring potential benefits such

as increased detectability of problematic areas during compaction, a larger amount of useful information, and enhanced reliability of testing results.

REFERENCES

1. Loulizi, A., I. L. Al-Qadi, and S. Lahouar. Optimization of Ground-Penetrating Radar Data to Predict Layer Thicknesses in Flexible Pavements. *Journal of Transportation Engineering*, Vol. 129, No. 1, Jan. 2003, pp. 93–99.

2. Lahouar, S., and I. L. Al-Qadi. Automatic Detection of Multiple Pavement Layers from GPR Data. *NDT & E International*, Vol. 41, No. 2, Mar. 2008, pp. 69–81.

3. Al-Qadi, I. L., S. Lahouar, K. Jiang, K. K. McGhee, and D. Mokarem. Accuracy of Ground-penetrating Radar for Estimating Rigid and Flexible Pavement Layer Thicknesses. *Transportation Research Record: Journal of the Transportation Research Board*, Vol. 1940, 2005, pp. 69–78.

4. Al-Qadi, I. L., and S. Lahouar. Use of GPR for Thickness Measurement and Quality Control of Flexible Pavements. *Asphalt Paving Technology: Association of Asphalt Paving Technologists-Proceedings of the Technical Sessions*, Vol. 73, 2004, pp. 501–528.

5. Al-Qadi, I. L., and S. Lahouar. Ground Penetrating Radar: State of the Practice for Pavement Assessment. *Materials Evaluation*, Vol. 62, No. 7, 2004, pp. 759–763.

6. Al-Qadi, I. L., S. Lahouar, and A. Loulizi. Successful Application of Ground-penetrating Radar for Quality Assurance-Quality Control of New Pavements. *Transportation Research Record: Journal of the Transportation Research Board*, Vol. 1861, 2003, pp. 86–97.

7. Lahouar, S., I. L. Al-Qadi, A. Loulizi, T. M. Clark, and D. T. Lee. Approach to Determining In Situ Dielectric Constant of Pavements: Development and Implementation at Interstate 81 in Virginia. *Transportation Research Record: Journal of the Transportation Research Board*, Vol. 1806, 2002, pp. 81–87.

8. Al-Qadi, I. L., and S. Lahouar. Measuring Layer Thicknesses with GPR – Theory to Practice. *Construction and Building Materials*, Vol. 19, No. 10, Dec. 2005, pp. 763–772.

9. Al-Qadi, I. L., and S. Lahouar. Measuring Rebar Cover Depth in Rigid Pavements with Ground-Penetrating Radar. *Transportation Research Record: Journal of the Transportation Research Board*, Vol. 1907, Jan. 2005, pp. 80–85.

10. Chen, D. H., and T. Scullion. Detecting Subsurface Voids Using Ground-Coupled Penetrating Radar. *Geotechnical Testing Journal*, Vol. 31, No. 3, 2008, pp. 217–224.

11. Ni, J. C., and W.-C. Cheng. Trial Grouting Under Rigid Pavement: A Case History in Magong Airport, Penghu. *Journal of Testing and Evaluation*, Vol. 40, No. 1, 2012, pp. 107–118.

12. Al-Qadi, I. L., Z. Leng, S. Lahouar, and J. Baek. In-Place Hot-Mix Asphalt Density Estimation Using Ground-Penetrating Radar. *Transportation Research Record: Journal of the Transportation Research Board*, Vol. 2152, Dec. 2010, pp. 19–27.

13. Leng, Z., I. L. Al-Qadi, and S. Lahouar. Development and Validation for In Situ Asphalt Mixture Density Prediction Models. *NDT&E International*, Vol. 44, No. 4, Jul. 2011, pp. 369–375.

14. Leng, Z., I. L. Al-Qadi, P. Shangguan, and S. Son. Field Application of Ground-Penetrating Radar for Measurement of Asphalt Mixture Density-Case Study of Illinois Route 72 Overlay. *Transportation Research Record: Journal of the Transportation Research Board*, Vol. 2304, 2012, pp. 133–141.

15. Shangguan, P., I. L. Al-Qadi, Z. Leng, R. Schmitt, and A. Faheen. Innovative Approach for Asphalt Pavement Compaction Monitoring Using Ground Penetrating Radar. *Transportation Research Record: Journal of the Transportation Research Board*, Vol. 2425, 2013, pp. 79–87.

16. AASHTO. AASHTO T 269: Standard Method of Test for Percent Air Voids in Compacted Dense and Open Asphalt Mixtures.

17. Brown, E. R. Density of Asphalt Concrete: How Much is Needed? *Transportation Research Record: Journal of the Transportation Research Board*, Vol. 1282, 1990, pp. 27–32.

18. Linden, R. N., J. P. Mahoney, and N. C. Jackson. Effect of Compaction on Asphalt Concrete Performance. *Transportation Research Record: Journal of the Transportation Research Board*, Vol. 1217, 1989, pp. 20–28.

19. Roberts, F. L., P. S. Kandhal, E. R. Brown, D.-Y. Lee, and T. W. Kennedy. *Hot Mix Asphalt Materials, Mixture Design and Construction*. NAPA Research and Education Foundation, 1996.

20. Rickards, I., S. Goodman, J. Pagani, A. El Halim, and R. Haas. Practical Realization of a New Concept for Asphalt Compaction. *Transportation Research Record: Journal of the Transportation Research Board*, Vol. 1654, Jan. 1999, pp. 27–35.

21. Xia, K., and T. Pan. Understanding Vibratory Asphalt Compaction by Numerical Simulation. *International Journal of Pavement Research & Technology*, Vol. 4, No. 3, May 2011, pp. 185–193.

22. Brown, E. R., M. R. Hainin, A. Cooley, and G. Hurley. *Relationship of Air Voids, Lift Thickness, and Permeability in Hot Mix Asphalt Pavements- NCHRP Report 531*. Transportation Research Board, National Research Council, Washington, D.C., 2004.

23. Masad, E., B. Muhunthan, N. Shashidhar, and T. Harman. Quantifying Laboratory Compaction Effects on the Internal Structure of Asphalt Concrete. *Transportation Research Record: Journal of the Transportation Research Board*, Vol. 1681, Jan. 1999, pp. 179–185.

24. AASHTO. AASHTO T 166: Bulk Specific Gravity of Compacted Hot Mix Asphalt Using Saturated Surface-Dry Specimens.

25. ASTM. ASTM D2726-11: Standard Test Method for Bulk Specific Gravity and Density of Non-Absorptive Compacted Bituminous Mixtures.

26. Buchanan, M. S., and T. D. White. Hot Mix Asphalt Mix Design Evaluation Using the Corelok Vacuum-Sealing Device. *Journal of Materials in Civil Engineering*, Vol. 17, No. 2, Apr. 2005, pp. 137–142.

27. AASHTO. AASHTO T 275: Standard Method of Test for Bulk Specific Gravity (Gmb) of Compacted Hot Mix Asphalt (HMA) Using Paraffin-Coated Specimens.

28. ASTM. ASTM D1188: Standard Test Method for Bulk Specific Gravity and Density of Compacted Bituminous Mixtures Using Coated Samples.

29. Nuclear Density Gauge. http://www.pavementinteractive.org.

30. Sawchuk, P., and R. Sovik. *Testing and Trial Deployment of a Cost-effective and Real-time Asphalt Pavement Quality Indicator System*. IDEA Program, Transportation Research Board, National Research Council, 1997.

31. Model 2701-B Pavetracker™ Plus Non-Nuclear Gauge. http://www.troxlerlabs.com.

32. Williams, S. G. *Non-Nuclear Methods for HMA Density Measurements MBTC 2075 Final Report*. 2008.

33. Sargand, S. M., S. S. Kim, and S. P. Farrington. *A Working Review of Available Non-Nuclear Equipment for Determining In-Place Density of Asphalt*. Ohio Department of Transportation, Columbus, OH, 2005.

34. Chang, G., Q. Xu, R. Jennifer, B. Horan, L. Michael, D. White, and P. Vennapusa. *Accelerated Implementation of Intelligent Compaction Technology for Embankment Subgrade Soils, Aggregate Base, and Asphalt Pavement Materials*. Federal Highway Administration, Washington, D.C., 2011.

35. Beainy, F., S. Commuri, M. Zaman, and I. Syed. Viscoelastic-Plastic Model of Asphalt-Roller Interaction. *International Journal of Geomechanics*, Vol. 13, No. 5, Oct. 2013, pp. 581–594.

36. Intelligent Compaction for Asphalt Materials. http://www.fhwa.dot.gov/pavement/ic/techbriefs/ic_hma.cfm.

37. Hughes, C. S. *Compaction of Asphalt Pavement*. Transportation Research Board, National Research Council, Washington, D.C., 1989.

38. Willoughby, K. A., J. P. Mahoney, L. M. Pierce, J. S. Uhlmeyer, K. W. Anderson, S. A. Read, S. T. Muench, T. R. Thompson, and R. Moore. *Construction-Related Asphalt Concrete Pavement Temperature Differentials and the Corresponding Density Differentials*. Research Report Prepared for Washington State Department of Transportation, 2001.

39. Hedderich, J. Pave-IR Update (Presentation at 56th Annual Asphalt Paving Conference). 2014.

40. Leng, Z. *Prediction of In-situ Asphalt Mixture Density Using Ground Penetrating Radar: Theoretical Development and Field Verification (Doctoral Dissertation)*. University of Illinois at Urbana-Champaign, Urbana, Illinois, 2011.

41. Weedon, W. H., W. C. Chew, and P. E. Mayes. A Step-Frequency Radar Imaging System for Microwave Nondestructive Evaluation. *Progress In Electromagnetics Research*, Vol. 28, Jan. 2000, pp. 121–146.

42. 3D-Radar GPR. http://www.3d-radar.com/.

43. Eide, E., and J. Sala. High Resolution Step-Frequency 3D GPR Using Wideband Antenna Arrays (Presentation at Seminar of Ground Penetrating Radar in Road Monitoring and Evaluation Now and the Future). 2012.

44. Bryant, G. H. *Principles of Microwave Measurements*. Peter Peregrinus Ltd., London, 1988.

45. Scott, M., J. Arnold, and D. Gibson. *Step Frequency Ground Penetrating Radar Characterization and Federal Evaluation Tests*. Federal Highway Administration, 2010.

46. Jin, J. *Theory and Computation of Electromagnetic Fields*. John Wiley & Sons, Hoboken New Jersey, 2010.

47. Lahouar, S. *Development of Data Analysis Algorithms for Interpretation of Ground Penetrating Radar Data (Doctoral Dissertation)*. Virginia Polytechnic Institute and State University, 2003.

48. Maser, K. R. Pavement Characterization Using Ground Penetrating Radar: State of the Art and Current Practice. *ASTM Special Technical Publication*, No. 1375, 1999, pp. 313–326.

49. Maser, K. R. Condition Assessment of Transportation Infrastructure Using Ground-Penetrating Radar. *Journal of Infrastructure Systems*, Vol. 2, No. 2, Jun. 1996, pp. 94–101.

50. Halabe, U., A. Sotoodehnia, K. R. Maser, and E. A. Kausel. Modeling the Electromagnetic Properties of Concrete. *ACI Material Journal*, Vol. 90, No. 6, 1993, pp. 552–563.

51. Cardimona, S., B. Willeford, D. Webb, S. Hickman, J. Wenzlick, and N. Anderson. *Automated Pavement Analysis in Missouri Using Ground Penetrating Radar*. Missouri Department of Transportation, 2003.

52. Saarenketo, T., and T. Scullion. Road Evaluation with Ground Penetrating Radar. *Journal of Applied Geophysics*, Vol. 43, No. 2–4, Mar. 2000, pp. 119–138.

53. Kassem, E., T. Scullion, E. Masad, and A. Chowdhury. Comprehensive Evaluation of Compaction of Asphalt Pavements and a Practical Approach for Density Predictions. *Transportation Research Record: Journal of the Transportation Research Board*, Vol. 2268, Dec. 2012, pp. 98–107.

54. Saarenketo, T. Using Ground-Penetrating Radar and Dielectric Probe Measurements in Pavement Density Quality Control. *Transportation Research Record: Journal of the Transportation Research Board*, Vol. 1575, Jan. 1997, pp. 34–41.

55. Chew, W. C. *Waves and Fields in Inhomogeneous Media*. IEEE Press, New York, 1995.

56. Belli, K., C. M. Rappaport, H. Zhan, and S. Wadia-Fascetti. Effectiveness of 2-D and 2.5-D FDTD Ground-Penetrating Radar Modeling for Bridge-Deck Deterioration Evaluated by 3-D FDTD. *IEEE Transactions on Geoscience and Remote Sensing*, Vol. 47, No. 11, 2009, pp. 3656–3663.

57. Yee, K. Numerical Solution of Initial Boundary Value Problems Involving Maxwell's Equations in Isotropic Media. *IEEE Transactions on Antennas and Propagation*, Vol. 14, No. 3, 1966, pp. 302–307.

58. Bernard, L., R. R. Torrado, and L. Pichon. Efficient Implementation of the UPML in the Generalized Finite-difference Time-domain Method. *IEEE Transactions on Magnetics*, Vol. 46, No. 8, 2010, pp. 3492–3495.

59. Giannopoulos, A. Modelling Ground Penetrating Radar by GprMax. *Construction and Building Materials*, Vol. 19, No. 10, Dec. 2005, pp. 755–762.

60. Wilson, V., C. Power, A. Giannopoulos, J. Gerhard, and G. Grant. DNAPL Mapping by Ground Penetrating Radar Examined via Numerical Simulation. *Journal of Applied Geophysics*, Vol. 69, No. 3–4, Dec. 2009, pp. 140–149.

61. Maclean, T. S. M., and Z. Wu. *Radiowave Propagation Over Ground*. Chapman & Hall, London, 1993.

62. Caterpillar Inc. *Specification of Caterpillar CD54 Vibratory Asphalt Compactor*. 2009.

63. Kao, C., J. Li, Y. Wang, H. Xing, and C. R. Liu. Measurement of Layer Thickness and Permittivity Using a New Multilayer Model From GPR Data. *IEEE Transactions on Geoscience and Remote Sensing*, Vol. 45, No. 8, 2007, pp. 2463–2470.

64. Giannakis, I., A. Giannopoulos, and N. Davidson. Incorporating Dispersive Electrical Properties in FDTD GPR Models Using a General Cole-Cole Dispersion Function. *Proceedings of 14th International Conference on Ground Penetrating Radar (GPR)*, 2012, pp. 232–236.

65. Belli, K., S. Wadia-Fascetti, and C. Rappaport. Model Based Evaluation of Bridge Decks Using Ground Penetrating Radar. *Computer-Aided Civil and Infrastructure Engineering*, Vol. 23, No. 1, Dec. 2007, pp. 3–16.

66. Shaalan, A. A. Performance Evaluation of GPR System Using Gaussian Pulse Excitation to Cover Entire Frequency Band of Operation. *IETE Journal of Research*, Vol. 55, No. 4, Jul. 2009, pp. 148–153.

67. Guo, L., H. Lin, B. Fan, X. Cui, and J. Chen. Forward Simulation of Root's Ground Penetrating Radar Signal: Simulator Development and Validation. *Plant and Soil*, 2013, pp. 1–19.

68. Li, X.-T. Sublayer-thickness Inversion of Asphalt Layer from Ground Penetrating Radar Data. *Nondestructive Testing and Evaluation*, Vol. 26, No. 2, Jun. 2011, pp. 187–196.

69. Chen, H.-W., and T.-M. Huang. Finite-difference Time-domain Simulation of GPR Data. *Journal of Applied Geophysics*, Vol. 40, No. 1-3, Oct. 1998, pp. 139–163.

70. Ernst, J. R. *2-D Finite-Difference Time-Domain Full-Waveform Inversion of Crosshole Georadar Data (Doctoral Dissertation)*. Swiss Federal Institute of Technology, Switzerland, 2007.

71. Belli, K., C. Rappaport, and S. Wadia-Fascetti. A Time Domain Equivalent Source Model of an Impulse GPR Antenna Based on Measured Radiation Fields. *Research in Nondestructive Evaluation*, Vol. 22, No. 4, Oct. 2011, pp. 197–207.

72. Leng, Z., and I. L. Al-Qadi. Railroad Ballast Evaluation Using Ground-Penetrating Radar. *Transportation Research Record: Journal of the Transportation Research Board*, Vol. 2159, 2010, pp. 110–117.

73. Al-Qadi, I. L., W. Xie, D. L. Jones, and R. Roberts. Development of a Time-frequency Approach to Quantify Railroad Ballast Fouling Condition Using Ultra-wide Band Ground-penetrating Radar Data. *International Journal of Pavement Engineering*, Vol. 11, No. 4, Aug. 2010, pp. 269–279.

74. Lai, W. L., T. Kind, and H. Wiggenhauser. A Study of Concrete Hydration and Dielectric Relaxation Mechanism Using Ground Penetrating Radar and Short-Time Fourier Transform. *EURASIP Journal on Advances in Signal Processing*, Vol. 2010, 2010, pp. 1–14.

75. Roberts, R., I. L. Al-Qadi, E. Tutumluer, and J. Boyle. *Subsurface Evaluation of Railway Track Using Ground Penetrating Radar*. Federal Railroad Administration, U. S. Department of Transportation, 2009.

76. Daubechies, I. *Ten Lectures on Wavelets*. Society for Industrial and Applied Mathematics, Philadelphia, Pennsylvania, USA, 1992.

77. Torrence, C., and G. P. Compo. A Practical Guide to Wavelet Analysis. *Bulletin of the American Meteorological Society*, Vol. 79, No. 1, 1998, p. 61.

78. Mallat, S. G. A Theory for Multiresolution Signal Decomposition: The Wavelet Representation. *IEEE Transactions on Pattern Analysis and Machine Intelligence*, Vol. 11, No. 7, 1989, pp. 674–693.

79. Vetterli, M. Wavelets, Approximation, and Compression. *IEEE Signal Processing Magazine*, No. 5, 2001, pp. 59–73.

80. Chui, C. K. *An Introduction to Wavelets*. Academic Press, San Diego, USA, 1992.

81. Donoho, D. L., and I. M. Johnstone. Adapting to Unknown Smoothness via Wavelet Shrinkage. *Journal of the American Statistical Association*, Vol. 90, Mar. 1995.

82. Young, R. K. *Wavelet Theory and Its Applications*. Kluwer Academic Publishers, Norwell, Massachusetts, USA, 1993.

83. Zhang, H., T. R. Blackburn, B. T. Phung, and D. Sen. A Novel Wavelet Transform Technique for On-line Partial Discharge Measurements Part 1: WT De-noising

Algorithm. *IEEE Transactions on Dielectrics & Electrical Insulation*, Vol. 14, No. 1, Feb. 2007, pp. 3–14.

84. Baili, J., S. Lahouar, M. Hergli, I. L. Al-Qadi, and K. Besbes. GPR Signal De-noising by Discrete Wavelet Transform. *NDT & E International*, Vol. 42, No. 8, Dec. 2009, pp. 696–703.

85. Evans, R., M. Frost, and R. Morrow. Assessing the Influence of Moisture on the Dielectric Properties of Asphalt. *Proceedings of 14th International Conference on Ground Penetrating Radar (GPR)*, 2012, pp. 536–541.

86. Shang, J. Q., and J. A. Umana. Dielectric Constant and Relaxation Time of Asphalt Pavement Materials. *Journal of Infrastructure Systems*, Vol. 5, No. 4, 1999, pp. 135–142.

87. Shang, J. Q. Effects of Asphalt Pavement Properties on Complex Permittivity. *International Journal of Pavement Engineering*, Vol. 3, No. 4, Dec. 2002, pp. 217–226.

88. Rial, F. I., H. Lorenzo, A. Novo, and M. Pereira. Checking the Signal Stability in GPR Systems and Antennas. *IEEE Journal of Selected Topics in Applied Earth Observations and Remote Sensing*, Vol. 4, No. 4, Dec. 2011, pp. 785–790.

89. Saarenketo, T., and T. Scullion. *Ground Penetrating Radar Applications on Roads and Highways*. Texas Department of Transportation, Austin, TX, 1994, p. 52.

90. Liu, L. *State-of-the-Art Rapid Non-Destructive Pavement Assessment: Ground Penetrating Radar (GPR) in Monostatic Survey Mode*. Connecticut Department of Transportation, Storrs, CT, 1999.

91. Scullion, T., C. H. Lau, and T. Saarenketo. Performance Specifications of Ground Penetrating Radar. *Proceedings of the 6th International Conference on Ground Penetrating Radar (GPR)*, 1996, pp. 341–346.

92. Oppenheim, A. V, R. W. Schafer, and J. R. Buck. *Discrete-time Signal Processing (2nd ed.)*. Prentice-Hall, Inc., New Jersey, USA, 1999.

APPENDIX A REFLECTION COEFFICIENT IN A THREE-LAYER MEDIUM

In this chapter, the generalized reflection coefficient for a three-layer medium is derived. The purpose is to derive the theoretical reflection coefficients and compare with the reflection coefficients obtained from simulation and real measurement, when different moisture contents are applied. The three-layer medium is shown in Figure A-1. Region 0 represents air. Region 1 represents the wet AC layer. Region 2 represents the dry AC layer. To simply the discussion, the region 2 is considered as infinite in the –z direction.

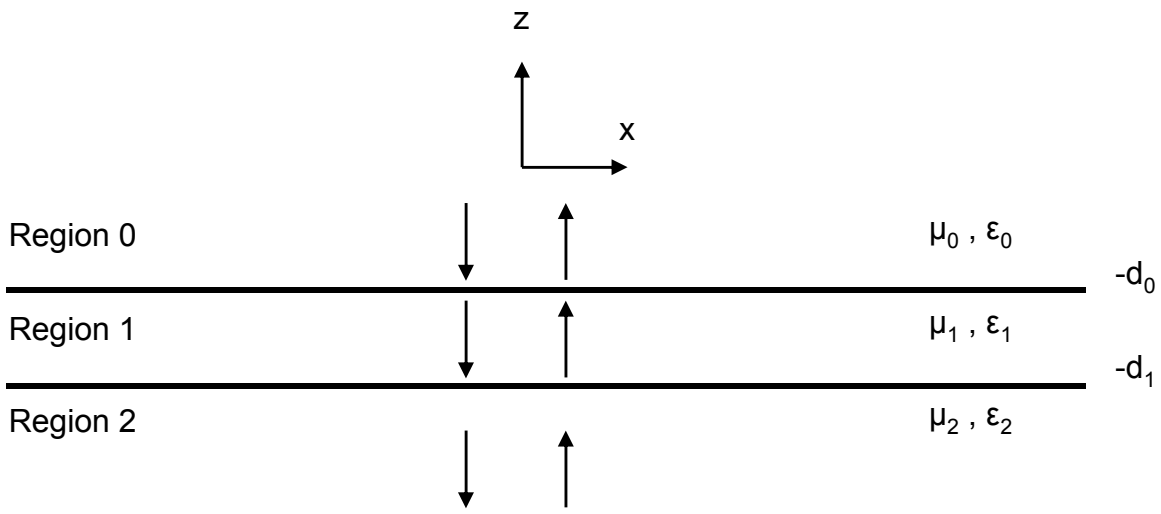

Figure A-1 A three-layer medium

The wave in region 0 can be written as

$$E_{0y} = A_0[e^{-ik_0 z} + \widehat{R_{01}} e^{ik_0 z + 2ik_0 d_0}] \quad \text{(A-1)}$$

where $\widehat{R_{01}}$ is a reflection coefficient that is the ratio of the upgoing wave amplitude and the downgoing wave amplitude at z=-d_0 .

The wave in region 1 can be written as

$$E_{1y} = A_1[e^{-ik_1 z} + R_{12}e^{ik_1 z + 2ik_1 d_1}] \quad \text{(A-2)}$$

where R_{12} is the Fresnel reflection coefficient for a downgoing wave in region 1reflected by region 2 (the region 2 extends to infinity in –*z* direction).

The wave in region 2 can be written as

$$E_{2y} = A_2 e^{-ik_2 z} \quad \text{(A-3)}$$

To solve the unknown parameters A_0, A_1 and A_2, constraint conditions are imposed at three interfaces. First, at the top interface, $z=-d_0$, the constrain condition is

$$A_1 e^{ik_1 d_0} = A_0 e^{-ik_0 d_0} T_{01} + R_{10} A_1 R_{12} e^{2ik_1 d_1 - ik_1 d_0} \quad \text{(A-4)}$$

This is because the downgoing wave in region 1 is a consequence of the transmission of the downgoing wave in region 0 (term 1) and the reflection of the upgoing wave in region 1 (term 2).

Second, at the top interface, $z=-d_0$, another constrain condition can be written

$$A_0 \widehat{R_{01}} e^{ik_0 d_1} = R_{01} A_0 e^{-ik_0 d_0} + T_{10} A_1 R_{12} e^{2ik_1 d_1 - ik_1 d_0} \quad \text{(A-5)}$$

This is because the upgoing wave in retion 0 is a consequence of the reflection of the downgoing wave region 0 and a transmission of the upgoing wave in region 1.

From Equations (A-4) and (A-5), the relation between A_0 and A_1 can be solved:

$$A_1 = \frac{T_{01} A_0 e^{i(k_0 - k_1)d_0}}{1 - R_{10} R_{12} e^{2ik_0(d_1 - d_0)}} \quad \text{(A-6)}$$

Furthermore, the generalized reflection coefficient can be solved:

$$\widehat{R_{01}} = R_{01} + \frac{T_{01}R_{12}T_{10}e^{2ik_1(d_1-d_0)}}{1 - R_{10}R_{12}e^{2ik_1(d_1-d_0)}} \quad \text{(A-7)}$$